TECHNISCHE UNIVERSITÄT MÜNCHEN
TUM SCHOOL OF NATURAL SCIENCES

PHENOMENOLOGY OF BOTTOM-QUARK PAIR PRODUCTION AT THE LHC

ALESSANDRO RATTI

Vollständiger Abdruck der von der TUM School of Natural Sciences der Technischen Universität München zur Erlangung des akademischen Grades eines

Doktors der Naturwissenschaften (Dr. rer. nat.)

genehmigten Dissertation.

Vorsitz:	Prof. Dr. Lukas Heinrich
Prüfende der Dissertation:	1. Prof. Dr. Giulia Zanderighi
	2. Prof. Dr. Lorenzo Tancredi
	3. Prof. Dr. Andreas Weiler

Die Dissertation wurde am 09.09.2024 bei der Technischen Universität München eingereicht und durch die TUM School of Natural Sciences am 01.10.2024 angenommen.

MAX PLANCK INSTITUTE
FOR PHYSICS

PHENOMENOLOGY OF BOTTOM-QUARK PAIR PRODUCTION AT THE LHC

ALESSANDRO RATTI

Novel Computational Techniques in Particle Physics

Max Planck Institute for Physics

August 2024

A Roberta e Luciano.

Abstract

In this thesis, we present our next-to-next-to-leading order (NNLO) QCD predictions for the bottom-quark pair production process at the Large Hadron Collider (LHC), matched with the parton shower (PS). Calculations have been carried out using the MiNNLO$_{\rm PS}$ method within the Powheg MC event generator, as it was presented in its recent extension to the heavy-quark pair production in hadronic collisions. The bottom quarks have been considered massive, while all lighter quarks have been treated in the massless approximation, according to the four-flavour scheme (4FS).

The employed tools, as well as their underlying theoretical framework, are reviewed in the first part of this work. In the second part, we detail our numerical implementation of the process in Powheg, and we perform its validation against fixed-order NNLO predictions obtained within the Matrix program. We then interface the NNLO+PS event generator with the Monte-Carlo parton shower Pythia8, to study the inclusive B-hadron production at the LHC. Our predictions are extensively compared with fiducial cross-sections and differential distributions measured by the ATLAS, CMS, and LHCb experimental collaborations at $\sqrt{s} = 7$TeV and $\sqrt{s} = 13$TeV centre-of-mass energy, as well as with 13TeV/7TeV cross-section ratios. The MiNNLO$_{\rm PS}$ results, which achieve a new level of accuracy for the observables above, showcase a good agreement with data.

A phenomenological study on the bottom-flavoured jet production in $b\bar{b}$ LHC events is also presented. In this case, bottom-pair production events in MiNNLO$_{\rm PS}$ have been provided as an input to Pythia8, to carry out their parton showering and hadronization. In the analysis, the FastJet package is employed to cluster events into hadronic jets, using the anti-k_T sequential recombination algorithm. The main idea of the study was to compare the impact of different jet flavour definitions on various observables. In particular, four jet flavour definitions have been examined. In the first case, the anti-k_T jets have been assigned bottom-flavour when containing at least one B-hadron, and in the second case only jets carrying an odd number of B-hadrons have been tagged as b-jets. The third and fourth case corresponds to the flavour assignment prescribed by two of the algorithms recently advanced to address the problem of jet flavour: the flavour dressing and the interleaved flavour neutralisation algorithms. We remark that the former two jet flavour assignments are infrared-unsafe, while the latter two methods have been designed for the exact purpose of giving infrared-safe results at any order in perturbation theory. We compare the four different predictions both for hardest b-jet and for di-b-jet observables. The most remarkable effect that we witness is due to the different treatment of the quasi-collinear $b\bar{b}$ emissions within the different jet-flavour assignments. However, other minor effects are documented and explained.

Finally, we present predictions for several b-jet cross-sections and differential distributions measured by the LHC collaborations. A remarkable agreement between our calculations and data from ATLAS and CMS is observed for various inclusive b-jet distributions at $\sqrt{s} = 7$TeV. ATLAS measurements of di-b-jet observables at $\sqrt{s} = 7$TeV are also considered in a rather exclusive setup, yielding a good agreement with our predictions but highlighting some shape discrepancies. As for LHCb, the results of a recent b-jet analysis at $\sqrt{s} = 13$TeV are examined, and quite large tensions with our calculations are observed.

We conclude by discussing some possible research outlooks, especially in view of the upcoming MiNNLO$_{\rm PS}$ implementation of the charm-pair production in hadronic collisions.

Zusammenfassung

In dieser Arbeit präsentieren wir unsere Vorhersagen zur Quark-Paar-Produktion zu nächst-zu-nächst-zu führender Ordnung (NNLO) QCD am LHC, die mit dem Parton Shower (PS) kombiniert wurden. Die Berechnungen wurden mit der MiNNLO$_{\rm PS}$ Methode innerhalb des Powheg MC Event-Generators durchgeführt, wie sie in der jüngsten Erweiterung für die Produktion von schweren Quark-Paaren in hadronischen Kollisionen vorgestellt wurde. Die Bottom-Quarks wurden als massiv angenommen, während alle leichteren Quarks in der masselosen Näherung gemäß dem *Four-Flavour-Scheme* (4FS) behandelt wurden.

Die verwendeten Werkzeuge sowie deren theoretische Grundlagen werden im ersten Teil dieser Arbeit beschrieben. Im zweiten Teil erläutern wir unsere numerische Implementierung des Prozesses in Powheg und validieren sie gegen Vorhersagen der festen Ordnung zu NNLO, die mit dem Matrix Programm erhalten wurden. Anschließend koppeln wir den NNLO+PS Event-Generator mit dem Monte-Carlo Parton Shower Pythia8, um die inklusive B-Hadronenproduktion am LHC zu untersuchen. Unsere Vorhersagen werden ausführlich mit Wirkungsquerschnitten und differentiellen Verteilungen verglichen, die von den experimentellen Kollaborationen ATLAS, CMS und LHCb bei $\sqrt{s} = 7$TeV und $\sqrt{s} = 13$TeV sowie mit den Wirkungsquerschnittsverhältnissen 13TeV/7TeV gemessen wurden. Die MiNNLO$_{\rm PS}$ Ergebnisse, die ein neues Maß an Genauigkeit für die oben genannten Observablen erreichen, zeigen eine gute Übereinstimmung mit den Daten.

Eine phänomenologische Studie zur Produktion von bottom-flavoured Jets in $b\bar{b}$ LHC Ereignissen wird ebenfalls vorgestellt. In diesem Fall wurden Bottom-Paar-Produktions-Ereignisse in MiNNLO$_{\rm PS}$ als Eingabe für Pythia8 verwendet, um deren Parton Showering und Hadronisierung durchzuführen. In der Analyse wird das FastJet Paket verwendet, um Ereignisse in hadronische Jets zu gruppieren, wobei der sequentielle anti-k_T Rekombinationsalgorithmus verwendet wird. Die Hauptidee der Studie war es, den Einfluss verschiedener Jet-Flavour-Definitionen auf verschiedene Observablen zu vergleichen. Insbesondere wurden vier Jet-Flavour-Definitionen untersucht. Im ersten Fall wurde den anti-k_T Jets Bottom-Flavour zugewiesen, wenn sie mindestens ein B-Hadron enthalten, und im zweiten Fall wurden nur Jets, die eine ungerade Anzahl von B-Hadrons tragen, als b-Jets markiert. Der dritte beziehungsweise vierte Fall entspricht der Flavour-Zuweisung, die von zwei der kürzlich entwickelten Algorithmen zur Lösung des Jet-Flavour-Problems vorgeschrieben wurde: dem Flavour-Dressing und dem Interleaved-Flavour-Neutralisation Algorithmus. Wir merken an, dass die ersten beiden Jet-Flavour-Zuweisungen infrarot-unsicher sind, während die letzten beiden Methoden genau für den Zweck entwickelt wurden, infrarot-sichere Ergebnisse in jeder Ordnung der Störungstheorie zu liefern. Wir vergleichen die vier verschiedenen Vorhersagen sowohl für die härtesten b-Jet- als auch für die di-b-Jet-Beobachtungsgrößen. Der bemerkenswerteste Effekt, den wir beobachten, resultiert aus der unterschiedlichen Behandlung der quasi-kollinearen $b\bar{b}$-Emissionen innerhalb der verschiedenen Jet-Flavour-Zuweisungen. Andere untergeordnete Effekte werden jedoch dokumentiert und erklärt.

Abschließend präsentieren wir Vorhersagen für mehrere b-Jet-Wirkungsquerschnitte und differentielle Verteilungen, die von den LHC Kollaborationen gemessen wurden. Eine bemerkenswerte Übereinstimmung zwischen unseren Berechnungen und den Daten von ATLAS und CMS wird für verschiedene inklusive b-Jet-Verteilungen bei $\sqrt{s} = 7$TeV beobachtet. ATLAS Messungen von di-b-Jet Beobachtungsgrößen bei $\sqrt{s} = 7$TeV werden ebenfalls in einem

exklusiven Setup betrachtet und zeigen eine gute Übereinstimmung mit unseren Vorhersagen, aber auch einige Formabweichungen. Bei LHCb werden die Ergebnisse einer b-Jet-Analyse bei $\sqrt{s} = 13\text{TeV}$ untersucht, wobei recht große Spannungen mit unseren Berechnungen beobachtet werden.

Wir schließen mit einer Diskussion möglicher Forschungsperspektiven, insbesondere im Hinblick auf die kommende MiNNLO$_{\text{PS}}$ Implementierung der Charm-Paar-Produktion in hadronischen Kollisionen.

Contents

Chapter 1

Introduction

Among the most important achievements of contemporary science, a central role is played by the *Standard Model of particle physics* (SM). Nowadays, the SM is regarded as the most advanced physics theory of the phenomena that govern the elementary particle world. Its current understanding required several decades of efforts from both the experimental and theoretical communities of particle physicists.

In the SM framework, three of the four fundamental interactions known in physics are consistently incorporated into a unified description: the electromagnetic, the weak, and the strong nuclear forces. The way these different interactions manifest and coexist is explained by the gauge symmetries underlying the SM, which is a Yang-Mills quantum field theory based on a $U(1) \times SU(2) \times SU(3)$ symmetry group. The elementary fields of the theory are divided into *fermion* fields, which have semi-integer spin values, and *boson* fields, which have integer spins.

Fermions are the building blocks of ordinary matter and can be further divided into three families of leptons and three families of quarks. Leptons include the electron e^-, muon μ^-, tau τ^-, and their corresponding neutrinos ν_e, ν_μ, ν_τ, and their dynamics are governed by the electroweak (EW) interactions. Quarks come in six different *flavours*: down (d), up (u), strange (s), charm (c), bottom (b), and top (t). Their dynamics are governed by both the electroweak interactions and the strong interactions. The latter are described by *Quantum Chromodynamics* (QCD), which acts on quarks according to the *colour* charges associated with them (red, green, blue). For all the aforementioned leptons and quarks, the respective antiparticles are included in the SM.

On the other hand, bosons are mediators of the fundamental forces, and their existence is necessary to realize the gauge symmetries of the theory. In particular, from the $SU(3)$ colour gauge symmetry in QCD follows the presence of eight massless *gluons*, while the $SU(2) \times U(1)$ weak isospin + weak hypercharge symmetry relates to the presence of four massless bosons mediating the electroweak interactions. However, as experimental evidence suggests, the $SU(2) \times U(1)$ symmetry appears to be spontaneously broken to the electromagnetic $U(1)_{\text{em}}$ gauge group. This phenomenon, independently theorized in 1964 by R. Brout and F. Englert[1], by P. Higgs [2], and by G. Guralnik, C. R. Hagen, and T. Kibble [3], predicts the existence of the massless photon and three weak bosons Z_0, W^+, and W^-, which acquire mass through interactions with a new bosonic field: the *Higgs* field. In general, the Higgs boson allows all fermions of the SM to be massive, thanks to the *Yukawa couplings*.

Although the picture we have just outlined is corroborated by an impressive amount of experimental evidence, some serious issues prevent us from considering the SM as the definitive theory of particle physics. For instance, the theory lacks the inclusion of the gravitational interaction, is based on 19 free parameters not derived from first principles, does not explain

Dark Matter and Dark Energy, and not even the recently discovered fact that neutrinos have mass. How can we then approach the SM? A possible way to look at it is as an *effective theory* of elementary particles that can provide an accurate description of phenomena in a certain range of physical scales. Eventually, the SM will fail at describing experimental phenomena at high energies, but the possibility of observing discrepancies between theoretical predictions and measurements is strongly linked to our ability to achieve *high precision* both in theory and experiments.

Nowadays, a prominent role in particle physics searches at high energies is played by the Large Hadron Collider (LHC), located at CERN, near Geneva (Switzerland). Here, proton beams are accelerated and then made to collide in four different detectors: ALICE, ATLAS, CMS, and LHCb. Since its first measured collisions in 2009, the LHC has significantly advanced our understanding of fundamental physics. The discovery of the Higgs boson in July 2012, carried out by ATLAS and CMS, is regarded as a milestone in contemporary physics. Moreover, the LHC has allowed for the observation of rare particle decays and some of the most precise measurements of the SM couplings and masses.

From a theoretical perspective, a proton-proton inelastic scattering at high centre-of-mass energy can be quantified via the following factorisation formula [4]

$$\sigma(pp \to X) = \sum_{i,j} \int dx_\oplus dx_\ominus \; f_{i/P_1}(x_\oplus) \; f_{j/P_2}(x_\ominus) \; \hat{\sigma}_{ij\to X}(\hat{s}) \;\; + \;\; \mathcal{O}\left(\frac{\Lambda_{\rm QCD}}{Q}\right) \,, \tag{1.1}$$

where $\sigma(pp \to X)$ is the total cross section for the production of a certain final state X. What eq. (1.1) tells us is that, up to some power corrections $\mathcal{O}(\Lambda_{\rm QCD}/Q)$, σ is the sum of elementary cross sections $\hat{\sigma}$ given by the interactions of free-moving primary *partons* (i.e. quarks and gluons), coming from the composite structure of the protons. We will then have one parton i from the left-coming proton P_1 and one parton j coming from the right-coming P_2. Parton i will undergo the scattering carrying a fraction $0 \leq x_\oplus \leq 1$ of the left-coming proton momentum P_1^μ, with a probability encoded in the *parton distribution function* (PDF) $f_{i/P_1}(x_\oplus)$, and analogously for parton j. The elementary cross section $\hat{\sigma}_{ij\to X}(\hat{s})$ will then depend on the flavours of the i, j pair and on a flux factor depending on the invariant mass of the partonic system $\hat{s} = (x_\oplus P_1 + x_\ominus P_2)^2$. To get the total cross section $\sigma(pp \to X)$, this will be summed over all possible flavour configurations of i, j and integrated over $0 \leq x_\oplus, x_\ominus \leq 1$. The great advantage of eq. (1.1) is that it reduces the problem of calculating hadronic cross sections to the problem of calculating cross sections of elementary particles (quarks, leptons, bosons). In particular, the SM couplings appear to be much smaller than 1 at the *hard scattering* ($ij \to X$) energy scales, allowing for the computation of $\hat{\sigma}_{ij\to X}(\hat{s})$ as a perturbative series of the couplings themselves. This involves, for instance, the computation of *scattering amplitudes* through the popular *Feynman diagrams*.

Generally, the most relevant contributions to the hard scatterings will come from QCD, as its strong coupling constant $\alpha_s \sim 0.1$ is around one order of magnitude larger than the EW couplings. Specifically, QCD can enter the computation of a hard scattering cross section both at the lowest order, the so-called *Leading Order* (LO), and at the following orders, namely the *Next-to-Leading Order* (NLO), the *Next-to-Next-to-Leading Order* (NNLO), and so on. These are the building blocks of the so-called *fixed order* computations, which nowadays represent one of the most powerful tools in precision physics. One of the consequences of considering corrections to eq. (1.1) beyond the leading order is the appearance of two

new scales: the factorization scale μ_F in PDFs, and the renormalisation scale μ_R in loop amplitudes. Their origins and treatment will be discussed thoroughly in the first part of this thesis.

Unfortunately, fixed order calculations are limited by some serious constraints. The most obvious one is the complexity of scattering amplitudes, which increases exponentially with the multiplicity of external particles and internal loops. As a consequence, exact results can be obtained only when considering final states X with a small number of particles, and fully *inclusive* (i.e. agnostic) over additional emissions. Moreover, realistic calculations often include some *large logarithmic* terms depending on ratios of some relevant physical scales, which appear at all orders and can endanger the convergence of the perturbative series. To overcome these problems, several approaches based on all-order *resummation* techniques have been proposed. *Parton Showers* provide an effective way to perform a numerical resummation through the application of Monte Carlo techniques. Indeed, these programs generate additional QCD (and EW) radiation starting from a fixed order configuration, simulating fully exclusive events similar to the ones observed at the LHC. Numerical techniques to reproduce non-perturbative effects, like the hadronization of showered partons at low energy scales and the decay of unstable hadrons, have also been studied and are nowadays incorporated with the Parton Shower within the so-called *General Purpose Monte Carlo* event generators (GPMC). On the other hand, interfacing fixed order predictions with GPMC is a non-trivial problem, and some methods have been developed to perform this *matching*. We also mention that GPMC manages to reproduce a peculiarity of QCD events, namely the fact that partons tend to be emitted in sprays of collimated radiation, forming *hadronic jets*. Ultimately, we will see that there is a leitmotif connecting this and all the aforementioned features of QCD, which is the *infrared* structure of the theory.

In the first part of this thesis, we will review the main features of fixed order calculations in chapter 2, as well as the general principles of Parton Showers and the strategies to perform their fixed order matching in chapter 3. We will mainly focus on the POWHEG method, which allows for the matching at NLO, and on its NNLO extension provided by the MiNNLO$_{\text{PS}}$ method. In chapter 4, we will summarize the basic concepts of hadronic jet physics in QCD.

The second part of the thesis will be devoted to presenting new phenomenological results related to a specific process that we examined: the inclusive *bottom-pair hadroproduction* ($pp \to b\bar{b} + X$). Given the large theoretical uncertainties related to this process, as we will discuss, high accuracy is fundamental for allowing a meaningful comparison with the huge amount of experimental measurements linked to it. In chapter 5, we will present the setup of our MiNNLO$_{\text{PS}}$ bottom-pair production generator in POWHEG, which represents the first NNLO+PS implementation available in literature. The main phenomenological applications of the event generator will be explored in chapter 6 and chapter 7. In particular, we will carry out an extensive comparison with LHC data on B-hadron production in chapter 6, while chapter 7 will be devoted to a study on the b-flavoured jet phenomenology in bottom-pair production events, along with a comparison with the LHC measurements.

In chapter 8, we will sum up the conclusions of our research and discuss possible future directions of research.

In this thesis, results reported in chapter 5 and 6 were originally presented in the following publication by the author:

- Javier Mazzitelli, Alessandro Ratti, Marius Wiesemann, and Giulia Zanderighi. B-hadron production at the LHC from bottom-quark pair production at NNLO+PS. *Phys. Lett. B*, 843:137991, 2023. doi: 10.1016/j.physletb.2023.137991

while results reported in chapter 7 will be the object of upcoming publications.

Part I

Theory and Tools for Precision Physics at the LHC

Chapter 2

Perturbative Calculations in QCD

2.1 The QCD Lagrangian

The Quantum Chromodynamics (QCD) lagrangian describes the strong interactions in terms of couplings involving quark and gluon fields. It is a Yang-Mills theory based on the gauge group $SU(3)$, acting on the colour algebra of the quark and gluon fields. Formally, it reads [6]

$$\mathcal{L}_{QCD} = -\frac{1}{4} F^{(a)}_{\mu\nu} F^{\mu\nu(a)} + \sum_f \bar{q}^i_f \left(i\gamma^\mu (D_\mu)_{ij} - m_f \delta_{ij} \right) q^j_f. \tag{2.1}$$

Here, quarks figure both with a flavour index f ($f = u, d, s, c, t, b$) and with a colour index i ($i = r, b, g$). $F^{(a)}_{\mu\nu}(x)$ is the gluon field strength, defined as

$$F^{(a)}_{\mu\nu} = \partial_\mu G^{(a)}_\nu - \partial_\nu G^{(a)}_\mu + g_s f^{abc} G^{(b)}_\mu G^{(c)}_\nu, \tag{2.2}$$

where $G^{(a)}_\mu(x)$ is the gluon field, with colour index $a = 1, \ldots, 8$, while g_s represents the coupling constants associated to interactions between colour quanta. We have also introduced the covariant derivative

$$(D_\mu)_{ij} = \delta_{ij}\partial_\mu - i g_s (t^a)_{ij} G^{(a)}_\mu. \tag{2.3}$$

where $t^{(a)}$ ($a = 1, \ldots, 8$) are the generators of the $\mathfrak{su}(3)$ Lie algebra. The group elements of $SU(3)$ are obtained via exponentiation of $\mathfrak{su}(3)$, as

$$U(x) \;=\; \exp[-i g_s \xi_a t^a] \,, \tag{2.4}$$

where ξ_a are the parameters of the local $SU(3)$ transformation. Quark fields live in the *fundamental* representation of $SU(3)$, thus transforming as

$$\begin{aligned} q'^i_f(x) &= [U(x)]_{ij}\, q^j_f(x) \\ \bar{q}'^i_f(x) &= \bar{q}^j_f(x) \left[U^\dagger(x) \right]_{ji} \,, \end{aligned}$$

while gluon fields live in the *adjoint* representation, and transform as

$$[G^\mu(x)]'_{ij} = \left[U(x) \cdot G^\mu(x) U^{-1}(x) \right]_{ij} + \frac{i}{g_s} \left[\partial^\mu U(x) U^{-1}(x) \right]_{ij} \,, \tag{2.5}$$

where we introduced the matrix field

$$[G^\mu(x)]_{ij} = \sum_{a=1}^{8} G_a^\mu(x) t_{ij}^a. \tag{2.6}$$

QCD can be quantized by using the standard path integral formalism. To deal with the gauge redundancy of the theory, it is standard to apply the Faddeev-Popov procedure. In this framework, some new grassmann-odd ghost fields c^a appear, although being actually scalar fields. They obey a *wrong statistics*, which makes them unphysical degrees of freedom. The QCD lagrangian is then enriched by the presence of a new term

$$\mathcal{L}_{FP} = \bar{c}^a \left(\partial^\mu D_\mu^{ac}\right) c^c, \tag{2.7}$$

where

$$D_\mu^{ac} = \delta^{ac}\partial_\mu - g_s f^{abc} G_\mu^a \,, \tag{2.8}$$

together with another gauge-fixing term, depending on a specific gauge choice. In the covariant gauge, for example, we will have

$$\mathcal{L}_{GF} = -\frac{1}{2\xi}\left(\partial_\mu G_a^\mu\right)^2 . \tag{2.9}$$

Whithin the assumption of g_s to be small, it is possible to carry out QCD calculation of physical observables in perturbation theory.

2.2 Ultraviolet Divergences in QCD

When computing loop integrals in QCD, it turns out that most of them give divergent contributions, whose interpretation might (and it effectively was in the past) puzzling. Today, we know that these infinities are due to an uncorrect interpretation of the parameters entering the lagrangian in eq. (2.1). These are indeed *bare* parameters and in fact cannot be measured. What can be measured, is the set of *renormalised* parameters of the theory, which relates to the bare parameters through the renormalisation contants. Before introducing them, it is convenient to rewrite eq. (2.1) in a form where all the coupling terms are explicit. After arranging the different flavoured quark fields q_f in a single vector Ψ, we can write

$$\begin{aligned}\mathcal{L}_{QCD} = &-\frac{1}{4}F_{0\mu\nu}^{(a)}F^{0\mu\nu\,(a)} + \bar{\Psi}_0(i\not{D} + m_0)\Psi_0 - \bar{c}_0^a\partial^2 c_0^a + g_0\bar{\Psi}_0\gamma^\mu t^a\Psi_0 A_{0\mu}^a \\ &- g_0 f_{abc}(\partial_\mu A_{0\nu}^a)A_0^{b\mu}A_0^{c\nu} - \frac{g_0^2}{4}f_{abc}f_{dec}A_{0\mu}^a A_0^{b\mu}A_0^{c\nu}A_0^{d\nu} - g_0 f_{abc}\bar{c}_0^a(\partial^\mu c_0^b)A_{0\mu}^c,\end{aligned} \tag{2.10}$$

where the subscript 0 means bare quantitity. Now we express every bare term $\Delta\mathcal{L}_0$ of the lagrangian in terms of renormalised parameters by mean of a renormalisation constant Z

$$\Delta\mathcal{L}_0 \;=\; Z\,\Delta\mathcal{L}\,, \tag{2.11}$$

so that the full QCD lagrangian will be

$$\begin{aligned}\mathcal{L}_{QCD} = &-\frac{1}{4}Z_3 F^{(a)}_{\mu\nu}F^{\mu\nu\,(a)} + Z_2\bar{\Psi}(i\not{D} + m)\Psi - Z_c\bar{c}^a\partial^2 c^a + Z_1 g\bar{\Psi}\gamma^\mu t^a\Psi A^a_\mu \\ &- Z_1^3 g f_{abc}(\partial_\mu A^a_\nu)A^{b\mu}A^{c\nu} - Z_1^4 g^2 f_{abc}f_{dec}A^a_\mu A^{b\mu}A^c_\nu A^{d\nu} - Z_1^c g f_{abc}\bar{c}^a(\partial^\mu c^b)A^c_\mu, \quad (2.12)\end{aligned}$$

or, rewriting every renormalisation constant as $Z = 1 + \delta Z$':

$$\begin{aligned}\mathcal{L}_{QCD} = &-\frac{1}{4}F^{(a)}_{\mu\nu}F^{\mu\nu\,(a)} + \bar{\Psi}(i\not{D} + m)\Psi - \bar{c}^a\partial^2 c^a + g\bar{\Psi}\gamma^\mu t^a\Psi A^a_\mu \\ &- g f_{abc}(\partial_\mu A^a_\nu)A^{b\mu}A^{c\nu} - g^2 f_{abc}f_{dec}A^a_\mu A^{b\mu}A^c_\nu A^{d\nu} - g f_{abc}\bar{c}^a(\partial^\mu c^b)A^c_\mu + \mathcal{L}_{\text{counter}}.\end{aligned} \quad (2.13)$$

From this definitions of the renormalisation constants, it is possible to derive the relation between the physical parameters and the bare ones. In this case, the field normalisations obey the following relations

$$\Psi_0 = \sqrt{Z_2}\Psi, \quad A^{a\mu}_0 = \sqrt{Z_3}A^{a\mu}, \quad c^a_0 = \sqrt{Z_c}c^a\ , \quad (2.14)$$

while for the coupling constant it holds, among the others, the following relation

$$Z_1 g = Z_2\sqrt{Z_3}g_0\ . \quad (2.15)$$

By computing systematically the 1-loop divergent amplitudes of the theory, it is possible to extract all the UV singularities that will enter the definition of the counterterms (thus inside the $\delta Z'$s). Being QCD a renormalisable theory, a finite number of counterterms will be sufficient to make the theory free of UV divergences and predictive at any order.
Nevertheless, computing the UV divergent loop amplitudes requires the adoption of a regularisation technique, namely a way to parametrize the divergence. Several examples have been proposed in literature to do this, but the most widely used in QCD calculations is the *dimensional regularisation*, which preserves the gauge invariance of the integrals. In this context, the QCD lagrangian is modified in a way that loop integrals turn out to be evaluated in $d = 4 - 2\epsilon$, where ϵ is a small positive parameter. By doing this, an additional mass scale μ_R must be introduced in eq. (2.12). Such scale, called *renormalisation scale*, has arbitrary value and a deep physical impact on the theory. Indeed, the requisite that physical observables must be independent on the choice of μ_R leads to the Callan-Symanzik equations, predicting the parameters of the theory evolve with the energy scale Q of the process in exam. In this sense, relevant phenomenological predictions are linked to the evolution of the strong coupling constant $\alpha_s = g_s^2/4\pi$. Defining $t = \log(Q^2/\mu_R^2)$, one finds

$$\frac{\partial\alpha_s(Q^2)}{\partial t} = \beta(\alpha_s(Q^2))\ , \quad (2.16)$$

where the β-function can be evaluated in renormalised perturbation theory. At 1-loop order, it reads

$$\beta(\alpha_s^2) = -\frac{\alpha_s^2}{4\pi}\left\{\frac{11}{3}C_A - \frac{2}{3}n_f\right\}\ , \quad (2.17)$$

where n_f represents the number of quark flavours and $C_A = 3$ (number of colours) is the Casimir of $SU(3)$ in the adjoint representation. By solving Eq. (2.26) we find that α_s actually decreases with the increasing of Q, obeying the equation

$$\alpha_s(Q^2) = \frac{\alpha_s(\mu_R^2)}{1 + \alpha_s(\mu_R^2) \cdot b \cdot \log(Q^2/\mu_R^2)} \,, \tag{2.18}$$

with $b = (33 - 2n_f)/12\pi$ (> 0 for $n_f = 6$).

A meaningful consequence of eq. (2.18) is represented by the concept of asymptotic freedom. When quarks and gluons approach high energies, α_s becomes low enough to let them behave as approximately free particles. In this context, processes can be analyzed using perturbation theory. This is the case of the parton composing hadrons which collide in deep inelastic scatterings. In the configuration space, this means that the nearer quarks are between each other, the more they behave as free particles. However, eq. (2.18) describes the sole α_s evolution with energy, but not its physical value, which has to be determined in experiments. Experiments show, for instance, that $\alpha_s(Q = 1\text{GeV}) \approx 0.4$: conventionally, this is the lowest energy scale where the perturbative approach is considered valid.

Another crucial phenomenon which we have to consider is the colour confinement, deeply related to the asymptotic freedom we have just discussed. Given the its evolution, it is natural wondering about what happens when $\alpha_s(Q^2)$ becomes too big to be used in a perturbative context. In this sense, a couple observations can be done. Indeed, we can try to get rid of the μ dependence in eq. (2.16). Firstly we separate variables as follows

$$\frac{d\alpha_s}{\beta(\alpha_s)} = dt, \tag{2.19}$$

and then we integrate both sides

$$\int_{\alpha_s(Q^2)}^{\infty} \frac{d\alpha_s}{\beta(\alpha_s)} = \int_{Q^2}^{\Lambda^2} dt, \tag{2.20}$$

where we have introduced a Λ fixed energy scale where we expect that α_s diverges. Eventually, such parameter can be determined in experiments (its measured value is $\Lambda \sim 200$ MeV). Now, performing the integrations, we get

$$\int_{\alpha_s(Q^2)}^{\infty} \frac{d\alpha_s}{\beta(\alpha_s)} = -\log\left(\frac{Q^2}{\Lambda^2}\right), \tag{2.21}$$

where the dependence on μ has been eliminated. Again, eq. (2.16) can be solved in perturbation theory, and we obtain at 1-loop order

$$\alpha_s(Q^2) = \frac{1}{b\log(Q^2/\Lambda^2)}. \tag{2.22}$$

This result explains the phenomenon of colour confinement. Λ is interpreted as a delimitation of the energy region where quarks appear to be strongly bounded. In the configuration space, this implies that quarks can't figure as separate entities and they are always confined

into hadrons. Indeed, hadrons bound states figure as colour singlets

$$\bar{q}^i q_i, \quad \epsilon^{ijk} q_i q_j q_l, \quad \epsilon^{ijk} \bar{q}_i \bar{q}_j \bar{q}_l,$$

respectively for mesons, baryons and antibaryons.

In closing, confinement is also responsible for the hadronisation process: in scatterings, final state partons cannot be directly detected, because other quarks are produced in the void around them in order to create colour singlets.

2.3 Electron-Positron Collisions and QCD corrections

Having introduced the QCD lagrangian and quickly highlighted some important aspects of renormalisation in QCD, we have now all the necessary ingredients to start making some physically interesting computations.
A really simple, albeit significative, process that we can study is the quark-antiquark production in electron-positron collisions mediated by a virtual photon γ^* [7], namely

$$e^- e^+ \quad \to \quad \gamma^* \quad \to \quad q\bar{q} \,, \tag{2.23}$$

in the massless quark approximation[1] What we aim to do now is to compute the total cross section of the process, therefore we start writing down the relevant feynman amplitudes contributing at the LO

$$\mathcal{A}_{q\bar{q}} \;=\; \mathcal{A}^{(0)}_{q\bar{q}} \;+\; \mathcal{O}(\alpha_s) \,. \tag{2.24}$$

In this case, the only tree-level Feynman diagram we can consider corresponds to the s-channel in fig. 2.1, whose amplitude reads

$$\mathcal{A}^{(0)}_{q\bar{q}} \;=\; \mathcal{M}^{\mu}_0 \; \bar{u}(p)(-ie\gamma^{\mu})v(p') \,, \tag{2.25}$$

where we used $\mathcal{M}^{\mu}_0$ to denote the $e^+e^- \to \gamma^*$ subamplitude, which remains fixed when going at higher QCD orders. By taking the squared of eq. (2.24) and performing the final-state phase space integration[2], one finally gets the LO cross section, summed over the quark flavours f

$$\sigma_{\text{LO}} \equiv \sigma(e^+e^- \to q\bar{q}) = \sigma_0 N \sum_f Q_f^2 \,, \tag{2.26}$$

where $N = 3$ is the number of colours, $\sigma_0 \equiv \frac{4\pi\alpha_s^2}{3E^2_{\text{cm}}}$ is the cross section of the leptonic scattering $e^+e^- \to \mu^+\mu^-$, and Q_f is the charge of the outgoing quark q_f in units of the positron charge, and depends on the flavour f.

If we want now to compute increase the perturbative accuracy of the result in eq. (2.26), we

[1] In the context of high energy collisions carried out in modern experiments, this is still considered a valid approximation for all quarks except from the top. Howevere, there are some subtelties that we will not focus on here. For now, we just imagine $q\bar{q}$ in eq. (2.23) to be a pair of light quarks, whatever the definition of *light quark* may signify in this context.

[2] And accounting for the sums/averages over colours and spin helicities

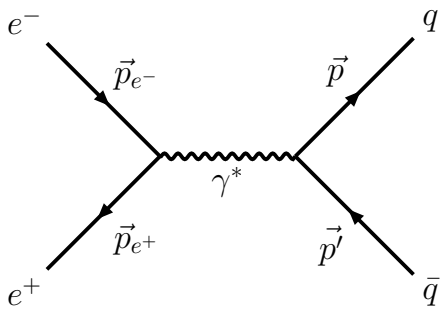

Figure 2.1: Feynman diagram for $e^+e^- \to \gamma \to q\bar{q}$

would naturally thing about including the 1-loop corrections to the amplitude in eq. (2.24)

$$\mathcal{A}_{q\bar{q}} \;=\; \mathcal{A}^{(0)}_{q\bar{q}} \;+\; \underbrace{\mathcal{A}^{(1)}_{q\bar{q}}}_{\text{1-loop}} + \mathcal{O}(\alpha_s)\,, \tag{2.27}$$

where $\mathcal{A}^{(1)}_{q\bar{q}}$ includes the 1-loop quark self energy corrections (in fig. 2.2b) and the 1-loop vertex correction to $\gamma^* \to q\bar{q}$ (in fig. 2.2a). Once we work out the calculations within the renormalised theory, the loop intrgrals will not produce UV ϵ poles. However, two new classes of singularities will arise, which can be parametrized in dimensional regularisation by using $d = 4 + 2\epsilon$ ($\epsilon > 0$):

- **Soft singularities**, occuring when the loop momentum vanishes.
- **Collinear singularities**, occurring in the loop integration regions where the loop momentum becomes parallel to an external (on-shell) momentum.

Then, squaring eq. (2.28), we get

$$|\mathcal{A}_{q\bar{q}}|^2 \;=\; |\mathcal{A}^{(0)}_{q\bar{q}}|^2 \;+\; \underbrace{2\,\Re(\mathcal{A}^{(0)*}_{q\bar{q}}\mathcal{A}^{(1)}_{q\bar{q}})}_{\text{1-loop}} + \mathcal{O}(\alpha_s)\,, \tag{2.28}$$

and integrating over the $q\bar{q}$ final state phase space, we end up with[3]

$$\sigma_{\text{NLO}} = \sigma_{\text{Born}} + \sigma_{\text{Virt}} \tag{2.29}$$

$$\sigma_{\text{Virt}} = \sigma_{\text{Born}} C_F \frac{\alpha_s}{2\pi} H(\epsilon) \left(-\frac{4}{\epsilon^2} - \frac{3}{\epsilon} - 8 + \pi^2 + O(\epsilon) \right)\,, \tag{2.30}$$

$H(\epsilon)$ representing a regular function in ϵ.

The question now is how to give a sense to the results in eq. (2.29) and eq. (2.30). Thinking about the point we started from, namely calculating the NLO cross section for the process in eq. (2.23), we try to see what happens if we relax the requirement to have just a $q\bar{q}$ pair

[3]Here we also introduced a rather general notation: *Born* refers to the leading-order contribution to the cross section (coming from the squared tree level amplitude, in this case). *Virtual* represents the 1-loop contribution, that here appears as the interference between the tree-level and the 1-loop diagrams.

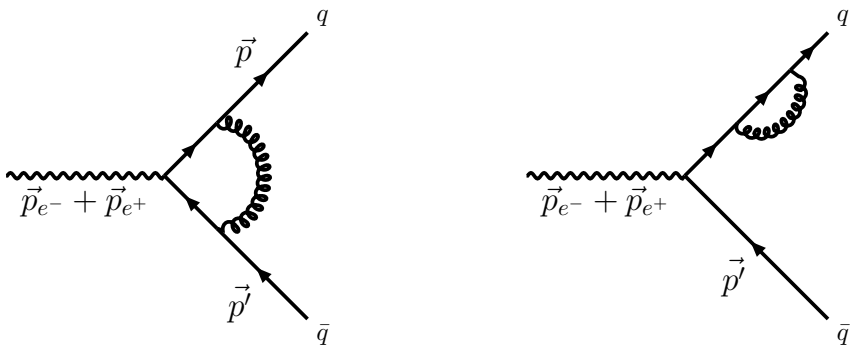

(a) Gluon vertex correction to $\gamma^* \to q\bar{q}$ splitting.

(b) Self-energy correction to outgoing quark line.

Figure 2.2: QCD loop corrections to $q\bar{q}$ production in e^-e^+ collisions.

in the final state. This corresponds to considering a process

$$e^-e^+ \quad \to \quad \gamma^* \quad \to \quad q\bar{q} \; + \; X \; , \tag{2.31}$$

where X represents additional QCD radiation, without specifying any further. This implies, in particular, that now the NLO cross section will also receive contributions from the amplitude[4]

$$\mathcal{A}_{q\bar{q}g} \; = \; g_s \mathcal{A}^{(0)}_{q\bar{q}g} \; + \; \mathcal{O}(g_s^3) \; , \tag{2.32}$$

so that the NLO cross section will be computed as

$$\sigma_{\text{NLO}} \; = \; \int d\Phi_{q\bar{q}} \Big[\underbrace{|\mathcal{A}^{(0)}_{q\bar{q}}|^2}_{\textbf{Born}} + \underbrace{2\Re(\mathcal{A}^{(0)*}_{q\bar{q}} \mathcal{A}^{(1)}_{q\bar{q}})}_{\textbf{Virtual}} \Big] \; + \; \int d\Phi_{q\bar{q}g} \underbrace{|\mathcal{A}^{(0)}_{q\bar{q}g}|^2}_{\textbf{Real}} \; + \; + \mathcal{O}(\alpha_s^2) \; . \tag{2.33}$$

Where we defined the *real* matrix element. To evaluate it, we start as usual by computing the amplitude using the Feynman rules. In this case, we can have a gluon emission coming from either the outgoing quark or antiquark (as represented in fig. 2.3). Using a similar notation to the one introduced in eq. (2.25), we define

$$\mathcal{A}^{(0)}_{q\bar{q}g} \; = \; \underbrace{\mathcal{M}_{0\,\mu}}_{e^+e^- \to \gamma^*} \; \mathcal{M}^{\mu}_{\text{rad}} \; , \tag{2.34}$$

and $\mathcal{M}^{\mu}_{\text{rad}}$ will read

$$\mathcal{M}^{\mu}_{\text{rad}} = \bar{u}(p)(-ig_s t^a \not{\epsilon}(k)) \frac{i(\not{p} + \not{k})}{(p+k)^2} (-ie\gamma^\mu) v(p') + \bar{u}(p)(-ie\gamma^\mu) \frac{i(\not{p}' - \not{k})}{(p'-k)^2} (-ig_s t^a \not{\epsilon}(k)) v(p'). \tag{2.35}$$

We proceed by squaring the whole amplitude $\mathcal{A}^{(0)}_{q\bar{q}g}$. Using the colour algebra, and sum-

[4]Notice that $\mathcal{A}^{(0)}_{q\bar{q}g}$ has a $g_s \sim \alpha_s^{\frac{1}{2}}$ constant coming from the vertex of the real gluon emission in fig. 2.3. We factorized it out in eq. (2.32)

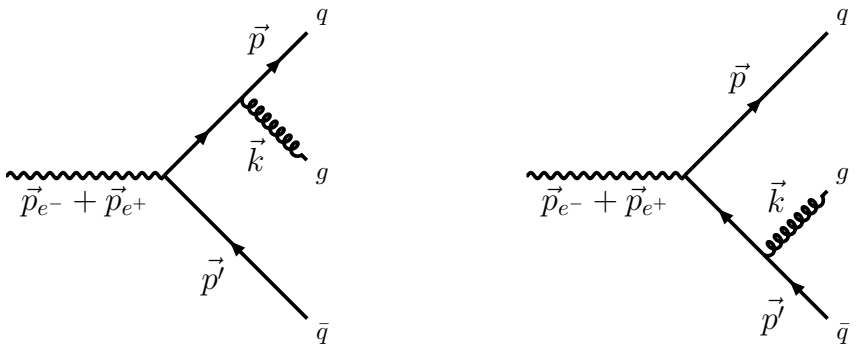

Figure 2.3: Radiative corrections to $e^-e^+ \to q\bar{q}$.

ming/averaging over final/initial state spins and colours we get

$$|\mathcal{A}^{(0)}_{q\bar{q}g}|^2 = \frac{4e^2Q_q^2 f_g^2 g_s^2 N_c}{s} C_F \frac{(p\cdot p_{e^-})^2 + (p\cdot p_{e^+})^2 + (p'\cdot p_{e^-})^2 + (p'\cdot p_{e^+})^2}{(p\cdot k)(p'\cdot k)}. \tag{2.36}$$

Finally, we integrate $|\mathcal{A}^{(0)}_{q\bar{q}g}|^2$ over the final state phase space. More specifically, $d\Phi_{q\bar{q}g}$ is given by the standard 3-body massless phase space

$$d\Phi_3(p_{e^-} + p_{e^-}; p, p', k) = \delta^4(p_{e^-} + p_{e^+} - p - p' - k)\frac{d^3p}{(2\pi)^3 2E}\frac{d^3p'}{(2\pi)^3 2E'}\frac{d^3k}{(2\pi)^3 2E_k}. \tag{2.37}$$

If we perform the explicit calculations in the CM reference frame, a couple of simplifications occur. Indeed, we can exploit the Dirac delta over the three-momenta $\delta^3(\vec{p}+\vec{p'}+\vec{k})$ to get rid of the integration over d^3k

$$d\Phi_3(p_{e^-} + p_{e^+}; p, p', k) = \delta^4(p_{e^-} + p_{e^+} - p - p' - k)\frac{d^3p}{(2\pi)^3 2E}\frac{d^3p'}{(2\pi)^3 2E'}\frac{d^3k}{(2\pi)^3 2E_k} \tag{2.38}$$

$$= \frac{1}{2(2\pi)^3 k}\frac{dp\, d\cos\theta\, d\phi}{2(2\pi)^3}\frac{dp'\, d\cos\beta\, d\alpha}{2(2\pi)^3}\delta(\sqrt{s} - p - p' - k)\ , \tag{2.39}$$

where we have defined the z axis along the initial-state beam. We have also parametrized $\vec{p}$ and $\vec{p'}$ in polar coordinates as

$$\begin{aligned} p^\mu &= (p, p\sin\theta\cos\phi, p\sin\theta\sin\phi, p\cos\theta) \\ p'^\mu &= (p', p'\sin\beta\cos\alpha, p'\sin\beta\sin\alpha, p'\cos\beta)\ , \end{aligned} \tag{2.40}$$

denoting $p = |\vec{p}|, p' = |\vec{p'}|, k = |\vec{k}|$. Furthermore, integrating the last δ over $d\beta$, one can get an even simpler form for the three-particle phase space

$$d\Phi_3(p_{e^-} + p_{e^+}; p, p', k) = \frac{1}{8(2\pi)^9} dp\, d\cos\theta\, d\phi\, dp'\, d\alpha \tag{2.41}$$

$$= \frac{s}{16(2\pi)^7} dx_1\, dx_2 \frac{d\cos\theta\, d\phi\, d\alpha}{2(2\pi)^2}. \tag{2.42}$$

where in the last step we have adopted the new variables $x_1 = 2p/\sqrt{s}$ and $x_2 = 2p'/\sqrt{s}$

(with $0 < x_i < 1$). Given the above, we can finally write the contribution of the real gluon emissions to the total cross section as

$$\sigma_{\text{real}} = \frac{1}{2s}\frac{s}{16(2\pi)^7}\int dx_1 dx_2 \frac{d\cos\theta\, d\phi\, d\alpha}{2(2\pi)^2}|\mathcal{A}^{(0)}_{q\bar{q}g}|^2 \,, \tag{2.43}$$

and replacing $\mathcal{M}_{\text{rad}}$ expressed in the new variables, some easy simplifications lead to

$$\sigma_{\text{real}} = \sigma_{\text{Born}} C_F \frac{\alpha_s}{2\pi}\int dx_1 dx_2 \frac{x_1^2 + x_2^2}{(1-x_1)(1-x_2)}. \tag{2.44}$$

where the integration above $d\cos\theta, d\phi, d\alpha$ has been carried out, and the Born level cross section results factorized. In eq. (2.43), we encounter some singularities that are really reminiscent of what we found in the virtual correction in eq. (2.30). Indeed, divergences appear now in two situations:

- **Collinear divergences**: when either x_1 or x_2 is fixed, and meanwhile $x_2/x_1 \to 1$. Physically, this happens in the phase space regions with the outgoing q and $\bar{q}$ has parallel momenta.
- **Soft divergences**: when the ratio $(1-x_1)/(1-x_2)$ is fixed, and meanwhile $x_1, x_2 \to 1$. Physically, this is linked to the gluon momentum approaching zero.

To understand better these divergences, we can arrange in a different way the same calculations seen above. Taking, for instance, k^μ parallel to p'^μ, we can write them as

$$k' = (1-z)q, \quad k = zq \,, \tag{2.45}$$

with $0 < z < 1$ and $q^2 = 0$. It is possible to calculate that, in this approximation (*collinear approximation*), the squared matrix amplitude $|\mathcal{M}_{\text{rad}}|^2$ factorizes as

$$|\mathcal{A}^{(0)}_{q\bar{q}g}|^2 \to |\mathcal{A}^{(0)}_{q\bar{q}}|^2 \frac{g_s^2}{p'\cdot k} C_F \frac{1+(1-z)^2}{z}, \tag{2.46}$$

and the phase space factorizes as well, because

$$dx_1 d\cos\theta\, d\phi\, dx_2\, d\alpha \to d\cos\theta\, \frac{1}{4} z(1-z)\, dz\, d\theta_{23}^2\, d\phi, \tag{2.47}$$

where we have used the angle θ_{23}^2 between $\vec{p}'$ and $\vec{k}$. Putting these results together, the cross section in the collinear limit reads

$$\sigma_{\text{real}} = \sigma_{\text{Born}} \int \frac{d\theta_{23}^2}{\theta_{23}^2} dz \frac{\alpha_s}{2\pi}\frac{1+(1-z)^2}{z} \,, \tag{2.48}$$

which diverges for $\theta_{23} \to 0$ (or π).
A similar reasoning can be done for the soft divergences. Under the approximation that the gluon momentum approaches zero, $\mathcal{M}_{\text{rad}}$ factorizes as

$$\mathcal{A}^{(0)}_{q\bar{q}g} \to \mathcal{A}^{(0)}_{q\bar{q}g}\, g_s t^a_{ij} \left(\frac{p^\mu}{p\cdot k} - \frac{p'^\mu}{p'\cdot k}\right)\epsilon_a(k) \,, \tag{2.49}$$

where the term in parenthesis is the *eikonal current* J^μ. Squaring $\mathcal{A}_{q\bar{q}g}$ in the soft-gluon approximation, we get

$$|\mathcal{A}^{(0)}_{q\bar{q}g}|^2 \to |\mathcal{A}^{(0)}_{q\bar{q}}|^2 g_s^2 C_F \frac{2p\cdot p'}{(p\cdot k)(p'\cdot k)} \,, \tag{2.50}$$

and in the phase space we have that $dx_1 dx_2 \to (2/s) E_k \, dE_k \, d\cos\theta$, so that we eventually find

$$\sigma_{\text{real}} = \sigma_{\text{Born}} C_F \frac{\alpha_s}{2\pi} \int \frac{dE_k}{E_k} d\cos\theta \frac{2(1-\cos\theta_{q\bar{q}})}{(1-\cos\theta_{qg})(1-\cos\theta_{\bar{q}g})} \,, \tag{2.51}$$

which diverges when the gluon energy E_k approaches zero.
Now that we have a clearer picture of how real IR singularities emerge in phase space integrations, we can go back to eq. (2.44) and use dimensional regularisation to evaluate the phase space integral. By doing this, we get

$$\sigma_{\text{real}} = \sigma_{\text{Born}} C_F \frac{\alpha_s}{2\pi} H(\epsilon) \left(\frac{4}{\epsilon^2} + \frac{3}{\epsilon} + \frac{19}{2} - \pi^2 + O(\epsilon) \right). \tag{2.52}$$

Surprisingly enough, the ϵ poles contained in the expression above are exactly the same the we reported in eq. (2.30)[5], but this time with opposite signs! This implies the exact cancelation of the IR virtual singularities with the ones of real origins in eq. (2.33). The final result will be

$$\sigma(e^+e^- \to q\bar{q} + X) = \sigma_0 \left(3 \sum_f Q_f^2 \right) \left[1 + \frac{\alpha_s}{\pi} + O(\alpha_s^2) \right]. \tag{2.53}$$

How could it happen that IR singularities canceled and that we ended up with a finite result? Is it something purely accidental, or is there something deeper behind? The answer is that we just studied a specific case of a broader result holding for generic Yang-Mills theories. Here, the celebrated *KLN Theorem* [8, 9] states that the infrared divergences coming from loop integrals are cancelled by IR divergences in phase space integrals, and that this occurs at every perturbative order. This makes QCD infrared safe and predictive, as far as one considers observables inclusive enough over extra QCD radiation at higher orders (as for eq. (2.33)).
Formally, we can express the infrared safety of a generic observable $\mathcal{O}$ through the following condition:

$$\mathcal{O}_{n+1}(k_1, \ldots, k_i, \ldots, k_j, \ldots, k_{n+1}) \xrightarrow{\vec{k}_i \| \vec{k}_j} \mathcal{O}_n(k_1, \ldots, k_i + k_j, \ldots, k_n) \tag{2.54}$$

$$\mathcal{O}_{n+1}(k_1, \ldots, k_s, \ldots, k_{n+1}) \xrightarrow{\vec{k}_s \to 0} \mathcal{O}_n(k_1, \ldots, k_{s-1}, k_{s+1}, \ldots, k_n) \,, \tag{2.55}$$

where $\mathcal{O}_n$ is the observable computed at the lowest order on a final n-body phase space, and $\mathcal{O}_{n+1}$ is the same observable computed on phase space with an additional real radiation. The conditions in eq. (2.54) and eq. (2.55) essentially tell us that any infrared safe observable must be insensitive from soft and collinear extra emissions. This is a quite general property and will turn useful when reviewing some basic concepts of jet physics in chapter 4.

[5] The regular function $H(\epsilon)$ in eq. (2.30) is also the same as the one in eq. (2.52).

2.4 Infrared Singular Behaviour of QCD amplitudes

In the previous section, we studied the quark pair production in electron-positron collisions to have a simple framework where to introduce IR singularities and their cancelation. The aim of this section is to generalize we saw in eq. (2.46) and eq. (2.50), showing that these formulas just represents specific cases of the universal factorisation of QCD squared matrix elements in the infrared limits. In general, these limits can be studied for different configurations [10, 11], including mixes of soft and collinear limits, possibly involving large sets of external partons. Loop corrections to these limits can also be analyzed in a systematic way [6].
As this chapter will especially focus on next-to-leading-order computations in QCD, we will restrict our attention on the singular limits effectively contributing at this perturbative order, namely:

- The two-parton collinear limit of tree-level amplitudes.
- The single soft parton limit of tree-level amplitudes.

In both cases, we will follow the calculations presented in [11], to which we refer the interested reader for more details.

2.4.1 The Collinear Limit

Considering a process with a generic number of QCD partons[7] in the final state and possibly other non-QCD partons (like colour singlets), we can write its tree-level amplitude as

$$\mathcal{A}^{c_1,c_2,\ldots;s_1,s_2,\cdots}_{a_1,a_2,\ldots}(p_1,p_2,\ldots), \tag{2.56}$$

where $\{c_1,c_2,\ldots\}$, $\{s_1,s_2,\ldots\}$ and $\{a_1,a_2,\ldots\}$ are respectively colour, spin and flavour indices. We are interested at analysing the behaviour of the squared amplitudes, that are usually summed over final-state colours and spins. Therefore, we generically introduce the notation

$$|\mathcal{A}_{a_1,a_2,\ldots}(p_1,p_2,\ldots)|^2\,, \tag{2.57}$$

to refer to squared amplitudes where the sum over colours and spin is understood, while we introduce a spin-polarisation tensor

$$\mathcal{T}^{s_1 s_1'}_{a_1,\ldots}(p_1,\ldots) \equiv \sum_{\text{spins}\neq s_1,s_1'} \sum_{\text{colours}} \mathcal{M}^{c_1,c_2,\ldots;s_1,s_2,\cdots}_{a_1,a_2,\ldots}(p_1,p_2,\ldots)\left[\mathcal{M}^{c_1,c_2,\ldots;s_1',s_2,\cdots}_{a_1,a_2,\ldots}(p_1,p_2,\ldots)\right]^\dagger\,, \tag{2.58}$$

to explicitely refer to squared amplitudes where the sum over colours/spins of the parton a_1 has not been performed. Given these definitions, we want to show the singular limits of eq. (2.57). However, since we are talking about singularities, it is essential to adopt a regularisation scheme. Following what done in Ref. [11], we choose the conventional dimensional regularisation (CDR)[8] for handling both UV and IR divergences. To parametrize

[6] See, for instance, Ref. [12]
[7] Namely gluons and massless quarks.
[8] This is quite standard and implies working out in $d = 4 - 2\epsilon$ dimensions, as usual, and considering two helicity states for massless quarks and $d-2$ helicity states for gluons.

the collinear limit for the momenta of two partons, like p_1 and p_2, we use the following decomposition

$$p_1^\mu = zp^\mu + k_\perp^\mu - \frac{k_\perp^2}{z}\frac{n^\mu}{2p\cdot n} \tag{2.59}$$

$$p_2^\mu = (1-z)p^\mu - k_\perp^\mu - \frac{k_\perp^2}{1-z}\frac{n^\mu}{2p\cdot n}n^\mu, \tag{2.60}$$

where $s_{12} = 2p_1\cdot p_2 = -\frac{k_\perp^2}{z(1-z)}$ for $k_\perp \to 0$. The vector p^μ represents the collinear direction, while $k_\perp$ is a space-like vector related to the trasverse component. The light-like vector n^μ is an auxiliary vector, necessary to define $k_\perp$, since $k_\perp \cdot p = k_\perp \cdot n = 0$.
The collinear limit of the squared amplitude in eq. (2.57) will finally read

$$|\mathcal{M}_{a_1,a_2,\ldots}(p_1,p_2,\ldots)|^2 \xrightarrow{\vec{p_1}\parallel\vec{p_2}} \frac{2}{s_{12}}4\pi^2\mu^{2\epsilon}\alpha_s \mathcal{T}^{ss'}_{a,\ldots}(p,\ldots)\hat{P}^{ss'}_{a_1a_2}(z,k_\perp;\epsilon)\ . \tag{2.61}$$

In the spin-polarisation tensor $T^{ss'}_{a,\ldots}(p,\ldots)$, the index a represents a the *mother* parton of a_1 and a_2: its momentum is p^μ and its flavour and colour are determined by conservation properties[9]. $\hat{P}^{ss'}_{a_1a_2}$ is the d-dimensional unregularized Altarelli-Parisi splitting functions [13–15]. It is a universal kernel, encoding the singular collinear behaviour of the squared amplitude and only depending on the kinematics and colour numbers of the collinear partons. It retains a spin-correlation factor, so we can think about it as the action of a general matrix $\hat{P}_{a_1a_2}$ on the spin indices s, s' of the mother parton a. The explicit expressions of $\hat{P}^{ss'}_{a_1a_2}$ are given b[10]:

$$\hat{P}^{ss'}_{qg}(z,k_\perp;\epsilon) = \hat{P}^{ss'}_{\bar{q}g}(z,k_\perp;\epsilon) = \delta_{ss'}C_F\left[\frac{1+z^2}{1-z} - \epsilon(1-z)\right], \tag{2.62}$$

$$\hat{P}^{ss'}_{gq}(z,k_\perp;\epsilon) = \hat{P}^{ss'}_{g\bar{q}}(z,k_\perp;\epsilon) = \delta_{ss'}C_F\left[\frac{1+(1-z)^2}{z} - \epsilon z\right], \tag{2.63}$$

$$\hat{P}^{ss'}_{q\bar{q}}(z,k_\perp;\epsilon) = \hat{P}^{ss'}_{\bar{q}q}(z,k_\perp;\epsilon) = \frac{1}{2}\left[-g^{\mu\nu} + 4z(1-z)\frac{k_\perp^\mu k_\perp^\nu}{k_\perp^2}\right], \tag{2.64}$$

$$\hat{P}^{ss'}_{gg}(z,k_\perp;\epsilon) = 2C_A\left[-g^{\mu\nu}\left(\frac{z}{1-z} + \frac{1-z}{z}\right) - 2(1-\epsilon)z(1-z)\frac{k_\perp^\mu k_\perp^\nu}{k_\perp^2}\right], \tag{2.65}$$

It is interesting to notice that the spin-correlations manifest a non-trivial structures only in eq. (2.65) and section 2.4.1, so for gluon collinear splittings. This translates into the presence of an azimuthal dependence with respect to the directions of the other momenta in the factorized matrix element. On the other hand, when averaging over the polarisations of the parent parton a, one gets the standard expressions

$$\langle\hat{P}_{qg}(z;\epsilon)\rangle = \langle\hat{P}_{\bar{q}g}(z;\epsilon)\rangle = C_F\left[\frac{1+z^2}{1-z} - \epsilon(1-z)\right], \tag{2.66}$$

[9] Where the quantum number conservation is imposed on the splitting vertex $a \to a_1a_2$.
[10] Where $C_F = (N_c^2-1)/2N_c$ is the Casimir of $SU(N_c)$ in the fundamental representation, and $C_A = N_c$ is the Casimir in the adjoint representation (N_c is the number of colours).

$$\langle \hat{P}_{gq}(z;\epsilon)\rangle = \langle \hat{P}_{g\bar{q}}(z;\epsilon)\rangle = C_F\left[\frac{1+(1-z)^2}{z} - \epsilon z\right], \tag{2.67}$$

$$\langle \hat{P}_{q\bar{q}}(z;\epsilon)\rangle = \langle \hat{P}_{\bar{q}q}(z;\epsilon)\rangle = \frac{1}{2}\left[1 - 2z(1-z)(1-\epsilon)\right], \tag{2.68}$$

$$\langle \hat{P}_{gg}(z;\epsilon)\rangle = 2C_A\left[\frac{z}{1-z} + \frac{1-z}{z} + z(1-z)\right]. \tag{2.69}$$

2.4.2 The Soft Limit

Considering now the behaviour of the generic n-parton amplitude in eq. (2.56) in the soft limit, it is helpful to introduce a new formalism to deal with its colour and spin dependence. Following what exposed in Ref. [11], a basis $\{|c_1,\ldots,c_n\rangle \otimes |s_1,\ldots,s_n\rangle\}$ in colour + helicity space is defined, so that eq. (2.56) can be seen as the component of a colour + spin vector $|\mathcal{M}_{a_1,\ldots,a_n}(p_1,\ldots,p_n)\rangle$, related to a specific basis vector. In formulas:

$$\mathcal{M}^{c_1,\ldots,c_n;s_1,\ldots,s_n}_{a_1,\ldots,a_n}(p_1,\ldots,p_n) \equiv \Big(\langle c_1,\ldots,c_n| \otimes \langle s_1,\ldots,s_n|\Big)|\mathcal{M}_{a_1,\ldots,a_n}(p_1,\ldots,p_n)\rangle\ . \tag{2.70}$$

Notice that $|\mathcal{M}_{a_1,\ldots,a_n}(p_1,\ldots,p_n)\rangle$ is, by definition, a colour-singlet state. The squared matrix element, summed over final-state colours and spins, will then read

$$|\mathcal{M}_{a_1,\ldots,a_n}(p_1,\ldots,p_n)|^2 = \langle \mathcal{M}_{a_1,\ldots,a_n}(p_1,\ldots,p_n)|\mathcal{M}_{a_1,\ldots,a_n}(p_1,\ldots,p_n)\rangle\ . \tag{2.71}$$

A colour charge operator $\mathbf{T}_i$ is also introduced, to acount for the colour contribution of a gluon emission from a parton i. It is defined as

$$\mathbf{T}_i \equiv \langle c|T^c_i\ , \tag{2.72}$$

and it acts on the colour structure of QCD amplitudes according to

$$\langle c_1,\ldots,c_i,\ldots,c_m,c|\mathbf{T}_i|b_1,\ldots,b_i,\ldots,b_m\rangle = \delta_{c_1b_1}\ldots T^c_{c_ib_i}\ldots\delta_{c_mb_m}. \tag{2.73}$$

Explicitely, we have that $T^c_{ab} \equiv if_{cab}$ when the emitting parton i is a gluon, $T^a_{\alpha\beta} \equiv t^a_{\alpha\beta}$ if i is a quark, and $T^a_{\alpha\beta} \equiv \bar{t}^a_{\alpha\beta} = -t^a_{\beta\alpha}$ if i is an antiquark[11]. The colour charge operator satisfies some important properties, in particular

- $\mathbf{T}_i\cdot\mathbf{T}_j = \mathbf{T}_j\cdot\mathbf{T}_i = T^c_iT^c_j \quad \text{if } i\neq j.$
- $\mathbf{T}^2_i = C_i$, where $C_i = C_A$ if i is a gluon and $C_i = C_F$ for i being (anti)quark.
- Colour conservation requires that

$$\sum_{i=1}^{n}\mathbf{T}_i|\mathcal{M}_{a_1,\ldots,a_n}(p_1,\ldots,p_n)\rangle = 0\ . \tag{2.74}$$

[11] Notice that the Latin letters are used for indices in the adjoint representation of $SU(N_c)$, while Greek letters are used for fundamental representation indices.

Let us consider now a tree-level process with n generic partons and a gluon of momentum q, colour c and spin index μ. According to the formalism introduced above, the process is described by a vector $|\mathcal{M}_{g,a_1,\dots,a_n}(q,p_1,\dots,p_n)\rangle\rangle$. When the gluon momentum vanishes, it can be shown that

$$\langle c;\mu|\mathcal{M}_{g,a_1,\dots,a_n}(q,p_1,\dots,p_n)\rangle\rangle \quad\to\quad g_s\mu^\epsilon J^{c;\mu}(q)|\mathcal{M}_{a_1,\dots,a_n}(p_1,\dots,p_n)\rangle\rangle, \tag{2.75}$$

which means that an amplitude with a soft gluon becomes proportional to the same amplitude without the gluon, multiplied by a universal kernel $J^{c;\mu}(q)$ containing the soft divergence. The factor $\mathbf{J}^\mu(q)=\langle c|J^{c;\mu}(q)$ corresponds to the eikonal current already introduced in eq. (2.49), and reads

$$\mathbf{J}^\mu(q)=\sum_{i=1}^n \mathbf{T}_i\frac{p_i^\mu}{p_i\cdot q}\ . \tag{2.76}$$

The eikonal current is a conserved current. Indeed, since $q_\mu\mathbf{J}^\mu(q)$ becomes exactly $\sum_{i=1}^n\mathbf{T}_i$, colour conservation in eq. (2.74) will just imply

$$q_\mu\mathbf{J}^\mu(q)|\mathcal{M}_{a_1,\dots,a_n}(p_1,\dots,p_n)\rangle\rangle=0\ . \tag{2.77}$$

Owing to the fact we just observed, eq. (2.75) implies the squared amplitude to behave in the following way under the soft gluon limit

$$|\mathcal{M}_{g,a_1,\dots,a_n}(q,p_1,\dots,p_n)|^2 \quad\to\quad -4\pi\alpha_s\mu^{2\epsilon}\sum_{i,j=1}^n S_{ij}(q)|\mathcal{M}^{(i,j)}_{a_1,\dots,a_n}(p_1,\dots,p_n)|^2, \tag{2.78}$$

where a scalar *eikonal function* has been defined

$$S_{ij}(q)=\frac{p_i\cdot p_j}{(p_i\cdot q)(p_j\cdot q)}=\frac{2s_{ij}}{s_{iq}s_{jq}}\ , \tag{2.79}$$

and where $|\mathcal{M}^{(i,j)}_{a_1,\dots,a_n}(p_1,\dots,p_n)|^2$ are colour-correlated squared amplitudes, according to

$$\begin{aligned}|\mathcal{M}^{(i,j)}_{a_1,\dots,a_n}(p_1,\dots,p_n)|^2 \equiv&\langle\mathcal{M}_{a_1,\dots,a_n}(p_1,\dots,p_n)|\mathbf{T}_i\cdot\mathbf{T}_j|\mathcal{M}_{a_1,\dots,a_n}(p_1,\dots,p_n)\rangle\rangle \\ =&\left[\mathcal{M}^{c_1,\dots b_i\dots b_j\dots c_n}_{a_1,\dots,a_n}(p_1,\dots,p_n)\right]^* T^c_{b_id_i}T^c_{b_jd_j}\mathcal{M}^{c_1\dots d_i\dots d_j\dots c_n}_{a_1,\dots,a_n}(p_1,\dots,p_n)\ .\end{aligned} \tag{2.80}$$

The squared matrix elements appears (summed over final-state colours and spins) appears therefore almost fully factorized in the soft limit, but colour conservation acts by introducing colour correlation terms, making it impossible to extract $|\mathcal{M}_{a_1,\dots,a_n}(p_1,\dots,p_n)|^2$ from the sum in eq. (2.78).

2.5 Factorisation of Parton Distribution Functions

The considerations and results we have presented in the previous sections finally allow us to study hadronic collisions, which will be the object of the phenomenological analyses we will detail in the second part od this thesis. We remind that the cross section for two hadrons h_1,h_2 scattering into a generic final state X can be effectively described by the following

master formula

$$\sigma(h_1 h_2 \to X) = \sum_{i,j} \int dx_\oplus dx_\ominus f_{i/h_1}(x_\oplus, \mu_F^2) f_{j/h_2}(x_\ominus, \mu_F^2) \hat{\sigma}_{ij,X}(\hat{s}, \mu_R^2, \mu_F^2) + \mathcal{O}\left(\frac{\Lambda_{\rm QCD}}{Q}\right) , \tag{2.81}$$

which expresses the factorisation theorem [4] for hadronic processes at high energies. In the introduction, we already presented the main ingredients entering eq. (2.81). What we aim to do, now, is to explain the physical origin of the *factorisation scale* that makes its appearance inside the parton distribution functions and the partonic cross section. Pratical details about the calculation of the same eq. (2.81) will be shown in the next section.
When we argumented the cancelation of infrared divergences due to the KLN theorem in section 2.3, we restricted our attention to an high nergy process involving a lepton pair $e^- e^+$ in the initial state. This allowed us to get a clear picture of what was going on, but on the other hand forbid us to appreciate a really genuine phenomenon that occurs when partons are present in the initial state. In this case, the emission of collinear radiation alters the momenta of initial-state partons before entering the hard scatterings, leading to an incomplete cancelation of the initial-state collinear singularities between real and virtual NLO corrections (and beyond). This is depicted in fig. 2.4.

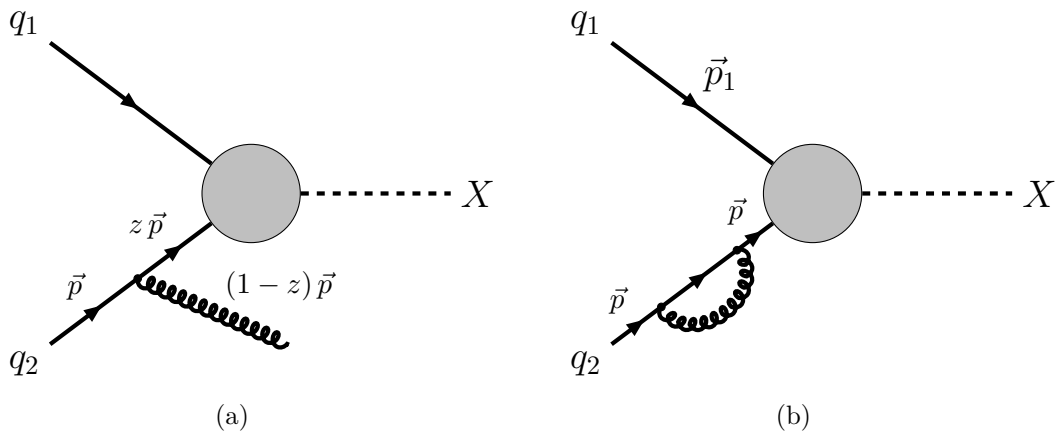

Figure 2.4: Initial-state radiative (a) and virtual (b) corrections to a generic process two incoming quarks q_1, q_2 that interact to generate a final state X. In (a), the momentum of q_2 is modified by the emission of a gluon with $(1-z)\,\vec{p}$ before undergoing the hard scattering (grey circle). In (b), the virtual correction does not affect the momentum $\vec{p}$ of q_2. As a result, the exact cancelation of singularities arising from the collinear gluon configuration in (a) and (b) only holds for $z \to 1$ (soft limit).

The way to handle these left over singularities is looking at the problem with the same philosophy upon which the renormalisation procedure is bases. The divergences are a sympthoms that we are using of bare PDFs. Where divergences are reabsorbed, giving finite physical PDFs, a new unphysical scale emerges, which is exactly the factorisation scale μ_F. It can be shown that the evolution of parton distribution functions with μ_F is dictated by the Dokshitzer-Gribov-Lipatov-Altarelli-Parisi (DGLAP) [13–15]. They compose a system of $2n_f + 1$ equations, where in particular: n_f predict the evolution of quark PDFs, n_f

the one of antiquark PDFs, and a last one dictates the gluon PDF evolution. By allowing the subscript i to run over all the possible light quark and antiquark falvours, the DGLAP equations can be arranged in the following form

$$\frac{\partial}{\partial \ln \mu^2}\begin{pmatrix} f_{q_i/h}(x,\mu^2) \\ f_{g/h}(x,\mu^2)\end{pmatrix} = \frac{\alpha_s(\mu^2)}{2\pi}\sum_{q_j,q_k}\int_x^1 \frac{dz}{z}\begin{pmatrix} P_{q_iq_j}\left(\frac{x}{z},\alpha_s(\mu^2)\right) & P_{q_ig}\left(\frac{x}{z},\alpha_s(\mu^2)\right) \\ P_{gq_j}\left(\frac{x}{z},\alpha_s(\mu^2)\right) & P_{gg}\left(\frac{x}{z},\alpha_s(\mu^2)\right)\end{pmatrix}\begin{pmatrix} f_{q_j/h}(z,\mu^2) \\ f_{g/h}(z,\mu^2)\end{pmatrix}, \tag{2.82}$$

where P_{ij} are the *regularized Altarelli-Parisi splitting functions*, admitting a strong coupling expansion

$$P_{ij}(z,\alpha_s(\mu^2)) = P_{ij}^{(0)}(z) + \frac{\alpha_s}{2\pi}P_{ij}^{(1)}(z) + \left(\frac{\alpha_s}{2\pi}\right)^2 P_{ij}^{(2)}(z) + \mathcal{O}(\alpha_s^3)\,, \tag{2.83}$$

where at the leading-order we have

$$P_{q_iq_j}^{(0)}(z) = \delta_{ij}C_F\left(\frac{1+z^2}{[1-z]_+} + \frac{3}{2}\delta(1-z)\right), \tag{2.84}$$

$$P_{q_ig}^{(0)}(z) = C_F\left(\frac{1+(1-z)^2}{z}\right), \tag{2.85}$$

$$P_{gq_i}^{(0)}(z) = \frac{1}{2}\left(z^2+(1-z)^2\right), \tag{2.86}$$

$$P_{gg}^{(0)}(z) = 2C_A\left(\frac{z}{[1-z]_+} + (1-z)z + \frac{1}{z}\right) + (11C_A - 2n_f)\,\frac{\delta(1-z)}{6}\,. \tag{2.87}$$

Notice the similarities with the unregolarized Altarelli-Parisi splitting functions presented in eqs. (2.66) to (2.69), except from the presence of the *plus prescription* in eq. (2.84) and eq. (2.87), that reads

$$\int_0^1 dz \frac{f(z)}{[1-z]_+} = \int_0^1 dz \frac{f(z)-f(1)}{1-z}. \tag{2.88}$$

2.6 Fixed-order Calculations at Next-to-Leading-Order in QCD

Given all the considerations in the above, we have now all the ingredients to deal with fixed order calculations beyond the leading-order in QCD. For the scope of this thesis, we will focus on next-to-leading-order computations in hadron-hadron collisons. In what follows, we will adopt the notation presented in [16–18], as it will turn useful in the formal developments presented in the next chapters.

The leading-order contribution of eq. (2.81) can be written for a $2 \to n$ process as

$$\sigma_{\rm LO} = \int d\mathbf{\Phi}_n\, \mathcal{L}\, \mathcal{B}(\Phi_n)\,, \tag{2.89}$$

where the phase space $\mathbf{\Phi}_n$ is defined as

$$\mathbf{\Phi}_n = \{x_\oplus, x_\ominus, k_1, \ldots, k_n\}\,, \tag{2.90}$$

and thus also including the final state parton momenta $\{k_1, \ldots, k_n\}$, as well as the partonic momentum fraction variables $x_\oplus$, $x_\ominus$, which relates to the initial state interacting parton momenta $k_\oplus$, $k_\ominus$ as

$$k_\oplus = x_\oplus K_\oplus, \quad k_\ominus = x_\ominus K_\ominus \,, \tag{2.91}$$

where $K_\oplus$, $K_\ominus$ are the incoming proton momenta. The phase space measure will then read

$$d\mathbf{\Phi}_n = dx_\oplus dx_\ominus d\Phi_n(k_\oplus + k_\ominus; k_1, \ldots, k_n) \,, \tag{2.92}$$

with $d\Phi_n$ the n-body stands for the final state phase space measure

$$d\Phi_n(q; k_1, \ldots, k_n) = (2\pi)^4 \delta^4 \left(q - \sum_{i=1}^{n} k_i \right) \prod_{i=1}^{n} \frac{d^3 k_i}{(2\pi)^3 2k_i^0} \,. \tag{2.93}$$

The factor $\mathcal{L}$ represents the parton luminosity

$$\mathcal{L} = \mathcal{L}(x_\oplus, x_\ominus) = f_\oplus(x_\oplus) f_\ominus(x_\ominus) \,, \tag{2.94}$$

whose flavour dependence has been omitted for ease of notation. Finally, the leading-order squared matrix element $|\mathcal{A}^{(0)}(\mathbf{\Phi}_n)|^2$ is encoded in $\mathcal{B}(\Phi_n)$. Possible sums and averages over spins and colours are also understood in $\mathcal{B}(\Phi_n)$, as well as the presence of a flux factor.
Going to to the next-to-leading-order, we have to include virtual $\mathcal{V}_b$ and real $\mathcal{R}$ contributions to the Born level. Indeed, when taking the perturbative expansions of the relevant renormalised amplitudes

$$\mathcal{A}_n(\mathbf{\Phi}_n) \;=\; \mathcal{A}_n^{(0)}(\mathbf{\Phi}_n) + \mathcal{A}_n^{(1)}(\mathbf{\Phi}_n) + \mathcal{O}(g_s^4) \tag{2.95}$$

$$\mathcal{A}_{n+1}(\mathbf{\Phi}_{n+1}) \;=\; \mathcal{A}_{n+1}^{(0)}(\mathbf{\Phi}_{n+1}) + \mathcal{O}(g_s^3) \,, \tag{2.96}$$

where $\mathcal{A}_n^{(1)}$ is the one-loop amplitude the $2 \to n$ process, and $\mathcal{A}_{n+1}^{(0)}$ the tree level amplitude for $2 \to n+1$ and squaring them, we get

$$\left|\mathcal{A}_n(\mathbf{\Phi}_n)\right|^2 \;=\; \underbrace{\left|\mathcal{A}_n^{(0)}(\mathbf{\Phi}_n)\right|^2}_{\mathcal{B}} + \underbrace{2\,\Re\big(\mathcal{A}_n^{(0)*}(\mathbf{\Phi}_n)\mathcal{A}_n^{(1)}(\mathbf{\Phi}_n)\big)}_{\mathcal{V}_b} + \mathcal{O}(\alpha_s^2) \tag{2.97}$$

$$\mathcal{A}_{n+1}(\mathbf{\Phi}_{n+1}) \;=\; \underbrace{\mathcal{A}_{n+1}^{(0)}(\mathbf{\Phi}_{n+1})}_{\mathcal{R}} + \mathcal{O}(\alpha_s^2) \,, \tag{2.98}$$

where $\mathcal{V}_b$ and $\mathcal{R}$ are introduced, again omitting spin/colour sums and averages for the ease of notation. The subscript b in $\mathcal{V}_b$ means *bare*, reminding that there are still infrared poles in it. When working out the loop integration in dimensional regual for $d = 4 - 2\epsilon$, this implies the presence of single and double ϵ poles in $\mathcal{V}_b$. When performing the phase space integration of the Born, real and virtual terms, we get

$$\int d\mathbf{\Phi}_n \mathcal{L} \left[\mathcal{B}(\Phi_n) + \mathcal{V}_b(\Phi_n)\right] + \int d\Phi_{n+1} \mathcal{L}\mathcal{R}(\Phi_{n+1}) \,, \tag{2.99}$$

where the $n+1$ body phase space reads

$$d\mathbf{\Phi}_{n+1} = dx_\oplus dx_\ominus d\Phi_{n+1}(k_\oplus + k_\ominus; k_1, \ldots, k_{n+1}). \tag{2.100}$$

Although the cancelation of IRC divergences take place as described in the previous sections, eq. (2.99) still features left-over **ISR** collinear singularities. We can therefore include two factorisation counterterms, so to get the following finite NLO cross section

$$\sigma_{\rm NLO} = \int d\mathbf{\Phi}_n \, \mathcal{L} \, [\mathcal{B}(\mathbf{\Phi}_n) + \mathcal{V}_b(\mathbf{\Phi}_n)] + \int d\mathbf{\Phi}_{n+1} \, \mathcal{L} \, \mathcal{R}(\mathbf{\Phi}_{n+1}) + \int d\mathbf{\Phi}_{n,\oplus} \, \mathcal{L} \, \mathcal{G}_{\oplus,b}(\mathbf{\Phi}_{n,\oplus}) + \int d\mathbf{\Phi}_{n,\ominus} \, \mathcal{L} \, \mathcal{G}_{\ominus,b}(\mathbf{\Phi}_{n,\ominus}). \tag{2.101}$$

Notice that the bare counterterms $\mathcal{G}_{\oplus,b}$ and $\mathcal{G}_{\ominus,b}$ are divergent in four dimension and are defined on the phase spaces $\mathbf{\Phi}_{n,\oplus}$ and $\mathbf{\Phi}_{n,\ominus}$, that also includes a new variable $0 < z < 1$, representing the fraction of momentum of the incoming parton after radiation. These phase spaces are constrained by momentum conservation, so that

$$\mathbf{\Phi}_{n,\oplus} = \{x_\oplus, x_\ominus, z, k_1, \dots, k_n\}, \quad \text{where} \quad z x_\oplus K_\oplus + x_\ominus K_\ominus = \sum_{i=1}^{n} k_i \tag{2.102}$$

$$\mathbf{\Phi}_{n,\ominus} = \{x_\oplus, x_\ominus, z, k_1, \dots, k_n\}, \quad \text{where} \quad x_\oplus K_\oplus + z x_\ominus K_\ominus = \sum_{i=1}^{n} k_i \, , \tag{2.103}$$

and

$$d\mathbf{\Phi}_{n,\oplus} = dx_\oplus \, dx_\ominus \, dz \, d\Phi_n(z k_\oplus + k_\ominus; k_1, \dots, k_n), \tag{2.104}$$

$$d\mathbf{\Phi}_{n,\ominus} = dx_\oplus \, dx_\ominus \, dz \, d\Phi_n(k_\oplus + z k_\ominus; k_1, \dots, k_n). \tag{2.105}$$

It may be also convenient to absorb the z dependence of eq. (2.102) and eq. (2.103) into an underlying n-body phase space $\mathbf{\Phi}_n$ defined as

$$\overline{\mathbf{\Phi}}_n = \{\overline{x}_\oplus, \overline{x}_\ominus, k_1, \dots, k_n\}, \quad \overline{x}_{\circledoplus} = z x_{\circledoplus}, \quad \overline{x}_{\circledominus} = x_{\circledominus} \, , \tag{2.106}$$

which we are going to use in the next section.

2.7 Subtraction Schemes at NLO

Putting things together, we can now express the expectation value of a certain observable O[12] as

$$\begin{aligned} \langle O \rangle = & \int d\mathbf{\Phi}_n \mathcal{L} \, O_n(\mathbf{\Phi}_n) \, [\mathcal{B}(\mathbf{\Phi}_n) + \mathcal{V}_b(\mathbf{\Phi}_n)] \\ & + \int d\mathbf{\Phi}_{n+1} \mathcal{L} \, O_{n+1}(\mathbf{\Phi}_{n+1}) \mathcal{R}(\mathbf{\Phi}_{n+1}) \\ & + \int d\mathbf{\Phi}_{n,\oplus} \mathcal{L} \, O_n(\overline{\mathbf{\Phi}}_n) \mathcal{G}_{\oplus,b}(\mathbf{\Phi}_{n,\oplus}) \\ & + \int d\mathbf{\Phi}_{n,\ominus} \mathcal{L} \, O_n(\overline{\mathbf{\Phi}}_n) \mathcal{G}_{\ominus,b}(\mathbf{\Phi}_{n,\ominus}) \, , \end{aligned} \tag{2.107}$$

[12] We require O to be infrared safe (i.e. finite) at the Born level. In this way, the leading-order computation of $\langle O \rangle$ will be naturally finite, while higher orders will still provide finite corrections thanks to the KLN theorem.

which is formally correct, but not suitable for a numerical implementations. Indeed, the phase space integration of $\mathcal{R}$, $\mathcal{G}_{\oplus,b}$ is only meaningful when regularized in $d = 4 - 2\epsilon$, which is not possible though standard numerical techniques. We recall that the real integration gives rise to singularities in three particular kinematics configurations:

1. In the soft regions (**S**): when one of the $n+1$ final state partons has vanishing four momentum.

2. In the final state collinear regions (**FSC**): when two massless final state momenta become parallel.

3. In the initial state collinear regions (**ISC**): when a final partom becomes collinear to an initial state parton.

However we can rearrange eq. (2.107) in a way to properly extract the phase space singularities in in $d\mathbf{\Phi}_{n+1}\mathcal{R}$ and $d\mathbf{\Phi}_{n,\oplus}\mathcal{G}_{\oplus,b}$ and let them cancel against the virtual IRC singularities before performing any integration. In this way, we would be left with some terms that can be integrated in $d = 4$ dimensions. This is the simple idea behind the *subtraction schemes*. More specifically, we can proceed by defining some functions $\mathcal{C}^{(a)}(\mathbf{\Phi}_{n+1})$ (the infrared counterterms), that mimic the singular behaviour of the real matrix elements in the IRC regions of real radiation, labeled with $\alpha \in \{\mathbf{S}, \mathbf{FSC}, \mathbf{ISC}\}$. We also require the $\mathcal{C}^{(a)}$ to be analytically integrable in the factorized radiation phase space, but we will elaborate more on this point later. By construction, we will have that

$$\mathcal{R}(\mathbf{\Phi}_{n+1})O_{n+1}(\mathbf{\Phi}_{n+1}) - \sum_{\alpha} C^{(\alpha)}(\mathbf{\Phi}_{n+1})O_{n+1}\left(\mathbf{\Phi}_{n+1}\right) \tag{2.108}$$

has at most integrable singularities in the 4-dimensional radiation phase space. However, the cancelation of singularities is guaranteed also if we relax the condition that the observable $O_{n+1}(\mathbf{\Phi}_{n+1})$ multiplying the counterterms $C^{(a)}$ is computed on $\mathbf{\Phi}_{n+1}$. There, we can also deform the $\mathbf{\Phi}_{n+1}$ into different phase spaces $\tilde{\mathbf{\Phi}}^{(\alpha)}_{n+1}$ for every α, so that

$$\mathcal{R}(\mathbf{\Phi}_{n+1})O_{n+1}(\mathbf{\Phi}_{n+1}) - \sum_{\alpha} C^{(\alpha)}(\mathbf{\Phi}_{n+1})O_{n+1}\left(\tilde{\mathbf{\Phi}}^{(\alpha)}_{n+1}\right) \ , \tag{2.109}$$

provided that $\tilde{\mathbf{\Phi}}^{(\alpha)}_{n+1}$ smoothly identifies with $\mathbf{\Phi}_{n+1}$ in the α singular region

$$\tilde{\mathbf{\Phi}}^{(\alpha)}_{n+1} \quad \xrightarrow{\alpha \text{ singular region}} \quad \mathbf{\Phi}_{n+1} \ . \tag{2.110}$$

For what will become clear later, it is also useful to introduce an underlying n-body configuration

$$\overline{\mathbf{\Phi}}^{(\alpha)}_{n} = \left[\left\{\overline{x}_{\oplus}, \overline{x}_{\ominus}, \overline{k}_1, \ldots, \overline{k}_n\right\}\right]_{\alpha} \ , \tag{2.111}$$

that projects each $\tilde{\mathbf{\Phi}}^{(\alpha)}_{n+1}$ onto a n-particle $\overline{\mathbf{\Phi}}^{(\alpha)}_{n}$ phase point in a way that

- If $\alpha \in \mathbf{S}$, then the null momentum parton is dropped.
- If $\alpha \in \mathbf{FSC}$, then the two parallel momenta are merged in one single momentum corresponding to their sum.

- If $\alpha \in \mathbf{ISC}$, then the initial state collinear radiative parton is removed and the momentum of the initial state emitter is replaced with its momentum after the collinear radiation.

It is not difficult to check that such procedure preserves the total four-momentum conservation.
We can now rewrite the real contribution in eq. (2.107) by subtracting and adding back the counterterms introduced in eq. (2.108), thus getting

$$\int \mathrm{d}\mathbf{\Phi}_{n+1} \mathcal{L}\, O_{n+1}(\mathbf{\Phi}_{n+1})\, \mathcal{R}(\mathbf{\Phi}_{n+1}) = \sum_\alpha \int \mathrm{d}\mathbf{\Phi}_{n+1} \left[\tilde{\mathcal{L}}\, O_n(\bar{\mathbf{\Phi}}_n)\, C(\mathbf{\Phi}_{n+1})\right]_\alpha \tag{2.112}$$
$$+ \int \mathrm{d}\mathbf{\Phi}_{n+1} \left\{ \mathcal{L}\, O_{n+1}(\mathbf{\Phi}_{n+1})\, \mathcal{R}(\mathbf{\Phi}_{n+1}) - \sum_\alpha \left[\tilde{\mathcal{L}}\, O_n(\bar{\mathbf{\Phi}}_n)\, C(\mathbf{\Phi}_{n+1})\right]_\alpha \right\} ,$$

where $\tilde{\mathcal{L}} = \mathcal{L}(\tilde{x}_\oplus, \tilde{x}_\ominus)$. Notice that in eq. (2.112) we performed the replacement

$$O_{n+1}(\tilde{\mathbf{\Phi}}_n)\, C(\mathbf{\Phi}_{n+1}) \quad \to \quad O_n(\bar{\mathbf{\Phi}}_n)\, C(\mathbf{\Phi}_{n+1}) \,. \tag{2.113}$$

This is a direct consequence of the infrared safety conditions on the observables, that we defined through eqs. (2.54) and (2.55). And here it comes the key point of the subtraction procedure. We factorize the radiation phase space from $\mathbf{\Phi}_{n+1}$ in each region α, by using

$$d\mathbf{\Phi}_{n+1} = d\overline{\mathbf{\Phi}}_n^{(\alpha)}\, d\mathbf{\Phi}_{\mathrm{rad}}^{(\alpha)} \,, \tag{2.114}$$

where $d\Phi_{\mathrm{rad}}^{(\alpha)}$ encodes three variables that parametrize the radiation, and whose ranges can depend on the underlying $\bar{\mathbf{\Phi}}_n^{(\alpha)}$. Then, if every counterterm is defined properly, its dependence on Φ_{rad} can be integrated analytically in $d = 4-2\epsilon$ (thus extracting the ϵ poles). What is left will a counterterm $\bar{\mathcal{C}}^{(\alpha)}$ just depending on the underlying n-parton configuration, according to

$$\left[\overline{C}(\overline{\mathbf{\Phi}}_n) = \int d\Phi_{\mathrm{rad}} \mathcal{C}(\mathbf{\Phi}_{n+1})\right]_{\alpha\in\{\mathbf{FSC},\mathbf{S}\}} \,, \tag{2.115}$$

and

$$\left[\overline{C}(\overline{\mathbf{\Phi}}_n, z) = \int d\mathbf{\Phi}_{\mathrm{rad}} \mathcal{C}(\mathbf{\Phi}_{n+1})\, z\delta\left(z - \frac{\overline{x}_\oplus}{\tilde{x}_\oplus}\right)\right]_{\alpha\in\{\mathbf{ISC}_\oplus\}} \,. \tag{2.116}$$

Regarding the functions $\mathcal{G}_{\oplus,b}(\mathbf{\Phi}_{n,\oplus})$, it turns out that it is always possible to write

$$\mathcal{G}_{\oplus,\mathrm{b}}(\mathbf{\Phi}_{n,\oplus}) + \sum_{\alpha\in\{\mathbf{ISC}_\oplus\}} \overline{C}^{(\alpha)}(\overline{\mathbf{\Phi}}_{n,\oplus}) = \underbrace{\mathcal{G}_\oplus(\mathbf{\Phi}_{n,\oplus})}_{\text{finite}} + \delta(1-z)\mathcal{G}_\oplus^{\mathrm{div}}(\overline{\mathbf{\Phi}}_n) \,, \tag{2.117}$$

and that the ϵ poles in $\mathcal{G}_\oplus^{\mathrm{div}}$ cancel against the virtual, giving a term $\mathcal{V}(\mathbf{\Phi}_n)$ defined as

$$\mathcal{V}(\mathbf{\Phi}_n) = \mathcal{V}_b(\mathbf{\Phi}_n) + \left[\sum_{\alpha\in\{\mathbf{FSC},\mathbf{S}\}} \overline{C}^{(\alpha)}(\overline{\mathbf{\Phi}}_n) + \mathcal{G}_\oplus^{\mathrm{div}}(\overline{\mathbf{\Phi}}_n) + \mathcal{G}_\ominus^{\mathrm{div}}(\overline{\mathbf{\Phi}}_n)\right]_{\overline{\mathbf{\Phi}}_n=\mathbf{\Phi}_n} \,, \tag{2.118}$$

so that we can finally write the following expression for $\langle O \rangle$

$$\begin{aligned}\langle O \rangle = &\int d\mathbf{\Phi}_n \, O_n(\mathbf{\Phi}_n) \left[B(\mathbf{\Phi}_n) + V(\mathbf{\Phi}_n) \right] \\ &+ \int d\mathbf{\Phi}_{n+1} \left\{ O_{n+1}(\mathbf{\Phi}_{n+1}) R(\mathbf{\Phi}_{n+1}) - \sum_\alpha \left[O_n(\overline{\mathbf{\Phi}}_n) C(\mathbf{\Phi}_{n+1}) \right]_\alpha \right\} \\ &+ \int d\mathbf{\Phi}_{n,\oplus} \, O_n(\overline{\mathbf{\Phi}}_n) \, G_\oplus(\mathbf{\Phi}_{n,\oplus}) + \int d\mathbf{\Phi}_{n,\ominus} \, O_n(\overline{\mathbf{\Phi}}_n) \, G_\ominus(\mathbf{\Phi}_{n,\ominus}),\end{aligned} \tag{2.119}$$

where the parton luminosity dependence has been reabsorbed by redefining the matrix elements and counterterms as

$$R = \mathcal{L}\mathcal{R}, \quad C^{(\alpha)} = \widetilde{\mathcal{L}}^{(\alpha)} \mathcal{C}^{(\alpha)}, \quad G_\oplus = \widetilde{\mathcal{L}} \mathcal{G}_\oplus, \quad B = \mathcal{L}\mathcal{B}, \quad V = \mathcal{L}\mathcal{V} \, . \tag{2.120}$$

Now, every integral in eq. (2.119) is finite and can evaluated numerically in 4 dimensions.

In literature, there are several examples of analytical subtraction method essentially based on different implementations of eq. (2.119), namely on different ways to define the counterterms and factorize the radiation phase space. At NLO, various schemes have been proposed [19–25], and two of them have become particularly popular: the Catani-Seymour (CS) scheme [22] and the Frixione-Kunst-Signer (FKS) scheme [21]. It must be also pointed out that other schemes, not based on the analytical subtraction of IRC divergences but rather on *phase-space slicing* techniques, have emerged over the years. In this case, the singular phase-space regions of the real radiation corrections are isolated and their matrix elements replaced by approximated expressions suitable for analytical integration. The integration is then performed up to an unphysical *slicing parameter*, whose residual dependence can be mitigated in different ways. A popular framework based on phase-space slicing is MATRIX [26], which has been succesfully implemented in several NLO and NNLO computations.
Anyways, analytical subtraction schemes appear to be the best candidates to be applied in Monte Carlo event generators, as analytical factorisation of the phase space allows is the key to generate well-defined underlying Born events at NLO accuracy. This fact will turn out to be crucial when we will discuss about the POWHEG method, in the next chapter. In particoular, POWHEG itself is based on an implementation of the FKS subtraction.
Beyond NLO, implementing analytical subtractions become significantly more involved, as the quantity of overlapping real singularities increases dramatically, and virtual poles are also mixed with phase space singularities (e.g. in real-virtual corrections at NNLO). However, several solutions have been investigated over the last few years [26–47]. On top of the already mentioned MATRIX method, Various *local subtraction* methods have also emerged, some of the more numerical-oriented, as in the case of *Loop-Tree Duality* [26], and others foremost analytical, as for the *Nested Soft-Collinear Subtraction* [36] and the *Local Analytic Sector Subtraction* [45, 48–50]. The efforts carried out by the community in this sense prove that subtraction schemes represent nowadays one of the most vibrant research areas in theoretical collider phenomenology.

One last important point has to be addressed. As already discussed above, virtual corrections entering eq. (2.119) will carry a dependence on the renormalisation scale μ_R, while PDFs entering luminosity factors will come with a factorisation scale μ_F. Of course, a choice must be made for these scales, bu no principle exists that contrains them uniquely. However, the values selected for μ_R and μ_F have an impact on the convergence of the perturbative

series, so that some choices are, in a sense, better than others. At a certain fixed-order, a general procedure consists in setting μ_R and μ_F to some *natural scale* μ_0 of the process under examination, and then estimating errors due to missing higher-order corrections through the so-called 7-*point scale variation*. This corresponds to calculating the observable for 7 different settings of (μ_R, μ_F), according to the constraint $\mu_R/\mu_F \in \{1/2, 1, 2\}$. Defining $\mu_R = K_R\mu_0$ and $\mu_F = K_F\mu_0$, the following values for K_R and K_F are considered

$$(K_R, K_F) \in \left\{\left(1,1\right); \left(\frac{1}{2},1\right); \left(1,\frac{1}{2}\right); \left(\frac{1}{2},\frac{1}{2}\right); \left(2,1\right); \left(1,2\right); \left(2,2\right)\right\}, \tag{2.121}$$

and the envelope of the 7 different predictions is interpreted as the uncertainty range around the central value corresponding to $\mu_R, \mu_F = \mu_0$.

Chapter 3

Monte Carlo Event Generators

In the last chapter, we introduced some general features about fixed-order (FO) calculations in QCD, and then focused on the next-to-leading order (NLO) case. As of today, a huge number of predictions in QCD have been carried out, and the next-to-next-to-leading order (NNLO) accuracy is now the state of the art for a vast amount of processes. In fact, fixed-order calculations appear to be the best way to compute inclusive observables, like the total production rates of some final states, at well-defined perturbative accuracy. Unfortunately, this approach is doomed by severe technical limitations, especially coming from the considerable complexity of scattering amplitudes, which increases exponentially with the number of loops and external legs. As a result, FO predictions can successfully address processes with a really limited final state, which is not even close to the extremely abundant and rich final state produced in high-energy hadronic collisions.
To get a more realistic description of the collider events, other tools have been introduced, namely the *Monte Carlo parton showers* (SMC). Exploiting the universal factorization properties of matrix elements in the infrared limits [1], parton showers use Monte Carlo techniques to rapidly increase the final state of the hard events they are given in input. In particular, QCD showers recursively simulate a cascade of light parton emissions in the low energy (soft) and parallel momentum (collinear) limits. Differently, from the FO case, parton showers do not provide more than leading-order accurate results, as they are based on the approximated behaviour of matrix elements in the aforementioned kinematical limits. However, they effectively perform a numerical all-order *resummation*, in a sense that will become clear in the next section, and thus a *logarithmic accuracy* can be associated with them.
Nowadays, parton showers are incorporated in the so-called *General Purposed Monte Carlo* event generators (GPMC), where nonperturbative effects auch as the hadronization of partons at the confinement scale and the decay of unstable hadrons are included. Some popular GPMC events generators are, e.g., Pythia [51], Herwig [52], Sherpa [53]. Moreover, various *matching techniques* have been studied to combine FO computations with GPMC programs. In this sense, the most widespread methods are MC@NLO [54] and Powheg [17].
In this chapter, we will highlight the main features of the GPMC event generators and we will see how they can be effectively interfaced with NLO and NNLO fixed-order calculations in QCD. In section 3.1, we will describe in more detail how parton showers work, with particular attention to Pythia8. In sections 3.2 and 3.3, we will review the main features of the Powheg method, and in sections 3.4 to 3.8 we will focus on the MiNLO' and MiNNLO$_{\rm PS}$ methods, recently incorporated into the Powheg framework. Indeed, the Powheg-Box, supplemented by the MiNNLO$_{\rm PS}$ prescriptions and matched to Pythia8, will be essen-

[1] See section 2.4

tial to achieve NNLO+PS accuracy in the phenomenological studies we will present in the upcoming chapters.

3.1 MC Parton Showers

When predicting the values of physical observables within the FO framework, it is common to apply restrictions on the full phase-space domain of the process under exam. This might happen, for example, when the goal is to carry out a comparison with measurements that include some experimental cuts. The values of the cuts will then enter perturbative calculations as new scales Q_i, giving rise to some logarithmic terms $L \equiv \log(Q_i/Q)$. These terms represent finite residuals of the partial cancellation of real emission terms and the virtual contributions to the process and are related to the restricted real phase-space integration bounds. It turns out that, if the logarithms L are large enough (such that, e.g., $\alpha_s L^2 \sim 1$), then the convergence of the series will be spoiled and loose predictivity. However, since these terms obey universal properties related to the infrared structure of the theory, it is possible to organize the perturbative series to account for the dominant logarithmically enhanced terms to all orders in α_s. In this way, any order n of the series will display *leading logarithmic* (LL) terms $(\alpha_s L^2)^n$, *next-to-leading logarithmic* (NLL) terms $(\alpha_s L)^n$, and so on. Often, the logarithmic terms can be rearranged in some overall exponential, that multiplies the rest of the series. In many cases, resummation can be performed analytically [2]. Otherwise, parton showers algorithms embedded in the GPMC generators can be used to obtain LL-resummed prediction[3].

To illustrate the main ideas PS is based on, we can start by illustrating the *time-like parton shower*, that generates final-state radiation. On the other hand, the initial-state radiation is treated by the so-called *space-like parton showers*, where particular care must be taken on the inclusion of the parton-distribution dependence carried out by the incoming partons. For the sake of clarity, all flavour indices in the formulas that we will review are omitted. The IRC factorization properties outlined in section 2.4 suggest that it is possible to introduce a probability for a final-state parton i to undergo a collinear splitting $i \to jk$, that is related to the unregularized Altarelli-Parisi splitting kernel $\hat{P}_{ij}$ as

$$dP_i(z,t) \;=\; F(z,t)\,dz\,dt \;=\; \frac{\alpha_s(t)}{2\pi}\frac{dt}{t}dz\hat{P}_{ji}(z), \tag{3.1}$$

depending on the z, the energy fraction of i carried by j, and on the *hardness* t, a generic scale that orders emissions from a starting value t_I down to a certain cutofft_0, where the shower stops. Different t choices can be adopted, and generally, they differ between the currently available GPMC generators. In Pythia, t corresponds to the transverse momentum at which the emission takes place. To avoid singularities stemming from eq. (3.1) in the exact collinear emission limit, it is usually introduced a resolution scale under which no splitting can be generated. This implies z to be defined over a restricted range $[z_{\min}, z_{\max}]$, and we

[2] See, e.g., Ref. [55–57]

[3] We report that, over the past few years, great efforts have been devoted to increasing the logarithmic accuracy of parton showers. In this sense, remarkable are the results obtained within the PanScales framework [58–60], whose numerical implementation has been proven to achieve NLL accuracy, and recently even NNLL accuracy [61], for a wide class of observables.

can define the z-integrated splitting probability as

$$dP_i(t) \;=\; \int_{z_{\min}}^{z_{\max}} F(z,t)\,dz\,dt \;=\; \frac{\alpha_s(t)}{2\pi}\frac{dt}{t}\int_{z_{\min}}^{z_{\max}} dz\hat{P}_{ji}(z)\,, \tag{3.2}$$

out of which it is not difficult to derive the probability that no splitting takes place in a $[t_1, t_2]$ range of hardness, namely

$$\Delta_i(t_1,t_2) = \exp\left(-\int_{t_1}^{t_2} dP_i(t)\right), \tag{3.3}$$

which is known as the *Sudakov form factor*.
In a Monte Carlo parton shower algorithm, a certain final-state configuration of partons is provided as an input and is linked to a starting value $t = t_I$ of the hardness scale. Then, a new scale $t = t'$ is generated according to the no-emission probability in eq. (3.3). At $t = t'$, the splitting probability in eq. (3.2) will dictate whether a parton i will or will not undergo a splitting with a certain $z = z'$. The procedure is then recursively repeated on the updated list of partons, therefore another $t'' < t'$ is sorted out and another splitting will (or will not) involve a parton i' at $z = z''$. The algorithm will stop when the cutoff of t is reached.
Regarding the space-like shower, this is carried out via *backward evolution*, namely probabilistic sequence of initial state splittings is reconstructed starting from the partons entering the hard scattering and moving backward in time. In this case, the probability associated with the backward splitting $i \to jk$ can be inferred from the DGLAP equations eq. (2.82) as

$$dP_i(t) = \frac{df_i(x,t)}{f_i(x,t)} = \frac{\alpha_s(t)}{2\pi}\left|\frac{dt}{t}\int_{z_{\min}}^{z_{\max}}\frac{dz}{z}f_j(z,t)\frac{1}{f_i(x,t)}\hat{P}_{ji}\left(\frac{x}{z}\right)\right|, \tag{3.4}$$

and it can be used to define a backward Sudakov form factor of the same form of eq. (3.3).
To understand the action of parton showers from a more formal perspective, it is useful to introduce the following notation used in Ref. [16]. Given a generic final-state ket $|k_1, m_1; \ldots; k_l, m_l\rangle$ of l particles with momentum k and quantum numbers m, that obeys the normalization condition

$$\langle k_1, m_1; \ldots; k_l, m_l | k'_1, m'_1; \ldots; k'_l, m'_l\rangle = \delta_{l,l'}\prod_{i=1}^{l}\delta^3(k_i - k'_i)\delta_{m_i,m'_i}, \tag{3.5}$$

it is possible to define the action of the parton shower as an operator

$$\mathbb{S} = \sum_{l=1}^{\infty}\sum_{m_1\ldots m_l}\int d^3k_1\ldots d^3k_l\, C(k_1,m_1;\ldots;k_l,m_l)\langle k_1,m_1;\ldots;k_l,m_l|\,. \tag{3.6}$$

In this way, if we take an infinitesimal cell $d\Psi = |k'_1, m'_1; \ldots; k'_l, m'_l\rangle\, d^3k'_1 \ldots d^3k'_l$, the product $\mathbb{S}\cdot d\Psi$ will be the probability that the shower generates a state in the cell $d\Psi$. Parton showers obey the unitarity, meaning that only one configuration is reached after applying eq. (3.6) on a generic final-state observable expressed as

$$\mathbb{G} = \sum_{l=1}^{\infty}\sum_{m_1\ldots m_l}\int d^3k_1\ldots d^3k_l\, g(k_1,m_1;\ldots;k_l,m_l)|k_1,m_1;k_2,m_2;\ldots;k_l,m_l\rangle\,, \tag{3.7}$$

which translates into the requirement that $\mathbb{S} \cdot \mathbb{G} = 1$.
In a SMC program, the algorithm will receive as an input a generci m-particle hard scattering event, associated with a phase-space configuration Φ_m. This will have been previously generated according to the Born matrix element $B(\Phi_m)$. Now, if we plug into eq. (3.6) the splitting probability and Sudakov form factor introduced above, we get to the following expression of the parton shower operator:

$$\mathcal{S}(\{t_I\}) = \Delta_R(\{t_I\}, t_0)\,\langle \mathbb{I}| + \sum_{i=1,m} \int_{t_0}^{t_I} dt dz\, \Delta_R(\{t_I\}, t) F_i(z,t) \mathbb{S}(z^2 t) \mathbb{S}((1-z)^2 t)\,, \quad (3.8)$$

where $\{t_I\} = \{t_I^0, \ldots, t_I^m\}$ is the set of initial hardness scales for all primary partons, and $\Delta_R(\{t_I\}) = \prod_{i=1,m} \Delta_R(t_I^i)$. With this in mind, we can finally write the differential cross-section $d\sigma_{\rm PS}$ of a Φ_m showered configuration with initial hardness $\{t_I\}$ in terms of the following recursive expression

$$\begin{aligned} d\sigma_{\rm PS}(\{t_I\}, \Phi_m) \equiv B(\Phi_m)\, d\Phi_m \Big[& \Delta_R(\{t_I\}, t_0) \\ & + \sum_{i=1,m} d\Phi_{{\rm rad},i}(t,z) \Delta_R(\{t_I\}, t) F_i(z,t)\; d\sigma_{\rm PS}(z^2 t)\; d\sigma_{\rm PS}((1-z)^2 t) \Big]\,, \end{aligned} \quad (3.9)$$

where $d\Phi_{{\rm rad},i}(z,t) \equiv \theta t_I^i - t dz dt \frac{d\phi}{2\pi}$ is the phase space cell associated with a shower emission at hardness $t < t_T^i$ and branching energy fraction z, from a parton $i \in \{1, \ldots, m\}$ (ϕ is the azimuthal angle of the emission).
As we mentioned above, the parton shower algorithm will stop at a certain lower cutoff scale t_0, reaching a final state configuration of partons. Moreover, In Pythia8, the Lund String Model [62, 63] has been implemented to simulate the hadronization of the showered partons. To this extent, a set of phenomenological parameters tuned to experimental data must be selected. The Pythia default choice is the Monash2013 tune [64], based on the the heavy-quark fragmentation and strangeness production constraints imposed by LEP and SLD. The subsequent decay of unstable hadrons is also simulated, by randomly selecting a decay channel with a probability proportional to their branching fraction. The decay products are then distributed on the phase space.

3.2 The Matching Problem

A question, at this point, might be asked: is it possible to interface fixed-order calculations with parton showers? A positive answer to this question would allow us to design MC simulations carrying the full fixed-order event generator accuracy for observables inclusive over soft and collinear extra emissions, as well as performing resummation of large logarithms and preserving the parton shower accuracy for a generic exclusive observable. Unfortunately, the problem (often referred to as *matching problem*) is not trivial beyond the LO. At NLO, one could naively imagine generating hard events according to NLO differential cross-section derived in eq. (2.119), and then give them as an input to a SMC program. However, this would lead to an incorrect result, because the first real radiation would be accounting both in the NLO computation (exactly) and in the first parton shower emission (approximately). Proper prescriptions must then be introduced to avoid this *double-counting* problem.

We will try now to pave the way to a solution to the matching problem. To this extent, it can be useful to look at the formal expressions for the fully differential cross-sections, as they are computed by a parton shower and in an exact NLO calculation. In eq. (3.9), we presented a general recursive formula for the differential cross-section of a showered m primary parton configuration. Within that formula, the probability for the hardest emission reads

$$d\sigma \;=\; B(\Phi_m)d\Phi_m \;\Big[\Delta_R(\{t_I\},t_0) \;+\; \Delta_R(\{t_I\},p_{\rm T}) \sum_{i=1,m} F_i(z,t)\theta(t_I^i - t)\,dz\,dt\,\frac{d\phi}{2\pi}\,,\Big] \tag{3.10}$$

where we can expand the Sudakov radiators, to get the following $O(\alpha_s)$ accurate formula

$$d\sigma \;=\; B(\Phi_m)d\Phi_m \;\Big[1 \;-\; \sum_{i=1,m}\int_{t_0}^{t} dt'dz'\,F(\{t'\},z') \;+\; \sum_{i=1,m} F_i(z,t)\theta(t_I^i - t)\,dz\,dt\,\frac{d\phi}{2\pi}\Big]\,, \tag{3.11}$$

also rearrangeable in terms of plus distributions as

$$d\sigma \;=\; B(\Phi_m)d\Phi_m \;\Big[1 \;+\; \sum_{i=1,m} F_i(z,t)_+\theta(t_I^i - t)\,dz\,dt\,\frac{d\phi}{2\pi}\Big] \tag{3.12}$$

Put in this form, eq. (3.12) manifestly preserves unitarity at the perturbative level, since the integration over $t_0 \le t \le t_I^i$ of the plus distribution $F_i(z,t)_+$ is zero.
Let us now consider the $O(\alpha_s)$ expansion of the differential cross-section associated with a hard event, as it can be generated within a parton event generator. As discussed above, NLO calculations in QCD can be explicitly carried out numerically only after proper treatment of their IR divergent behaviour. In a NLO event generator context, this means that parton events into real emission will be generated according to a real matrix element regulated by a set of IR counterterms, one for each possible singular configuration. Practically speaking, every event defined on the real phase space $d\Phi_{m+1}$ will be associated with a negative weighted counter-event, defined according to a chosen local subtraction scheme. The differential cross-section will read

$$d\sigma \;=\; B(\Phi_m)d\Phi_m \;+\; V(\Phi_m)d\Phi_m \tag{3.13}$$

$$+\;\Big[R(\Phi_{m+1})d\Phi_{m+1} \;-\; \sum_i C_i(\Phi_{m+1})d\Phi_{m+1}\mathbf{P}_i\Big]\,. \tag{3.14}$$

The operator $\mathbf{P}$ has the function of projecting the Φ_{m+1} real kinematic configuration on an underlying Φ_m phase space point. This has to be done in a way to ensure the IR safety of the inclusive calculation, namely requiring that:

$$\mathbf{P}\,\{p_1,\ldots,p_i,\ldots,p_{m+1}\} \;=\; \{p_1,\ldots,p_{i-1},p_{i+1},\ldots,p_{m+1}\} \qquad \text{for } p_i \to 0 \tag{3.15}$$

$$\mathbf{P}\,\{p_1,\ldots,p_k,\ldots,p_l,\ldots,p_{m+1}\} \;=\; \{p_1,\ldots,p_k+p_l,\ldots,p_{m+1}\} \qquad \text{for } p_k \parallel p_l\,. \tag{3.16}$$

As a consequence, projections will be defined differently according to the particular singular configuration of the real phase space, to which the label i is associated in (3.13). Note that the countertems have to be defined so as to make the difference between R and $\sum_i C_i$ to IR finite over the entire real phase space.

Having now in mind what a SMC and a parton event generators compute at $O(\alpha_s)$, we can approach solutions to the matching problem. In general, two different NLO+PS matching schemes have become popular and have been corroborated by a vast literature: the MC@NLO method [54] and the POWHEG method [17]. As the latter will be the framework in which the results of this thesis have been obtained, we will devote the following section to describe it in detail.

3.3 A POstitive Weighted Hardest Emission Generator

As mentioned above, another method to perform the NLO+PS matching is commonly used in modern phenomenological studies, namely the POWHEG method. Firstly introduced in a seminal paper by P. Nason [16], its numerical implementation has been developed in a fully general framework [17, 18] and tested for a rather large amount of hard processes. As the name itself suggests, POWHEG has been introduced to avoid negative weighted events, which feature a strong presence in the MC@NLO matching. Differently from MC@NLO, POWHEG is not SMC specific and, in this sense, does not require to compute the Monte Carlo NLO approximation for different Parton Shower algorithms. The really general idea behind POWHEG is to generate the hardest QCD real emission to a certain process first, retaining exact NLO accuracy, and let the SMC generate the subsequent softer emissions. To understand how this is done, let us consider again equation (3.13) and manipulate it in the following way

$$d\sigma \;=\; B d\Phi_m \;+\; V d\Phi_m \;+\; \left[R\, d\Phi_m d\phi_r \;-\; C\, d\Phi_m d\phi_r \mathbf{P}\right] \tag{3.17}$$

$$=\; \left[V + (R - C)\, d\phi_r \mathbf{P}\right] d\Phi_m \;+\; B d\Phi_m \left[1 + \frac{R}{B}(1 - \mathbf{P}) d\phi_r\right] , \tag{3.18}$$

where we assumed the real radiation phase space could be written in a factorized form, as $d\Phi_{m+1} = d\Phi_m d\phi_r$. Such phase space factorisation is defined within the subtraction scheme adopted when carrying out the NLO calculation, and it generally depends on the specific singular configuration that is being subtracted by the single counterterms. Here, for the sake of clarity, we didn't specify this dependence. For the same reason, we also omitted the dependence of B,V,R,C on their respective phase spaces. We can now recast (3.17) as

$$d\sigma \;=\; \bar{B}\, d\Phi_m \left[1 + \frac{R}{B}(1 - \mathbf{P}) d\phi_r\right] , \tag{3.19}$$

where we introduced a new function

$$\bar{B} \;=\; B \;+\; V \;+\; \int d\phi_r (R \;-\; C) , \tag{3.20}$$

which captures the complete NLO correction to the process at hand. Note that (3.19) coincides with eq. (3.17) up to terms which are of order $O(\alpha_s^2)$ relative to the strong coupling order of the Born matrix element. As presented in eq. (3.19), the NLO differential cross-section is expressed in a form that reminds us of eq. (3.12). To make the analogy with the

$O(\alpha_s)$ parton shower formula, we can even define a new function

$$\Delta_R^{(\mathrm{NLO})}(p_\mathrm{T}) \;\equiv\; e^{-\int d\phi_r \frac{R}{B}\theta(k_t(\phi_r)-p_\mathrm{T})}\,, \tag{3.21}$$

so that eq. (3.19) reads, up to $O(\alpha_s^2)$

$$d\sigma \;=\; \bar{B}\, d\Phi_m \left[\Delta_R^{(\mathrm{NLO})}(0) \,+\, \Delta_R^{(\mathrm{NLO})}(p_\mathrm{T})\frac{R}{B}d\phi_r\right], \tag{3.22}$$

which is precisely the master formula of the POWHEG method. Since $\bar{B}$ is forced to be positive by the consistency of perturbation theory, the master formula we just derived cannot feature negative weighted events.
With eq. (3.22), one can generate the first hardest emission in a similar way to what is done in SMC algorithms, and then interface the parton level output to a p_T-ordered parton shower[4]. A veto is applied to the shower, so to generate extra radiation softer than the hard emission transverse momentum.
Several modifications to eq. (3.22) can be adopted when looking at a numerical implementation of the POWHEG method. An example is the treatment of the real matrix element figuring in eq. (3.21) and eq. (3.22). Instead of using R, one can replace it with a modified $\tilde{R}$, and then add back the difference $R-\tilde{R}$ with standard Monte Carlo reweighting techniques at the event generation level. Necessary to this scope is to avoid spurious singularities in defining $\tilde{R}$, so one should make sure that the modified real matrix element reproduces the same IR structure of the actual R. A common way to achieve this, is to define

$$\tilde{R} \;=\; R \,\times\, h(p_\mathrm{T})\,, \tag{3.23}$$

where $h(p_\mathrm{T})$ is a damping factor going to one when $p_\mathrm{T} \to 0$ and smoothly vanishing at high p_T. Such a prescription can help the Monte Carlo generator avoid instabilities linked to the exponentiation of large NLO corrections away from the singular regions.
Before moving on, it might be convenient to review the formulas we derived above in a slightly more rigorous way. To start off with, we consider the $\bar{B}$ function introduced in eq. (3.20). Using the notation introduced in section 2.6, we can formally write

$$\begin{aligned}\bar{B}(\Phi_m) \;&= B(\Phi_m) \,+\, V(\Phi_m) \\ &+ \Big[\int d\phi_r \big[R(\Phi_{m+1} - C(\Phi_{m+1})\big] \int \frac{dz}{z}\big[G_\oplus(\Phi_{m,\oplus}) + G_\ominus(\Phi_{m,\ominus})\big]\Big]^{\bar{\Phi}_m\,=\,\Phi_m}\,,\end{aligned} \tag{3.24}$$

where, we recall, $G_\oplus$ and $G_\ominus$ are counterterms introduced to cancel collinear singularities arising from the initial state, which are not compensated by the virtual corrections. Note that we also assumed the phase spaces Φ_{m+1}, $\Phi_{m,\oplus}$ and $\Phi_{m,\ominus}$ to be expressed in terms of barred variables when integrating over the extra radiation phase space, and letting $\bar{\Phi}_m$ coincide with Φ_m after the integration. The modified Sudakov form factor in eq. (3.21) reads

$$\Delta(\Phi_m, p_\mathrm{T}) \;=\; \exp\left\{-\int \frac{[d\phi_r\, R(\Phi_{m+1})\theta(k_T(\Phi_{m+1}) - p_\mathrm{T})]^{\bar{\Phi}_m=\Phi_m}}{B(\Phi_m)}\right\}. \tag{3.25}$$

[4] As shown in [16], it is also possible to adapt the method to showers with different orderings, like angular ordered showers, by introducing *truncated showers* and a proper *veto procedure*.

Finally, the differential cross-section in eq. (3.22) can be written as

$$d\sigma \;=\; \bar{B}(\Phi_m)\, d\Phi_m \left\{ \Delta(\Phi_m, p_{\mathrm{T}}^{\mathrm{min}}) \;+\; \Delta(\Phi_m, k_T(\Phi_{m+1})) \frac{R(\Phi_{m+1})}{B(\Phi_m)} d\phi_r \right\}_{\bar{\Phi}_m = \Phi_m} , \tag{3.26}$$

where we also introduced a $p_{\mathrm{T}}^{\mathrm{min}}$ to prevent the generation of extra radiation below the hadronisation scale, similar to what is done in SMC programs. Although these formulas allow us to study the method in a more precise way, it might be even more beneficial to go one step further and understand how subtraction of IR singularities is carried out in eq. (3.26), within a certain subtraction scheme. In the case of POWHEG, the FKS subtraction was adopted to this extent. According to the FKS prescriptions [21], sectors are introduced to separate and organize in a systematic way all the different IR singular phase space regions of R. Labeling the flavour structures contributing to the Born process with an index f_b, we will have a set of FKS sectors for each different f_b. We denote with i the index running over these FKS sectors, so that we can define $\bar{B}$ in a specific flavour structure f_b as

$$\bar{B}^{f_b}(\Phi_m) \;=\; \left[B(\Phi_m) \;+\; V(\Phi_m)\right]_{f_b} \;+\; \sum_{i \in \{i | f_b\}} \int d\phi_r \left[R(\Phi_{m+1} - C(\Phi_{m+1})\right]_i^{\bar{\Phi}_m^i = \Phi_m} \tag{3.27}$$

$$+ \sum_{i_\oplus \in \{i_\oplus | f_b\}} \int \frac{dz}{z} G^i_\oplus(\Phi_{m,\oplus}) \;+\; \sum_{i_\ominus \in \{i_\ominus | f_b\}} \int \frac{dz}{z} G^i_\ominus(\Phi_{m,\ominus})^{\bar{\Phi}_m = \Phi_m} , \tag{3.28}$$

and analogously, for the POWHEG Sudakov radiator

$$\Delta^{f_b}(\Phi_m, p_{\mathrm{T}}) \;=\; \exp\left\{ - \sum_{i \in \{i | f_b\}} \int \frac{\left[d\phi_r\, R(\Phi_{m+1}) \theta(k_T(\Phi_{m+1}) - p_{\mathrm{T}})\right]_i^{\bar{\Phi}_m^i = \Phi_m}}{B^{f_b}(\Phi_m)} \right\} . \tag{3.29}$$

Putting pieces together, to differential cross-section will read

$$\begin{aligned} d\sigma \;=\; \sum_{f_b} \bar{B}^{f_b}(\Phi_m)\, d\Phi_m \Bigg\{ & \Delta^{f_b}(\Phi_m, p_{\mathrm{T}}^{\mathrm{min}}) \\ & + \sum_{i \in \{i | f_b\}} \frac{\left[\Delta^{f_b}(\Phi_m, k_T(\Phi_{m+1})) R(\Phi_{m+1}) d\phi_r \right]_i^{\bar{\Phi}_m^i = \Phi_m}}{B^{f_b}(\Phi_m)} \Bigg\} . \end{aligned} \tag{3.30}$$

To persuade ourselves that eq. (3.30) effectively yields NLO accuracy for a generic infrared-safe observables O, let us use it to carry out the explicit computation of O

$$\begin{aligned} \langle O \rangle \;=\; \sum_{f_b} \int d\Phi_m\, \bar{B}^{f_b}(\Phi_m) \Bigg\{ & \Delta^{f_b}(\Phi_m, p_{\mathrm{T}}^{\mathrm{min}})\, O_m(\Phi_m) \\ & + \sum_{i \in \{i | f_b\}} \frac{\left[\int d\phi_r\, \Delta^{f_b}(\Phi_m, k_T(\Phi_{m+1})) R(\Phi_{m+1})\, O_{m+1}(\Phi_{m+1}) \right]_i^{\bar{\Phi}_m^i = \Phi_m}}{B^{f_b}(\Phi_m)} \Bigg\} , \end{aligned} \tag{3.31}$$

and then, replacing O_{m+1} with $O_m + (O_{m+1} - O_m)$

$$\begin{aligned}\langle O\rangle \;=\; & \sum_{f_b}\int d\Phi_m\,\bar{B}^{f_b}(\Phi_m) \\ \times & \left\{\left[\Delta^{f_b}(\Phi_m,p_{\mathrm{T}}^{\min}) + \sum_{i\in\{i|f_b\}}\frac{\left[\int d\phi_r\,\Delta^{f_b}(\Phi_m,k_T(\Phi_{m+1}))R(\Phi_{m+1})\,O_{m+1}(\Phi_{m+1})\right]_i^{\bar{\Phi}^i_m=\Phi_m}}{B^{f_b}(\Phi_m)}\right]O_m(\Phi_m)\right. \\ & \left. + \sum_{i\in\{i|f_b\}}\frac{\left[\int d\phi_r\,\Delta^{f_b}(\Phi_m,k_T(\Phi_{m+1}))R(\Phi_{m+1})\,(O_{m+1}(\Phi_{m+1})-O_m(\Phi_m))\right]_i^{\bar{\Phi}^i_m=\Phi_m}}{B^{f_b}(\Phi_m)}\right\}.\end{aligned} \tag{3.32}$$

It is possible to show now that the expression multiplying $O_m(\Phi_m)$ in the second line of eq. (3.32) is equal to one. Expanding then up to $O(\alpha_s)$ the last term, one ends up with the following formula

$$\begin{aligned}\langle O\rangle \;=\; & \sum_{f_b}\int d\Phi_m\left\{\bar{B}^{f_b}(\Phi_m)\,O_m(\Phi_m)\right. \\ & \left. + \sum_{i\in\{i|f_b\}}\left[\int d\phi_r\,R(\Phi_{m+1})\,(O_{m+1}(\Phi_{m+1})-O_m(\Phi_m))\right]_i^{\bar{\Phi}^i_m=\Phi_m}\right\},\end{aligned} \tag{3.33}$$

which explicitly proves the NLO accuracy of the POWHEG master formula for inclusive observables, up to power terms of $p_{\mathrm{T}}^{\min}$ which can be neglected.
Now we can finally discuss how to implement eq. (3.26) in an event generator framework, as it is done in the POWHEG-BOX [18]. Schematically, we can imagine the algorithm to be organized in two steps, given a generic process:

1. A Born level event is generated on the Φ_m phase space with a certain Born flavour structure f_b, according to a probability equal to $\bar{B}^{f_b}(\Phi_m)d\Phi_m$.

2. The hard radiation is generated with a certain ϕ_r^i on a real flavour configuration $i \in \{i|f_b\}$, according to a probability defined by

$$\left[\frac{R(\Phi_{m+1})}{B(\Phi_m)}\Delta^{f_b}(\Phi_m,k_T(\Phi_{m+1}))\right]_i^{\bar{\Phi}^i_m=\Phi_m}d\phi_r\;. \tag{3.34}$$

The first step is customary in MC event generators and there are well-known techniques to approach it. To design rather optimized programs, usually, an importance sampling is performed via the *hit and miss* procedure. The procedure works like this: instead of generating a set of variables according to their actual distribution probability, this is generated according to another distribution that is greater or equal to the original one in every point of its domain. Such function, known as *upper bound*, is supposed to look simpler than the original probability distribution. This allows, in turn, to generate points distributed along with the upper bound function with significantly less computational power expenses. After a point

is generated, it is accepted or rejected with a probability equal to the ratio of the original probability and its upper bound. The more the upper bound approximates the probability distribution, then more points will be accepted, drastically reducing the running time of the program. Unfortunately, eq. (3.27) poses another problem that threatens the performances of event generations. Every time the program is asked to accept or reject a certain event, an integration over $d\phi_r$ is required to compute the full $\bar{B}$ POWHEG function. To smart our way out of this issue, we can parametrize the real radiation phase space ϕ_r using three variables in the unit cube $X_{\text{rad}} = \{X^{(1)}, X^{(2)}, X^{(3)}\}$, where $0 < X^{(i)} < 1$ for $i = 1, 2, 3$. A new function can then be introduced based on eq. (3.27), which looks like

$$\begin{aligned}\tilde{B}^{f_b}(\Phi_m, X_{\text{rad}}) \;&= \left[B(\Phi_m) \,+\, V(\Phi_m)\right]_{f_b} \\ &+ \sum_{i\in\{i|f_b\}} \left[\left|\frac{\partial\phi_r}{\partial X_{\text{rad}}}\right| R(\Phi_{m+1} - C(\Phi_{m+1})\right]_i^{\bar{\Phi}^i_m = \Phi_m} \\ &+ \sum_{i_\oplus\in\{i_\oplus|f_b\}} \frac{1}{z}\left|\frac{\partial z}{\partial X^{(1)}}\right| G^i_\oplus(\Phi_{m,\oplus}) \,+ \sum_{i_\ominus\in\{i_\ominus|f_b\}} \frac{1}{z}\left|\frac{\partial z}{\partial X^{(1)}}\right| G^i_\ominus(\Phi_{m,\ominus}) \,.\end{aligned} \tag{3.35}$$

By construction, eq. (3.35) reduces to eq. (3.27) when integrating over the X_{rad} variables. The full $\tilde{B}$ function will be defined as the sum over the flavour-dependent $\tilde{B}^{f_b}$, analogously to how the full $\bar{B}$ is defined. Generating Born phase space points can now be made way easier by applying a simple trick. Instead of directly generating a $\Phi_m^{f_b}$ configuration, a set of variables $\{\Phi_m, X_{\text{rad}}\}$ is generated according to $\tilde{B}(\Phi_m, X_{\text{rad}})$, and f_b is chosen with a probability of $\tilde{B}^{f_b}(\Phi_m, X_{\text{rad}})/\tilde{B}(\Phi_m, X_{\text{rad}})$. The X_{rad} variables are then discarded, ending up with a $\Phi_m^{f_b}$ point effectively generated according to eq. (3.27), but avoiding any integrations.
While the procedure just presented allows to generate unweighted events, some peculiar situations make it preferable to work with weighted events. The difference between the two kinds of events is pretty simple, and we'll try now to illustrate it using a couple of relevant examples. Let us suppose that the process we are studying in POWHEG features IR singularities already at the Born level. This naturally happens when the production of light jets is considered, maybe in association with colour singlet particles[5]. In this case, $\tilde{B}$ will become singular as the transverse momentum of the light jet vanishes, leading to the number of events generated in this region to blow up, and leaving a much smaller number of events to populate the harder regions. Such a scenario is pretty unfortunate when the user aims to analyze fiducial distributions with standard LHC analyses, that always set a transverse momentum selection cut on the clustered jets in each event (usually around 20GeV). To overcome this issue, one can hard-code a generation cut of the Born phase space of the process, reducing the domain of $\tilde{B}$ to the hard jet regions. A widely applied alternative consists on introducing a *suppression factor* $W(\Phi_m)$, and generating events distributed according to $\tilde{B}(\Phi_m) \times W(\Phi_m)$. The bias induced in the event generation is then corrected by reweighting every event by $W^{-1}(\Phi_m)$. A well-designed suppression factor is such, that in the IR singular

[5] Many processes like these are phenomenologically relevant at the LHC and have been studied within the POWHEG-BOX framework over the last few years. For example, release implementations are currently available for $pp \to$ di-jet [65], $pp \to$ tri-jet [66], $pp \to W^+W^-$ + jet [67, 68], $pp \to W^\pm Z$ + j [69], $pp \to H$ + n-jets [70, 71]. Moreover, the colour singlet production processes in association with one jet (like W^+W^- + jet and H + jet) are also the starting point of the MiNNLO$_{\text{PS}}$ method implementation, as it will be widely discussed in sections 3.5 and 3.6.

regions of $\tilde{B}(\Phi_m)$ one has

$$\tilde{B}(\Phi_m) \times W(\Phi_m) \;\rightarrow\; \text{finite} \,, \tag{3.36}$$

while no spurious singularities are introduced. With this procedure, the event spreading will be pulled out of the singular phase space regions, but hard events will count less than softer ones because of the reweighting. The statistical precision of fiducial cross-sections and distributions will increase, without their accuracy being biased. Sometimes, suppression factors can even be employed to just increase statistics in lower cross-section phase space regions, without the necessity of avoiding singularities. As we will see, the application of this technique will be central to successfully study the hard regime of some $b-$jet observables in chapter 7.

Finally, let us consider the hardest radiation generation in POWHEG. Now that we have a point (Φ_m, f_b), we must generate a radiation phase space point $(\phi_r^{\alpha_i}, \alpha_i)$, where α_i represents the real flavour structure associated with the sector i in eq. (3.35). In particular, $(\phi_r^{\alpha_i}, \alpha_i)$ has to be selected according to the probability defined in eq. (3.34). In POWHEG, this task is carried out by applying two well-established algorithms, that we are going to discuss. To illustrate them, we formalize the problem as follows: given an integer number k and a set of d real numbers x_k associated to each k, how can we sample $\{k, x_k\}$ according to a probability

$$f_k(x_k) \prod_i \Delta_i(h_k(x_k)) d^d x_k \,. \tag{3.37}$$

We can start by applying the *Highest bid procedure*. This means that we consider all the possible values of k, and we generate the variables x_k according to the probability

$$f_k(x_k) \Delta_k(h_k(x_k)) d^d x_k \,, \tag{3.38}$$

and then we pick the k value corresponding to the largest $h_k(x_k)$ for the given sets of x_k. In fact, it is not difficult to show that the probability for a given $\{k, x_k\}$ to have the largest $h_k(x_k)$ is precisely the probability for the k configuration to produce one emission at $h_k(x_k)$ (which is eq. (3.38)), multiplied by the probability of the other configurations to not emit, which is given by

$$\prod_{i \neq k} \Delta_i(h_k(x_k)) d^d x_i \,, \tag{3.39}$$

giving indeed eq. (3.37).

For what concerns the probability of generating a sample x_k according to eq. (3.37), this is done with the *Veto technique*, which we discuss now. Ignoring the label k for the sake of clarity, we want to generate a set $x \in \mathbb{R}^d$ with probability $f(x)\Delta(h(x))d^d x$, where

$$\Delta(h) \equiv \exp\left\{ -\int d^d x' f(x') \theta(h(x') - h) \right\} , \tag{3.40}$$

and[6]

$$\Delta(0) \equiv \exp\left\{ -\int d^d x' f(x') \right\} . \tag{3.41}$$

With these ingredients, it is not difficult to show that the probability for the variable h to fall within an infinitesimal range $\{h_0, h_0 + dh\}$ is uniform in $d\Delta(h)$, which is

$$d\Delta(h) \;=\; dh \int d^d x' \delta(h - h(x)) f(x) \exp\left\{ -\int d^d x' f(x') \theta(h(x') - h) \right\} . \tag{3.42}$$

In principle, one could then use a standard uniform sampling technique for $\Delta(h)$ to get a certain $\delta(H)$ and then generate the set of x on the surface $\delta(H - h(x))$ and with a distribution function proportional to $f(x)\delta(H - h(x))$[7]. Unfortunately, doing this analytically is really hard in general, but here it comes the veto method. The key is to define a function $F(x)$ which will be the upper bounding function of f, namely $F(x) \geq f(x)$ for all x in the domain, then introduce a new Sudakov radiator

$$\Delta_F(h) = \exp\left[-\int d^d x' F(x') \theta(h(x') - h) \right] . \tag{3.43}$$

The upper bounding function should be chosen in a way to allow for a much simpler solution to the sampling of h and x presented above. If an F is found with the properties required, then the veto techniques are articulated in the following steps:

1. A real $H_{\max}$ is found by solving $\Delta_F(H_{\max}) = 1$.
2. A random number $0 < r < 1$ is generated.
3. A real H is found by solving $\Delta_F(H)/\Delta(H_{\max}) = r$.
4. The set of x is generated according to $F(x)\delta(h(x) - H)$.
5. A new random number r' is generated.
6. It is checked whether $r' > f(x)/F(x)$. If true, the event is vetoed, $H_{\max}$ is set to the H above and the loop starts again from step 2. If false, the algorithm stops.

3.4 Multi-Scale Improved NLO

If in the previous sections, we broadly discussed how to preserve the fixed-order NLO accuracy of event generators with parton showers, we pretended for a moment to ignore other problems affecting realistic QCD predictions, potentially endangering results already at the leading order. The first problem is about how to choose the renormalisation scale μ_R and the factorisation scale μ_F for concrete processes. To be fair, this problem is a general matter of debate transcending the technicalities of event generators. Even if these scales appear in the renormalisation and factorisation procedures as completely arbitrary, the value they are actually set to can have deep consequences on the convergence of perturbative series. Naively,

[6] Here we assumed the unrestricted integral of f to be divergent.
[7] The exponential factor in eq. (3.42) is just a number.

we can imagine that μ_R and μ_F are properly chosen when the theoretical uncertainties computed with the 7-point scale variation [8] decrease by increasing orders, and central values come to converge. While this observation is coherent with good scale choices, elevating it to a criterion to fine-tune μ_R and μ_F a posteriori can be highly misleading. Indeed, some other genuine physical effects can produce large higher-order contributions, and hiding them by a spurious scale compensation mechanism may lead to unreliable results.
Sometimes, the process under exam speaks for itself, and scales can be assigned in a natural way. This happens when the physics of the problem is dictated by one single physical scale, like the mass of the Higgs boson M_H in Higgs boson hadroproduction via gluon fusion. Cross-sections will carry logarithms of the ratio of M_H and μ_R, μ_F, which can be canceled when defining the scales. The situation becomes more convoluted though, when one considers the exclusive Higgs boson production in association with a light jet. Now the process will be characterised by two scales, the Higgs boson mass and the jet transverse momentum p_{T}, and their presence will reflect in some double logarithms potentially large at low p_{T} (the *Sudakov region*). The problem must then be approached at a deeper level.
Unbiased ways to perform scale choices have been the object of researches, starting from the studies on the leading-order/parton shower matching. One advancement was represented by the CKKW method [72], whose innovative prescriptions had an impact on the whole formalism that we will develop in the next sections. The method applies to production processes involving coloured partons in the final state, and works as follows

1. A $N-$parton production event in hadronic collisions is generated with leading order precision, by using its squared tree-level amplitude $|A_N^{(0)}|^2$.

2. The k_T-clustering algorithm is applied to reconstruct the event branching history.

3. For each vertex i ($i = 1, \dots, n$) of the branching history, a nodal scale $q_i = p_{\mathrm{T}}^{i_1 i_2}$ is assigned, where $p_{\mathrm{T}}^{i_1 i_2}$ corresponds to the relative transverse momentum of the parton couple (i_1, i_2) clustered in i.

4. Jets are considered resolved above a certain resolution scale Q_0, beneath which the radiative phase space will be populated by the parton shower. The set of clustered jets will compose the so-called *primary system*, to which the scale Q is assigned to be equal to its invariant mass.

5. The α_s strong couplings present in the tree-level matrix element used at (1) are reweighted: n of them are evaluated at the nodal scales defined at (3), the remaining $m = N - n$ are evaluated at the primary system scale Q at (4). Schematically

$$\alpha_s^N \quad \longrightarrow \quad \alpha_s(q_1) \times \ \dots \ \times \alpha_s(q_n) \ \times \ \alpha_s^m(Q) \ . \tag{3.44}$$

6. Another reweighting factor is included, by assigning to each intermediate line between nodes i and j in the branching history a factor

$$\frac{\Delta_{f_{ij}}(Q_0, q_i)}{\Delta_{f_{ij}}(Q_0, q_j)} \ , \tag{3.45}$$

[8] See section 2.6.

where Δ_f is the f flavoured Sudakov form factor[9]

$$\Delta_f(Q,Q') \;=\; \exp\left\{ -\int_{Q'^2}^{Q^2} \frac{dq^2}{q^2}\Big[A(\alpha_s(q^2))\log\frac{Q^2}{q^2} + B(\alpha_s(q^2))\Big]\right\}, \tag{3.46}$$

with $A(\alpha_s)$ and $B(\alpha_s)$ admitting a universal α_s expansion

$$\begin{aligned} A(\alpha_s) \;&=\left(\frac{\alpha_s}{2\pi}\right)A^{(1)} + \left(\frac{\alpha_s}{2\pi}\right)^2 A^{(2)} + \dots \\ B(\alpha_s) \;&=\left(\frac{\alpha_s}{2\pi}\right)B^{(1)} + \left(\frac{\alpha_s}{2\pi}\right)^2 B^{(2)} + \dots\ , \end{aligned} \tag{3.47}$$

and where f_{ij} is the flavour of the line connecting i and j. For the external lines, the factor will be $\Delta_f(Q_0, q_i)$ (i denoting the nodes connected to the external lines and f the external line flavours).

7. The factorisation scale entering PDF's is reweighted to the resolution scale Q_0.

8. The reweighted event is finally interfaced to a parton shower program, properly vetoed to prevent from generating radiation above the resolution scale Q_0, which is effectively the matching scale of the process.

As the method we just summarized represents an effective way to match exact leading-order QCD matrix elements for multi-parton processes with MC parton showers, one can imagine if its features can be applied in the NLO+PS matching context. Such a question has a positive answer, and the POWHEG framework turns out to be extremely versatile to be adapted for this scope. We are now going to discuss the *Multi-scale improved NLO* [74], also known as MINLO.

When trying to adapt the CKKW scheme to an NLO calculation, it is fundamental that the new reweighting factors that are introduced don't spoil the formal NLO accuracy of the calculation. In other words, all possible modifications to the NLO cross-section have to be at most of order $O(\alpha_s^2)$ relative to the Born of the process at hand. To understand how to perform different scale choices without affecting the NLO cross accuracy of our calculations, let us examine the μ_R dependence of a generic NLO cross-section

$$\frac{d\sigma}{d\Phi} \;=\; \alpha_s^N(\mu_R)B \;+\; \alpha_s^{N+1}(\mu_R)\Big[V + Nb_0\log\frac{\mu_r^2}{Q^2}B\Big] \;+\; \alpha_s^{N+1}(\mu_R)R\,. \tag{3.48}$$

Where the explicit virtual dependence on μ_R is proportional to the Born matrix element[10]. When changing the renormalisation scale of a strong coupling from μ_r' to μ_r'', this effectively behaves as $\alpha_s(\mu_r') = \alpha_s(\mu'') + O(\alpha_s^2)$ according to the renormalisation group equations. Since the $O(\alpha_s^{N+1})$ terms introduced by varying the Born strong coupling scales are exactly

[9] For the explicit flavour-dependent expressions of the A and B coefficients up NLL accuracy, we refer to eqs. (2.5-2.6) of Ref. [73].

[10] b_0 is the one-loop beta function coefficient

$$b_0 \;=\; \frac{33-2n_f}{12\pi}\,. \tag{3.49}$$

compensated by the virtual contributions in eq. (3.48), different scale choice will affect the cross-section only starting from $O(\alpha_s^{N+2})$. If we are willing to evaluate couplings at different scales, as the CKKW method prescribes, then what we just observed will still hold when converting eq. (3.48) into

$$\frac{d\sigma}{d\Phi} \;=\; \prod_{i=1}^{N} \alpha_s^N(\mu_r^{(i)})B \;+\; \alpha_s^{N+1}(\mu'_R)\Big[V + b_0 \sum_{i=1}^{N} \log \frac{(\mu_r^{(i)})^2}{Q^2} B\Big] \;+\; \alpha_s^{N+1}(\mu''_R)R\,, \tag{3.50}$$

which is consistent with setting the central scale μ'_r of virtual contribution to

$$\mu'_r \;=\; \Big(\prod_{i=1}^{N} \mu_r^{(i)}\Big)^{\frac{1}{N}}\,, \tag{3.51}$$

namely the geometric average of the $\mu_r^{(i)}$.
Regarding the overall Sudakov form factors entering the CKKW reweighting prescription, we notice that their α_s expansions would introduce new $O(\alpha_s^{N+1})$ terms in eq. (3.48). These terms will be proportional to the Born, and must be properly subtracted from it to preserve the NLO accuracy of the cross-section.
With all the above considerations in mind, we can now present how the MiNLO method was designed and successfully implemented in Powheg. Schematically, every event is treated according to the following prescriptions

1. A k_T clustering is performed on the same footing of the CKKW scheme, and the scales $Q, q_1, \ldots, q_n$ are sorted out. For real kinematics events, an additional q_0 scale is determined.

2. The resolution scale Q_0 is set to be equal to q_1.

3. Among the N powers of α_s associated to the Born, n of them are evaluated at the scales $\mu_r^{(i)} = K_r q_i$ $(i = 1, \ldots)$ and the $m + N - n$ at $\mu_Q = K_r Q$. The factor K_r is usually varied between 1/2 and 2 to perform the customary scale variation.

4. The same scale setting of the Born is adopted for N of the $N+1$ α_s powers of the real and virtual contributions.

5. The remaining $(N+1)^{\text{th}}$ α_s multiplying R and V is set to the average of the other N α_s

$$\tilde{\alpha}_s \;=\; \frac{1}{N}\Big(\sum_{i=1}^{n} \alpha_s(\mu_r^{(i)}) + m\alpha_s(\mu_Q)\Big)\,. \tag{3.52}$$

6. For the Born and the virtual skeleton lines, Sudakov form factors are introduced similarly to the CKKW procedure. For the real configurations, only the branching history after the first clustering is considered. As for the coefficients entering the Sudakov form factor, $A^{(1)}$, $A^{(2)}$ and $B^{(1)}$ are accounted [11].

[11] See eq. (3.47)

7. A subtraction term is introduced at the Born level to compensate for the $O(\alpha_s^{N+1})$ terms resulting from the perturbative expansion of the Sudakov form factors $\Delta = 1 + \frac{\alpha_s}{2\pi}\Delta^{(1)} + O\big(\big(\frac{\alpha_s}{2\pi}\big)^2\big)$. Effectively, the Born undergoes the following replacement

$$B \longrightarrow B \times \left(1 - \frac{\tilde{\alpha}_s}{2\pi} \sum_{i,j\ (q_i > q_j)} [\Delta^{(1)}_{f_{ij}}(Q_0, q_i) - \Delta^{(1)}_{f_{ij}}(Q_0, q_j)] - \frac{\tilde{\alpha}_s}{2\pi} \sum_l \Delta^{(1)}_{f_l}(Q_0, q_{k_l})\right). \tag{3.53}$$

   The two terms in the square brackets will compensate for the internal leg Sudakov, while the last sum will cancel the $O(\frac{\alpha_s}{2\pi})$ term resulting from expanding the external leg Sudakov. f_{ij} denotes the flavour of the intermediate line between the i and j nodes, and f_l the one of the external l lines. Notice that the strong coupling is set to eq. (3.52) consistently with the real and virtual setting, but other prescriptions are possible.

Designed in the way we summarized, MiNLO'MiNLO improves the description of NLO inclusive observables in Powheg by introducing a simple reweighting of the generated events. All the discussed modifications are formally NNLO accurate. However, a big improvement is observed in the description of the Sudakov regions, resulting in higher accuracy results.

3.5 The MiNLO' Method

Along with the studies on the matching problem, another question was addressed by the community working on MC event generators in the past decades. This question, which we can name as the *Merging problem*, relates to how to combine different jet multiplicity generators in the calculation of some classes of observables. An intuitive description of the problem is presented in Ref. [73], which we will summarize here. Suppose that we are interested in predicting the transverse momentum of the Higgs boson in gluon fusion. By definition, such an observable requires additional QCD partons to recoil against the Higgs boson for $p_{\mathrm{T}}^{(H)} > 0$. The Higgs boson Powheg generator **H** will give an LO accurate result for this observable, since just the real kinematics events (involving one additional jet) will populate its bins. On the other hand, the Higgs+jet generator **HJ** will produce NLO accurate results by definition. However, the low-$p_{\mathrm{T}}^{(H)}$ region of the distribution will be plagued by a large Sudakov logarithmic enhancement, effectively screwing up the formal NLO accuracy provided by the generator. Relatively to this example, a merging technique is supposed to take the best of both generators and obtain a NLO accurate prediction throughout the whole p_{T}^H spectrum.

Some of the first solutions to the merging problem were based on the introduction of a merging scale. The idea is quite simple, and we can explain it by sticking to the same example of p_{T}^H. If we define a scale $p_{T,\mathrm{cut}}$ we can imagine filling the bins below it only with **H** events, and the ones above it only with **HJ** events. The result will be NLO accurate at high p_{T}^H and insensitive to large logarithms at low p_{T}^H. Unfortunately, the trickiest point is tp choose the artificial merging scale without biasing the result with its spurious dependence on it. Removing the bias is impossible, but some techniques have been proposed to mitigate its presence. Is it possible, however, to merge different jet configurations with no merging scale?

Connecting the dots of what we discussed so far, it appears that the MiNLO method was

already doing something similar, in a way. As it was numerically checked in Ref. [73], the MiNLO-improved **HJ** generator significantly improved the stability of the low $p_{\rm T}^{(H)}$ regions, giving results close to the **H** Powheg prediction[12]. Nonetheless, MiNLO is still missing some ingredients to achieve formal NLO accuracy for jet-inclusive observables. We will discuss now these ingredients and understand how they can be implemented to achieve a fully merged calculation. We will see that small variations will be applied to the MiNLO scheme, in the case of a Higgs boson production (via gluon fusion) in association with a jet.
At this point, it is convenient to introduce some useful notation. We will refer to (0) accuracy when considering the **H** generator, formally NLO for extra radiation inclusive observables. As an example, LO$^{(0)}$ and NLO$^{(0)}$ will mean leading and next-to-leading order accuracy in the Higgs boson inclusive distributions. The **HJ** generator accuracy will be referred to as (1).
Including the MiNLO prescriptions in the $\bar{B}$ definition of the **HJ** generator, this will read

$$\bar{B} \;=\; \alpha_s^2(M_H^2)\alpha_s(q_T^2)\Delta_g^2(M_H,q_T)\left[B\left(1-\frac{\tilde{\alpha}_s}{\pi}\Delta_g^{(1)}(M_H,q_T)\right)+V+\int d\phi_{\rm rad}R\right], \qquad (3.54)$$

with $\tilde{\alpha}_s$ calculated according to eq. (3.52). By construction, eq. (3.54) yields NLO$^{(1)}$ accuracy and contains singular terms for q_T approaching zero. The same singular parts are also encoded in the following NNLL resummation formula for the H transverse momentum q_T at fixed rapidity y

$$\frac{d\sigma}{dydq_T^2} \;=\; \sigma_0\frac{d}{dq_T^2}\Big\{\prod_{i=a,b}[C_{gi}\otimes f_{i/P_i}](x_i,q_T)\;e^{S(Q,q_T)}\Big\} \;+\; R_f\;, \qquad (3.55)$$

where the product runs over the incoming partons a from the proton P_a and b from the proton P_b. The parton distribution functions f are convoluted with the universal coefficient functions, emerging in the factorisation of the initial-state collinear radiation, thus reading

$$C_{ij}(\alpha_s,z) \;=\; \delta_{ij}\delta(1-z)+\sum_{n=1}^{\infty}\alpha_s^n C_{ij}^{(n)}(z)\;, \qquad (3.56)$$

according to the standard convolution operation

$$(f\otimes g)(x) \;\equiv\; \int_x^1\frac{dz}{z}f(z)g\left(\frac{x}{z}\right). \qquad (3.57)$$

The Sudakov exponent is defined as

$$e^{S(Q,q_T)} \;\equiv\; \Delta_g^2(Q,q_T) \;=\; \exp\left\{-\int_{Q'^2}^{Q^2}\frac{dq^2}{q^2}\Big[A(\alpha_s(q^2))\log\frac{Q^2}{q^2}+B(\alpha_s(q^2))\Big]\right\}, \qquad (3.58)$$

and R_f denotes the non-singular terms of the cross-section. Notice that μ_R and μ_F in eq. (3.55) are set to q_T.
The idea now is to expand the NNLL formula in series and understand which terms must be

[12] Analogous comparisons have been performed for other observables. The MiNLO-improved **HJJ** calculation has also been studied and compared to the standard **HJ** Powheg calculation.

kept to guarantee the inclusive rapidity distributions are NLO accurate. In other words, the expansion of eq. (3.55) should contain all the necessary ingredients that, after integration over q_T, characterise NLO$^{(0)}$ accuracy. After doing that, we will be able to compare the final expression with eq. (3.54) and single out the missing pieces needed to provide MiNLO with NLO$^{(0)}$ accuracy.
If we integrate eq. (3.55) over q_T^2, we get the relatively simple expression

$$\frac{d\sigma}{dy} \;=\; \sigma_0\,[C_{ga}\otimes f_{a/P_a}](x_a,Q)\;\times\;[C_{gb}\otimes f_{b/P_b}](x_b,Q)\;+\;\int dq_T^2 R_f\;, \tag{3.59}$$

which would naively push us to include all terms up to $O(\alpha_s)$ accuracy relative to the Born-level of the H production. That would end up in taking the $O(\alpha_s)$ expansion of the coefficient functions (including $C_{ij}^{(1)}$) and the LO$^{(1)}$ accurate terms in the finite reminder R_f. No constraints would be imposed on the Sudakov form factors, as they are no longer present after the integration[13]. However, the formal NLO$^{(1)}$ of the unintegrated formula forces us to include the A_1 and A_2 terms, and the B_1 and B_2 terms.
A more detailed analysis, though, allows us to drop more higher-order terms and preserve NLO$^{(0)}$ accuracy. Indeed, we can perform the q_T derivative present in eq. (3.55) and get (after defining $L\equiv\log Q^2/q_T^2$)

- Terms proportional to $\alpha_s L$ and $\alpha_s^2 L$ from the derivative of A_1 and A_2.
- Terms of order α_s and α_s^2 from the derivative of B_1 and B_2.
- Terms of order α_s from each derivative of $C_{ij}^{(1)}$.
- Terms of order α_s from the derivative of the PDFs.

To summarize, all terms will have the following terms

$$\sigma_0\frac{1}{q_T^2}[\alpha_s,\alpha_s^2,\alpha_s^3,\alpha_s^4,\alpha_s L,\alpha_s^2 L,\alpha_s^3 L,\alpha_s^4 L]\;e^{S(Q,q_T)}\;, \tag{3.60}$$

where the terms contating $\alpha_s,\alpha_s^2,\alpha_s L,\alpha_s^2 L$ must be included to get NLO$^{(1)}$ accuracy. Then, to understand which other terms are necessary to preserve NLO$^{(0)}$ after the q_T integration, we can size the α_s power of each term in eq. (3.60) by the formula [14]

$$\int_{\Lambda^2}^{Q^2}\frac{dq_T^2}{q_T^2}\;e^{S(Q,q_T)}\;\alpha_s^n(q_T^2)\;\log^m\left(\frac{Q^2}{q_T^2}\right)\;\approx\;[\alpha_s(Q^2)]^{n-\frac{m+1}{2}}\;. \tag{3.61}$$

With this, we easily see that only one more higher-order term in eq. (3.60) must be accounted for, namely $\alpha_s^3 L$. This will contribute at NLO$^{(0)}$ with a term of order $[\alpha_s(Q^2)]^{3-\frac{2}{2}}=\alpha_s^2(Q^2)$. All the other terms are unnecessary to the present discussion and can be neglected
Comparing the result we ended up with the singular terms of eq. (3.54), it is possible to check that their singular parts are identical, except for the absence of B_2 in MiNLO. All things considered, we will only need to modify eq. (3.54) by

[13] This happens because $\exp S(Q,q_t)$ in simply 1 on the upper integration extreme Q, and approaches zero in the low q_t limit.
[14] See eq. (2.18) of [73].

1. Including B_2 in the MiNLO Sudakov form factor.
2. Setting μ_F and the scales μ_R entering V, R and $\Delta^{(1)}$ to q_T.

The new set of prescriptions goes under the name of MiNLO'. Finally, the new MiNLO' method can be easily embedded in the Powheg framework via a redefinition of the $\bar{B}$ function in eq. (3.20) as

$$\left[\bar{B}(\Phi_{\rm FJ})\right]^{\rm MiNLO'} \equiv e^{-\tilde{S}(p_{\rm T})}\left\{\frac{\alpha_s(p_{\rm T})}{2\pi}\left[\frac{d\sigma_{\rm FJ}}{d\Phi_{\rm FJ}}\right]^{(1)}\left(1+\frac{\alpha_s(p_{\rm T})}{2\pi}\tilde{S}^{(1)}(p_{\rm T})\right) + \left(\frac{\alpha_s(p_{\rm T})}{2\pi}\right)^2\left[\frac{d\sigma_{\rm FJ}}{d\Phi_{\rm FJ}}\right]^{(2)}\right\}, \tag{3.62}$$

and despite the rigid constraints on the scale settings, a scale variation procedure has been put into practice and tested thoroughly.

3.6 The MiNNLO$_{\rm PS}$ Method

Merging of **H** and **HJ** at NLO was, all in all, a matter of power counting. A question might come up now: can we generalize the reasoning just exposed to even merge the NLO$^{(1)}$ with the NNLO$^{(2)}$ accuracy? the MiNNLO$_{\rm PS}$ method [75] is the answer to this question, as we are going to show in the following.

Before going through the formal extension of MiNLO' into its NNLO empowered version, MiNNLO$_{\rm PS}$, it is worth mentioning another technique was invented first to this precise extent: this is the NNLO *reweighting* procedure [76]. Although the technique is based on a rather simple idea, reweighting all events at NNLO accuracy is computationally demanding and difficult to scale up. However, reweighting results at NNLO can always serve as a cross check of the MiNNLO$_{\rm PS}$ results, as successfully done in Ref. [77–80].

To derive the MiNNLO$_{\rm PS}$ master formula, we start with a resummation formula as in the previous section, but this time with N^{3}LL logarithmic accuracy. For the sake of generality, we consider a cross-section differential in the transverse momentum $p_{\rm T}$ of the colour singlet F and in the entire colour singlet phase space Φ_F[15]

$$\frac{d\sigma}{d\Phi_F dp_{\rm T}} = \frac{d}{dp_{\rm T}}\left\{e^{\tilde{S}(p_{\rm T})}\mathcal{L}(p_{\rm T})\right\} + R_f(p_{\rm T}), \tag{3.63}$$

where the *luminosity factor* $\mathcal{L}$ is defined as

$$\mathcal{L}(p_{\rm T}) = \sum_{c,c'}\frac{d|M^F|^2_{cc'}}{d\Phi_F}\sum_{i,j}\left\{\left(\tilde{C}^{[a]}_{ci}\otimes f^{[a]}_i\right)\tilde{H}(p_{\rm T})\left(\tilde{C}^{[b]}_{c'i}\otimes f^{[b]}_j\right)\right. \tag{3.64}$$

$$\left. + \left(G^{[a]}_{ci}\otimes f^{[a]}_i\right)\tilde{H}(p_{\rm T})\left(G^{[b]}_{c'i}\otimes f^{[b]}_j\right)\right\}. \tag{3.65}$$

[15] to be more precise, Φ_F stands for the phase space of F recoiling against a generic phase space Φ with extra QCD emissions ($\Phi = \Phi_{\rm FJ}, \Phi_{\rm FJJ}, \dots$). Such phase space is formally defined through a projection of Φ onto Φ_F.

We will now briefly comment on some of the ingredients figuring in eq. (3.63) and eq. (3.64)[16]. Although we can recognize some similarities with eq. (3.55), a new element is represented by the hard function $\tilde{H}$, encoding the virtual corrections to the F hadroproduction process as

$$\tilde{H}(p_{\mathrm{T}}) \;=\; 1 \;+\; \left(\frac{\alpha_s(p_{\mathrm{T}})}{2\pi}\right) H^{(1)}(p_{\mathrm{T}}) \;+\; \left(\frac{\alpha_s(p_{\mathrm{T}})}{2\pi}\right)^2 \tilde{H}^{(2)}(p_{\mathrm{T}}) \;+\; \dots \;, \tag{3.66}$$

with

$$H^{(1)} \;=\; \frac{2\,\mathbf{Re}\{A^{(0)^*}A^{(1)}\}}{|A^{(0)}|^2} \tag{3.67}$$

$$\tilde{H}^{(2)} \;=\; \frac{|A^{(1)}|^2 + 2\,\mathbf{Re}\{A^{(0)^*}A^{(2)}\}}{|A^{(0)}|^2} \;-\; 2\zeta_3 A^{(1)}B^{(1)} \;, \tag{3.68}$$

where $B^{(1)}$ is defined in eq. (3.47). Notice that the IR poles in the $|A^{(1)}\rangle$ and $|A^{(2)}\rangle$ have been properly subtracted by using a subtraction operator $\mathbf{I}$, according to

$$|A\rangle \;=\; (1-\mathbf{I})\,|A^{\text{IR-div.}}\rangle \;. \tag{3.69}$$

The Sudakov form factor $\tilde{S}(p_{\mathrm{T}})$ is defined as in eq. (3.58) and eq. (3.46), except that this time the $A(\alpha_s)$ and $B(\alpha_s)$ coefficients are expanded as follows

$$A(\alpha_s) \;=\; \left(\frac{\alpha_s}{2\pi}\right)A^{(1)} + \left(\frac{\alpha_s}{2\pi}\right)^2 A^{(2)} + \left(\frac{\alpha_s}{2\pi}\right)^3 A^{(3)} \tag{3.70}$$

$$B(\alpha_s) \;=\; \left(\frac{\alpha_s}{2\pi}\right)B^{(1)} + \left(\frac{\alpha_s}{2\pi}\right)^2 \tilde{B}^{(2)} \;, \tag{3.71}$$

where $A^{(3)}$ and $\tilde{B}^{(2)}$ are accounted to reach N^{3}LL accuracy. $\tilde{B}^{(2)}$ stands for a modified version of the universal $B^{(2)}$ coefficient, namely

$$\tilde{B}^2 \;=\; B^{(2)} + 2\zeta_3\left(A^{(1)}\right)^2 + 2\pi\beta_0 H^{(1)} \;, \tag{3.72}$$

where $H^{(1)}$ is proportional to the virtual correction to the F production process, and ζ_3 and β_0 constants. Such modification is a byproduct of the formal derivation of eq. (3.63), carried out in Ref. [75]. We will encounter an expression similar to eq. (3.72) when extending MiNNLO$_{\mathrm{PS}}$ to the heavy quark pair production case in chapter 5.
The coefficient functions $\tilde{C}_{ij}(z,\alpha_s)$ in eq. (3.64) encode constant contributions to the factorisation theorem, due to initial-state collinear radiation. They admit a universal expansion reported in eq. (3.56), except that the strong couplings are bound to be evaluated at $\mu_F = p_{\mathrm{T}}$ and the second order term undergoes the following modification

$$C^{(2)}(z) \quad \to \quad \tilde{C^{(2)}}(z) \;=\; C^{(2)} - 2\zeta_3 A^{(1)}\hat{P}^{(0)}(z) \;, \tag{3.73}$$

$\hat{P}^{(0)}(z)$ being the first order term of the regularized splitting function in eqs. (2.84) to (2.87). The G_{ij} functions, instead, contain the azimuthal correlations that have been isolated from

[16] For the derivation of the transverse-momentum resummation formula in momentum space, we refer the reader to Ref. [81, 82], while for the consequent derivation of eq. (3.63) we refer to section 4 of [75].

the coefficient functions. These terms are non-zero only for processes that are gg-initiated, like the Higgs boson production via gluon fusion that we studied above.
Now that we have a clearer picture of all the elements coming to place, we can go back to eq. (3.63) and massaging it to make it clear which terms in its expansion should be kept to guarantee NNLO$^{(0)}$ accurate predictions. We first perform the $p_{\rm T}$ derivative and factor out the Sudakov exponential

$$\frac{d\sigma}{d\Phi_F dp_{\rm T}} \;=\; e^{\tilde{S}(p_{\rm T})}\left[\frac{d\tilde{S}(p_{\rm T})}{dp_{\rm T}}\mathcal{L}(p_{\rm T}) \;+\; \frac{d\mathcal{L}(p_{\rm T})}{dp_{\rm T}} \;+\; \frac{R_f(p_{\rm T})}{e^{\tilde{S}(p_{\rm T})}}\right], \tag{3.74}$$

and we define

$$D(p_{\rm T}) \;=\; \frac{d\tilde{S}(p_{\rm T})}{dp_{\rm T}}\mathcal{L}(p_{\rm T}) \;+\; \frac{d\mathcal{L}(p_{\rm T})}{dp_{\rm T}}\,, \tag{3.75}$$

obtaining then

$$\frac{d\sigma}{d\Phi_F dp_{\rm T}} \;=\; e^{\tilde{S}(p_{\rm T})}\left[D(p_{\rm T}) \;+\; e^{-\tilde{S}(p_{\rm T})}R_f(p_{\rm T})\right]. \tag{3.76}$$

Now we observe that

- On the left-hand side of eq. (3.76), the full differential cross-section can expanded as usual as[17]

$$\frac{d\sigma}{d\Phi_F dp_{\rm T}} \;=\; \frac{\alpha_s(p_{\rm T})}{2\pi}\left(\frac{d\sigma}{d\Phi_F dp_{\rm T}}\right)^{(0)} \;+\; \left(\frac{\alpha_s(p_{\rm T})}{2\pi}\right)^2\left(\frac{d\sigma}{d\Phi_F dp_{\rm T}}\right)^{(1)} \;+\; O(\alpha_s^2) \tag{3.77}$$

  where

$$\left(\frac{d\sigma}{d\Phi_F dp_{\rm T}}\right)^{(1)} \;=\; B(\Phi_{\rm FJ}) \tag{3.78}$$

$$\left(\frac{d\sigma}{d\Phi_F dp_{\rm T}}\right)^{(2)} \;=\; V(\Phi_{\rm FJ}) + \int d\phi_{\rm rad}\, R(\Phi_{\rm FJ},\phi_{\rm rad})\,. \tag{3.79}$$

- The $D(p_{\rm T})$ function can also be expanded in α_s as

$$D(p_{\rm T}) \;=\; \frac{\alpha_s(p_{\rm T})}{2\pi}D^{(0)}(p_{\rm T}) \;+\; \left(\frac{\alpha_s(p_{\rm T})}{2\pi}\right)^2 D^{(1)}(p_{\rm T}) \;+\; O(\alpha_s^2)\,. \tag{3.80}$$

- The finite reminder R_f can be expressed, according to the same eq. (3.76), as

$$R_f(p_{\rm T}) \;=\; \frac{d\sigma}{d\Phi_F dp_{\rm T}} - e^{\tilde{S}(p_{\rm T})}D(p_{\rm T})\,, \tag{3.81}$$

[17] Notice that we explicitly factored out the $\alpha_s(p_{\rm T})$ powers relatively to the underlying colour singlet production Born. Since eq. (3.76) requires an additional radiation on top of the colour singlet, the expansions correctly start from $O(\alpha_s)$.

which can also be expanded, giving

$$\begin{aligned} R_f(p_{\rm T}) \;=\; & \frac{\alpha_s(p_{\rm T})}{2\pi}\left[\left(\frac{d\sigma}{d\Phi_F dp_{\rm T}}\right)^{(0)} - e^{\tilde{S}(p_{\rm T})}D^{(0)}(p_{\rm T})\right] \\ & + \left(\frac{\alpha_s(p_{\rm T})}{2\pi}\right)^2\left[\left(\frac{d\sigma}{d\Phi_F dp_{\rm T}}\right) - e^{\tilde{S}(p_{\rm T})}D^{(1)}(p_{\rm T})\right] \;+\; O(\alpha_s^2)\,. \end{aligned} \tag{3.82}$$

The crucial point now is to plug the expansions eq. (3.77),eq. (3.80) and eq. (3.82) back into eq. (3.76), but taking care of keeping all the necessary terms up to $O(\alpha_s^2)$ after integration over $p_{\rm T}$.
Being finite at vanishing $p_{\rm T}$, $R_f(p_{\rm T})$ will just contribute up to $O(\alpha_s^2)$, thus exactly with terms explicit in eq. (3.82). More attention should be paid to the $D(p_{\rm T})$ terms, which include $p_{\rm T}$ singular terms and their α_s order after integration can be estimated again by eq. (3.61). We can then write

$$\begin{aligned} \frac{d\sigma}{d\Phi_F dp_{\rm T}} \;=\; & e^{\tilde{S}(p_{\rm T})}\left[e^{-\tilde{S}(p_{\rm T})}\frac{\alpha_s(p_{\rm T})}{2\pi}\left(\frac{d\sigma}{d\Phi_F dp_{\rm T}}\right)^{(0)}\right. \\ & \left. + \; e^{-\tilde{S}(p_{\rm T})}\left(\frac{\alpha_s(p_{\rm T})}{2\pi}\right)^2\left(\frac{d\sigma}{d\Phi_F dp_{\rm T}}\right)^{(1)} \;+\; \left(\frac{\alpha_s(p_{\rm T})}{2\pi}\right)^3 D^{(3)}(p_{\rm T}) \;+\; O(\alpha_s^4)\right]. \end{aligned} \tag{3.83}$$

Finally, after expanding the $\exp(-\tilde{S}(p_{\rm T}))$ factor inside the square brackets and using eq. (3.78) and eq. (3.79), we get the MiNNLO$_{\rm PS}$ master formula

$$\begin{aligned} \left[\frac{d\sigma}{d\Phi_F dp_{\rm T}}\right]^{\rm MiNNLO_{PS}} \;=\; & e^{\tilde{S}(p_{\rm T})}\left[\frac{\alpha_s(p_{\rm T})}{2\pi}\left(1-\frac{\alpha_s(p_{\rm T})}{2\pi}\tilde{S}^{(1)}(p_{\rm T})\right)B \;+\; \left(\frac{\alpha_s(p_{\rm T})}{2\pi}\right)^2 V\right. \\ & \left. + \left(\frac{\alpha_s(p_{\rm T})}{2\pi}\right)^2\int d\phi_{\rm rad}R \;+\; \left(\frac{\alpha_s(p_{\rm T})}{2\pi}\right)^3 D^{(3)}(p_{\rm T})\right], \end{aligned} \tag{3.84}$$

where we refer to Appendix C of Ref. [75] for an explicit expression of the coefficients entering $D^{(3)}(p_{\rm T})$.
We finally observe that $D^{(3)}(p_{\rm T})$ can be neglected if one just asks for NLO$^{(0)}$ accuracy, for which we easily recover the MiNLO' result

$$\begin{aligned} \left[\frac{d\sigma}{d\Phi_F dp_{\rm T}}\right]^{\rm MiNLO'} \;=\; & e^{\tilde{S}(p_{\rm T})}\left[\frac{\alpha_s(p_{\rm T})}{2\pi}\left(1-\frac{\alpha_s(p_{\rm T})}{2\pi}\tilde{S}^{(1)}(p_{\rm T})\right)B \;+\; \left(\frac{\alpha_s(p_{\rm T})}{2\pi}\right)^2 V\right. \\ & \left. + \left(\frac{\alpha_s(p_{\rm T})}{2\pi}\right)^2\int d\phi_{\rm rad}R\right]. \end{aligned} \tag{3.85}$$

While incorporating the MiNLO prescriptions in the Powheg $\bar{B}$ function does not present major issues, the inclusion of $D^{(3)}$ in minnlo creates some issues that will be addressed in the following section. However, we remark that manipulations to this formula are also allowed,

provided they do not screw up the perturbative accuracy we achieved. Indeed, we will widely exploit the arbitrariness left in eq. (3.85) and eq. (3.84) in the next section.

3.7 Numerical Implementation of MiNLO' and MiNNLO$_{\mathrm{PS}}$

The Spreading of $D^{(3)}(\Phi_{\mathrm{F}}, p_{\mathrm{T}})$ on Φ_{FJ}

As the $D^{(3)}$ term in eq. (3.75) depends on the Φ_F phase space and on the recoiling system transverse momentum p_{T}, it is not suitable to be plugged into $\bar{B}(\Phi_{\mathrm{FJ}})$ just as it is. A function must be introduced, in a way to supplement eq. (3.75) with the missing phase space information. In other words, $D^{(3)}(\Phi_{\mathrm{F}}, p_{\mathrm{T}})$ must be spread onto Φ_{FJ} in a consistent way, and without spoiling the perturbative accuracy of the result. This also implies that projection must behave smoothly for $p_{\mathrm{T}} \to 0$.
A pretty general procedure consists of multiplying $D^{(3)}$ by a *spreading function* defined as

$$F_l^{\mathrm{corr}}(\Phi_{\mathrm{FJ}}) \;=\; \frac{J_l(\Phi_{\mathrm{FJ}})}{\sum_{l'} \int d\Phi'_{\mathrm{FJ}} J_{l'}(\Phi'_{\mathrm{FJ}}) \delta(p_{\mathrm{T}} - p'_{\mathrm{T}}) \delta(\Phi_{\mathrm{F}} - \Phi'_{\mathrm{F}})} \,, \tag{3.86}$$

which doesn't modify the values of colour singlet observables inclusive over extra radiation (like the inclusive rapidity y_{F}). Indeed, when integrating over Φ_{FJ} a function $G(\Phi_{\mathrm{F}}, p_{\mathrm{T}})$ we obtain

$$\sum_l \int d\Phi'_{\mathrm{FJ}} G(\Phi'_{\mathrm{F}}, p'_{\mathrm{T}}) F_l^{\mathrm{corr}}(\Phi'_{\mathrm{FJ}}) \;=\; \int d\Phi_{\mathrm{F}} dp_{\mathrm{T}} G(\Phi_{\mathrm{F}}, p_{\mathrm{T}}) \,. \tag{3.87}$$

On the other hand, the accuracy of observables defined on Φ_{FJ}, $F_l^{\mathrm{corr}}(\Phi_{\mathrm{FJ}}) D^{(3)}(\Phi_{\mathrm{F}}, p_{\mathrm{T}})$ is not touched. As $F_l^{\mathrm{corr}}(\Phi_{\mathrm{FJ}}) D^{(3)}(\Phi_{\mathrm{F}}, p_{\mathrm{T}})$ is still $O(\alpha_s^3)$, this term contributes beyond NLO$^{(1)}$, and the high p_{T} behaviour of $F_l^{\mathrm{corr}}(\Phi_{\mathrm{FJ}})$ is then arbitrary to the extents of the MiNNLO$_{\mathrm{PS}}$ method.
A trivial choice for $J_l(\Phi_{\mathrm{FJ}})$ is just

$$J_l(\Phi_{\mathrm{FJ}}) = 1 \,, \tag{3.88}$$

which allows us to solve analytically the phase space integral in the denominator of eq. (3.86). Unfortunately, such an option introduces spurious behaviours at large rapidities of the jet [75].
Other options have been tested and provided better numerical results. A more physical strategy consists of spreading $D^{(3)}(\Phi_{\mathrm{F}}, p_{\mathrm{T}})$ according to the actual fully differential distribution of the F+J cross-section, namely

$$J_l(\Phi_{\mathrm{FJ}}) = |A_l^{\mathrm{FJ}}(\Phi_{\mathrm{FJ}})|^2 (f^{[\mathrm{a}]} f^{[\mathrm{b}]})_l \,, \tag{3.89}$$

where $(f^{[\mathrm{a}]} f^{[\mathrm{b}]})_l$ is the product of the parton distribution functions for the initial states a and b in a given l flavour structure. However, using eq. (3.89) is numerically expensive. A faster, yet physically oriented option, is to consider the collinear limit of eq. (3.89)

$$|A_l^{\mathrm{FJ}}(\Phi_{\mathrm{FJ}})|^2 \quad \longrightarrow \quad |A_l^{\mathrm{F}}(\Phi_{\mathrm{F}})|^2 P_l(\phi_{\mathrm{rad}}) \,, \tag{3.90}$$

which becomes, after simplifying with the denominator of eq. (3.86)

$$J_l(\Phi_{\rm FJ}) = P_l(\phi_{\rm rad})(f^{[\rm a]} f^{[\rm b]})_l \ , \tag{3.91}$$

which is now the default choice for most processes studied with MiNNLO$_{\rm PS}$.
Wrapping up the spreading procedure, we can finally define the MiNNLO$_{\rm PS}$ $\bar{B}$ function for the colour singlet F hadroproduction as

$$\begin{aligned}\left[\bar{B}(\Phi_{\rm FJ})\right]^{\rm MiNNLO_{PS}} \equiv e^{-\tilde{S}(p_{\rm T})}\Bigg\{ &\frac{\alpha_s(p_{\rm T})}{2\pi}\left[\frac{d\sigma_{\rm FJ}}{d\Phi_{\rm FJ}}\right]^{(1)}\left(1+\frac{\alpha_s(p_{\rm T})}{2\pi}\tilde{S}^{(1)}(p_{\rm T})\right) \\ &+\left(\frac{\alpha_s(p_{\rm T})}{2\pi}\right)^2\left[\frac{d\sigma_{\rm FJ}}{d\Phi_{\rm FJ}}\right]^{(2)} + \left(\frac{\alpha_s(p_{\rm T})}{2\pi}\right)^3 D^{(3)}(p_{\rm T})F^{\rm corr}(\Phi_{\rm FJ})\Bigg\} \ .\end{aligned} \tag{3.92}$$

Inclusion of Subleading Terms in MiNNLO$_{\rm PS}$

In [83], it has been noticed that the truncation of the full $D(p_{\rm T})$ expression in eq. (3.75) at $O(\alpha_s^3(p_T))$ drops out some subleading terms that might become relevant in specific phase space regions[18]. These are $O(\alpha_s^4(p_{\rm T}))$ terms that can be accounted for in the MiNNLO$_{\rm PS}$ master formula by replacing

$$\left(\frac{\alpha_S(p_T)}{2\pi}\right)^3 [D(p_T)]^{(3)} \to D(p_T) - \frac{\alpha_S(p_T)}{2\pi}[D(p_T)]^{(1)} - \left(\frac{\alpha_S(p_T)}{2\pi}\right)^2 [D(p_T)]^{(2)} \ . \tag{3.93}$$

Formally, this corresponds to keeping the total derivative in eq. (3.63), avoiding any approximations. In Ref. [83], the full derivative is computed computed numerically for each event, leading to NNLO inclusive predictions remarkably close to their fixed-order computation and with comparable scale uncertainties.

MiNLO and MiNNLO$_{\rm PS}$ at High-$p_{\rm T}$

As we discussed above, the introduction of the Sudakov form factor in the MiNLO' master formula relates to the goal of merging the NLO$^{(1)}$ accuracy of a Powheg **FJ** generator with the NLO$^{(0)}$ accuracy in **F**-inclusive observables. Apart from higher order terms though, $\tilde{S}(p_{\rm T})$ does not influence the NLO$^{(1)}$ accuracy for well-resolved FJ configurations, thus at large p_T values of the F system. We can then introduce some prescriptions to turn it off at scales $p_{\rm T} \gtrsim Q$. A way to do that is to modify the $p_{\rm T}$-dependent logarithms of eq. (3.85) figuring in $\tilde{S}(p_{\rm T})$ and $\tilde{S}(p_{\rm T})$ by the following replacement

$$\ln\frac{Q}{p_T} \to L \equiv \frac{1}{p}\ln\left(1+\left(\frac{Q}{p_T}\right)^p\right), \tag{3.94}$$

where p is a free positive parameter. The larger is p, the quicker the modified logarithm L will vanish at high $p_{\rm T}$.

[18] The case examined in Ref. [83] is the inclusive Z boson production. There, a sizeable difference was witnessed in the y_Z rapidity tails between the fixed-order inclusive NNLO prediction and the MiNNLO$_{\rm PS}$ result.

The modified logarithms can also be plugged into the MiNNLO$_{\rm PS}$ formula. In line with the philosophy of the previous section though, we must preserve the total derivative in eq. (3.63). In Ref. [83], this has been done by modifying the scale setting of $D(p_{\rm T})$ and $D^{(3)}(p_{\rm T})$ as

$$\mu_R = p_T \quad \to \quad K_R Q e^{-L} \tag{3.95}$$

$$\mu_F = p_T \quad \to \quad K_F Q e^{-L} \,, \tag{3.96}$$

then changing the lower integration bound of the Sudakov as

$$p_T \quad \to \quad Q e^{-L} \,, \tag{3.97}$$

and finally, multiplying $D(p_{\rm T})$ and $D^{(3)}(p_{\rm T})$ for an overall Jacobian factor defined as

$$\mathcal{J}_Q \equiv \frac{\left(\frac{Q}{p_T}\right)^p}{1+\left(\frac{Q}{p_T}\right)^p}. \tag{3.98}$$

MiNLO and MiNNLO$_{\rm PS}$ at low-$p_{\rm T}$

When going to very low values of $p_{\rm T}$, we might have to deal with scales close to the non-perturbative regime. A way to deal with this issue is to regulate the scales in eq. (3.99) as

$$\mu_R \;=\; K_R(Qe^{-L} + Q_0 g(p_{\rm T})) \tag{3.99}$$

$$\mu_F \;=\; K_F(Qe^{-L} + Q_0 g(p_{\rm T})) \,, \tag{3.100}$$

so that a positive value of Q_0 will set a lower bound on μ_R and μ_F , thus avoiding the Landau singularity. The damping function $g(p_{\rm T})$ can be defined with a certain freedom. However the default choice is

$$g(p_{\rm T}) \;=\; \frac{1}{1+\frac{Q}{Q_0}e^{-L}} \,. \tag{3.101}$$

Once again, the total derivative in eq. (3.63) will be preserved only by mean of an overall Jacobian factor $\mathcal{J}_Q$ multiplying $D^{(3)}(p_{\rm T})$. With the introduction of the *freezing scale* Q_0, the expression provided in eq. (3.98) will modify as

$$\mathcal{J}_Q D(p_T) \to \mathcal{J}_Q \left(\frac{d\tilde{S}(p_T)}{dp_T}\mathcal{L}(p_T) + \mathcal{J}_{Q_0}\frac{d\mathcal{L}(p_T)}{dp_T} \right) \,, \tag{3.102}$$

where

$$\mathcal{J}_{Q_0} \equiv Q e^{-L} \frac{1-g^2(p_T)}{Qe^{-L}+Q_0 g(p_T)} \,. \tag{3.103}$$

Evolution of Parton Sistribution Functions with HOPPET

As a final step, we address the treatment of the PDFs at low factorisation scales in MiNNLO$_{\rm PS}$. PDF sets are frozen or cut off at certain low scales $\Lambda_{\rm PDF}$, typically close to 1GeV or even

larger. For certain processes in MiNNLO$_{\rm PS}$, the PDF freezing scale may be too high. This is due to the fact that sometimes the peak of the p_T distribution of the system is located near $\Lambda_{\rm PDF}$, and setting PDFs to zero right below this threshold may produce artifacts in results. Therefore, a consistent prescription for PDF evolution to lower scales is necessary. In Ref. [83], it has been proposed to carry out the DGLAP evolution of PDFs below their thresholds. In practice, this has been achieved by interfacing the calculation with the HOPPET package [84]. PDF sets from LHAPDF are thus converted into HOPPET grids, and there evolved down to $\mu_F \sim \Lambda$.

3.8 Further Extensions of the MiNNLO$_{\rm PS}$ Method

After being applied to deal with Higgs boson production and Drell-Yan production in hadronic collisions [75], the MiNNLO$_{\rm PS}$ method had quickly been extended and empowered to be applied in different scenarios. At first, the method was adapted to the study of diboson production processes like W^+W^- [78], ZZ [79], $Z\gamma$ [77, 85], $\gamma\gamma$ [86] as well as the Higgstrahlung processes $H^+W^\pm$, HZ [80, 87]. Shortly after, MiNNLO$_{\rm PS}$ was succesfully extended to deal with heavy-quark pair production at the LHC [88], finding its first application in the top-pair production [89], and later in the bottom-pair production [5]. In the meanwhile, broad new strategies have been investigated, as in the case of the jettiness formulation of MiNNLO$_{\rm PS}$ presented in Ref. [90]. More recently, the Higgs production via bottom-quark fusion has been presented in Ref. [91], as well as the Higgs production in gluon-fusion with exact top-quark mass dependence [92]. The method has also been extended to the associated heavy quark and colour singlet production in Ref. [93], where a first application in the $Zb\bar{b}$ production was studied.

For all the processes mentioned above, MiNNLO$_{\rm PS}$ has remarkably allowed to achieve NNLO+PS accuracy for the first time, providing numerical implementations naturally embedded in the open-source Powheg framework.

Chapter 4

Jet Physics

When particles collide at high energy, the detected outcome generally consists of a large number of stable particles. These include leptons, hadrons, and some reconstructed missing energies identified as neutrinos, which together describe a typical final state. Moreover, hadrons are typically observed to be emitted in collimated, *wide-angle*, and small invariant mass sprays, which are called *jets*.
Historically, the first hints of wide-angle jets came from the early development of the Parton Model, supported by deep-inelastic scattering (DIS) experiments starting in the late 1960s. Protons were understood as composite particles with primary constituents called quarks, which could interact at very short distances with the incoming lepton when collision energy was high enough. This phenomenon was theoretically explained by Quantum Chromodynamics (QCD), thanks to the studies on asymptotic freedom by D. Gross, F. Wilczek [94], and D. Politzer [95] in 1973. However, a new question arose: if partons can interact and produce other partons as a final state, how should we expect to observe them? Would colour confinement prevent us from seeing bare partons?
SLAC answered these questions in 1975 by detecting dijet events in electron-positron collisions. Later, the higher energy e^+e^- collider PETRA (DESY) showed the presence of trijet events, proving the existence of gluons. Experimental research on high transverse momentum jets advanced significantly with the creation of hadron-hadron colliders. These colliders also allowed, for the first time, the study of collisions between asymptotically free sea gluons in hadrons. From ISR and Fermilab in the 1980s, passing through HERA, Tevatron Run I, and LEP I and II in the 1990s, and finally to Tevatron Run II and the LHC from the 2000s onward, a vast range of jet production phenomena in high-energy hadron collisions has been observed. At the typical TeV scales of the LHC, jet events emerge from collisions occurring at distance scales around $\delta x \sim \frac{\hbar c}{1\text{TeV}} \sim 2 \times 10^{-19}\text{m}$, and they are observed by detector elements up to about 10 meters away. This covers 20 orders of magnitude in a single experiment, highlighting the extraordinary nature of jet physics.

From the theoretical perspective, the origin of jets in QCD is explained by the infrared properties of the theory. As we widely discussed in chapter 2, matrix elements of processes containing soft and collinear emissions are strongly enhanced by universal large logarithmic terms, related to the factorization properties exposed in section 2.4. This picture can be effectively modeled by dressing partons generated at high virtualities in hard scatterings with a subsequent series of soft and collinear splittings. As we saw, this is precisely what parton shower algorithms manage to simulate at leading-logarithmic accuracy, and possibly beyond. The result will consist of jets of collimated partons. This represents, however, just an approximated picture, since the same concept of primary partons is intrisically ill-defined. In fact, fixed-order calculations unequivocally show that higher order splittings cannot be

uniquely assigned to specific primary parton configurations, due to the interference effects between different production channels [96]. This can be well illustrated by considering the example of the dijet production in $q\bar{q} \to q\bar{q}$ events, in chapter 4. At the lowest order, the final-state quark and anti-quark can be regarded as primary hard partons. However, when looking at the real correction $q\bar{q} \to q\bar{q}g$, two new channels open up. In the first case, an extra gluon is emitted from either q or $\bar{q}$ (in $q\bar{q} \to q\bar{q} \to q\bar{q}g$). In a second case, two glons are produced first, and one of them splits into a $q\bar{q}$ pair (in $q\bar{q} \to gg \to q\bar{q}g$). When the real emissions are soft or collinear, one would be led to identify the primary partons as $q\bar{q}$ in the first configuration, and as gg in the second configuration, as if they represented two different and independent processes. This would give rise to an evident inconsistency, as the different channels are not individually gauge-invariant and they interfere in the real squared matrix element. On top of that, hadronization and decay of unstable particles introduce further complications in the picture.

Nevertheless, we can still introduce rigorous procedures to define the properties and kinematics of hadronic jets. If such procedures lead to finite results in theoretical predictions and are relatively easy to implement in experimental analyses, then proper comparisons can be carried out and jets can provide a powerful tool in the high-precision program.

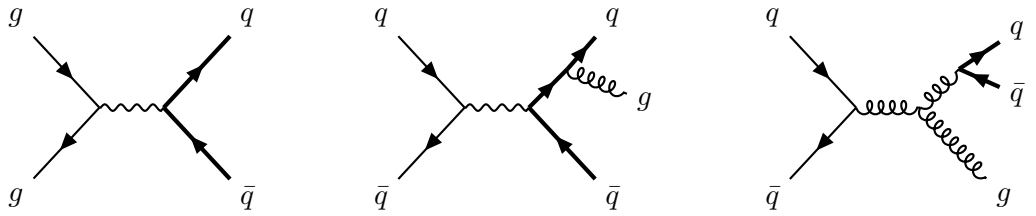

Figure 4.1: Dijet production channels in $q\bar{q}$ collisions. In the left figure, the $q\bar{q} \to q\bar{q}$ configuration; in the middle figure, the $q\bar{q} \to q\bar{q} \to q\bar{q}g$ configuration; in the right figure, the $q\bar{q} \to gg \to q\bar{q}g$.

4.1 Consistent Definitions of Jets

In general, a *jet definition* consists of two building blocks:

- A **clustering algorithm**, namely a procedure that takes as an input the full ensemble of n final state particles in an event (with momenta p_i^μ, $i = 1, \ldots, n$), and gives as an output a number m of jets.
- A **recombination scheme**, namely a prescription to assign each j_k ($k = 1, \ldots, m$) a jet momentum $p_{j_k}^\mu$.

Over the years, several ways to clustering algorithms and recombination schemes have been advanced and studied, both in experiments and in theoretical studies. We are going to analyze some of the most popular clustering algorithms in the next section. However, we can already make some general considerations about what can be seen as a good jet definition[1]. In

[1]For a thorough explanation on the basics of jet physics at colliders, we refer the reader to the seminal review "Towards Jetography" by G. Salam [97], and to the textbook "Jet Physics at the LHC: The Strong Force beyond the TeV Scale" by K. Rabbertz [98].

doing this, we should always consider both the theoretical and the experimental perspectives, as the success of *jetography* ultimately relies on finding the best compromise between what can be calculated consistently and with reasonable accuracy, and what can be measured and analyzed with an acceptable amount of resources.
A systematic list of desiderata from a jet definition, known as the *Snowmass accord* [99], was presented in 1990 by a group of influential theorists and experimenters. It articulates in five properties so that an ideal jet definition should be:

1. Simple to use in experimental analysis.
2. Simple to use in theoretical calculations.
3. Defined at any order in QCD.
4. Providing finite results at any order in perturbation theory (IR-safety).
5. Relatively insensitive to hadronization and, in hadron colliders, to the underlying event (UE).

Though considerable time has passed since the accord was established, its points remain valid today. The first and second points are related to the ease of implementation. In experiments, key points related to this issue are the computational efficiency and predictability, the ease of calibration, and the minimization of resolution smearing and angular biasing. The third point relates to the order-independence of the algorithms, meaning that they should be equally appliable to partons, particles, or measured tracks and energy depositions. This is essential when comparing parton-based theory predictions with experiments, and in general when establishing a *truth-level* at which to perform comparisons.
The fourth point is mostly theory-driven and we will elaborate more on it, as it is maybe the most important one to the extent of this work. As we already discussed in detail in chapter 2, pQCD is plagued by infrared divergences stemming from soft and collinear configurations, both in real and virtual corrections to a given process. To ensure the computation of observables to be infrared-safe, their definition should be inclusive enough to allow the real divergences to naturally cancel against the virtual ones, according to the KLN theorem. When an observable is not IR safe, measurements cannot be compared to perturbative fixed-order calculation, thus introducing large limitations.
In the language of jets, this implies that the jet definition should be insensitive of soft and collinear emissions, as we will show now with a simple example.

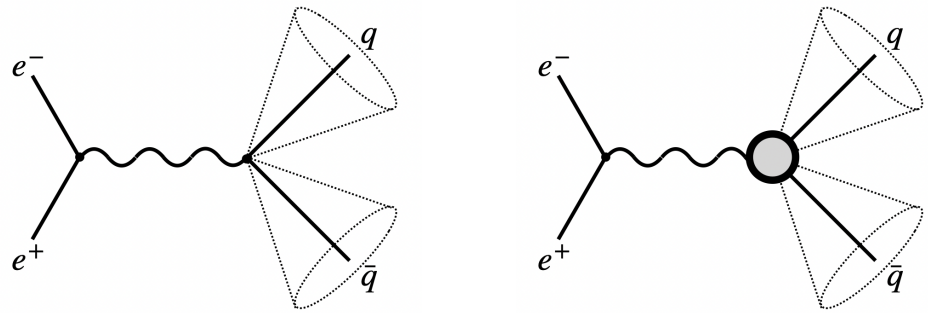

(a) Tree level diagram

(b) 1-loop QCD correction

Figure 4.2: Dijet production in e^+e^- collisions.

Let us consider the production of two wide-angle jets in an e^+e^- high-energy collision. In perturbation theory, the leading-order contribution to this process is represented in fig. 4.2a, where a pair of well-separated quark and anti-quark are emitted. In general, every clustering procedure will identify them with two jets. What happens now when considering the next-to-leading-order correction to this process, is that the 1-loop correction in fig. 4.2b will not touch the final state kinematics, thus leading to the same jet configuration of the leading-order. However, now observable computed on the dijet final state will have infrared ϵ^{-1} and ϵ^{-2} poles[2], which must be subtracted for the result to be meaningful. Now, the real correction will contribute with an additional gluon, that might eventually be soft (or collinear to the emitter) and carry infrared singularities. These singularities will properly cancel the 1-loop IR poles only and only if the soft/collinear regions of the $q\bar{q}g$ final state will be clustered in the same exact LO dijet configuration, as it happens in fig. 4.3a.

However, some clustering procedures might spoil this picture. If the original quark splits into a hard collinear qg pair, some algorithms may not be anymore able to cluster them both in a jet, therefore identifying only the anti-quark jet in the event, as in fig. 4.3b. Conversely, an emission of a soft wide-angle gluon in between q and $\bar{q}$ may let some algorithms cluster the three partons all together in a single jet, as in fig. 4.3c.

[2]We recall that ϵ parametrize the dimensional regularization procedure for integrals defined on $d = 4 - 2\epsilon$ dimensions.

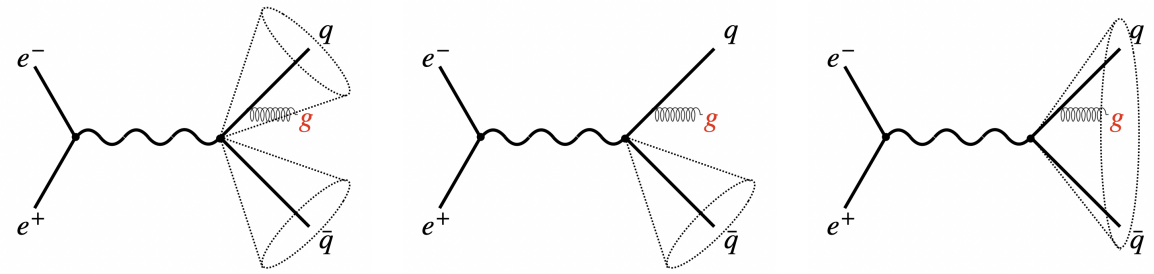

(a) (b) (c)

Figure 4.3: Real soft/wide-angle gluon emission in the $e^+e^- \to q\bar{q}$ process, giving rise to different jet configurations. In (a), two jets are identified; in (b), only the anti-quark jet is identified; in (c), the gluon and quarks are clustered in one single jet.

Notice that this has both implications on the clustering procedure and on the recombination scheme, thus constraining the jet definition as a whole.

4.2 Jet Clustering Algorithm

After stressing the properties we look for in a jet-defining procedure, we can review some concrete examples of clustering algorithms that have been advanced over the last few decades. The recombination schemes will be discussed in the next section.
When talking about clustering algorithms, it must be said that almost all of them fall in two broad categories[3]:

- The **Cone algorithms**, clustering particles into jets with a geometric approach.
- The **Sequential recombination algorithms**, clustering particles in iterative steps and stop when all jets have been identified.

Historically, the cone algorithms have been the first ones to appear, probably because of their really intuitive features. Unfortunately, most of the cone algorithms turned out to be IR-unsafe, and several optimization strategies had been put into practice to mitigate the issue [97]. The community also started to investigate alternatives, ultimately coming up with sequential recombination algorithms. The first example of this new class of algorithms made is the Jade algorithm [105, 106], which made its first appearance in the middle of the 1980's. Later, more and more sophisticated algorithms have been proposed, three of which had remarkable success: The k_T *algorithm* (or *Durham* algorithm) [107]; the *Cambridge/Aachen algorithm* [108]; the *anti-k_T algorithm* [109]. The last one, in particular, si nowadays widely adopted by all the LHC experimental collaborations.

We will devote the rest of the section to describing how the quoted algorithms work.

[3]For the sake of completeness, we also mention that some alternative types of algorithms have also been studied, although not having found remarkable application in phenomenological analyses. Some examples of different algorithms, based on minimisation techniques, can be found in Ref. [100–104].

4.2.1 The Cone Algorithms

Among the jet clustering algorithms, *cone algorithms* were the first ones to be designed and implemented in experimental analyses. Nowadays, several cone algorithms are available in the literature, but they all share the same underlying concepts. To introduce them, we can consider the first-ever jet algorithm, developed by G. F. Sterman and S. Weinberg in the 1970s to study hadronic jets in e^+e^- collisions [110]. The idea main idea was that an event would have a number n of jets if at least a fraction $1-\epsilon$ of its total energy was included in n cones of opening half-angle δ. The arbitrariness of such jet definition would then be all contained in the parameters δ and ϵ, whose values could influence the number of clustered jets. Although physically intuitive, the procedure could generate potential issues when applied in the context of hadronic collisions, when the total energy of events is not directly related to the total energy of the partonic system interacting in the hard scattering. Moreover, a number of jets greater than two could be related to configurations with overlapping cones, making it difficult to understand whose jet a certain final-state parton or hadron belongs to. To address the problems above, as well as infrared-safety issues, cone algorithms have gone through several changes and refinements over the last few decades. Nowadays, most of them are based on *iterative cones* (IC) procedures [111, 112]. Broadly speaking, a seed particle i is considered to set an initial direction, and any particle j within a distance ΔR_{ij}^2, defined as

$$\Delta R_{ij}^2 \;=\; (y_i - y_j)^2 + (\phi_i - \phi_j)^2 \;<\; R^2 \,, \tag{4.1}$$

are clustered into one single jet. In eq. (4.1), y is the rapidity and ϕ the azimuthal angle on the given particles, and R is some arbitrary dimensionless parameter, which sets the size of cones.
Once this step is carried out, the resulting jet direction[4] is set as the new seed direction, and the procedure iterates until the cone becomes stable. The remaining particles are clustered by following the same steps just described, until all jets are identified.
The main difference between cone algorithms essentially lies in how seed directions are chosen and how overlapping cones are treated. Several variants of the cone algorithms have been widely used over the years by the CERN and Tevatron collaborations.

4.2.2 The Jade Algorithm

As mentioned above, the JADE algorithm was the first example of sequential recombination algorithms to be out and it was conceived for e^+e^- colliders [105, 106]. It introduced a notion of *distance measure* y_{ij} between final state partons i and j is introduced as

$$y_{ij} = \frac{2E_iE_j(1-\cos\theta_{ij})}{Q^2} \,, \tag{4.2}$$

where Q represents the total energy of the event, namely the energy of the initial state e^+e^-. As it is designed, the Jade distance will generally be small in the presence of soft collinear emissions. In fact, of $y_{ij} \to 0$ when either of i,j is soft (so for small E_i,E_j) and/or when the angle between them is small, so that $\cos\theta_{ij} \approx 1$. Notice that the numerator of y_{ij} in (4.2) precisely coincides with the invariant mass of the (i,j) pair, when i,j are massless. The

[4] The direction of the jet four-momentum is related to the particular recombination scheme which is adopted. We will discuss recombination schemes in section 4.3.

algorithm is also required to provide a value for a threshold y_{cut}, whose usage will be clear in the next few lines.
The algorithm is articulated in the following iterative steps:

1. The distance is computed for every pair of particles in the final state $A = \{1, \ldots, n\}$ and put in a list Y
$$Y \;=\; \{y_{12}, y_{13}, \ldots, y_{1n}, \ldots, y_{n-1\,n}\}\;. \tag{4.3}$$

2. The minimum of Y is found, corresponding to a certain couple ij
$$y_{\text{min}} \;=\; \min(Y) \;=\; y_{ij}\;. \tag{4.4}$$

3. It is checked how y_{min} compares to y_{cut}:
   - If $y_{\text{min}} < y_{\text{cut}}$, then particles i, j are removed from the list A, clustered in a single particle called *pseudo-jet* $\tilde{J}_{ij}$, whose kinematics will depend on the chosen recombination scheme. $\tilde{J}_{ij}$ is added to A and the loop starts again from point 1.
   - If $y_{\text{min}} > y_{\text{cut}}$, then all that is left in the list A is declared to be a jet and the iteration stops.

A few considerations can now be made. The value one assigns to y_{cut} is to many extents arbitrary. The smaller it is chosen, the higher the number of soft/collinear emissions turning into resolved independent jets. Thus here the number of jets relates to a single parameter (the distance) rather than the two parameters (energy and angle) of cone algorithms.
An essential feature of the Jade algorithm is its infrared safety. Indeed, soft and collinear particles will be more likely to be clustered at the beginning of the procedure. On the other hand, if we imagine having a set of fully resolved jets, adding to it additional soft or collinear particles, and turning the algorithm on again, they will be naturally clustered with the jets already found. A criticality of the Jade algorithm though, is that it can give rise to spurious phenomena. The fact that E_i and E_j multiply in (4.2) can make two soft back-to-back particles i, j cluster together in the first iterations, leading to a physically inaccurate picture plagued by non-exponential double logarithms [113–116].

4.2.3 The k_{T} Algorithm

A simple modification to the Jade algorithm, conceived to address issues pointed out above, was proposed with the k_{T} algorithm [107], which was also extended to the hadron collider case [117–119]. As the main concerns about the Jade algorithm were related to its distance definition, the k_t algorithm redefined the y_{ij} for the e^+e^- case as follows

$$y_{ij} = \frac{2\min(E_i^2, E_j^2)(1 - \cos\theta_{ij})}{Q^2}\;. \tag{4.5}$$

In this definition relies the same origin of the name of the algorithm: in the collinear limit θ_{ij}, (4.5) just reduces to $(\min(E_i, E_j)\theta_{ij})^2$, namely the transverse momentum k_T of the softer particle between i and j. With this choice, a soft particle will be more likely to be clustered with a hard particle close to it in angle, rather than with another soft particle with large angular separation. Moreover, (4.5) has an clear physical interpretation. It is essentially

proportional to the squared inverse of the splitting probability of a mother parton into i, j in the soft/collinear limit, that reads[5]

$$\frac{dP_{k\to ij}}{dE_i d\theta_{ij}} \sim \frac{\alpha_s}{\min(E_i, E_j)\theta_{ij}} , \tag{4.6}$$

thus allowing for a more physical reconstruction of the branching history of the event, from a semiclassical viewpoint. This also corroborates the choice of the k_T alogorithm within the CKKW method [72], described in section 3.4.
In the context of the k_T algorithm, extensions to deal with jet studies in pp collisions have been developed. In this context, modifications must be implemented to address at least three new features:

- The concept of total energy Q in (4.5) is not well defined in hadron scatterings, since the beam total energy doesn't reflect univoquely on the parton total energy of events.
- Divergent behaviours in the matrix elements are also caused by final state soft/collinear emissions from the initial state particle-beams.
- It is prefereable to adopt a distance measure definition featuring Lorentz invariance under longitudinal boosts.

Different versions of a k_T for hadron colliders have been proposed, but we report here the one which was widely adopted by the community, also known as *inclusive k_T algorithm* [119]. Here, y_{ij} is (4.5) is replaced by

$$d_{ij} = \min(p_{t,i}^{2p}, p_{t,j}^{2p})\frac{\Delta R_{ij}^2}{R^2}, \quad \Delta R_{ij}^2 = (y_i - y_j)^2 + (\phi_i - \phi_j)^2 , \tag{4.7}$$

which is, in fact, longitudinally invariant. No threshold value for d_{ij} is introduced, although a new arbitrary parameter R figures now in (4.7), which replaces Q and makes the distance dimensionless. The impact of its choice will become clear below. Moreover, to account for the initial state soft/collinear emissions, a notion of *beam distance* is introduced as

$$d_{iB} = p_{t,i}^{2p} . \tag{4.8}$$

With these new definitions in mind, the algorithm articulates as follows:

1. Given a set of n particles (in the final state), all the d_{ij} and d_{iB} are computed and put in a list
$$D \;=\; \{d_{12}, d_{13}, \ldots, d_{n-1\,n}, \ldots, d_{1B}, \ldots, d_{nB}\} . \tag{4.9}$$
2. The minimum $d_{\min} = \min(D)$ is found and two cases are possible:
   - If d_{min} is of type d_{ij}, then i and j are clustered together and the algorithm restarts from step 1.

[5] Strictly speakin, this is true only when the softer particle is a gluon, therefore for $g \to gg$ and $q \to qg$ (when the gluon is softer). In case of a softer (anti)quark, there is no singular behaviour, as pointed out in Ref. [96]: this point will be crucial in the development of the *Flavour$-k_T$ algorithm*, that we will review in section 7.1.

- If d_{min} is of type d_{iB}, then i is declared a final state jet and removed from D. The algorithm restarts from step 1.

3. When D is empty, the algorithm stops.

We can now undertand the role of the *radius parameter* R: a particle will become a jet when there are no more particles within a distance ΔR less then R from it. This can also occur for soft particles emitted at small p_t. However, these soft jets will be typically removed by imposing some fiducial cuts on the jet's minimum transverse momentum, which is standard in LHC analyses.
The importance of the k_T algorithm in the development of collider jet physics relates to the fact that it's relatively simple and, above all, infrared-safe. Unfortunately, it appeared not to be optimal in numerical implementations[6], especially in terms of speed issues and irregular geometrical effects.

4.2.4 The Cambridge/Aachen Algorithm

Another rather simple algorithm which was advanced by the community was the Cambridge/Aachen algorithm [108], called like this because developed in Aachen but recalling some ideas behind the Cambridge algorithm[7]. It can be seen as a simplified version of the k_T algorithm. In this regard, it adopts the same definition of the angular distance ΔR_{ij}, as well as difining a radius R, but no beam distance is used. It can be summarized in the following steps:

1. For all pairs of particles, ΔR is computed and put in a list.

2. The minimum of the list is found for some pair (i, j), for which there are two options:
   - If $\Delta R_{ij} < R$, i and j are clustered and the procedure restarts from point 1.
   - If $\Delta R_{ij} > R$, then the algorithm stops and all particles are identified as jets.

The Cambridge/Aachen algorithm found large applications in DIS analyses [108]. Similarly to the k_T algorithm, it also showcases geometrical irregularities in the jet configurations it provides.

4.2.5 The Anti-k_T Algorithm

The last algorithm we are going to describe is the Anti-k_T algorithm [109]. This is, by far, the algorithm that had the most success among the experimental community, to the point that is broadly used in current LHC analyses. It is based on the formal observation that the k_T and the C/A distance measurements can be seen as particular cases of a generalized distances:

$$d_{ij} = \min(p_{ti}^{2p}, p_{tj}^{2p}) \frac{\Delta R_{ij}^2}{R^2}, \quad \Delta R_{ij}^2 = (y_i - y_j)^2 + (\phi_i - \phi_j)^2, \tag{4.10}$$

$$d_{iB} = p_{ti}^{2p}, \tag{4.11}$$

where, in essence:

[6] See, e.g., Ref. [120]
[7] Another e^+e^- algorithm introduced in Ref. [121].

- $p = 1$ for the k_T algorithm.
- $p = 0$ for the C/A algorithm.

With $p = -1$, one then gets a new algorithm which is indeed the Anti-k_T. Apart from that, the procedure is the same as the one schematized above for the k_T case. This special choice of the p_T power in (4.10) implies that hard partons will be the first ones to undergo the clustering, collecting soft/collinear particles in their vicinity (corresponding to small values of $\Delta R < R$). This allows for a much more stable algorithm that still preserves infrared safety. However, given the fact that anti-k_T pseudo-jets expand from harder to softer particles while the algorithm is running, it is not really appropriate to reconstruct the branching history of a process.
Among all the ones described above, the anti-k_T algorithm is the most popular among the experimental community. In fact, it is really the presence of hard *seeds* clustering first which prevents from the irregular behaviour observed in the k_T and in the C/A algorithms.

4.3 Recombination Schemes

We can now finally discuss about the kinematics of jets, which is defined through the so called *recombination schemes*. In the context of sequential recombination algorithms, different recombination schemes can be used in two stages of the calculation:

- One is used when the algorithm is running to cluster particles (thus deinining the pseudo-jet kinematics).
- Another one can be used after all particles have been associated to a jet, to define the jet 4-momentum out of its particles.

However, the same scheme is generally chosen for both stages, and the most common and somwehat natural one goes under the name of *E-scheme* (or *4-vector recombination scheme*) [122]. The E-scheme just prescribes to associate to a set of clustered particle a 4-momentum corresponding to the sum of their 4-momenta. Notice that this allows for the creation of massive jets out of massless particles. For example, when considering two massless particles with energies E_1, E_2 and with a relative angle θ in their directions:

$$P_1^\mu \;=\; \Big(E_1, E_1\vec{v}_1\Big), \qquad P_2^\mu \;=\; \Big(E_2, E_2\vec{v}_2\Big)\,, \tag{4.12}$$

where $|\vec{v}_1|^2 = |\vec{v}_2|^2 = 1$ and $\vec{v}_1 \cdot \vec{v}_2 = \cos(\theta)$, it happens that the squared mass of their sum is

$$M \;=\; \sqrt{2E_1E_2(1-\cos(\theta))} \;\geq\; 0\,. \tag{4.13}$$

The E-scheme is normally recommended because preserves the Lorentz invariance of the procedure. Other prescriptions, like the E_t weighted recombination scheme [99], were more poluar in the past but look now outdated.

Part II

Phenomenology of Bottom Pair Production

Chapter 5

Bottom Pair Production in MiNNLO$_{\mathrm{PS}}$

The bottom-pair hadroproduction appears to be an extremely interesting process, as it yields a remarkably vast amount of phenomenological applications in collider physics and beyond. When studying this production channel, two different approaches can be usually adopted to carry out perturbative calculations. Given the relatively light mass of the bottom quark, predictions can be obtained either within massless approximations, in the so-called five-flavour scheme (5FS), or retaining the m_b information as in the four-flavour scheme (4FS). In the former case, the process can be initiated by channels involving bottom (anti)quarks in the initial state, that will be accompainied by the respective bottom parton distribution functions. Running couplings will the evolve according to the renormalization group equations on a number $n_f = 5$ of light flavours, and similarly the PDFs themselves will evolve through the DGLAP equations eq. (2.82) with $n_f = 5$. To ensure the cancelation of infrared divergences arising from massless loop corrections beyond the leading-order, b quark emissions will be included in the real corrections. On the other hand, a 4FS calculation will provide a more accurate description of the final state bottom kinematics. In this framework, one single massive $b\bar{b}$ will be produced, and the IRC virtual divergences will be naturally regulated by the finite bottom mass value.
When studying the bottom-pair production in the 4FS, including higher-order corrections is mandatory to achieve level of accuracy comparable to the ecperimental results. This is due to the relatively small natural scale of the process, close to the bottom mass, that implies large values of the strong coupling contant and a slow convergence of the QCD series. Next-to-leading order (NLO) corrections in QCD have been widely studied in the past few decades [123–126], and recently the impact of the bottom-quark mass renormalization on theoretical uncertainties has been analyzed [127]. To treat the large logarithms arising at high bottom transverse momenta, resummed calculations have been presented in [128–134]. Eventually, NLO+NLL predictions have also been made possible within the FONLL approach [135–138], also in combination with non-perturbative fragmentation functions[139, 140], which has been the reference prediction in experimental analyses for a long time. Regarding the matching of fixed order calculations with parton showers, NLO+PS predictions in QCD have been studied within various schemes and employng different tools [141–143], enabling a fully realistic NLO accurate description of B hadrons in hadronic collsions. However, next-to-next to the leading order QCD predictions have been proven to be responsible for sizeable corrections, both in the total inclusive rate[144, 145], as implemented in the numerical code Hathor [146, 147], and in differential distributions [148], recently studied within the Matrix framework [26].
In this chapter, we will present our novel NNLO+PS implementation of the bottom-pair production process in MiNNLO$_{\mathrm{PS}}$. In section 5.1, we will review the extension of the

MiNNLO$_{\rm PS}$ method to heavy quark pair production processes, which was firstly applied in the $pp \to t\bar{t}+X$ process [88, 89]. Details about the $pp \to b\bar{b}+J$ generator in POWHEG, which will be the starting point of our MiNNLO$_{\rm PS}$ numerical implementation, will be discussed in section 5.2. In section 5.3, we will report how the 4FS calculation has been implemented in MiNNLO$_{\rm PS}$, and we will carry out a fixed order validation of our code against MATRIX.

5.1 Extension of MiNNLO$_{\rm PS}$ to Heavy-Quark Pair Production

As we already anticipated in chapter 3, the extension of the MiNNLO$_{\rm PS}$ method to the study of the heavy quark pair hadroproduction $pp \to QQ$ has been recently presented [88, 89]. As for the colour singlet case, also the derivation of the new master formula starts from a resummation formula. However, two are the most obvious difference between colour singlet production processes and processes incolving QCD partons in their final states. The first one is comes natural: the colour dependence of the final state. The second is related to the presence of gluon exchanges between the initial and the final state in terms of virtual corrections. Soft modes for such gluon exchanges will be effectively resummed in a resummation
For the time being, no exact N^{3}LL resummation formula in momentum space exists for the process $pp \to Q\overline{Q}$, but a resummation formula in b-space has actually been presented in [149–151] and reads:

$$\frac{\mathrm{d}\sigma}{\mathrm{d}^2\vec{p}_T\,\mathrm{d}\Phi_{Q\bar{Q}}} = \sum_{c=q,\bar{q},g} \frac{|M^{(0)}_{c\bar{c}}|^2}{2m^2_{Q\bar{Q}}} \int \frac{\mathrm{d}^2\vec{b}}{(2\pi)^2} e^{i\vec{b}\cdot\vec{p}_T} e^{-S_{c\bar{c}}\left(\frac{b_0}{b}\right)} \sum_{i,j} \mathrm{Tr}(\mathbf{H}_{c\bar{c}}\mathbf{\Delta})\left((\mathcal{C}_{ci}\otimes f_i)(\mathcal{C}_{\bar{c}j}\otimes f_j)\right) \ . \tag{5.1}$$

Although the reader might expect to find some similarities with the N^{3}LL colour singlet differential cross section reported in eq. (3.63), some new ingredients come to place and it is worth discussing them in detail. Sticking to the notation used in [89], we begin by observing that the formula is differential in the trasnverse momentum of the $Q\bar{Q}$ system and on $d\Phi_{Q\bar{Q}} \equiv d\bar{x}_1 d\bar{x}_2 [d\Phi_2]$, where $\bar{x}_{1,2} = m_{Q\bar{Q}}/\sqrt{s}e^{\pm y_{Q\bar{Q}}}$[1]. Notice also that eq. (5.1) is summed over all the possible initial state channels of the process, namely $gg \to Q\bar{Q}$ and $q_f\bar{q}_f \to Q\bar{Q}$ (the index f running over the light quark flavours). Regarding the amplitudes figuring above, they will be treated as vectors in the colour basis[2]. They are renormalized in the $\bar{M}S$ scheme their infrared poles have been properly subtracted by

$$|M_{c\bar{c}}\rangle = (\mathbf{1} - \mathbf{I}_{c\bar{c}})\,|M^{\text{IR-div.}}_{c\bar{c}}\rangle \ , \tag{5.3}$$

[1] $y_{Q\bar{Q}}$ is the rapidity of the $Q\bar{Q}$ system and $m_{Q\bar{Q}}$ is its invariant mass, while $[d\Phi_2]$ is the standard massive two=body phase space at a fixed center of mass enery $\sqrt{s}$.

[2] We recall that an m-parton amplitude associated to a specific set of values for the colour and the spin indices $(c_1, \dots c_m; s_1, \dots s_m)$ can be expressed as:

$$\mathcal{A}_m^{c_1,\dots,c_m;s_1,\dots,s_m}(p_1,\dots,p_m) \equiv (\langle c_1,\dots,c_m| \otimes \langle s_1,\dots,s_m|)\,|\mathcal{A}_m\rangle \ , \tag{5.2}$$

where $|\mathcal{A}_m\rangle$ is a vector in the colour+spin base of the process. For more details on this formalism, we refer to Ref. [22].

where the subtraction operator $\mathbf{I}_{c\bar{c}}$ is defined in Ref. [152] and admits a perturbative expansion

$$\mathbf{I}_{c\bar{c}} = \sum_i \left(\frac{\alpha_s(\mu)}{2\pi}\right)^i \mathbf{I}^{(i)}_{c\bar{c}} \,. \tag{5.4}$$

Regarding the renormalization scale choice, we have that $\mu_R = m_{Q\bar{Q}}$ for the amplitudes appearing inside the Fourier integral. The two additional overall α_s powers of $|M^{(0)}_{c\bar{c}}|$ in eq. (5.1) can be set with more arbitrarity. However, it will be always evaluated at dynamical scale $\mu_R^{(0)} \sim m_{Q\bar{Q}}$. We will delve deeper into this point in the following sections.
Now, going point-by-point through the elements in the second-hand side of the formula, we find:

- The Born matrix element of the process $|M^{(0)}_{c\bar{c}}|$, for a given $c\bar{c} \to Q\bar{Q}$ channel.
- The Fourier integral over the two-dimensional impact parameter $\vec{b}$, where the $b = |\vec{b}|$ and $b_0 \equiv 2e^{-\gamma_E}$.
- The Sudakov radiator

$$S_{c\bar{c}}\left(\frac{b_0}{b}\right) \equiv \int_{\frac{b_0^2}{b^2}}^{\frac{m^2_{Q\bar{Q}}}{q^2}} \frac{\mathrm{d}q^2}{q^2}\left[A_{c\bar{c}}(\alpha_s(q)) \ln\frac{m^2_{Q\bar{Q}}}{q^2} + B_{c\bar{c}}(\alpha_s(q))\right] \,, \tag{5.5}$$

  which is obtained via the resummation of the large logarithms due to initial-state collinear and sof-collinear emissions. Although universal, $A_{c\bar{c}}(\alpha_s(q)$ and $B_{c\bar{c}}(\alpha_s(q)$ depend on the initial-state flavour. They admit, as usual, a perturbative expansion in $\alpha_s(q)$.

- The convolution of the parton distribution functions f_i,f_j with the universal coefficient functions

$$C_{ij} \equiv C_{ij}(z, p_1, p_2, \vec{b}; \alpha_s(b_0/b)) \,, \tag{5.6}$$

  emerging in the factorization of the initial-state collinear radiation. Although not explicitely reported, it is understood that $(C_{ci} \otimes f_i)(C_{\bar{c}j} \otimes f_j)$ also includes additional azimuthal correlations for the gg-initiated channel.

- The trace $\mathrm{Tr}(\mathbf{H}_{c\bar{c}}\mathbf{\Delta})$ runs over the colour indices and it is tensorially contracted with the convoluted PDFs as

$$\mathrm{Tr}(\mathbf{H}_{c\bar{c}}\mathbf{\Delta})(C_{ci} \otimes f_i)(C_{\bar{c}j} \otimes f_j) \equiv \frac{\langle M_{c\bar{c}}|\mathbf{\Delta}|M_{c\bar{c}}\rangle}{|M^{(0)}_{c\bar{c}}|^2}(C_{ci} \otimes f_i)(C_{\bar{c}j} \otimes f_j) \,. \tag{5.7}$$

  Notice that the operator $\mathbf{H}_{c\bar{c}}$ is a genaralization of the colour singlet hard function[3] to $Q\bar{Q}$ amplitudes in the colour basis formalism. It formally reads

$$\mathbf{H}_{c\bar{c}} = \frac{|M_{c\bar{c}}\rangle\langle M_{c\bar{c}}|}{|M^{(0)}_{c\bar{c}}|^2} \,. \tag{5.8}$$

[3] See eq. (3.66)

- The $\mathbf{\Delta}$ operator can be expressed as

$$\mathbf{\Delta} = \mathbf{V}^\dagger \mathbf{D} \mathbf{V} \,, \tag{5.9}$$

being $\mathbf{V}$ the exponentiation of the anomalous dimension for heavy-quark pair production $\Gamma_t(\Phi_{Q\bar{Q}}; \alpha_s(q))$, thus reading

$$\mathbf{V} = \mathcal{P} \exp\left\{ - \int_{\frac{b_0^2}{b^2}}^{m^2_{Q\bar{Q}}} \frac{\mathrm{d}q^2}{q^2} \Gamma_t(\Phi_{Q\bar{Q}}; \alpha_s(q)) \right\} \,, \tag{5.10}$$

where $\mathcal{P}$ represents the path ordering operator, with increasing scales from left to right. The operator $\mathbf{D} \equiv \mathbf{D}(\Phi_{Q\bar{Q}}, \vec{b}; \alpha_s(b_0/b))$ encodes the azimuthal correlations of the $Q\bar{Q}$ system at low transverse momentum, due to soft-wide angle emissions. For the time being, the second order term $(\frac{\alpha_s}{2\pi})^2 \mathbf{D}^{(2)}$ of the $\mathbf{D}$ expansion has not been computed analytically. However, it's azimuth average is $[\mathbf{D}]_\phi = \mathbf{1}$, and that will be enough in the following.

Schematically, an intuitive picture of the interplay bewteen the different reummation ingredients is depicted in fig. 5.1.

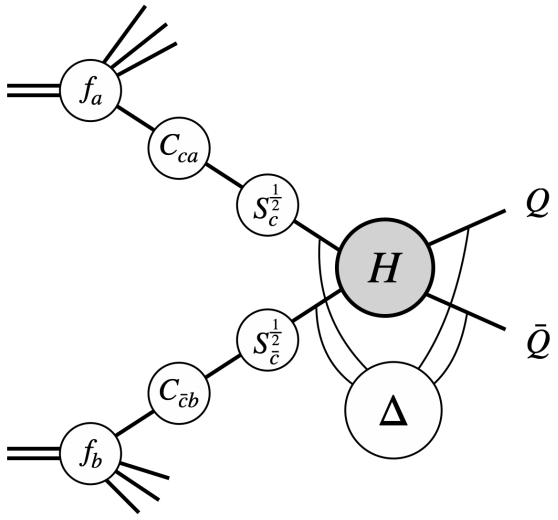

Figure 5.1: Heuristic representation of the main ingredients of the heavy-quark hadroproduction resummation. Going from left to right: Two primary partons a and b from the incoming protons interact with a probability dictated by the PDFs f_a and f_b, which are then convoluted with the coefficient functions C_a, C_b, resumming initial-state collinear radiation and eventually changing the flavour of the partons undergoing the hard scattering ($a \to c$ and $b \to \bar{c}$). Large logarithmic contributions from the initial-state collinear and soft-collinear emissions are then resummed by the Sudakov radiators $S_c^{\frac{1}{2}}$ and $S_{\bar{c}}^{\frac{1}{2}}$. At last, the soft-wide angle emissions are resummed by the Δ operator, that introduces colour connection between states entering the hard scattering.

After introducing all elements entering eq. (5.1), the next step would be to convert it into a resummation formula in direct space, analogous to the colour singlet production formula in eq. (3.63). Unfortunately this task is quite involved, and no such formula has been derived so far. However, the N^{3}LL accuracy is not something really required when performing the NNLO merging. What instead is really needed, is the NNLO accuracy after integratig eq. (5.1) over $p_{\rm T}^{Q\bar{Q}}$. We are now going to apply a series of approximations which will allow as to restate the heavy quark resummation formula as a total $p_{\rm T}^{Q\bar{Q}}$ derivative, plus some finite reminder. From there, getting to the MiNNLO$_{\rm PS}$ master formula for $Q\bar{Q}$ will be relatively easy.
As a first step, the anomalous dimension $\Gamma_t(\Phi_{Q\bar{Q}};\alpha_s(q))$ inside $\mathbf{V}$ in eq. (5.10) is expanded up to $O(\alpha_s^2)$ using

$$\Gamma_t(\Phi_{Q\bar{Q}};\alpha_s(q)) = \frac{\alpha_s(q)}{2\pi}\Gamma_t^{(1)} + \frac{\alpha_s^2(q)}{(2\pi)^2}\Gamma_t^{(2)} + \mathcal{O}(\alpha_s^3)\,, \tag{5.11}$$

and then the exponentiation of the $\Gamma_t^{(2)}$ contribution is factored out, expanded up to $O(\alpha_s^2)$ and takes out of the path-ordering symbol. In doing this, the N^{3}LL accuracy has been lost, but not the NNLO$^{(0)}$ one. Indeed one can alway use the scale evolution $\alpha_s(\mu)$ to switch scales $\mu_1 \leftrightarrow \mu_2$ in a product $\alpha_s(\mu_1)\alpha_s(\mu_2)$, only introducing higher order corrections $O(\alpha_s^3)$. As a result, we get

$$\mathbf{V}_{\rm N^3LL} \to \mathbf{V} = \underbrace{\mathcal{P}\left[\exp\left\{-\int_{\frac{b_0^2}{b^2}}^{m^2_{Q\bar{Q}}}\frac{\mathrm{d}q^2}{q^2}\frac{\alpha_s(q)}{2\pi}\Gamma_t^{(1)}\right\}\right]}_{\mathbf{V}_{\rm NLL}} \times \left(1 - \int_{\frac{b_0^2}{b^2}}^{m^2_{Q\bar{Q}}}\frac{\mathrm{d}q^2}{q^2}\frac{\alpha_s^2(q)}{(2\pi)^2}\Gamma_t^{(2)}\right) + \mathcal{O}(\alpha_s^3)\,. \tag{5.12}$$

Now, when the approximated eq. (5.12) is plugged back into the operator $\mathbf{\Delta}$ in eq. (5.9), it contributes to the trace $\mathrm{Tr}(\mathbf{H}_{c\bar{c}}\mathbf{\Delta})$ with a term

$$-\frac{\langle M_{c\bar{c}}^{(0)}|\Gamma_t^{(2)\dagger}+\Gamma_t^{(2)}|M_{c\bar{c}}^{(0)}\rangle}{|M_{c\bar{c}}^{(0)}|^2}\int_{\frac{b_0^2}{b^2}}^{m^2_{Q\bar{Q}}}\frac{\mathrm{d}q^2}{q^2}\frac{\alpha_s^2(q)}{(2\pi)^2} \quad\subset\quad \mathrm{Tr}(\mathbf{H}_{c\bar{c}}\mathbf{\Delta})\,, \tag{5.13}$$

which formally has the same functional structure of the $\mathcal{O}(\alpha_s^2)$ term associated with the $B_{c\bar{c}}^{(2)}$ coefficient in eq. (5.5). Therefore, it is possible to reabsorb it into the Sudakov radiation the following redefinition of $B_{c\bar{c}}^{(2)}$

$$B_{c\bar{c}}^{(2)} \to B_{c\bar{c}}^{(2)} + \frac{\langle M_{c\bar{c}}^{(0)}|\Gamma_t^{(2)\dagger}+\Gamma_t^{(2)}|M_{c\bar{c}}^{(0)}\rangle}{|M_{c\bar{c}}^{(0)}|^2}\,. \tag{5.14}$$

What we are left with is now

$$\mathbf{\Delta} = \mathbf{V}_{\rm NLL}^\dagger\mathbf{D}\mathbf{V}_{\rm NLL} + \mathcal{O}(\alpha_s^3)\,. \tag{5.15}$$

Although $\mathbf{D}$ contributes with an azimuthal correlation, we observed above that $[\mathbf{D}]_\phi = 1$. After averaging on ϕ, we then have that

$$\Gamma_t^{(1)}\mathbf{D}^{(1)} \subset \mathbf{V}_{\rm NLL}^\dagger\mathbf{D}\mathbf{V}_{\rm NLL}\,, \tag{5.16}$$

and this allows to approximate $\mathrm{Tr}(\mathbf{H}_{c\bar{c}}\mathbf{\Delta})$ in the following way

$$\frac{\langle M_{c\bar{c}}|\mathbf{V}_{\mathrm{NLL}}^{\dagger}\mathbf{D}\mathbf{V}_{\mathrm{NLL}}|M_{c\bar{c}}\rangle}{|M_{c\bar{c}}^{(0)}|^2} = \frac{\langle M_{c\bar{c}}|\mathbf{V}_{\mathrm{NLL}}^{\dagger}\mathbf{V}_{\mathrm{NLL}}|M_{c\bar{c}}\rangle}{|M_{c\bar{c}}^{(0)}|^2}\mathrm{Tr}(\mathbf{H}_{c\bar{c}}\mathbf{D}) + \underbrace{E_{c\bar{c}}(\Phi_{Q\bar{Q}},\vec{b})}_{\text{negligible}} + \mathcal{O}(\alpha_s^3)\ , \quad (5.17)$$

where $E_{c\bar{c}}(\Phi_{Q\bar{Q}},\vec{b})$ encodes quoted $\mathcal{O}(\alpha_s^2)\ln(m_{Q\bar{Q}}b)$ terms which vanish upon azimuthal integration. In Ref. [89], their contribution is neglected.
Regarding now the expectation value of $\mathbf{V}_{\mathrm{NLL}}^{\dagger}\mathbf{V}_{\mathrm{NLL}}$ (on the right-hand side of eq. (5.17)), we can write, up to $\mathcal{O}(\alpha_s^3)$ accuracy

$$\begin{aligned}
\frac{\langle M_{c\bar{c}}|\mathbf{V}_{\mathrm{NLL}}^{\dagger}\mathbf{V}_{\mathrm{NLL}}|M_{c\bar{c}}\rangle}{|M_{c\bar{c}}^{(0)}|^2} \to & \frac{\langle M_{c\bar{c}}^{(0)}|\mathbf{V}_{\mathrm{NLL}}^{\dagger}\mathbf{V}_{\mathrm{NLL}}|M_{c\bar{c}}^{(0)}\rangle}{|M_{c\bar{c}}^{(0)}|^2}\frac{\langle M_{c\bar{c}}|M_{c\bar{c}}\rangle}{|M_{c\bar{c}}^{(0)}|^2} \\
& + 2\mathcal{R}\left[\frac{\langle M_{c\bar{c}}^{(1)}|M_{c\bar{c}}^{(0)}\rangle}{|M_{c\bar{c}}^{(0)}|^2}\right]\frac{\langle M_{c\bar{c}}^{(0)}|\Gamma_t^{(1)\dagger}+\Gamma_t^{(1)}|M_{c\bar{c}}^{(0)}\rangle}{|M_{c\bar{c}}^{(0)}|^2}\frac{\alpha_s(m_{Q\bar{Q}})}{2\pi}\int_{\frac{b_0^2}{b^2}}^{m_{Q\bar{Q}}^2}\frac{\mathrm{d}q^2}{q^2}\frac{\alpha_s(q)}{2\pi} \\
& - 2\mathcal{R}\left[\frac{\langle M_{c\bar{c}}^{(1)}|\Gamma_t^{(1)\dagger}+\Gamma_t^{(1)}|M_{c\bar{c}}^{(0)}\rangle}{|M_{c\bar{c}}^{(0)}|^2}\right]\frac{\alpha_s(m_{Q\bar{Q}})}{2\pi}\int_{\frac{b_0^2}{b^2}}^{m_{Q\bar{Q}}^2}\frac{\mathrm{d}q^2}{q^2}\frac{\alpha_s(q)}{2\pi} \\
& + \mathcal{O}(\alpha_s^3).
\end{aligned} \quad (5.18)$$

The idea behing this approximation is to factorize the loop corrections in $\langle M_{c\bar{c}}|\mathbf{V}_{\mathrm{NLL}}^{\dagger}\mathbf{V}_{\mathrm{NLL}}|M_{c\bar{c}}\rangle$ without spoling the NNLO perturbative accuracy. To this extent, the approximation in the first line of eq. (5.18) is corrected up to $\mathcal{O}(\alpha_s^3)$ by:

1. Subtracting the 1-loop order expansion of the unaccurate approximation, giving a term proportional to
$$2\mathcal{R}\left[\frac{\langle M_{c\bar{c}}^{(1)}|M_{c\bar{c}}^{(0)}\rangle}{|M_{c\bar{c}}^{(0)}|^2}\right]\frac{\langle M_{c\bar{c}}^{(0)}|\Gamma_t^{(1)\dagger}+\Gamma_t^{(1)}|M_{c\bar{c}}^{(0)}\rangle}{|M_{c\bar{c}}^{(0)}|^2}\ . \quad (5.19)$$

2. Adding back the correct 1-loop order expansion of the exact result on the left-hand side of eq. (5.18), namely the term proportional to
$$2\mathcal{R}\left[\frac{\langle M_{c\bar{c}}^{(1)}|\Gamma_t^{(1)\dagger}+\Gamma_t^{(1)}|M_{c\bar{c}}^{(0)}\rangle}{|M_{c\bar{c}}^{(0)}|^2}\right]\ . \quad (5.20)$$

Above, the $\alpha_s(m_{Q\bar{Q}})$ couplings can be brought inside the q integrals and their scale dependence modified with $\alpha_s(m_{Q\bar{Q}}) = \alpha_s(q) + \mathcal{O}(\alpha_s^2)$. Once again, this allows both terms on the second and third line of eq. (5.18) to be reabsorbed in the Sudakov radiator via redefinition

of $B^{(2)}_{c\bar{c}}$. The result reads

$$\begin{aligned} B^{(2)}_{c\bar{c}} \quad \to \quad \hat{B}^{(2)}_{c\bar{c}} = B^{(2)}_{c\bar{c}} &+ \frac{\langle M^{(0)}_{c\bar{c}}|\Gamma^{(2)\dagger}_t + \Gamma^{(2)}_t|M^{(0)}_{c\bar{c}}\rangle}{|M^{(0)}_{c\bar{c}}|^2} \\ &- 2\mathcal{R}\left[\frac{\langle M^{(1)}_{c\bar{c}}|M^{(0)}_{c\bar{c}}\rangle}{|M^{(0)}_{c\bar{c}}|^2}\frac{\langle M^{(0)}_{c\bar{c}}|\Gamma^{(1)\dagger}_t + \Gamma^{(1)}_t|M^{(0)}_{c\bar{c}}\rangle}{|M^{(0)}_{c\bar{c}}|^2}\right] \\ &+ 2\mathcal{R}\left[\frac{\langle M^{(1)}_{c\bar{c}}|\Gamma^{(1)\dagger}_t + \Gamma^{(1)}_t|M^{(0)}_{c\bar{c}}\rangle}{|M^{(0)}_{c\bar{c}}|^2}\right]. \end{aligned} \tag{5.21}$$

After this passage, what is left in the right-hand side of eq. (5.17) is just $\mathrm{Tr}(\mathbf{H}_{c\bar{c}}\mathbf{D})$, which is eventually tensorially contracted with the convoluted PDFs in eq. (5.7). More specifically, the vanishing behaviour of $\mathbf{D}$ upon azimuthal average can be used to get the following compact expression

$$\begin{aligned} &\Big[\mathrm{Tr}(\mathbf{H}_{c\bar{c}}\mathbf{D})(C_{c_i}\otimes f_i)(C_{\bar{c}_j}\otimes f_j)\Big]_\phi \equiv \Big[H_{c\bar{c}}(C_{c_i}\otimes f_i)(C_{\bar{c}_j}\otimes f_j)\Big]_\phi \\ &+\left(\frac{\alpha_s(b_0/b)}{2\pi}\right)^2\left[\left(\frac{\langle M^{(0)}_{c\bar{c}}|\mathbf{D}^{(1)}|M^{(0)}_{c\bar{c}}\rangle}{|M^{(0)}_{c\bar{c}}|^2}\right)\Big((C^{(1)}_{c_i}\otimes f_i)(f_{\bar{c}}) + (f_c)(C^{(1)}_{\bar{c}_j}\otimes f_j)\Big)\right]_\phi + \mathcal{O}(\alpha_s^3)\,, \end{aligned} \tag{5.22}$$

where the quantity $H_{c\bar{c}}$ is reminiscent of the hard function in the colour-singlet production, even if defined with a different IR-subtraction operator, and reads

$$H_{c\bar{c}} \equiv \frac{|M_{c\bar{c}}|^2}{|M^{(0)}_{c\bar{c}}|^2} = 1 + \frac{\alpha_s}{2\pi}H^{(1)}_{c\bar{c}} + \frac{\alpha_s^2}{(2\pi)^2}H^{(2)}_{c\bar{c}} + \mathcal{O}(\alpha_s^3)\,. \tag{5.23}$$

Notice that eq. (5.22) retains a $\mathcal{O}(\alpha_s^2)$ dependence on $\mathbf{D}^{(1)}$, due to its interference with the polarization-dependent coefficient functions G_{ij}.
Finally, we can insert back in the resummation formula eq. (5.1) the replacements derived in eq. (5.18), eq. (5.22), and perform the Fourier integration. After some calculation, one gets to the following expression

$$\begin{aligned} \frac{\mathrm{d}\sigma}{\mathrm{d}p_T\mathrm{d}\Phi_{Q\bar{Q}}} =& \frac{\mathrm{d}}{\mathrm{d}p_T}\Bigg\{\sum_c \frac{e^{-\tilde{S}_{c\bar{c}}(p_T)}}{2m^2_{Q\bar{Q}}}\langle M^{(0)}_{c\bar{c}}|(\mathbf{V}_{\mathrm{NLL}})^\dagger\mathbf{V}_{\mathrm{NLL}}|M^{(0)}_{c\bar{c}}\rangle \\ &\times\sum_{i,j}\Big[\mathrm{Tr}(\tilde{\mathbf{H}}_{c\bar{c}}\mathbf{D})(\tilde{C}_{c_i}\otimes f_i)(\tilde{C}_{\bar{c}_j}\otimes f_j)\Big]_\phi\Bigg\} + R_{\mathrm{finite}}(p_T) + \mathcal{O}(\alpha_s^5)\,, \end{aligned} \tag{5.24}$$

which can be further simplified by diagonalizing the soft anomalous dimension $\mathbf{V}_{\mathrm{NLL}}$, according to

$$e^{-\tilde{S}_{c\bar{c}}(p_T)}\langle M^{(0)}_{c\bar{c}}|(\mathbf{V}_{\mathrm{NLL}})^\dagger\mathbf{V}_{\mathrm{NLL}}|M^{(0)}_{c\bar{c}}\rangle = |M^{(0)}_{c\bar{c}}|^2\sum_{i=1}^{n_c}\mathcal{C}^{[\gamma_i]}_{c\bar{c}}(\Phi_{Q\bar{Q}})e^{-\tilde{S}^{[\gamma_i]}_{c\bar{c}}(p_T)}\,, \tag{5.25}$$

where the phase-space dependent coefficients $\mathcal{C}_{c\bar{c}}^{[\gamma_i]}$ obey the constraint

$$\sum_{i=1}^{n_c} \mathcal{C}_{c\bar{c}}^{[\gamma_i]}(\Phi_{Q\bar{Q}}) \;=\; 1\;. \tag{5.26}$$

More specifically, the number n_c depends on the $SU(3)$ representation of a given initial state flavour structure, being $n_c = 4$ for the $q\bar{q}$ channel and $n_c = 9$ for the gg channel. We can therefore come to an expression which is closely reminiscent of the p_T resummation formula employed in the colour-singlet case[4]

$$\frac{\mathrm{d}\sigma}{\mathrm{d}p_T \mathrm{d}\Phi_{Q\bar{Q}}} = \frac{\mathrm{d}}{\mathrm{d}p_T}\left\{\sum_c \left[\sum_{i=1}^{n_c} C_{c\bar{c}}^{[\gamma_i]}(\Phi_{Q\bar{Q}}) e^{-\tilde{S}_{c\bar{c}}^{[\gamma_i]}(p_T)}\right] \mathcal{L}_{c\bar{c}}(\Phi_F, p_T)\right\} + R_{\text{finite}}(p_T) + \mathcal{O}(\alpha_s^5)\;, \tag{5.27}$$

where $\tilde{S}_{c\bar{c}}$, $\mathbf{H}_{c\bar{c}}$ and $\tilde{C}_{ij}$ are now evaluated at the scale p_T, and where the following replacements have been made

$$\begin{aligned}
B_{c\bar{c}}^{(1)} &\to \tilde{B}_{c\bar{c}}^{(1)} \equiv B_{c\bar{c}}^{(1)} + \gamma_i(\Phi_{Q\bar{Q}}) \\
\hat{B}_{c\bar{c}}^{(2)} &\to \tilde{B}_{c\bar{c}}^{(2)} \equiv \hat{B}_{c\bar{c}}^{(2)} + 2\zeta_3 (A_{c\bar{c}}^{(1)})^2 + 2\pi\beta_0 H_{c\bar{c}}^{(1)}, \\
H_{c\bar{c}}^{(2)} &\to \tilde{H}_{c\bar{c}}^{(2)} \equiv H_{c\bar{c}}^{(2)} - 2\zeta_3 A_{c\bar{c}}^{(1)} B_{c\bar{c}}^{(1)}, \\
C_{ci}^{(2)}(z) &\to \tilde{C}_{ci}^{(2)}(z) \equiv C_{ci}^{(2)}(z) - 2\zeta_3 A_{c\bar{c}}^{(1)} \hat{P}_{c_i}^{(0)}(z)\;,
\end{aligned} \tag{5.28}$$

where the functions $\gamma_i \equiv \gamma_{c\bar{c},i}$ can be derived from the eigenvalues of $\mathbf{\Gamma}_t^{(1)}$, and $\hat{P}^{(0)}(z)$ is the tree-level regularized AP splitting function. Moreover, the luminosity factor $\mathcal{L}_{c\bar{c}}$ has been introduced as

$$\mathcal{L}_{c\bar{c}}(\Phi_F, p_T) \equiv \frac{|\mathcal{M}_{c\bar{c}}^{(0)}|^2}{2m_{Q\bar{Q}}^2} \sum_{i,j} \Big[\mathrm{Tr}(\tilde{\mathbf{H}}_{c\bar{c}}\mathbf{D})(\tilde{C}_{c_i} \otimes f_i)(\tilde{C}_{\bar{c}_j} \otimes f_j)\Big]_\phi\;. \tag{5.29}$$

One can now use eq. (5.27) to derive the MiNNLO$_{\text{PS}}$ $\bar{B}_{Q\bar{Q}}$ function, following the same steps we reviewed in the colour singlet production case. This will result in

$$\begin{aligned}
\tilde{B}_{Q\bar{Q}}(\Phi_{\text{FJ}}, \Phi_{\text{rad}}) \equiv \sum_{\text{c}_{\text{FJ}}} \Bigg\{ & \sum_{i=1}^{n_{\text{c}_{\text{F}} \leftarrow \text{c}_{\text{FJ}}}} \mathcal{C}_{\text{c}_{\text{F}} \leftarrow \text{c}_{\text{FJ}}}^{[\gamma_i]}(\Phi_{\text{F}}) \exp\left[-\tilde{S}_{\text{c}_{\text{F}} \leftarrow \text{c}_{\text{FJ}}}^{[\gamma_i]}(\Phi_{\text{F}}, p_T)\right] \\
& \times \left[B_{\text{c}_{\text{FJ}}}(\Phi_{\text{FJ}}) \left(1 + \frac{\alpha_s(p_T)}{2\pi} [\tilde{S}_{\text{c}_{\text{F}} \leftarrow \text{c}_{\text{FJ}}}^{[\gamma_i]}(\Phi_{\text{F}}, p_T)]^{(1)}\right) + V_{\text{c}_{\text{FJ}}}(\Phi_{\text{FJ}})\right] \\
& + \sum_{\text{c}_{\text{FJJ}}} \Bigg\{ \sum_{i=1}^{n_{\text{c}_{\text{F}} \leftarrow \text{c}_{\text{FJJ}}}} \mathcal{C}_{\text{c}_{\text{F}} \leftarrow \text{c}_{\text{FJJ}}}^{[\gamma_i]}(\Phi_{\text{F}}) \exp\left[-\tilde{S}_{\text{c}_{\text{F}} \leftarrow \text{c}_{\text{FJJ}}}^{[\gamma_i]}(\Phi_{\text{F}}, p_T)\right] \Bigg\} R_{\text{c}_{\text{FJJ}}}(\Phi_{\text{FJ}}, \Phi_{\text{rad}}) \\
& + \sum_{\text{c}_{\text{FJ}}} \Bigg\{ \sum_{\text{c}_{\text{F}}} \sum_{i=1}^{n_{\text{c}_{\text{F}}}} \mathcal{C}_{\text{c}_{\text{F}}}^{[\gamma_i]}(\Phi_{\text{F}}) \exp\left[-\tilde{S}_{\text{c}_{\text{F}}}^{[\gamma_i]}(\Phi_{\text{F}}, p_T)\right] D_{\text{c}_{\text{F}}}^{[\gamma_i],(\geq 3)}(\Phi_{\text{F}}, p_T) \Bigg\} F_{\text{c}_{\text{FJ}}}^{\text{corr}}(\Phi_{\text{FJ}}) \Bigg\}\;,
\end{aligned} \tag{5.30}$$

[4] See eq. (3.63)

where the $D_{c_F}^{[\gamma_i],(\geq 3)}$ term is defined as

$$D_{c_F}^{[\gamma_i],(\geq 3)}(\Phi_F, p_T) = D_{c_F}^{[\gamma_i]}(\Phi_F, p_T) - \frac{\alpha_s(p_T)}{2\pi}\left[D_{c_F}^{[\gamma_i]}(\Phi_F, p_T)\right]^{(1)} - \left(\frac{\alpha_s(p_T)}{2\pi}\right)^2\left[D_{c_F}^{[\gamma_i]}(\Phi_F, p_T)\right]^{(2)},$$
$$D_{c_F}^{[\gamma_i]}(\Phi_F, p_T) = -\frac{d\tilde{S}_{c_F}^{[\gamma_i]}(\Phi_F, p_T)}{dp_T}\mathcal{L}_{c_F}(\Phi_F, p_T) + \frac{d\mathcal{L}_{c_F}(\Phi_F, p_T)}{dp_T}. \tag{5.31}$$

We conclude now with a few comments on the $\tilde{B}_{Q\bar{Q}}$ so obtained. Since the coefficient $\mathcal{C}_{c\bar{c}}^{[\gamma_1]}$ depend on the phase space Φ_F, a projection must be introduced to map Φ_{FJ} onto Φ_F. We refer to Ref. [89] for more details on the procedure that has been implemented. Regarding the p_T dependence entering the Sudakov radiators, this is evaluated either on Φ_{FJ} or on Φ_{FJJ}, according to the matrix element which accompanies it. In the sums, $c_{FJ} = \{gg, gq, q\bar{q}\}$ represents set of all possible initial-state flavour compositions related to the FJ process. $c_F \leftarrow c_{FJ}$ refers to the flavour configurations of the final state F corresponding to the flavour projection of the FJ final state, and similarly $c_F \leftarrow c_{FJJ}$ relates the FJJ flavour structures to the F ones.
To suppress the resummation effects in eq. (5.30) at large p_T values, some prescriptions have been introduced on the same footing of what we discussed in section 3.7. However, we remark that a different version of the modified logarithms has been introduced, namely

$$L \equiv \begin{cases} \ln\frac{Q}{p_T} & \text{if } p_T \leq \frac{Q}{2}, \\ \ln\left(a_0 + a_1\frac{p_T}{Q} + a_2\left(\frac{p_T}{Q}\right)^2\right) & \text{if } \frac{Q}{2} < p_T \leq Q, \\ 0 & \text{if } p_T > Q, \end{cases} \tag{5.32}$$

where $Q \sim m_{Q\bar{Q}}$ is the resummation scale[5] where the coefficients $a_0 = 5$, $a_1 = -8$, $a_2 = 4$ have been tuned in a way to make L and its p_T-derivative continuous at $Q/2$ and vanishing at Q.

5.2 The $b\bar{b}J$ Powheg Generator

Now that we have reviewed the derivation of eq. (5.30) and commented on the main differences from the colour-singlet MiNNLO$_{PS}$ master formula in eq. (3.92), we can present our numerical implementation. Our first step was to set up the $pp \to b\bar{b}+$jet process in Powheg-Box-Res, which is based on the following $\bar{B}$ expression

$$\bar{B}(\Phi_{b\bar{b}j}) \;=\; B(\Phi_{b\bar{b}j}) \;+\; V(\Phi_{b\bar{b}j}) \;+\; \int d\phi_{\rm rad}\, R(\Phi_{b\bar{b}jj})\,, \tag{5.33}$$

where the sum over the Born-level flavour structures is understood, as well as the FKS subtraction of the real IRC singularities in the second jet emission against the virtual poles of $V(\Phi_{b\bar{b}j})$. The calculations have been carried out in the four-flavour scheme (4FS). More specifically:

- Bottom quarks have been treated as massive, and their pole mass is set to $m_b =$

[5] Both in the top- and bottom-pair production MiNNLO$_{PS}$ implementations Q is set by default to $m_{Q\bar{Q}}/2$. However, the value can be modified by tuning the parameter $K_Q \equiv Q/m_{Q\bar{Q}}$.

4.92GeV.

- Denoting by q the light quarks in the 4FS ($q = d, u, s, c$), The Born-level flavour structures $\{f_b\}$ entering eq. (5.33) are

$$\begin{aligned} gg &\to b\bar{b}\,g \\ q\bar{q} &\to b\bar{b}\,g \\ qg &\to b\bar{b}\,q\,. \end{aligned} \tag{5.34}$$

  along with their conjugated configurations. The tree-level and the one-loop amplitudes entering the Born $[B(\Phi_{b\bar{b}j})]_{f_b}$ matrix elements and the subtracted virtual corrections $[V(\Phi_{b\bar{b}j})]_{f_b}$ in eq. (5.33) have been obtained through the POWHEG interface with OPENLOOPS [153–155], developed in [156].

- Analogously, the tree-level amplitudes have been obtained from the OPENLOOPS interface, and correspond to the following flavour structures

$$\begin{aligned} gg &\to b\bar{b}\,gg & gg &\to b\bar{b}\,q\bar{q} \\ q\bar{q} &\to b\bar{b}\,gg & q\bar{q} &\to b\bar{b}\,q\bar{q} \\ qg &\to b\bar{b}\,qg & qq' &\to b\bar{b}\,qq' \end{aligned} \tag{5.35}$$

  along with their respective conjugated configurations.

- The renormalization scales μ_R entering the strong coupling constants and the matrix elements in eq. (5.33) are consistently set to the same value. In particoular, the value of $\alpha_s(\mu_R)$ is obtained from the POWHEG interface with internal strong coupling evolution routines of LHAPDF [157]. The evolution is performed with $N_f = 4$ light flavours.

- For the PDFs, we chose the NNLO set of NNPDF3.1 [158] consistent with $N_f = 4$ number of light quark flavours[6].

Finally, we performed a numerical validation of the code against the fixed order results from MATRIX. Notice that any fully inclusive observable would turn out to be divergent in this context, because of the presece of a light radiation at the Born level, carrying an IRC divergent behaviour in the soft/collinear phase-space regions. Therefore, to be able to access well defined distributions, fiducial cut has been introduced on the leading light-jet transverse momentum. More precisely, the anti-k_T algorithm[7] with $R = 0.4$ was used to define light jets on the Born and Real kinematics of $pp \to b\bar{b}+$jet, and an analysis cut on the leading light jet $p_{T,J} \geq 20$GeV was imposed. In fig. 5.2, we present the comparison between the POWHEG and the MATRIX results for the transverse momentum and the rapidity distributions of the light jet[8] at the leading-order. The corresponding next-to-leading order results are shown in fig. 5.3.

[6] Specifically, we used NNPDF31_nnlo_as_0118_nf_4.

[7] See section 4.2.5.

[8] Notice that, in this case, the leading light jet corresponds to the final-state gluon of the Born flavour structures reported in eq. (5.34).

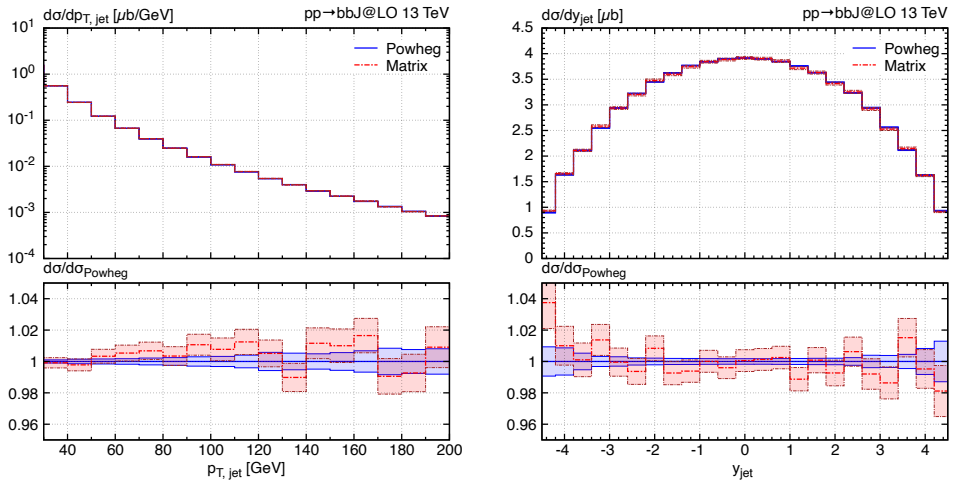

Figure 5.2: Validation plots for the $pp \to b\bar{b} + \text{jet}$ POWHEG implementation at the leading order. On the left figure, The transverse momentum of the leading light jet. On the right figure, the rapidity of the leading light jet. The reported bands correspond to the MC statistical uncertainties of the results.

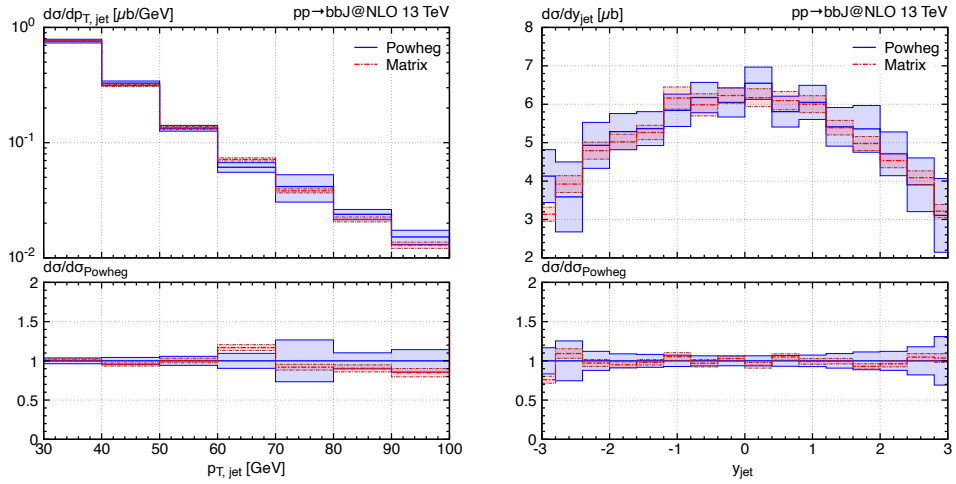

Figure 5.3: Validation plots for the $pp \to b\bar{b} + \text{jet}$ POWHEG implementation at next-to-next to the leading order. On the left figure, The transverse momentum of the leading light jet. On the right hand figure, the rapidity of the leading light jet. The reported bands correspond to the MC statistical uncertainties of the results.

5.3 MiNNLO$_{PS}$ Implementation and Validation of $pp \to b\bar{b} + X$

Upon the POWHEG implementation of $pp \to b\bar{b} + \text{jet}$, we included the MiNNLO$_{PS}$ prescriptions described in section 5.1, closely following the MiNNLO$_{PS}$ top-quark pair production

simulation already realized in POWHEG-BOX-V2 [88, 89]. As our code was developed in POWHEG-BOX-RES, we first adapted and validated the V2 version of the MiNNLO$_{\rm PS}$ $t\bar{t}$ code in the RES package, which was then used as a starting point for the implementation of the $b\bar{b}$ process in MiNNLO$_{\rm PS}$. Then, the flavour-dependent ingredients in eq. (5.30) have been consistently adapted according to the 4FS. For the sake of clarity, we now clarify a notation that will be widely used in the rest of this thesis. Within our bottom-pair production implementation:

- **MiNNLO$_{\rm PS}$** will be used to denote the predictions obtained withe full $\bar{B}_{Q\bar{Q}}$ function reported in eq. (5.30).
- **MiNLO'** will refer to the results obtained using eq. (5.30), but setting to zero[9] the terms in $D^{(\geq 3)}$.

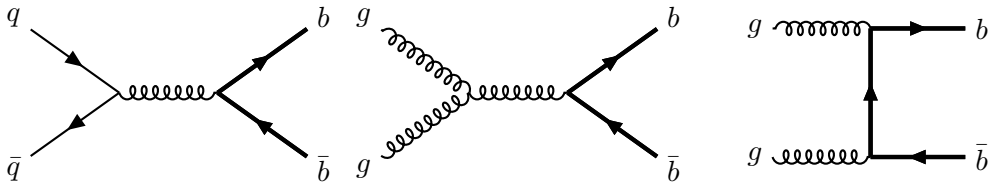

(a) s-channel $q\bar{q}$ diagram (b) s-channel gg diagram (c) t-channel gg diagram

Figure 5.4: Feynman diagrams for the process $pp \to b\bar{b}$ at LO.

The matrix elements entering the hard function $H_{b\bar{b}}$ include the Born level, the virtual and the double virtual corrections of the $pp \to b\bar{b}$ process. The tree-level Feynman diagrams contributing to the calculation are represented in fig. 5.4, with the s-channel of the *quark-initiated* configuration, and the s- and t-channel the *gluon-initiated* configuration. Schematically, the one-loop and two-loop order coefficients of the hard function read

$$\begin{aligned} H^{(1)}_{b\bar{b}} &= \frac{2\mathcal{R}\{\langle M^{(0)}_{b\bar{b}} | M^{(1)}_{b\bar{b}} \rangle\}}{|M^{(0)}_{b\bar{b}}|^2} \\ H^{(2)}_{b\bar{b}} &= \frac{|M^{(1)}_{b\bar{b}}|^2}{|M^{(0)}_{b\bar{b}}|^2} + \frac{2\mathcal{R}\{\langle M^{(0)}_{b\bar{b}} | M^{(2)}_{b\bar{b}} \rangle\}}{|M^{(0)}_{b\bar{b}}|^2} , \end{aligned} \tag{5.36}$$

where the sum over the flavour structures is understood, as well as the colour and spin configurations. In our implementation, $2\mathcal{R}\{\langle M^{(0)}_{b\bar{b}} | M^{(1)}_{b\bar{b}} \rangle$ and $|M^{(1)}_{b\bar{b}}|^2$ were included by calling the OPENLOOPS interface routines forementioned, while the two-loop contribution $2\mathcal{R}\{\langle M^{(0)}_{b\bar{b}} | M^{(2)}_{b\bar{b}} \rangle\}$ was obtained by interpolating numerical grids computed within the framework of Ref. [159].

For the PDFs we sticked with the same set used in the POWHEG $b\bar{b}+$ jet code, namely NNPDF31_nnlo_as_0118_nf_4, with the strong coupling running corresponding to that set. As done within all the MiNNLO$_{\rm PS}$ implementations, PDFs were read via the `LHAPDF` interface

[9] Notice that the MiNLO' $\bar{B}$ definition in heavy-quark pair production differs from the one presented in colour-singlet production (as in (3.54)), since in the former case the same Sudakov radiator expression both in MiNNLO$_{\rm PS}$ and in MiNLO' is used.

[157], and then interfaced with the `HOPPET` code [84] to carry out their internal evolution and the relevant convolutions. The renormalization (μ_R) and factorization (μ_F) scales have been set according to the MiNNLO$_{\rm PS}$ prescriptions, with the only exception of the scale entering the two powers of α_s already present at Born level of $pp \to b\bar{b}$. For it, we explored three different options, namely:

- $\mu_R^{(0)} = K_R\, m_{b\bar{b}}/2$, which was used for validation purposes.
- $\mu_R^{(0)} = K_R\, H_T^{b\bar{b}}/2$ (with $H_T^{b\bar{b}} = \sqrt{m_b^2 + p_{T,b}^2} + \sqrt{m_b^2 + p_{T,\bar{b}}^2}$), which was used in our B hadron production analysis[10].
- $\mu_R^{(0)} = K_R\, (H_T^{b\bar{b}} + \sum_{\rm jets} p_T^{\rm jet})/2$, that was used in our b-jet analysis[11].

We also employed the definition of the modified logarithm L reported ineq. (5.32), to switch off the resummation effects at large transverse momenta with the standard scale choice of $Q = m_{b\bar{b}}/2$. For the central scale choices, we used $K_R = K_F = 1$, and the theoretical uncertainties due to missing higher order contributions have been estimated within the standard 7-point scale variation, thus varying K_R and K_F by a factor of two in each direction with the constraint $1/2 \leq K_R/K_F \leq 2$. All the other technical settings have been kept as in Ref. [89][12].

We finally presents the results of our MiNLO' and MiNNLO$_{\rm PS}$ validation against the NNLO fixed order results from Matrix. Strictu sensu, such a validation cannot be performed exactly, as the MiNNLO$_{\rm PS}$ method prescribes constraints on the choice of the renormalization and factorization scales, while different settings are adopted for $\mu_R^{(0)}$, as detailed above. On the other hand, the Matrix predictions have been calculated using the same dynamical central scales $\mu_R = \mu_F = m_{b\bar{b}}$ in all their occurencies. However, having reached the next-to-next to leading order accuracy, it is legit to expect the two different predictions to be in good agreement.

First of all, we compare results for the fully inclusive cross section $\sigma(pp \to b\bar{b} + X)$. In this case, MiNNLO$_{\rm PS}$ predicts a value amounting to $428.7(6)^{+13\%}_{-11\%}$ pb, while the fixed-order NNLO QCD result is $435(2)^{+16\%}_{-15\%}$ pb. The two predictions are therefore in perfect agreement. To characterise the comparison thoughout the $\Phi_{b\bar{b}}$ phase space, we also generated Les-Houches-Event (LHE) level without showering effects, and used them to compute differential distributions numerically. In fig. 5.5, we report the differential cross section as a function of the $b\bar{b}$-average rapidity $y_{b_{\rm av}} = (y_b + y_{\bar{b}})/2$, the pseurapidity $\eta_{b_{\rm av}}$ and the transverse momentum $p_{T,b_{\rm av}}$. These observables feature genuine NNLO accuracy, as they feature a non trivial dependence on the Born phase space $\Phi_{b\bar{b}}$. This can also be observed in the correction that the MiNNLO$_{\rm PS}$ distributions, formally NNLO accurate, bring to the MiNLO' result, which provides NLO accuracy in this inclusive setup. However, we remind that MiNLO' also includes the $\mathcal{O}(\alpha_s^4)$ double real correction to $pp \to b\bar{b}$, contributing beyond next-to-leading order accuracy. In the rapidity and pseudorapidity distributions, this correction amounts of $\mathcal{O}(+10\%)$, and it looks quite flat throughout their full range. Moreover, the improvement in the size of scale uncertainties is striking, as these turn from around $\pm 25\%$ in MiNLO' into around $\pm 10 - 15\$$ in MiNNLO$_{\rm PS}$. Remarkably, the agreement between fixed order NNLO

[10] See chapter 6.
[11] See chapter 7.
[12] E.g. we set $Q_0 = 2$, as we witnessed numerical instablities at lower values of Q_0.

and MiNNLO$_{\rm PS}$ predictions is excellent. Regarding the transverse momentum distribution, we also witness an improvement in the MiNNLO$_{\rm PS}$ result compared to the MiNLO' both in terms of uncertainties and in the central values, apart from some small shape effects in the tail. In particoular, the MiNNLO$_{\rm PS}$ central values appear to be almost on top of the NNLO result. At last, we also point out an overall agreement between the NNLO and the MiNNLO$_{\rm PS}$ uncertainty bands, with the latter ones being slightly smaller than the former ones.

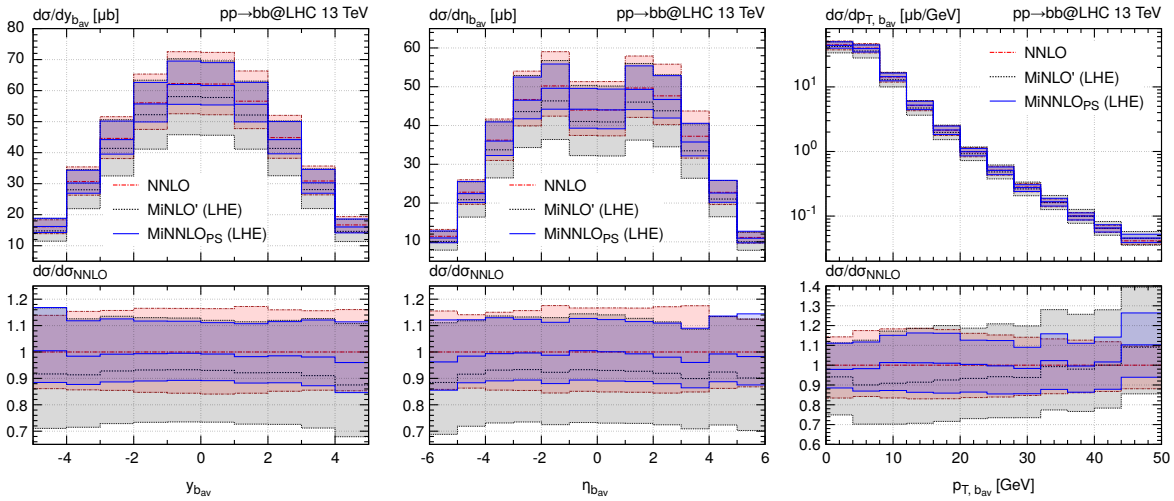

Figure 5.5: Validation plots for MiNNLO$_{\rm PS}$ (solid blue) and MiNLO' (dashed black) against the fixed order NNLO results from Matrix (solid red). All the reported distributions are obtained by averaging the respective bottom and anti-bottom distributions at the level of Les-Houches-events (LHE). See text for more details.

Chapter 6

B-hadron Production in $b\bar{b}$ Events at NNLO+PS

In this chapter, we will present the first phenomenological application that we investigated through the MiNNLO$_{\rm PS}$ bottom-pair production generator, whose implementation has been documented in chapter 5. Indeed, by interfacing our POWHEG code with PYTHIA8, we could extract predictions for the inclusive B-hadron production at the LHC, and compare with a wide set of experimental measurements. The setup of our analysis will be discussed in section 6.2. In section 6.1, we review the role of B-hadron at the LHC, mentioning the state of the art of the related theoretical predictions. In section 6.3, we present the comparison of our NNLO+PS results with data from ATLAS [160]. In section 6.4, we compare with fiducial cross-sections and differential distributions from CMS [161]. At last, three different LHCb analyses [162–164] are considered in section 6.5.

6.1 The Role of B-hadron at the LHC

Although being regarded as a heavy quark like the top, the bottom quark has a relatively long lifetime because of strong CKM suppression. As a consequence, bottoms hadronize before decaying, and measuring the inclusive B-hadron production is the only possible way to access the production of bottom-antibottom pairs produced in the hard scatterings. In practice, the process that is measured is the following

$$pp \;\to\; B \,+\, X\;, \tag{6.1}$$

where B represents one (or more) species of hadron containing either a bottom or an anti-bottom quark, but not both, and X denotes inclusivity over the rest of the final state. Several experimental analyses have been conducted over the years, starting from the UA1 collaboration at CERN Sp$\bar{\rm p}$S, then followed by the CDF and D0 collaborations at the Fermilab Tevatron. More recently, new measurements have been performed by the ATLAS, CMS and LHCb collaborations, both at $\sqrt{s} = 7$TeV and $\sqrt{s} = 13$TeV center-of-mass energies, as we will detail below.

From the theoretical point of view, the production of B-hadrons in bottom-pair events it considered a classic test of perturbative QCD. Moreover, the study of ration B-hadron differential distributions between different center-of-mass (CoM) energies has recently attracted the attention of the collider phenomenology community. One compelling reason for analyzing the ratio of heavy quark cross-sections is that it mitigates many significant theoretical and experimental uncertainties, which are often highly correlated across different center-of-mass energies, by effectively canceling them out in the ratio. Moreover, this ratio remains sensitive

to the form of the gluon PDF at both low and high values of Björken-x [165]. As a result, incorporating heavy quark data at the ratio level into global proton structure analyses can enhance the accuracy of the gluon PDF description. For a long time, the state-of-the-art calculations were based on fixed NLO QCD with NLL large transverse momentum resummation, within the FONLL approach [135–138]. Thus, the FONLL method provided full NLO accuracy at moderate p_{T} values, and NLL accuracy at high p_{T}. This could be achieved by consistently merging resummed calculations in a massless approximation, accurate in the hard regions, with a full massive NLO calculation, reliable at small p_{T}. In Ref. [5], it was effectively possible to get new results at NNLO accuracy over the full spectrum of inclusive observables, thanks to the MiNNLO$_{\mathrm{PS}}$ approach, supplemented by the leading-logarithmic accuracy provided by the Pythia8 parton shower.

The experimental analyses that we considered in comparing our predictions are the following

1. **ATLAS** [166], for the measurement of the inclusive $B^{\pm}$ meson production at $\sqrt{s} = 7TeV$.

2. **CMS** [161], for the measurement of the inclusive $B^{\pm}$ meson production at $\sqrt{s} = 13TeV$.

3. **LHCb** [162], for the measurement of the inclusive B^{+},B^{0} and B_s^0 (and respective charge-conjugated mesons) production at $\sqrt{s} = 7$TeV.

4. **LHCb** [163], for the measurement of the inclusive $B^{\pm}$ meson production at both $\sqrt{s} = 7$ and 13TeV, along with CoM energy ratio measurements.

5. **LHCb** [164], for the measurement of the inclusive bottom pair production at both $\sqrt{s} = 7$ and 13TeV, along with CoM energy ratio measurements. In this case, all B-mesons and baryons with nonnegligible production rates have been accounted for.

6.2 Settings for Theoretical Predictions in MiNNLO$_{\mathrm{PS}}$

The predictions we are going to present in the following sections have been obtained by analyzing events generated in Powheg and interfaced with PYTHIA8. As we already discussed in the previous chapter, we have been able to obtain NNLO accurate Powheg events for inclusive observables in the $b\bar{b}$ phase space, through the implementation of the MiNNLO$_{\mathrm{PS}}$ method to simulate $pp \to b\bar{b}$ in the 4FS. Given the massive scheme choice, we set the bottom mass to its pole value $m_b = 4.92$GeV. For the PDFs, we used the NNLO set of the NNPDF3.1 [158][1] with $n_f = 4$ active light flavours for the running of the strong coupling and $\alpha_s(m_Z) = 0.118$. However, as discussed in section 3.7, the PDF evolution has been effectively carried out through the HOPPET package [84].
The matching to PYTHIA8 effectively improves the accuracy of prediction via the leading-logarithm (LL) resummation provided by the parton shower. Moreover, it also allows carrying out the hadronization of showered parton events and models the multi-parton-interaction (MPI) effects. As for the tuning of the parton shower parameters, we adopted the Monash 2013 tune, which is a quite standard choice for this kind of calculation. All unstable hadrons

[1] Specifically `NNPDF31_nnlo_as_0118_nf_4`.

generated by the parton shower have been let decay to stable particles, except from the relevant B mesons and baryons that we considered in our phenomenological study. In this way, it was possible to extract predictions directly comparable to the experimental measurements of B-hadron observables.
The theoretical uncertainties we will report are estimated with the 7-point scale variation. As for the central values of μ_R and μ_F, we remind that all of them are constrained by the MiNNLO$_{\rm PS}$ prescriptions reported in section 5.1, except for the renormalization scale $\mu_R^{(0)}$ entering the overall α_s^2 in the Born matrix elements of $pp \to b\bar{b}$. For the latter one, we used

$$\mu_R^{(0)} \;=\; \frac{H_T^{b\bar{b}}}{2} \quad \text{with} \quad H_T^{b\bar{b}} \;=\; \sqrt{m_b^2 + p_{\mathrm{T},b}^2} \;+\; \sqrt{m_{\bar{b}}^2 + p_{\mathrm{T},\bar{b}}^2}\,. \tag{6.2}$$

6.3 Comparison with Data from the ATLAS Collaboration

We start our comparison to the experimental measurements by considering the results of an analysis published by the ATLAS collaboration in 2013 [166]. Results are reported in terms of a differential cross-section of B^+ meson production in pp collisions, at center-of-mass energy at $\sqrt{s} = 7$TeV and using data collected at an integrated luminosity of 2.4 fb^{-1} (and relative 1.8% uncertainty). However, both B^+ and B^- events have been accounted for, and then B^+ distributions derived by assuming charge symmetry in the $B^\pm$ production, relative to the phase space accessible by the detector. The decay channel $B^+ \to J/\psi K^+ \to \mu^+\mu^- K^+$ has been considered to reconstruct the B^+ events. The measured inclusive cross-section $\sigma(pp \to B^+ X)$ is differential in both y_{B^+} and p_{T,B^+}, and are measured using

$$\frac{\mathrm{d}^2\sigma(pp \to B^+X)}{\mathrm{d}p_{\mathrm{T},B^+}\mathrm{d}y_{B^+}} \;=\; \mathcal{B}^{-1}\,\frac{N^{B^+}}{\mathcal{L}\cdot\Delta p_{\mathrm{T},B^+}\cdot\Delta y_{B^+}}\,, \tag{6.3}$$

where

$$\mathcal{B} \;\equiv\; \mathcal{B}(B^+ \to J/\psi K^+ \to J/\psi \to \mu^+\mu^-) \;=\; (6.03 \pm 0.21)\times 10^{-5} \tag{6.4}$$

corresponds to the total branching ratio of the signal decay. The reported value is the combination of the world-average values of the branching ratios for $B^+ \to J/\psi K^+$ and $J/\psi \to \mu^+\mu^-$ [167]. N^{B^+} is the number of measured signal decays $B^+ \to J/\psi K^+$, whose reconstructed B^+ have trasnverse momentum and rapidity within, respectively, a given $\Delta p_{\mathrm{T},B^+}$ and Δy_{B^+} range. As usual, restrictions on the phase space covered by the ATLAS detector reflect the imposition of some fiducial cuts in the analysis. In this case, B^+ events have been selected when falling within the kinematical cuts reported in table 6.1. In the denominator of the right-hand side of eq. (6.3), $\mathcal{L}$ represents the integrated luminosity of the data sample. In Ref. [166], a comparison of results with theoretical prediction has been realized, considering two different simulations. One of them was done by generating NLO accurate events with the Heavy-Quark pair production implementation (HVQ) available in POWHEG-BOX 1.0 [168], and then interfacing them with PYTHIA8, analogously to the procedure followed to get the MiNNLO$_{\rm PS}$ results we are going to present. The other approach was to match MC@NLO with the Herwig parton shower program. On top of the simulations described above, other theoretical predictions obtained within the FONLL method, therefore at NLO+NLL accuracy in the hard scattering $pp \to b\bar{b}$, has also been calculated for the comparison. In this case, the B^+ quark distributions have been obtained from the b^+ quark ones using an

hadronization fraction of value $f_{b\to B^+} = 0.401 \pm 0.008$ [167]. We refer to Ref. [166] for further details, but we just summarize the main conclusion of the mentioned comparison. Both the POWHEG and the MC@NLO distributions appeared to be in good agreement with data, although affected by quite large uncertainties, with scale variation bands ranging up to $\mathcal{O}(\pm 40\%)$ in certain phase space regions. Regarding the FONLL result, the agreement was still good and the theoretical bands turned out to be smaller, as expected by the increased logarithmic accuracy of the calculation.

Fiducial cuts for $pp \to B^+ X$ at $\sqrt{s} = 7$GeV
$9\text{GeV} \leq p_{\text{T}\,B^+} \leq 120\text{GeV}$
$\lvert y_{B^+} \rvert \leq 2.25$

Table 6.1: Fiducial cuts for $pp \to B^+ X$ production from Ref. [166].

Now, we can finally discuss about the MiNNLO$_{\text{PS}}$ predictions. In all the reported plots, the MiNLO' prediction is included as well, so to get an estimate of the improvement brought by the inclusion of the $D^{(3)}(p_{\text{T}})^{b\bar{b}}$ term of eq. (5.30). In fig. 6.1, the $p_{\text{T},\,B^+}$ differential distributions integrated over different ranges of rapidity y_{B^+} are showed, while the $p_{\text{T},\,B^+}$ integrated over the full ficucial range $y_{B^+} < |2.25|$ in reported in fig. 6.2 (left panel). Apart from some isolated bins, our prediction looks in good agreement with the data. The difference between the MiNLO' and the MiNNLO$_{\text{PS}}$ central curves look rather small at low values of $p_{\text{T},\,B^+}$, and increases up to $\sim 20\%$ in the tails of the distributions. In these same regions, we can also observe that MiNNLO$_{\text{PS}}$ predicts a softer behaviour compared to MiNLO', leading to a better description of the data. Regarding the theoretical uncertainties, these appear compatible with the standard NLO uncertainties for bottom-pair hadroproduction in MiNLO', while MiNNLO$_{\text{PS}}$ represents a remarkable improvement, leading to uncertainty bands of about $\pm 10\%$. In general, the data and the MiNNLO$_{\text{PS}}$ uncertainties overlap and no remarkable tensions are observed.
In fig. 6.1 (right panel), we reported the comparison between the y_{B^+} single differential distributions, integrated over $9\text{GeV} \leq p_{\text{T},B^+} \leq 120\text{GeV}$. In this setup, MiNLO' and MiNNLO$_{\text{PS}}$ are essentially on top of each other, and again MiNNLO$_{\text{PS}}$ features a remarkable improvement in terms of scale variation bands.
In table 6.2, we also report the predicted values for the fiducial cross-sections, comparing the measured value, the FONLL prediction from Ref. [166] and the MiNNLO$_{\text{PS}}$ prediction.

Fiducial cross-section $\sigma(pp \to B^+X)$ at $\sqrt{s} = 7$TeV	
Measured by ATLAS	$10.6 \pm 0.3_{(\text{stat})} \pm 0.7_{(\text{syst})} \pm 0.2_{(\text{lumi})} \pm 0.4_{(\text{bf})}$ μb
MiNNLO$_{\text{PS}}$	$10.17(5)^{+13.3\%}_{-14.0\%}$ μb
FONLL	$8.6^{+34.9\%}_{-22.1\%} \pm 0.6_{(m_b)}$ μb

Table 6.2: Comparison with ATLAS: Fiducial cross-section for $pp \to B^+X$. The sources of uncertainty associated to the measured value are reported in brackets (statistical, systematical, luminosity, branching fraction). Results for MiNNLO$_{\text{PS}}$, MiNLO', FONLL are reported with their upper and lower scale variation bands, and the uncertainty associated with the mass of the bottom is also quoted in the FONLL prediction.

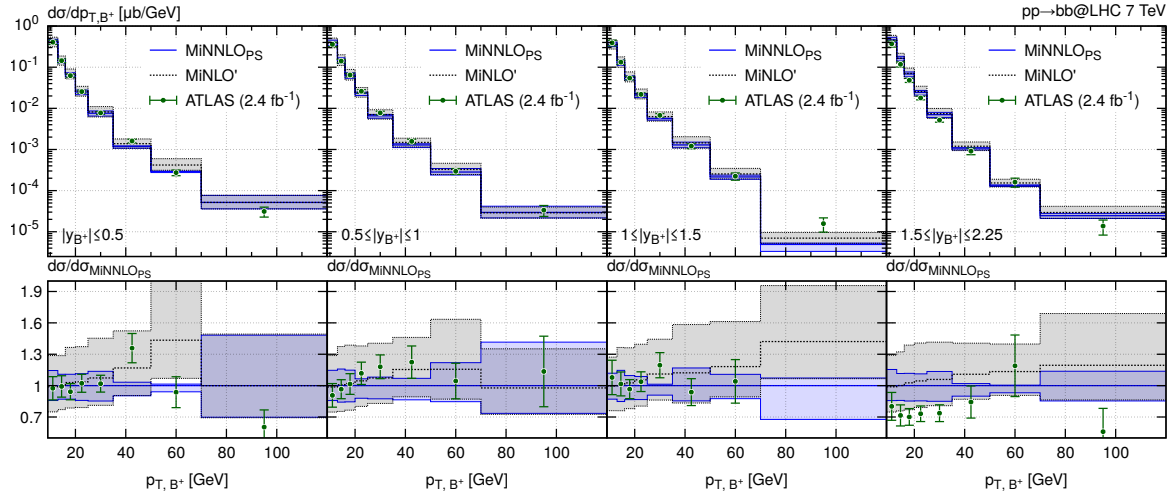

Figure 6.1: Comparison with ATLAS: Transverse momentum distributions of B^+, integrated over different ranges of $|y_{B^+}|$. The rapidity ranges are reported in the lower left corner of the upper panels. The lower panels show results normalized to the MiNNLO$_{\text{PS}}$ predictions.

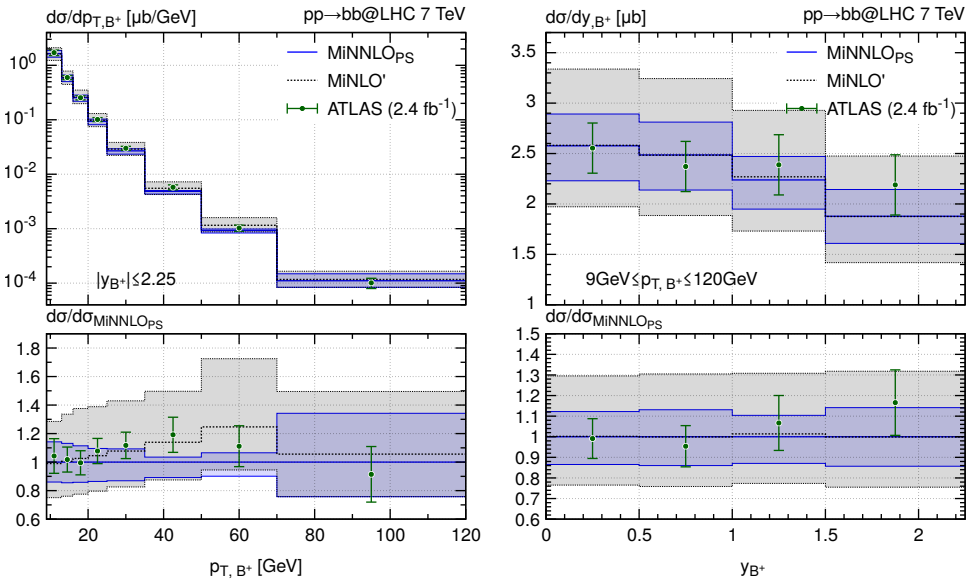

Figure 6.2: Comparison with ATLAS. On the left: transverse momentum distribution of B^+, integrated over $|y_{B^+}| \leq 2.25$; on the right: rapidity distribution of B^+, integrated over $9\text{GeV} \leq p_{\text{T},B^+} \leq 120\text{GeV}$.

6.4 Comparison with Data from the CMS Collaboration

We now turn to another set of measurements, published by the CMS collaboration in 2017 [161]. In this analysis, differential cross-sections B^+ meson production in pp collisions at $\sqrt{s} = 13\text{TeV}$ were measured for the first time, with data at an integrated luminosity of 48.1 pb^{-1}. The paper reports distributions in terms of the B^+ transverse momentum p_T^B, and rapidity y^B. Analogously to what done by the ATLAS collaboration in Ref. [166], B^+ mesons have been reconstructed by tracking the decay channel $B^+ \to J/\psi K^+$ and $J/\psi \to \mu^+\mu^-$, according to the same formula in eq. (6.3)[2]. In this case, the value of the total branching fraction $\mathcal{B}$ was obtained by combining the individual $\mathcal{B}(B^+ \to J/\psi K^+) = (1.026 \pm 0.031) \times 10^{-3}$ and $\mathcal{B}(J/\psi \to \mu^+\mu^-) = (5.961 \pm 0.033) \times 10^{-2}$ reported in [169]. Events have been selected for various sets of fiducial cuts, reported in table 6.3.

On top of the experimental results, the collaboration also provided a comparison to predictions from FONLL and PYTHIA-8.205, the former being $NLO + NLL$ accurate in the inclusive $pp \to b\bar{b}$ production and the latter being essentially LL accurate and fully exclusive in the final state. The agreement between predictions and data appeared to be acceptable in terms of distribution shapes, although it was not optimal in terms of normalization, as the experimental and the theoretical uncertainties did not overlap in several bins.
The MiNLO' and MiNNLO$_{\text{PS}}$ predictions that we present showcase a similar scenario, even if we can arguably claim an improvement in the overall description of data. In fig. 6.3, we show the p_{T,B^+} and the y_{B^+} distributions, where in both cases we reported two sets of data,

[2]Here, again, measurements have been performed by assuming charge conjugation symmetry in B^+ and B^- production.

Fiducial cuts for $pp \to B^+ X$ at $\sqrt{s} = 13$GeV	
CMS-setup 1	$p_{T,B^+} \in [17, 100]$GeV and $y_{B^+} \in [1.45, 2.1]$
CMS-setup 2	$p_{T,B^+} \in [10, 100]$GeV and $y_{B^+} \in [0, 1.45]$
CMS-setup 3	$p_{T,B^+} \in [0, 17]$GeV and $y_{B^+} \in [0, 1.45]$
CMS-setup 4	$p_{T,B^+} \in [17, 100]$GeV and $y_{B^+} \in [0, 2.1]$

Table 6.3: Fiducial cuts for $pp \to B^+ X$ production from Ref. [161].

labeled with different colours. In the transverse momentum of the B^+ meson (left panel), the MiNLO' and the MiNNLO$_{\rm PS}$ central curves have small deviations at low p_{T,B^+}, then increasing up to about 20% in the tail of the distribution. However, as the differential cross-section sharply decreases at high p_{T,B^+}, MiNLO' and MiNNLO$_{\rm PS}$ differ much less in the rapidity distribution y_{B^+} (right panel), which is integrated over p_{T,B^+} as detailed in fig. 6.3. For what concerns the theoretical uncertainties, we observe a remarkable improvement in going from MiNLO', with $\mathcal{O}(\pm 20\%)$ scale variation bundles, to MiNNLO$_{\rm PS}$, with a much more contained $\mathcal{O}(\pm 10\%)$. Comparing our predictions to the CMS data, we can conclude that the agreement is quite good, even though we observe data to be above the predictions in all bins. This behaviour consistently reflects on the fiducial cross-sections, that we report in table 6.7.

Fiducial cross-section $\sigma(pp \to B^+X)$ at $\sqrt{s} = 13$TeV	
Measured by CMS	$15.3 \pm 0.4_{\rm (stat)} \pm 2.1_{\rm (syst)} \pm 0.4_{\rm (lumi)}$ μb
MiNNLO$_{\rm PS}$	$11.47(6)^{+11.3\%}_{-13.2\%}$ μb
MiNLO'	$11.87(5)^{+23.2\%}_{-17.9\%}$ μb

Table 6.4: Comparison with CMS: Fiducial cross-section for $pp \to B^+X$. Values are obtained by integrating the differential cross-section in $y_{B^+} \in [0, 2.1]$ and $p_{T,B^+} \in [10, 100]$GeV.

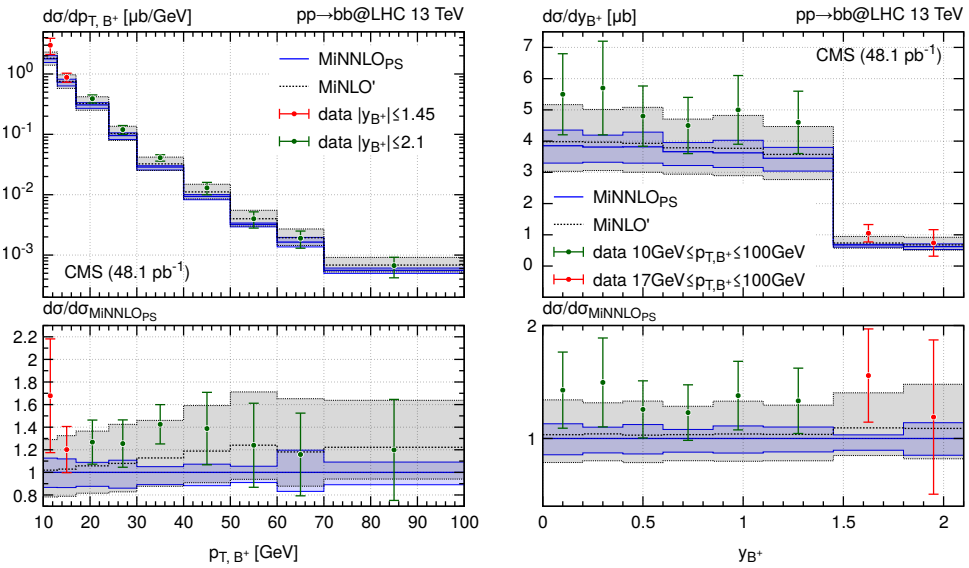

Figure 6.3: Comparison with CMS. On the left: transverse momentum distribution for the B^+ meson. The red dots correspond to data measured in the CMS-setup 3, while the green dots are values measured in the CMS-setup 4; on the right: the rapidity distribution of the B^+ meson, where red dots correspond to measurements in the CMS-setup 1, and green dots in the CMS-setup 2.

6.5 Comparison with Data from the LHCb Collaboration

6.5.1 B^+,B^0 and B_s^0 Production at $\sqrt{s} = 7$TeV

We can now consider some experimental results for B meson production at LHCb. We start our study with an analysis published in 2013 [162]. In this analysis, the production of different species of B mesons has been measured, specifically B^+,B^0, and B_s^0, along with their respective charge conjugated mesons. Results have been obtained by analysing events produced at a center of mass energy of $\sqrt{s} = 7$TeV and integrated luminosity of 0.36 fb^{-1}. The exclusive decays employed to reconstruct the B mesons are

$$\begin{aligned} B^+ &\to J/\psi\, K^+ \to \mu^+\mu^- K^+ \\ B^0 &\to J/\psi\, K^{*0} \to \mu^+\mu^- K^+\pi^- \\ B_s^0 &\to J/\psi\, \phi \to \mu^+\mu^- K^+K^- \,. \end{aligned}$$

As for the branching fraction values, $\mathcal{B}(B^0 \to J/\psi K^{*0})$ was set to the one measured by the Belle collaboration in Ref. [170], $\mathcal{B}(B_s^0 \to J/\psi\phi)$ from Ref. [171], and all the others were obtained from Ref. [167]. The results presented by LHCb have been presented in terms of differential distributions and fiducial cross-section, integrated over the B meson transverse momentum and rapidity ranges reported in table 6.5.

In our study, we only considered the measurements of the fiducial cross-sections, and carried out our comparison with the values predicted by MiNLO' and MiNNLO$_{\rm PS}$. The

Fiducial cuts for B meson production at $\sqrt{s} = 7$GeV
$0\text{GeV} \leq p_{T,B} \leq 40\text{GeV}$
$2.0 \leq y_B \leq 4.5$

Table 6.5: Fiducial cuts for $pp \to B^+ X$ production from Ref. [162]. We generically denoted with B the mesons B^+,B^0,B_s^0 and their charge conjugated particles. It is important to notice that the cut on y_B is one-directional, as a consequence of the asymmetric detector design of LHCb, but allows for a significantly large upper bound of it.

results are reported in table 6.5. the sum over the cross-section for the production of a B meson species and their charge conjugated is understood, namely $\sigma(pp \to B+X)$ corresponds to $[\sigma(pp \to B+X)+\sigma(pp \to \bar{B}+X)]$, where $B \in \{B^+, B^0, B_s^0\}$. It appears that the agreement between our predictions and the data is quite remarkable.

Fiducial cross-section $\sigma(pp \to B^+X)$ at $\sqrt{s} = 13$TeV			
Process	Measured by LHCb (μb)	MiNLO' (μb)	MiNNLO$_{\text{PS}}$ (μb)
$pp \to B^+ + X$	$38.9 \pm 0.3_{(\text{stat})} \pm 2.5_{(\text{syst})} \pm 1.3_{(\text{bf})}$	$42.3(5)^{+24.7\%}_{-18.2\%}$	$42.2(1)^{+13.9\%}_{-11.4\%}$
$pp \to B^0 + X$	$38.1 \pm 0.6_{(\text{stat})} \pm 3.7_{(\text{syst})} \pm 4.7_{(\text{bf})}$	$42.7(2)^{+26.2\%}_{-19.8\%}$	$42.3(1)^{+14.7\%}_{-11.3\%}$
$pp \to B_s^0 + X$	$10.5 \pm 0.2_{(\text{stat})} \pm 0.8_{(\text{syst})} \pm 1.0_{(\text{bf})}$	$9.39(1)^{+24.1\%}_{-17.4\%}$	$9.32(6)^{+13.6\%}_{-11.5\%}$

Table 6.6: Comparison with CMS: Fiducial cross-section for $pp \to B^+X$. Values are obtained by integrating the differential cross-section in $y_{B^+} \in [0, 2.1]$ and $p_{T,B^+} \in [10, 100]$GeV.

6.5.2 $B^\pm$ Production at $\sqrt{s} = 7$ and 13TeV

We continue our study on the LHCb measurements with a more recent analysis, published in 2017 [163]. In that paper, the production of $B^\pm$ mesons in pp was considered at $\sqrt{s} = 7$TeV and, for the first time at LHCb, also at $\sqrt{s} = 13$TeV. The 7TeV measurements were obtained by analysing events at an integrated luminosity of $1.0 fb^{-1}$, while the 13TeV events corresponded to a an integrated luminosity of $0.3 fb^{-1}$ and were collected in 2015. Similarly to the results presented by the other collaborations, $B^\pm \to J/\psi K^\pm$ was the decay channel employed for the $B^\pm$ reconstruction. The fiducial cuts adopted are reported in table 6.5. In terms of differential cross-sections, double differential distributions in rapidity and transverse momentum of the B mesons were presented. In this case, results for the B^+ and B^- production were summed together, according to the following formula

$$\frac{\mathrm{d}^2\sigma}{\mathrm{d}y\mathrm{d}p_T} = \frac{N_{B^\pm}}{\mathcal{L} \times \epsilon_{\text{tot}} \times \mathcal{B}(B^\pm \to J/\psi K^\pm) \times \mathcal{B}(J/\psi \to \mu^+\mu^-) \times \Delta y \times \Delta p_T} , \tag{6.5}$$

where $N_{B^\pm}$ is the number of reconstructed $B^\pm$ mesons and $\epsilon_{\rm tot}$ the bin-dependent total efficiency. Moreover, taking measurements for different values of the center-of-mass energy allowed for the estimation of 13TeV/7TeV ratio observables, namely:

$$R_{13/7}(p_T) \;=\; \frac{\left(\frac{d\sigma}{dp_T}\right)_{13\text{TeV}}}{\left(\frac{d\sigma}{dp_T}\right)_{7\text{TeV}}} \qquad\qquad R_{13/7}(y) \;=\; \frac{\left(\frac{d\sigma}{dy}\right)_{13\text{TeV}}}{\left(\frac{d\sigma}{dy}\right)_{7\text{TeV}}}\,, \tag{6.6}$$

where luminosity uncertainties were considered 50% correlated, systematics associated with branching fractions, mass values completely correlated, and all other uncertainties uncorrelated. We will discuss these results at the end of the section. In Ref. [163], data have also been compared to theoretical predictions based on FONLL calculations.

We present now the results obtained in the comparison between measurements, MiNLO' and MiNNLO$_{\rm PS}$ predictions. Starting with the $\sqrt{s} = 7$TeV results, transverse momentum distributions for $p_{T,B^\pm}$, integrated over different rapidity regions, are given in fig. 6.4. The $p_{T,B^\pm}$ integrated over the full fiducial range of $y_{B^\pm}$ (see table 6.5), is shown in fig. 6.5 (left panel). Analogously, the 13TeV results are reported in fig. 6.6 and fig. 6.7. Although the very fine binning in $p_{T_{B^\pm}}$, that challenges our Monte Carlo calculations and exposes some statistical fluctuations, the comparison between the data and MiNNLO$_{\rm PS}$ looks quite impressive, as data points fall within the MiNNLO$_{\rm PS}$ uncertainty bands in most bins. This, combined with the fact that the same MiNNLO$_{\rm PS}$ uncertainties are consistently smaller than the MiNLO', is proof that MiNNLO$_{\rm PS}$ improves the description of data at an unprecedented level of accuracy and precision. The only exception to this picture is represented by the behaviour of predictions for really small values of the $B^\pm$, e.g. in the bins below $3-4$GeV. Here, scale variation bands observe an important increase, and uncertainties corresponding to MiNLO' and MiNNLO$_{\rm PS}$ become comparable.

The situation appears a bit different when looking at the $B^\pm$ rapidity distributions in the right panels of fig. 6.5 and fig. 6.7. Even if data and predictions still agree within the respective uncertainties, we cannot avoid noticing a shape tension, especially in the $\sqrt{s} = 7$TeV result. We will comment more on this discrepancy in the next section, where we will present some pseudorapidity results obtained by LHCb in a different analysis.

We also report in table 6.7 the fiducial cross-sections obtained within the LHCb setup (see table 6.5) at 7 and 13TeV.

Fiducial cross-section $\sigma(pp \to B^+X)$ at LHCb			
Energy	Measured by LHCb (μb)	MiNLO' (μb)	MiNNLO$_{\rm PS}$ (μb)
7TeV	$43.0 \pm 0.2_{\rm (stat)} \pm 2.5_{\rm (syst)} \pm 1.7_{\rm (bf)}$	$45.4(4)^{+25.2\%}_{-19.1\%}$	$42.2(1)^{+13.9\%}_{-11.4\%}$
13TeV	$86.6 \pm 0.5_{\rm (stat)} \pm 5.4_{\rm (syst)} \pm 3.4_{\rm (bf)}$	$82.2(1)^{+19.4\%}_{-17.3\%}$	$78.5(3)^{+9.0\%}_{-9.3\%}$

Table 6.7: Comparison with LHCb: Fiducial cross-sections for $pp \to B^\pm + X$.

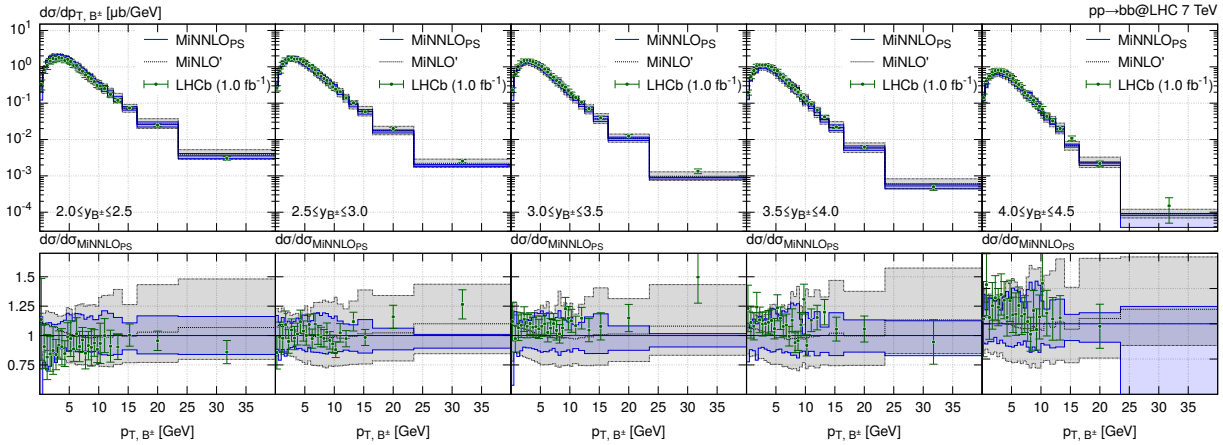

Figure 6.4: Comparison with LHCb: transverse momentum distributions for $p_{T,B^\pm}$ at $\sqrt{s} =$ 7TeV, integrated over the rapidity ranges reported on the bottom-left corner of the upper panels.

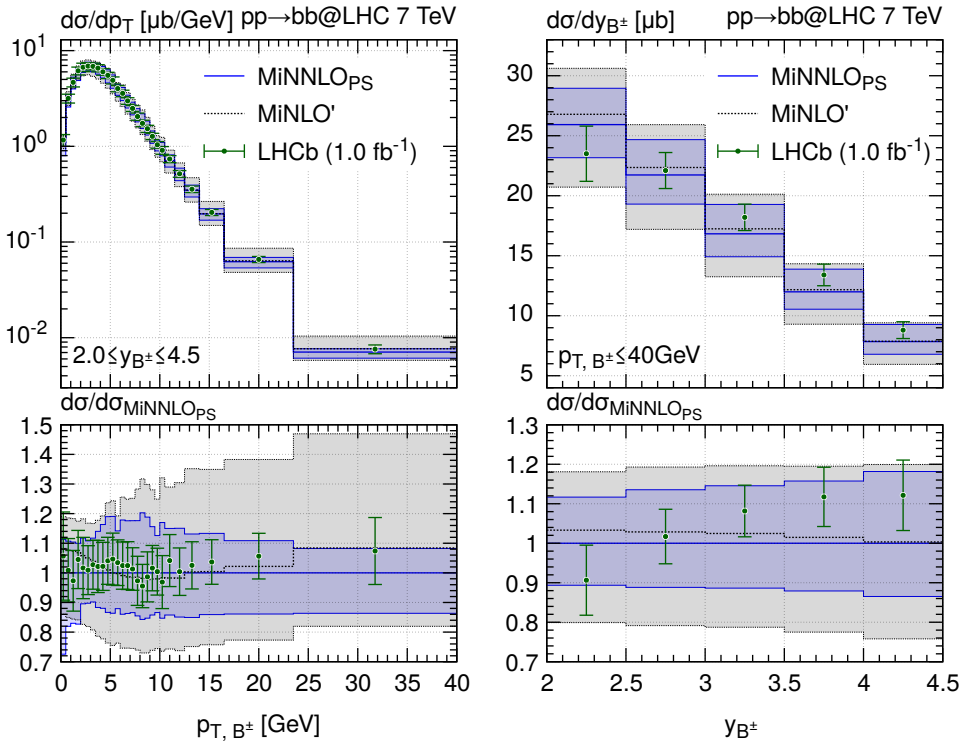

Figure 6.5: Comparison with LHCb. On the left-hand side, the $B^\pm$ transverse momentum at $\sqrt{s} = 7$TeV, integrated over $y_{B^\pm} \in [2.0, 4.5]$. On the right-hand side, the $B^\pm$ rapidity, integrated over $p_{T,B^\pm} \in [0, 40]$GeV

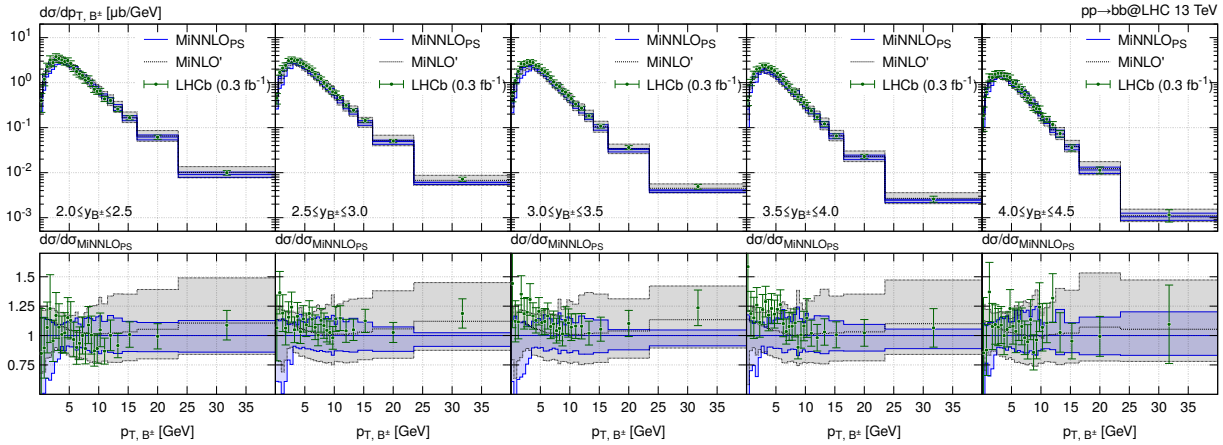

Figure 6.6: Comparison with LHCb: $B^{\pm}$ transverse momentum distributions at $\sqrt{s} = 14$TeV

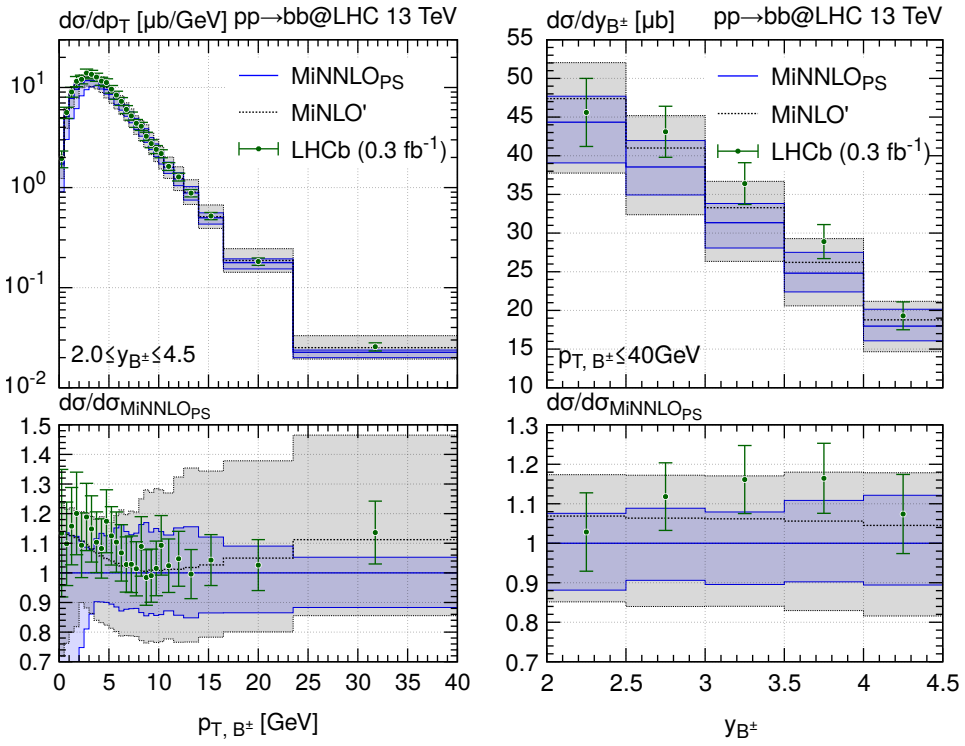

Figure 6.7: Comparison with LHCb: $B^{\pm}$ inclusive transverse momentum and rapiditiy at $\sqrt{s} = 13$TeV

Finally, we can study the ratio distributions mentioned in eq. (6.6). The results for $p_{T,B^{\pm}}$ and for of $y_{B^{\pm}}$ are shown in fig. 6.8. To obtain the MiNLO' and MiNNLOPS uncertainty bands, we correlated the scale choices in the different center of mass energy calculations. More specifically, we adopted the following procedure:

1. We separately obtained the 7-point scale predictions on the $\sqrt{s} = 7$TeV and the $\sqrt{s} = 13$TeV events.

2. For every fixed choice of (μ_R, μ_F), we computed the ratio distributions $R_{13/7}(\mu_R, \mu_F)$, thus getting seven different distributions.

3. We then computed the scale variation bundle in the usual way, considering the seven different $R_{13/7}(\mu_R, \mu_F)$.

As argued in [165], this appears to be a safe procedure, since the scale dependence of the process is mostly independent of the beam energy, being mainly a function of the process transverse kinematics at the partonic level. This leads to a drastic reduction in the scale variation dependence of the overall calculation, as now the logarithmic structure of the scale dependence compensates when dividing out the numerators and denominators of eq. (6.6). The effect of this mechanism is quite evident when considering $p_{T,B^\pm}$ (left-hand side of fig. 6.8). Although the theoretical uncertainties are still large in the low transverse momentum region[3], the MiNNLO$_{\text{PS}}$ bundles shrink down to sizes below $\pm 10\%$ around the central value for $p_{T,B^\pm} \gtrsim 5$GeV. Overall, MiNNLO$_{\text{PS}}$ provides a surprisingly good description of the experimental measurement. Regarding the rapidity ratio distribution (right-hand side of fig. 6.8), the agreement between data and predictions is overall good, although it reflects the shape tensions highlighted above for the different beam energy results.

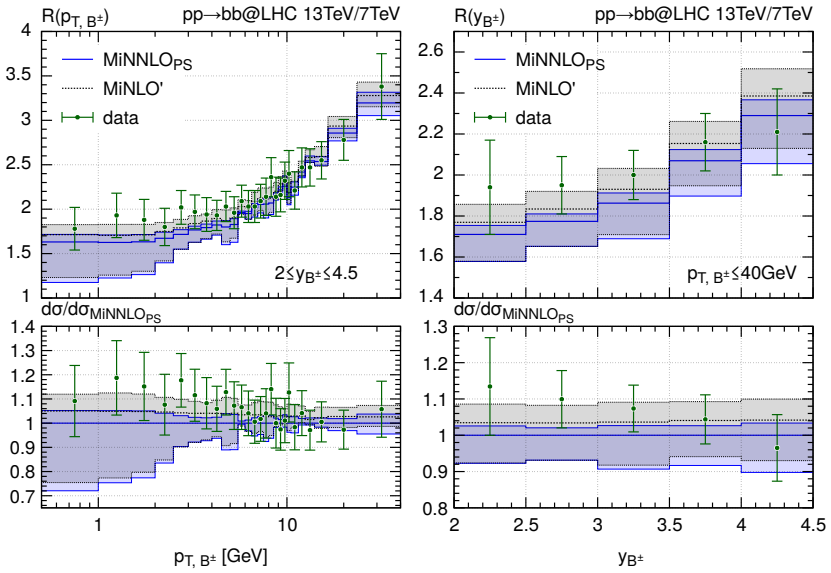

Figure 6.8: Comparison to LHCb: 13TeV/7TeV ratio distributions.

6.5.3 Bottom-Quark Pair Production at $\sqrt{s} = 7$TeV and $\sqrt{s} = 13$TeV

We finally discuss the results of one last analysis from LHCb [164]. In this case, the purpose of the analysis was to determine the cross-section associated with the production of bottom-

[3] This effect is related to the peculiar behaviour of the transverse momentum distributions already observed above.

quark pairs in $pp \to b\bar{b} + X$ events, both at $\sqrt{s} = 7\text{TeV}$ and $\sqrt{s} = 13\text{TeV}$. In fact, having access to the $\sigma(pp \to b\bar{b} + X)$ would allow for a direct comparison with theoretical results from fixed order calculations, as it has been done in Ref. [148]. Practically speaking, the collaboration measured the differential cross-sections for the production of a vast amount B hadrons in which the hard b quarks can fragmentate, and then combined the results according to the following formula

$$\begin{aligned}\sigma(pp \to H_b X) \; = & \frac{1}{2}\left[\sigma(B^0) + \sigma(\bar{B}^0)\right] + \frac{1}{2}\left[\sigma(B^+) + \sigma(B^-)\right] \\ & + \frac{1}{2}\left[\sigma(B_s^0) + \sigma(\bar{B}_s^0)\right] + \frac{1+\delta}{2}\left[\sigma(\Lambda_b^0) + \sigma(\bar{\Lambda}_b^0)\right] \; ,\end{aligned} \tag{6.7}$$

where H_b represent a generic B hadron $H_b \in \{B^0, \bar{B}^0, B^+, B^-, B_s^0, \bar{B}_s^0, \Lambda_b^0, \bar{\Lambda}_b^0\}$. The parameter $\delta = (0.25 \pm 0.10)$ represents a correction accounting for the production of Ξ_b and Ω_b^- baryons. Its value is based on the consideration that [172]:

$$\Gamma(\Xi_b^- \to \Xi^- X \mu^- \bar{\nu}) = \Gamma(\Lambda_b^0 \to \Lambda X \mu^- \bar{\nu}) \; , \tag{6.8}$$

and

$$\frac{\sigma(\Xi_b^-)}{\sigma(\Lambda_b^0)} = 0.11 \pm 0.03 \pm 0.03 \; . \tag{6.9}$$

Such value was then doubled, according to isospin invariance, to include the Ξ_b^0 hadrons. To account for the Ω_b^- contribution, estimated as 15% of the Ξ_b, it was derived the final value of δ reported above. Moreover, charmed B_c mesons were neglected, since their presence was estimated to be around the 0.1% of total amounts of observed B hadrons in Ref. [173]. Differently from the procedure adopted by the analyses discussed above, here the B hadrons were reconstructed by tracking their semileptonic decays[4] $B \to DX\mu\nu$ ($X\mu\nu$ denoting the leptonic component of the decay).
As a result, the following formula was applied to relate the detected signals to eq. (6.7):

$$\begin{aligned}\sigma(pp \to H_b X) = & \frac{1}{2\mathcal{L}}\Bigg\{\left[\frac{n(D^0\mu)}{\epsilon_{D^0} \times \mathcal{B}_{D^0}} + \frac{n(D^+\mu)}{\epsilon_{D^+} \times \mathcal{B}_{D^+}}\right]\frac{1}{\mathcal{B}(B \to DX\mu\nu)} \\ & + \left[\frac{n(D_s^+\mu)}{\epsilon_{D_s^+} \times \mathcal{B}_{D_s^+}}\right]\frac{1}{\mathcal{B}(B_s \to D_s X\mu\nu)} + \left[\frac{n(\Lambda_c^+\mu)}{\epsilon_{\Lambda_c^+} \times \mathcal{B}_{\Lambda_c^+}}\right]\frac{1+\delta}{\mathcal{B}(\Lambda_b^0 \to \Lambda_c^+ X\mu\nu)}\Bigg\} \; ,\end{aligned} \tag{6.10}$$

where $\mathcal{L}$ is the integrated luminosity corresponding to the collected events, namely $284.10 \pm 4.86\,\text{pb}^{-1}$ at $\sqrt{s} = 7\text{TeV}$, and $4.60 \pm 0.18\,\text{pb}^{-1}$ at $\sqrt{s} = 13\text{TeV}$. $n(X_c\mu)$ ($X_c = D^0, D^+, D_s^+, \Lambda_c^+$) is the number of detected charm hadron in association with muons, and their charge-conjugates. The efficiencies are labeled with ϵ_{X_c}. The expression $\mathcal{B}(B \to DX\mu\nu)$ stays for the average branching fraction for $\bar{B}^0$ and B^- semileptonic decays.
In the paper, the results were reported in terms of pseudorapidity distribution $\eta_{H_b} =$

[4] The reason behind this peculiar choice is that the semileptonic B^0 and B^- branching fractions are known in literature with reasonable accuracy, and the equality of semileptonic widths for all b-hadrons has been proved by several experimental evidences. On the other hand, the more standard procedure to reconstruct B hadrons through J/ψ production assumes that the B hadrons are produced in the same proportions as at LEP [169]. Considering just using one species of B hadron would instead require the knowledge of B hadron fractions to extrapolate to the total B hadron production.

$-\ln[\tan(\theta/2)]$[5], where θ is the angle of the H_b hadrons with respect to the beam direction, and integrated over the full transverse momentum p_{T,H_b} range. The covered pseudorapidity range was $2.0 < \eta < 5.0$, corresponding to the acceptance of the LHCb experiment. Also in this case, the 13TeV/7TeV was presented. The measured distributions were also compared to the FONLL predictions for $pp \to b\bar{b} + X$, showing a quite puzzling picture. Indeed, although data and theoretical predictions appeared to be compatible within their respective uncertainties, evident shape tensions were observed.
We present now the comparison of the MiNLO' and MiNNLO$_{\rm PS}$ predictions with data. In fig. 6.9 we show the pseudorapidity distributions at 7TeV (left-hand side of the figure) and 13TeV (right-hand side). The ratio distribution, calculated with the same methodology exposed in the previous section, is reported in fig. 6.10. For the values of the fiducial cross-sections, we refer to table 6.8. In our calculation, instead of considering the parton level $b\bar{b}$ production, we worked out the same B hadron cross-section formula in eq. (6.7). This allowed for a more direct comparison with the data, including the effect of hadronization and MPI modeled in PYTHIA8. As expected, the MiNNLO$_{\rm PS}$ prediction is affected by uncertainties much smaller than the FONLL ones in Ref. [173]: around $\pm 10 - 15\%$ at fixed beam energy and down to $\pm 5 - 10\%$ for the ratio result. Nevertheless, we have also observed the presence of a shape tension between data and theory, analogously to the one emerging in the comparison to FONLL. The tension appears dramatical in the central bins of η_B at $\sqrt{s} = 13$TeV, where our predictions undershoot data beyond the uncertainties. Nevertheless, these discrepancies seem to cancel out in the ratio of the pseudorapidities, where we observe a quite good agreement between MiNLO', MiNNLO$_{\rm PS}$ and the data points.
As a final remark, we point out that this set of LHCb measurements has gone through a long revision, and that understanding these results has been the object of research by the community in the last few years[6]. More recently, a comparison with the fixed order NNLO prediction obtained within the Matrix framework has also been advanced in Ref. [148].

Fiducial cross-section $\sigma(pp \to H_b X)$ at LHCb		
Energy	Measured by LHCb (μb)	MiNNLO$_{\rm PS}$ (μb)
7TeV	$72.0 \pm 0.3_{\rm (stat)} \pm 6.8_{\rm (syst)}$	$65.3(1)^{+12.6\%}_{-10.5\%}$
13TeV	$144 \pm 1_{\rm (stat)} \pm 21_{\rm (syst)}$	$116.2(3)^{+7.6\%}_{-12.3\%}$
13TeV/7TeV	$2.00 \pm 0.02_{\rm (stat)} \pm 0.26_{\rm (syst)}$	$1.77(9)^{+2.6\%}_{-9.3\%}$

Table 6.8: Comparison with LHCb: Fiducial cross-sections for $pp \to H_b + X$ (see text for more details).

[5] In the following, we will adopt the notation η_B when referring to η_{H_b}
[6] See, e.g, Ref. [174].

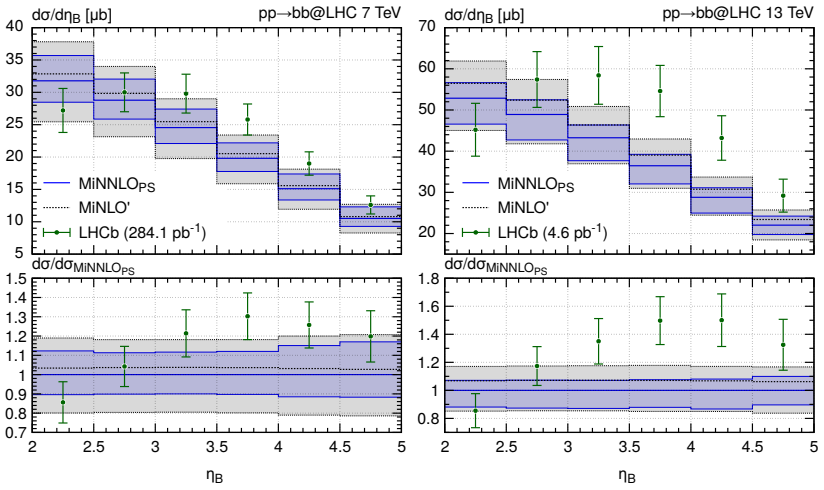

Figure 6.9: Comparison with LHCb: B hadron pseudorapidities at 7TeV and 13TeV

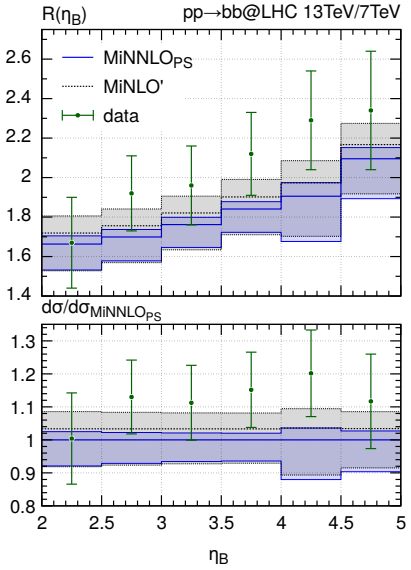

Figure 6.10: Comparison with LHCb: ratio of B hadron pseudorapidities at 7TeV/13TeV

Chapter 7

Jet Flavour Study on $b\bar{b}$ Events

In this chapter, we will present the results of another interesting study that we performed, namely the analysis of the bottom flavoured jets in the bottom-pair production events at the LHC. We devoted chapter 4 to describe and define in a rigorous way the hadronic jets that are observed in high energy collisions. One of the main reasons that motivated the community to develop a better understanding of the topic, was that hadronic jets somewhat represent the closest object we can think about when we mean to probe the physics of primary partons produced in hard events at colliders. When it comes to study primary partons, however, a question appears natural and legit: is it also possible to determine the flavour of hard quarks (and antiquarks), by looking into the particle content of jets?
Addressing this question goes far beyond the purely academic interest, as identifying the flavour content of hard scatterings plays a crucial role in several searches in an beyond the Standard Model. Bottom- and charm-flavoured jets relate to the presence of long-lived B and D mesons in the clustered hadronic jets. They can be obtained alone (in the pure QCD $pp \to b\bar{b} + X$ and $pp \to c\bar{c} + X$ channels), in association with heavy particles like the Higgs or the vector bosons, or in heavy particle decays like $H \to b\bar{b}$ and $t \to bW^+$. Several are the phenomena that have been studied in the field, and we will now just mention a few of them. In the context of the top physics, the accurate determination of b-jets allows for accurate measurements of the top-pair production [175, 176]. In fact, on top of being one of the most relevant processes at the LHC, the forward production of $pp \to t\bar{t} + X$ has deep relations with PDFs at high Bjorken-x values, and implications on BSM physics [177–179]. The di-b-jet production in $pp \to b\bar{b} + X$ represents a background for the decay of the Higgs boson[180, 181, 181, 181] and of new BSM heavy particles, and can be used to study charge asymmetries. Finally, we also mention that the c-jet production associated with the Z boson is relevant in the study of the intrinsic charm component of the proton, which is now a new field of investigation in phenomenology.
On the theoretical side, defining the flavour of jets is definitely not trivial. Although one would naively expect to associate the flavour of a jet by just looking at its flavour content, coming up with IR-unsafe jet flavour definitions, or coming across a flavour misidentification, appears relatively easy. For this reason, the problem of designing a consistent jet flavour definition has been studied extensively in the literature. In the following sections, we will review some of the most recent available algorithms advanced to solve these issues. We specify that these algorithms represent a subset of all the algorithms that have been proposed in the last few years [96, 182–184]. Afterward, we will exploit the $pp \to b\bar{b} + X$ events already considered in our B-hadron study to perform a systematic comparison of these new algorithms, for different types of observables. Finally, we will present an exhaustive comparison of our MiNNLO$_{\rm PS}$ predictions with the inclusive b-jet and di-b-jet measurements carried out by

the LHC collaborations.

7.1 Definition of Jet Flavour

When studying flavoured jets, two main ingredients are essential for uniquely identifying the matter:

1. A **jet definition**, namely a clustering algorithm and a recombination scheme, which are applied to get the number of jets in a given event, along with their respective kinematics.

2. A **flavour assignment** procedure, which sorts out the flavoured jets among the whole set of jets identified in the first step.

In general, three flavour-recombination schemes have been considered in literature to address the second point. Sticking with the notation introduced in [184], they are the following:

- *Any-flavour scheme*, where any combination having at least one flavoured particle yields a flavoured result.

- *Net-flavour scheme*, where the net flavour of the combination is considered, namely the total number of quarks minus antiquarks for each quark flavour.

- *Flavour modulo-2 scheme*, where the combination is assigned a flavour f if it contains an odd number of f-flavoured particles[1].

The impact of the different schemes applied on simple parton configurations are shown in table 7.1

	Any-flavour	**Net-flavour**	**Flavour modulo-2**
$\{q_f, \bar{q}_f\}$	f-flavoured	flavourless	flavourless
$\{q_f, q_f\}$	f-flavoured	f-flavoured	flavourless
$\{q_f, g\}$	f-flavoured	f-flavoured	f-flavoured

Table 7.1: Flavour recombination schemes on simple parton configuarions.

In experiments, some additional steps must be considered. At the LHC, it is nowadays customary to cluster events through the anti-k_t algorithm, already discussed in section 4.2.5, and carry out the jet kinematics within the E-scheme described in section 4.3. To understand how flavour is assigned to jets, we can take as an example the case of b-flavoured jets. As B hadrons are more likely to decay before being detected, a *Secondary vertex* (SV) reconstruction must be put into practice to reconstruct their kinematics. The reconstructed B hadrons are then associated with the anti-k_T jets already defined, according to some kinematic criteria going under the name of *track-jet matching*[2]. Once all identified B hadrons have been

[1] This scheme is particularly suited for the experimental analyses, where it is not possible to distinguish flavour from anti-flavour, e.g. because of $B_0 - \bar{B}_0$ oscillations.

[2] E.g. requirements on the angular distance between B hadrons and jet axes.

associated with jets or discarded via kinematical cuts, the flavour of jets is evaluated within the any-flavour recombination scheme. This represents, in other words, the core of the jet *b-tagging*. As an example, a detailed explanation of the procedures adopted by ATLAS in Run 2 of the LHC can be found in Ref. [185]. However, the procedures adopted generally vary to many extents according to what appears to be more efficient and optimised, and depend on the experiments. For instance, the tracks undergoing clustering are selected to obey different cuts on their transverse momentum and on other parameters. the radius R adopted within the anti-k_t algorithm is also generally different, and so are the fiducial cuts imposed on the jet kinematics.

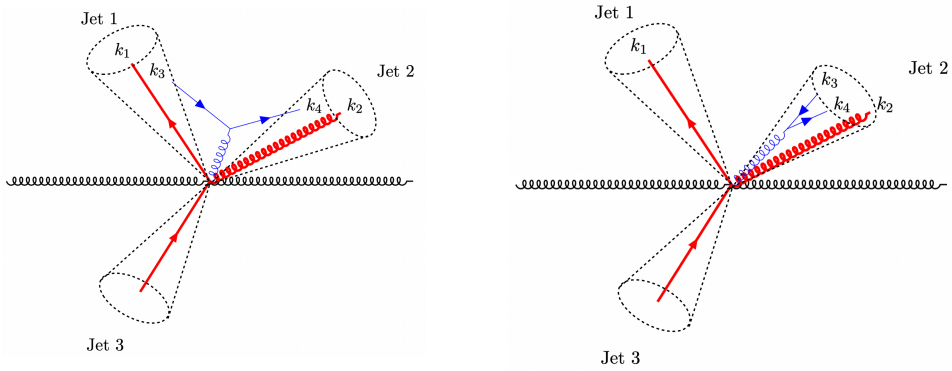

Figure 7.1: Higher order corrections to flavoured jet productions from soft gluon emissions splitting in a $b\bar{b}$ pair. In both figures, two incoming gluons scatter into a $b\bar{b}g$ final state (in red), originating two b-jets (Jet 1 and Jet 3), and a light jet (Jet 2). A gluon splitting into a $b\bar{b}$ (in blue), is then included. In the left figure, the $b\bar{b}$ pair has a relatively wide angle and pollutes the flavour content of Jet 1 and Jet 2. In the right figure, the gluon splitting is quasi-collinear, and pollutes the light Jet 2.

Identifying b-jets with the Any-flavour scheme is, unfortunately, not the best option from the theoretical perspective. In section 4.1, we stressed that a consistent jet definition should produce jet configurations that are insensitive to extra soft or collinear emissions. For the same reasons explained there, related to the IR safety of the calculations, this must be also true for a consistent flavoured jet definition. However, it is not difficult to prove how the current experimental way to approach flavoured jets violates that principle. If we take an event and imagine modifying it with an extra emission of a soft gluon, then splitting into a $b\bar{b}$ (or $c\bar{c}$) pair, two unfortunate scenarios are possible:

- The quarks in the pair could be generated with a wide relative angle, and they could be clustered in different light jets, thus polluting their flavour content (see left figure of fig. 7.1).
- The quark pair could be quasi-collinear and clustered with another light jet, that would then be identified as flavoured (see the right figure of fig. 7.1).

Moreover, one could argue that such flavour assignment could be potentially misleading, as none of the flavoured jets obtained in these scenarios would be really linked to heavy

flavours produced in the hard scattering of the event. At this point, one might stick with the anti-k_T algorithm and define flavours via the Net-flavour or the Flavour modulo-2 schemes. However, this would only solve the second problem we pointed out, and would not represent a definitive strategy. In section 7.2, we will denote as **Naive** the b-jets defined in this way.

A first attempt to solve both issues exposed above and give an IR-safe definition of jet flavoured was proposed in Ref. [96], within the *Flavour-k_T algorithm*. The idea was to modify the pre-existing k_T-algorithm, according to two fundamental criteria:

1. The *closeness* between particles, induced by the clustering distance, should relate to IR divergences from the factorization formulas.

2. No *spurious closeness* (i.e. not related to an IR divergent behaviour), should be introduced by the distance adopted.

In this sense, the distance in eq. (4.5) was not really suitable, because it was tailored on the $g \to gg$ splitting probability. Therefore, a pair of quarks $q_i\bar{q}_j$ would be assigned a small distance if $\bar{q}_j$ is soft (for example), while that configuration is not related to a soft divergence in the $g \to g_i q_j$, since

$$[dk_j] \left| M^2_{g\to g_i g_j}(k_j) \right| \simeq \frac{\alpha_s C_A}{\pi} \frac{dE_j}{E_j} \frac{d\theta^2_{ij}}{\theta^2_{ij}}, \quad (E_j \ll E_i,\, \theta_{ij} \ll 1)\,, \tag{7.1}$$

and an analogous situation arose for a quark-gluon pair with a soft quark.
The proposal was to modify the Flavout-k_T prescriptions according to the flavour of the particles considered. For hadronic collisions, the distance measure in eq. (4.5) now becomes

$$d^{(F)}_{ij} = (\Delta\eta^2_{ij} + \Delta\phi^2_{ij}) \times \begin{cases} \max(k^2_{T,i}, k^2_{T,j}), & \text{softer of } i,j \text{ is flavoured} \\ \min(k^2_{T,i}, k^2_{T,j}), & \text{softer of } i,j \text{ is flavourless} \end{cases} \tag{7.2}$$

where *softer* corresponds to lower transverse momentum. Regarding the beam distance, the situation is different. Looking at eq. (4.8), we see it involves only a scale, making it less obvious how to introduce a maximum and a minimum. Moreover, as the flavour of each of the incoming beams should play a role, it is also necessary to specify which of the two beams the particles recombine with. This led to the definition of two new scale $k_{T,B}$ and $k_{T,\bar{B}}$

$$k_{T,B}(y) = \sum_i k_{T,i} \left(\Theta(y - y_i) + \Theta(y - y_i) e^{y_i - y}\right)\,, \tag{7.3}$$

$$k_{T,\bar{B}}(y) = \sum_i k_{T,i} \left(\Theta(y_i - y) + \Theta(y_i - y) e^{y - y_i}\right)\,, \tag{7.4}$$

and to two rapidity-dependent beam distances, one for the right-moving beam B and one for the left-moving beam $\bar{B}$ according to

$$d^{(F)}_{iB} = \begin{cases} \max(k^2_{T,i}, k^2_{T,B}), & i \text{ is flavoured} \\ \min(k^2_{T,i}, k^2_{T,B}), & i \text{ is flavourless} \end{cases} \tag{7.5}$$

$$d^{(F)}_{i\bar{B}} = \begin{cases} \max(k^2_{T,i}, k^2_{T,\bar{B}}), & i \text{ is flavoured} \\ \min(k^2_{T,i}, k^2_{T,\bar{B}}), & i \text{ is flavourless} \end{cases} \tag{7.6}$$

Apart from these different definitions, the algorithm essentially articulates in the same steps already described for the standard k_T algorithm. In particular, eq. (4.9) will be by including the distances between the particles and the two beams in eq. (7.5), and a particle i will be recombined with either of the incoming beams if $d_{iB}^{(F)}$ (or $d_{i\bar{B}}^{(F)}$) happens to be the smallest distance in the set. In case $d_{iB}^{(F)} = d_{i\bar{B}}^{(F)}$, particle i will recombine with the beam that has the smaller $k_{tB}(y_i), k_{t\bar{B}}(y_i)$.

Notice that the new flavour-dependent distance introduced in eq. (7.2) eliminates the spurious closeness of the soft wide-angle $q\bar{q}$ splitting (see the left figure of fig. 7.1) induced by eq. (4.9). Indeed, if q and $\bar{q}$ have similar energies $E_3 \sim E_4 \ll Q$, then $y_{34} \sim E_3^2/Q^2 \ll 1$ and $y_{13} \sim y_{14} \sim y_{23} \sim y_{24} \sim 1$. This will make q and $\bar{q}$ recombine first into a flavourless gluon pseudo-jet, which will eventually recombine with another jet only in the following steps. At the same time, the flavour-k_T algorithm preserves IR safety guaranteed by the standard k_T, as it was extensively demostrated in Ref. [96]. For what concerns the flavour jets, this can be assigned either via the Net-flavour or via the Flavour modulo-2 scheme. Flavourless Jets will then be identified as gluon jets. In case a jet appears to have more than one flavour, no defined flavour can be assigned to it[3].

7.1.1 The Flavour Dressing Algorithm

The flavour-k_T algorithm provides an infrared safe procedure to identify b-jets, and its phenomenological impact has been discussed in Refs. [96, 186]. A more recent work [80] has also studied its application in identifying b-jets originating from the $H \to b\bar{b}$ decay in the Higgstrahlung processes $pp \to W^+H \to e^+\nu_e b\bar{b}$ within MiNNLO$_{\rm PS}$, and compared it to the k_T and anti-k_T algorithms.
Unfortunately, the necessity of equipping the k_T distance measure with flavour information makes the flavour-k_T highly not trivial to be implemented in current experimental analyses. Moreover, implementing drastic modifications to the currently used algorithm can be quite involved for the experimental collaborations. In this sense, it appears more feasible to adopt an infrared safe procedure that assigns flavours to jets already clustered with standard algorithms, like the widely used anti-k_T algorithm. This is the fundamental idea behind an algorithm advanced in recent years, namely the *Flavour dressing* algorithm [182]. We will now summarize its main features, while we refer the reader to section 7.2 for an analysis of its impact on the b-jet hadroproduction in MiNNLO$_{\rm PS}$.
In a given event, the inputs of the flavour dressing algorithm are essentially the following:

- **Flavour agnosic jets.** The list of jets $\{j_1, \ldots, j_m\}$ already clustered with an infrared safe algorithm.
- **Flavoured particles** The list of particles $\{p_1, \ldots, p_n\}$, with flavours $\{f_1, \ldots, f_n\}$[4].
- **Association criterion.** A criterion that establishes whether a flavoured particle p_i

[3] Tipically, one is interested in studying only one species of flavoured jets (e.g. b-jets or c-jets), so the flavour recombination scheme is worked out with a single flavour f ($f = b, c$), and the other light-flavours are neglected. In cases where the study is done on more heavy-flavoured jets, like the associated b-jet and c-jet production, only jets with a well-defined b and c flavour are accounted.
[4] These can be partons, hadrons or proxy particles like the recontructed secondary vertices SV

can be associated with a jet, and to which one[5]. To this extent, a distance measure is introduced and its function will be detailed below. Given two final-state objects a and b, it reads

$$d_{ab} = 2\left[\frac{1}{\omega^2}(\cosh(\omega\Delta y_{ab}) - 1) - (\cos\Delta\phi - 1)\right]\max(k_{T,a}^{\alpha}, k_{T,b}^{\alpha})\min(k_{T,a}^{2-\alpha}, k_{T,b}^{2-\alpha})\ , \tag{7.7}$$

and the default choice of the parameters was: $\alpha = 1$ and $\omega = 2$. Distances between the particle p_i and the incoming beams $B^{\pm}$ are also introduced by applying minor modifications to the corresponding flavour-k_T definitions[6]. Specifically, the α-dependent generalized version [186] of eq. (7.5) is used

$$d_{p_i,B^{\pm}} \ = \ \max\left(k_{T,i}^{\alpha}, k_{T,B^{\pm}}^{\alpha}(y_i)\right)\min\left(k_{T,i}^{2-\alpha}, k_{T,B^{\pm}}^{2-\alpha}(y_i)\right)\ , \tag{7.8}$$

where the $k_{T,B^{\pm}}(y)$ in defined in eq. (7.3).

- **Flavour recombination scheme.** Either the Net-flavour or the Flavour modulo-2 schemes can be adopted, according to the analysis one is performing.

With these inputs, the algorithm recursively applies the association criterion to assign flavoured particles to pre-existing jets. Then, the jet flavours are defined by applying the accumulation criterion to the set of particles assigned to the respective jets. In practice, the algorithm works as follows:

1. The set of jets $\{j_1, \ldots, j_m\}$ in the event is found with standard IRC safe algorithms (e.g. the anti-k_T).

2. A set D of distance measures is introduced, computed with eq. (7.7) on all the allowed particle pairings according to

$$D \ = \ \{d_{p_1p_2}, d_{p_1p_3}, \ldots, d_{p_ij_k}, \ldots, d_{p_iB^{\pm}}, \ldots\}\ . \tag{7.9}$$

   In particular, $d_{p_ip_j}$ is included if either both p_i and p_j are flavoured, or if at least one of them is unflavoured and they belong to the same jet. When a particle p_i is associated with a jet j_k, also the distance $d_{p_ij_k}$ is included. At last, the beam distances $d_{p_iB^{\pm}}$ are added if p_i does not belong to any jet.

3. While D is not empty, the pairing with the smallest distance is singled out. If the smallest distance pairing is composed of two particles p_i and p_j, these are merged together and removed from the list. If $d_{p_ij_k}$ is the smallest, then p_i is assigned to j_k, and all entries involving p_i are removed from D. In the third case, when $d_{p_iB^{\pm}}$ is the smallest, the particle p_i is just discarded and so are all entries of D involving it.

4. Finally, the flavour of any jet j_k is defined according to the accumulated flavours of particles assigned to it in the previous step.

[5] An obvious choice would be to assign a particle p_i with flavour f_i to the same jet it has been clustered in. However, this might not be possible in case where the particle does not enter the jet algorithm as input. For a more detailed discussion on this point, we refer to Ref. [182].

[6] Notice that eq. (7.7) correctly reproduces eq. (7.2) in the collinear limit.

As a result, the algorithm so designed is IRC safe at all orders in perturbation theory, as proved in Ref. [182]. Moreover, it is suitable to be applied both in theoretical MC calculations and in experimental analyses, as the input particles can be partons, heavy-flavour hadrons, and proxy particles reconstructed in an experimental environment. The flavour dressing algorithm has also been tested in some phenomenological studies, such as the $pp \to Z + b$-jet [182] and the $pp \to Z + c$-jet process [187].

7.1.2 Interleaved Flavour Neutralisation

We now introduce the last algorithm that will be relevant to the extent of this thesis, namely the *Interleaved flavour neutralisation* (IFN) algorithm [184]. The main goal behind the IFN algorithm is similar to the one that motivated the flavour dressing procedure, namely to find an infrared-safe procedure that assigns flavour to jets clustered with the widely used sequential recombination algorithm (specifically the anti-k_T and the Cambridge-Aachen algorithms). In this sense, the strategy proposed by the IFN algorithm is to run a standard clustering algorithm and carry out, before any clustering takes place, a flavour neutralisation procedure that globally redefines the flavours of involved particles. The flavour neutralisation, as we will see, requires a *neutralisation distance measure* to be adopted. Similarly to the flavour dressing algorithm[7], the distance used is the one reported in eq. (7.7). We will now summarize the main features of the algorithms, assuming to choose the anti-k_T to perform the clustering. For the sake of clarity, we will first review the neutralisation procedure, and then see how it is interleaved at each step of the clustering.
The flavour neutralisation is always performed relative to a particle or pseudo-jet i, which serves as the pivot of the procedure. We can denote by C the list of all potential neutralisation candidates and with E the candidates which must be excluded because already considered in previous steps. Along with them, a distance scale $d_{\max}$ is given as a threshold above which to ignore neutralisation candidates. We can now imagine implementing the procedure in a computer routine that will have the aforementioned ingredients as inputs, namely $N(i, d_{\max}, C, E)$. Schematically, the routine will

N1: Populate a list L with distances d_{ik}, where $k \in (C - E)$, and only if $d_{ik} < d_{\max}$

$$L \;=\; \{d_{i1}, d_{i2}, \dots\}\,. \tag{7.10}$$

N2: Find the k that gives the smallest d_{ik} in L: this will be the selected candidate for the flavour neutralisation with i.

N3: Before going ahead with k, run the routine $N(k, d_{ik}, C, E)$ to find any other particle/pseudo-jet j that could be more naturally paired with k (such that $d_{jk} < d_{ik}$)[8]. If such a j exists, it is used to neutralise flavour in k. E.g., if j has a net bottom flavour content of three ($f_j = bbb$) and k has a net anti-bottom flavour of two ($f_k = \bar{b}\bar{b}$), the neutralisation

[7] To be precise, the distance reported in eq. (7.7) was first introduced in the IFN algorithm [184], while the original formulation of the flavour dressing algorithm was based on the same generalized flavour$-k_T$ distance reported in [186]. However, as pointed out in Ref. [184], such distance choice would cause infrared-unsafety issues arising in high order corrections, and was therefore replaced by eq. (7.7).
[8] As detailed in Ref. [184], this passage is essential for the IRC safety of the algorithm.

will annihilate two b from j with two $\bar{b}$ from k, so that:

$$f_j = bbb \quad \rightarrow \quad f'_j = b\,, \tag{7.11}$$
$$f_k = \bar{b}\bar{b} \quad \rightarrow \quad f'_k = 0\,. \tag{7.12}$$

N4: Now, the left flavour content in k is used to neutralise the flavour of i, in the same way described above. If k is flavourless, d_{ik} is removed from the list L and the loop starts again from point 2. If L is empty, exit the routine.

N5: If i is flavourless, exit the routine.

A routine N such implemented can then be used in the IFN algorithm, which interleaves N with the anti-k_T clustering works as follow:

1. Before any pair of particles/pseudo-jets i and j (with $p_{T,i} < p_{T,j}$) is about to recombine within the anti-k_T algorithm, $i + j$ will have the same flavour of j if i is flavourless.

2. If i is flavoured, initialize a list C with all the flavoured pseudo-jets declared so far, and a list $E = \{i, j\}$. Then run the routine $N(i, d_{ij}, C, E)$.

By construction, the IFN algorithm will generate flavour jets with exact anti-k_T kinematics. This leaves open the possibility of running the flavour neutralisatias as an add-on, after all jets have been identified. Moreover, the same definition of the neutralisation distance and the recursive property of the procedure will guarantee the IRC of the algorithm at all orders in perturbative calculations. Two more properties are worth being mentioned. One is the *multi-scale flavour resolution*, meaning that the flavour of pseudo-jets is well defined at any step of the anti-k_T clustering, allowing for jet substructure analyses. The other one is the *single parton consistency*, namely the fact that events containing only one parton per jet do not have their flavour altered by the algorithm. In other words, leading order jet calculations carried out with the IFN provide the same result of the plain anti-k_T algorithm.
Although we focused on the b flavour, the procedure can be extended to deal with multiple flavours, eventually including c. In general, two ways to do this are allowed, possibly leading to different results. A way to do this is to first neutralise the b and then neutralise the c flavour, for each interleaved step. Another option is to carry out a single flavour neutralisation that considers both b and c at a time. As a consequence, flavour neutralisation triggered by the bottom content of a pseudojet may affect the c flavour of other pseudojets.

7.2 A Comparative Study on the b-jet Clustering in $b\bar{b}$ Events

Having introduced some of the infrared-safe algorithms currently available to define flavoured jets, we can present the result of a study we performed on the MiNNLO$_{\rm PS}$ $pp \to b\bar{b} + X$ events, whose goal is to compare the impact of the different clustering techniques on several b-jet observables.
Before going through the details of the calculation, it is worth making some general considerations about the main production channel that contributes to the b-jet production. At the leading order, we have the so-called *flavour creation* (FCR) channel, where two initial

state gluons scatter into a $b\bar{b}$ pair. This is described by the s-channel and a t-channel tree-level diagrams in figs. 7.2a and 7.2b. In hard events where the bottom quarks are emitted back-to-back, the FCR configuration brings the largest contribution. Going to the next order, we have an additional gluon emission. This can feature as a radiative correction to the (FCR) channel, or as part of two new channels: the *gluon-splitting* (GSP) in fig. 7.3a and the *flavour excitation* (FEX) channel in fig. 7.3b. The GSP case can be understood as a heavy-quark radiative correction to the tree-level of $gg \to gg$, where one of the final state gluons splits into a $b\bar{b}$ pair. On the other hand, the FEX topology is given by an initial state gluon splitting into $b\bar{b}$, of which one b quark will be directly part of the final state and the other will go through the hard scattering. Both the GSP and the FEX configurations are affected by a logarithmic enhancement due to quasi-collinear bottom pair emission. This goes like $\alpha_s^2\alpha_s^n \ln^{2n-1}(p_T/m_b)$ in the GSP configuration, and like $\alpha_s^2(\alpha_s \ln(p_T/m_b))^n$ in the FEX case ($n \geq 1$ is the number of $g \to b\bar{b}$ splittings) [188–192]. In our 4FS calculation, we have only one final state $b\bar{b}$ pair, therefore both configurations will receive a $\alpha_s^3 \ln(p_T/m_b)$ enhancement, starting from the NLO.

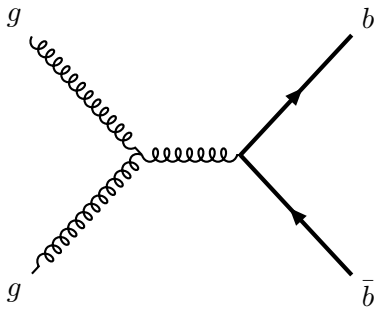

(a) Flavour creation, s-channel

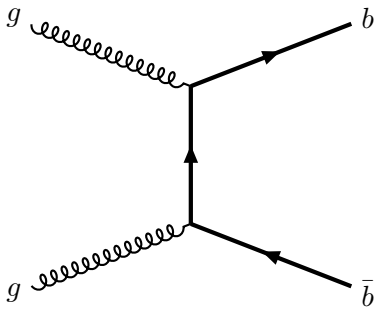

(b) Flavour creation, t-channel

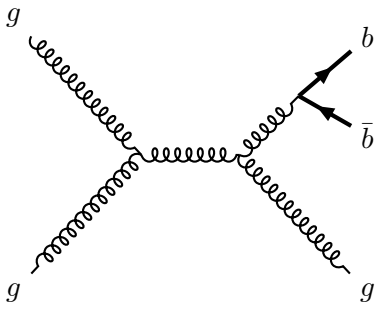

(a) Gluon-splitting channel

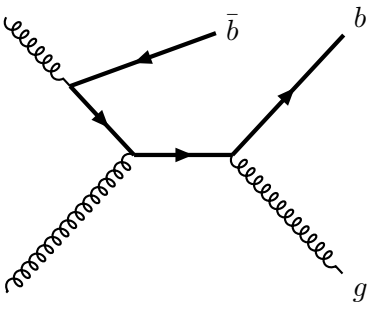

(b) Flavour-excitation channel

In the following sections, we will take under exam different b-jet observables, as well as di-b-jet observables computed on the kinematics of the hardest and second-hardest b-jet in the event. The effect we will observe, by comparing the observables and the results obtained within different clustering techniques, will be strictly related to the different production channels just discussed, as their roles may be enhanced or suppressed according to the situation.

7.2.1 Setup of the Calculation

We will now describe the setup adopted for the study on the comparison of different clustering algorithms. Schematically, the results of our simulations can be summarized in the following three steps:

1. **Event generation.** Using our MiNNLO$_{\rm PS}$ implementation of the $pp \to b\bar{b} + X$ process, we generated samples of Powheg events at $\sqrt{s} = 7$TeV and $\sqrt{s} = 13$TeV. In terms of bottom mass, PDFs, and other parameters of the calculation (e.g. the values of K_Q, Q_0 etc.), we essentially adopted the same choices already detailed in section 5.3. The only relevant difference from the setup presented in the previous chapters is related to the Born $\mu_R^{(0)}$ central scale. For it, we looked for a dynamical scale that could be more representative of a typical b-jet event kinematics. Given that light radiation becomes important when considering clustered objects like the b-jets (we illustrate this point in fig. 7.1, we finally opted for

$$\mu_R^{(0)} \;=\; \frac{H_T^{b\bar{b}} + \sum_i p_{T,j_i}}{2} \;, \tag{7.13}$$

   where $H_T^{b\bar{b}} = \sqrt{m_b^2 + p_{T,b}^2} + \sqrt{m_{\rm b}^2 + p_{T,{\rm b}}^2}$ is the usual sum of the transverse masses of b and $\bar{b}$. To include the kinematics of the additional light partons produced in the hard scattering, the sum over their transverse masses (effectively their transverse momenta) is also accounted[9].
   In order to increase the accuracy of our results in the hard regions of the b-jet production, we exploited a suppression factor[10] $W(\Phi_{b\bar{b}g})$ on the Born phase-space kinematics of POWHEG $b\bar{b} + J$ generator. Given the highly nontrivial correspondence between $\Phi_{b\bar{b}g}$ and the phase space of the final clustered b-jets, we tested different functional form for W, and we finally opted for

$$W(\Phi_{b\bar{b}g}) \;=\; \left(\frac{\frac{1}{\Lambda_{\rm cut}^2}}{\frac{1}{\Lambda_{\rm cut}^2} + \frac{1}{H_T^2(\Phi_{b\bar{b}g})}} \right)^2 \;, \tag{7.14}$$

   where $\Lambda_{\rm cut}$ is a hard scale that was set to 300GeV and

$$H_T(\Phi_{b\bar{b}g}) \;=\; p_{T,b} + p_{T,\bar{b}} + p_{T,g} \;. \tag{7.15}$$

2. **Interface with parton shower.** The events so generated have been interfaced with the MC parton shower program PYTHIA8, allowing to generate showered events both at the parton level and at the hadron level (with and without the multi-parton interaction effects). In the generation of hadron final states, we turned off the decay of B mesons ($B^0, \bar{B}^0, B^+, B^-, B_s^0, \bar{B}_s^0$) and baryons ($\Lambda_b^0, \bar{\Lambda}_b^0$), that could then be directly used for the flavour assignment of the identified jets. All the other unstable hadrons have been let to decay.

[9] Working out with the $pp \to b\bar{b}J$ Powheg generators empowered with the MiNNLO$_{\rm PS}$ prescriptions, we can have either one or two more light partons in the hard scattering configuration, being the event generated either in the Born or in the real kinematics.

[10] See eq. (3.36).

3. **Jet analysis.** At last, we performed an on-the-fly jet analysis on all the particles generated in the final state, event per event, via an interface with the FastJet-3.4.2. According to the clustering algorithm and to the b-tagging technique employed, we obtained four different classes of predictions, which will be labeled in the following:
   - **EXP**: where the anti-k_T algorithm has been employed and b-jets have been defined with the any-flavour scheme.
   - **Naive**: where the anti-k_T algorithm has been employed and b-jets defined with the flavour modulo-2 scheme.
   - **FD**: where the anti-k_T + flavour dressing algorithm has been used and b-jets defined with the flavour modulo-2 scheme.
   - **IFN**: where the anti-k_T + inteleaved flavour neutralisation algorithm has been used and b-jets defined with the flavour modulo-2 scheme.

   In all the listed cases, the anti-k_T jet radius was set to $R = 0.4$.

In our analysis, we introduced a minimal set of fiducial cuts on the kinematics of the identified b-jets, in a way to simulate a prototype of experimental analysis similar to the ones carried out by the collaborations at the LHC. Specifically, the following cuts have been imposed on the transverse momentum and rapidity of all the identified b-jets:

$$p_T^{\text{b-jet}} > 30\text{GeV}, \qquad |\eta^{\text{b-jet}}| < 2.5\,. \tag{7.16}$$

7.2.2 Hardest b-jet Observables

We present now our MiNNLO$_{\text{PS}}$ results for observables computed on the hardest b-jet. We start with the differential cross-section as a function of the transverse momentum $p_{T,b}^{(\text{hard})}$, in fig. 7.4. In this plot, what appears evident at first glance is the significant difference between the EXP curve and the other predictions. The large discrepancy can be fully explained by the flavour-recombination scheme that is adopted in the EXP calculation and that differs from the Naive, FD, and IFN calculations. Indeed, while the any-flavour scheme implies the presence of hardest b-jets containing $b\bar{b}$ pairs in the EXP prediction, this is not possible within the modulo-2 scheme used in the other cases. As a result, the EXP cross-section will include the logarithmically enhanced contributions coming from the quasi-collinear $b\bar{b}$ emissions in the GSP and FEX channels. The effect of these terms increases with the jet transverse momentum, as can be observed. Moreover, the EXP hardest b-jet will be also sensitive to all the quasi-collinear $g \to b\bar{b}$ splittings generated by the parton shower, leading to an increase in the difference with the other b-jet definitions.

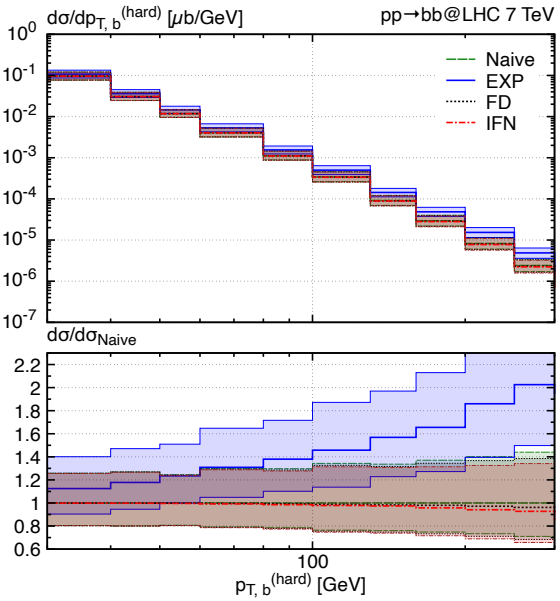

Figure 7.4: Transverse momentum of the hardest b-jet in $pp \to b\bar{b} + X$ production at $\sqrt{s} = 7$TeV, comparing the effect of the different b-jet definitions introduced in section 7.2.1.

On the other hand, we observe small differences between the Naive, FD, and IFN curves. These essentially overlap in the soft regions and differ by a $\sim 5\%$ factor for $p_{T,b}^{\text{hard}} \sim 300$GeV. In this case, the Naive prediction receives contributions from the soft wide-angle $b\bar{b}$ emissions described in section 7.1, which are generally excluded in the FD and IFN clustering. However, these emissions can only generated by the parton shower in a 4FS calculation, and their impact appears quite modest. At last, differences between the FD and the IFN are essentially due to technical aspects of the related to the respective flavour assignment procedures.
In terms of scale uncertainties, we do not observe a relevant improvement by comparing the different predictions. Indeed, all of them are affected by around $\pm 20\%$ uncertainties at low transverse momentum, increasing up to around $\pm 35\%$ in the hard regions.
To mitigate the effect of the $b\bar{b}$ quasi-collinear production in the GSP and FEX channels, one can compute the same hardest b-jet transverse momentum distribution but requiring the presence of two well-separated b-jets in the events. This is done in fig. 7.5. In this case, the increase in the EXP prediction will be mainly due to the $g \to b\bar{b}$ quasi-collinear splitting generated by the parton shower. As a result, a sizeable difference is still present between the EXP differential cross-section and the other ones, but appears much more contained than in fig. 7.4.

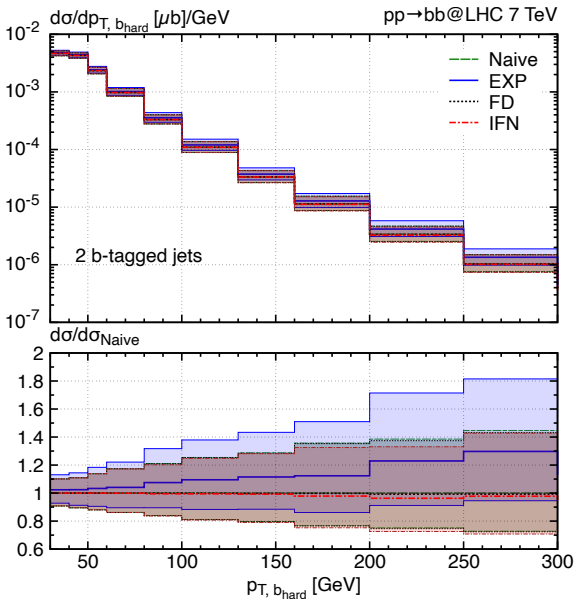

Figure 7.5: Transverse momentum of the hardest b-jet in events with two well-separated b-jets, comparing different b-jet definitions.

We now present the pseudorapidity of the hardest b-jet in fig. 7.6. In this case, the observable is integrated over the whole transverse momentum spectrum, resulting in a more homogeneous behaviour than the one observed in $p_{T,b}^{(\mathrm{hard})}$. Specifically, the difference bewteen the EXP prediction and the other three turn into a uniform $\sim +20\%$ offset over the full range of pseudorapidities. The small differences between the Naive, FD, and INF predictions are now completely absent, as they were visible only in the tail of $p_{T,b}^{(\mathrm{hard})}$, corresponding to a cross-section $\sim 4-5$ magnitude order lower than the peak. The same uniform behaviour characterises the scale uncertainties, which are around $-20\% + 25\%$ throughout the whole spectrum.

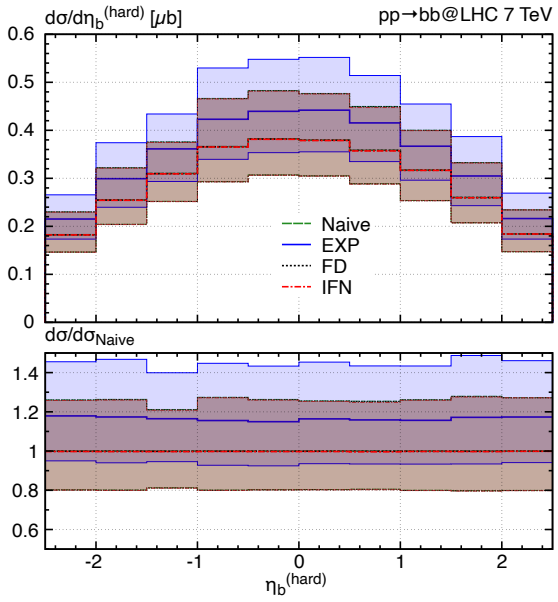

Figure 7.6: Pseudorapidity of the hardest b-jet, comparing different b-jet definitions.

7.2.3 $b\bar{b}$-Dijet Observables

We can now consider some observables defined on the di-b-jet system. To start off with, we present the di-b-jet transverse momentum in fig. 7.7. In this case, we observe that all the different predictions are essentially compatible, with the EXP calculation being only slightly above the Naive and the FD ones, and the IFN curve slightly below them. In general, this observable requires a $b\bar{b}$ pair recoiling against at least one hard gluon. As this scenario can occur only within the GSP and the FEX channels at the lowest order, so at $O(\alpha_s^3)$, MiNNLO$_{\text{PS}}$ will effectively provide NLO accuracy. This is confirmed by the relatively large size of the uncertainty bands, which makes them compatible with the uncertainties of a standard NLO calculation for the $b\bar{b}$ hadroproduction. Moreover, the hard $b\bar{b}$ pair has to be separated enough to produce two hard b-jets, thus suppressing the logarithmic enhancement that we observed in the EXP result of fig. 7.4. Within the EXP calculation, a hard b-jet could also appear whenever the parton shower induces a $g \to b\bar{b}$ slitting on the Born-level gluon of the $b\bar{b}g$ phase space. In this case, the gluon would originate a EXP b-jet, that can eventually belong to the di-b-jet system and give a contribution to fig. 7.7.

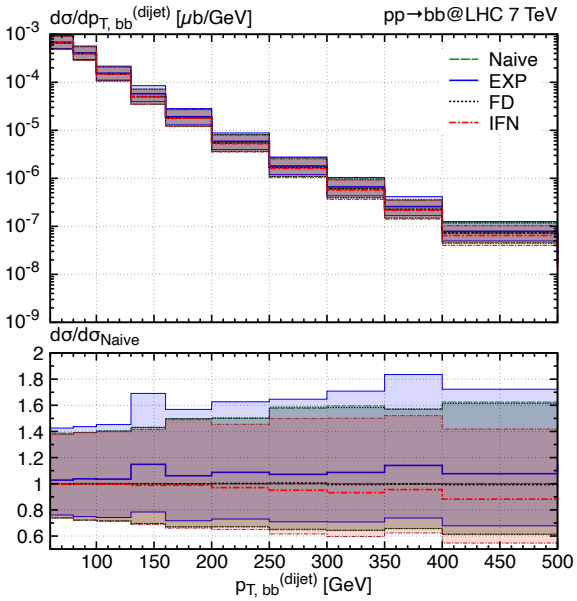

Figure 7.7: Di-b-jet transverse momentum, comparing different b-jet definitions.

At last, we consider the invariant mass of the di-b-jet system, in fig. 7.8. As this observable can receive $\mathcal{O}(\alpha_s^2)$ contributions from the FCR channel, the MiNNLO$_{\text{PS}}$ prediction effectively yields NNLO accuracy. This can also be understood by looking at the size scale variation bands, which is around $\pm 10\%$ for all the reported predictions, thus fully compatible with a standard $pp \to b\bar{b} + X$ NNLO calculation. Again, we observe a deviation of the EXP curve from the other predictions, mainly due to the different treatment of the GSP channel discussed above. Indeed, as we already commented, a scenario that can have an impact on the EXP calculation is a hard gluon originating a b-jet through the parton shower, recoiling against a quasi-collinear $b\bar{b}$ pair that is also identified with a b-jet. This effect, however, only comes to place starting from the NLO correction to the process.

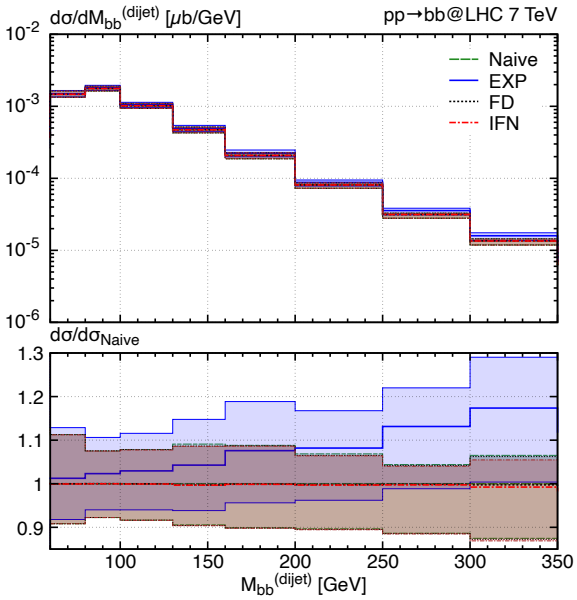

Figure 7.8: Invariant mass of the Di-b-jet system, comparing different b-jet definitions.

7.3 Comparison with Data from the ATLAS Collaboration

We will now present a comparison of the MiNLO' and MiNNLO$_{\text{PS}}$ b-jet productions predictions with experimental data from ATLAS, CMS and LHCb. For details about the setup of the calculation, we refer the reader to section 7.2.1. To define the flavour of jets, we adopted the EXP definition, where the any-flavour recombination scheme applied on anti-k_T jets allowed us to simulate the results of the experimental analyses.

7.3.1 Inclusive b-jet and Di-b-jet Production at $\sqrt{s} = 7$TeV

To start off with, we consider the measurements carried out by the ATLAS collaboration. First, we examine a set of results for the inclusive b-jet and di-b-jet production at $\sqrt{s} = 7$TeV [193]. Events from RUN-1 have been used in the analysis, corresponding to an integrated luminosity $34\,pb^{-1}$. B hadrons inside jets have been reconstructed by applying two different and independent techniques:

- A *lifetime-based method*, where long-lived B hadrons are identified by looking at the secondary vertices (SV) of their decay, which are generally significantly displaced from the primary vertex (PV) of the hard interactions. The SV is obtained by studying the invariant mass of the B hadron charged decay products, within the SV0 algorithm [194].
- A *muon-based method*, where the presence of muons is linked to the semileptonic decays of B hadrons.

We will not dive more into the details of the experimental techniques involved for the track identification and the vertex reconstruction, as they do not play an important role in our

analysis. For more information on the matter, we refer the reader to Ref. [193]. Regarding the b-jet definition, we mention that identified tracks have been clustered with the anti-k_T algorithm, using a jet radius parameter $R = 0.4$. Reconstructed B hadron have been required to have $p_T > 5$GeV, and to be found within $\Delta R = \sqrt{\Delta\phi^2 + \Delta\eta^2} = 0.3$ of the jet axis they are assigned to. Two different measurements have been performed: one of the inclusive b-jet transverse momentum distributions, and one on some di-b-jet observables. In the inclusive b-jet analysis, all identified b-jets have been used to populate the bins of the measured transverse momentum differential cross-section, while the di-b-jet observables have been obtained by taking the hardest and the second-hardest b-jets in each event with at least two identified b-jets. The fiducial cuts adopted in the two analyses are reported in table 7.2. A comparison with theoretical predictions has also been performed. POWHEG+Pythia and MC@NLO+Herwig have been used to get NLO+PS calculations, and a third prediction was obtained within Pythia standalone, after a proper normalization. In general, a good agreement was found between the predictions and the measurements, for all the studied observables. The only exception to this picture was noticed when looking at the MC@NLO predictions for the inclusive b-jet analysis. We quote from the conclusions of Ref. [193]: "MC@NLO + Herwig, however, predicts a significantly different behaviour of the double-differential cross section that is not observed in the data".

Setup of the ATLAS b-jet analysis at $\sqrt{s} = 7$TeV	
Anti-k_T clustering with $R = 0.4$,	
B hadrons with $p_T > 5$GeV and $\Delta R < 0.3$	
inclusive b-jets	$20\text{GeV} \leq p_{\text{T}}^{\text{b-jet}} \leq 200\text{GeV}$
analysis	$\lvert y^{\text{b-jet}} \rvert \leq 2.1$
di-b-jet	$p_{\text{T}}^{\text{b-jet}} \geq 40\text{GeV}$
analysis	$\lvert y^{\text{b-jet}} \rvert \leq 2.1$
	$110\text{GeV} \leq m_{ij} \leq 760\text{GeV}$

Table 7.2: Setup of the ATLAS b-jet analysis at $\sqrt{s} = 7$TeV at ATLAS. In the upper panel, the b-jet definition. In the middle panel, the fiducial cuts on the inclusive b-jet analysis. In the lower panel, the fiducial cuts on the di-b-jet analysis.

We present now the results we obtained in MiNLO' and MiNNLO$_{\text{PS}}$. In fig. 7.9, we compared with measurements of the inclusive b=jet transverse momentum, within different rapidity regions. In this setup, the MiNLO' and MiNNLO$_{\text{PS}}$ central predictions differ by a factor $\sim 5 - 10\%$, the difference becoming slightly in the P_T tails. In terms of uncertainty bundles, their size is $\mathcal{O}(\pm 25\%)$ in MiNLO' and $\mathcal{O}(\pm 20\%)$ in MiNNLO$_{\text{PS}}$. We observe a really good agreement between our predictions and the experimental data. In fig. 7.10, we show the results for the transverse momentum distribution integrated over the full fiducial rapidity range $y_{\text{b-jet}} < 2.1$. The considerations we can make here are fully analogous to

the ones holding for the results in different rapidity bins. We just remark on how theoretical uncertainties are still much larger than data relative errors, the latter ones being about $\pm 15\%$ in fig. 7.10. A somewhat different picture emerges when looking at the invariant mass of the di-b-jet system, in fig. 7.11. Here, MiNLO' and MiNNLO$_{\rm PS}$ present evident differences. In terms of normalization, MiNNLO$_{\rm PS}$ provides a $\sim 30\%$ flat correction on the MiNLO' prediction, and we observe a reduction of the scale uncertainties from $\mathcal{O}(\pm 20\%)$ (in MiNLO') down to $\mathcal{O}(\pm 10\%)$ (in MiNNLO$_{\rm PS}$). On the other hand, data are affected by quite large errors, and they are agree with theorectical predictions. In this sense, we remark that MiNNLO$_{\rm PS}$ improves the description of measurements, compared to MiNLO'.
The reason behind this peculiar behaviour might lie in the setup differences between the inclusive b-jet and the di-b-jet calculations. Indeed, while hard events with a quasi-collinear emission of a $b\bar{b}$ pair contribute to the transverse momentum distributions, high invariant mass values of the di-b-jet system require two well distinguished b-jets and receive sizeable contributions from the $b\bar{b}$ back-to-back emission. In the former case, MiNLO' and MiNNLO$_{\rm PS}$ provide the same accuracy, but in the latter case MiNNLO$_{\rm PS}$ effectively achieves NNLO accuracy.

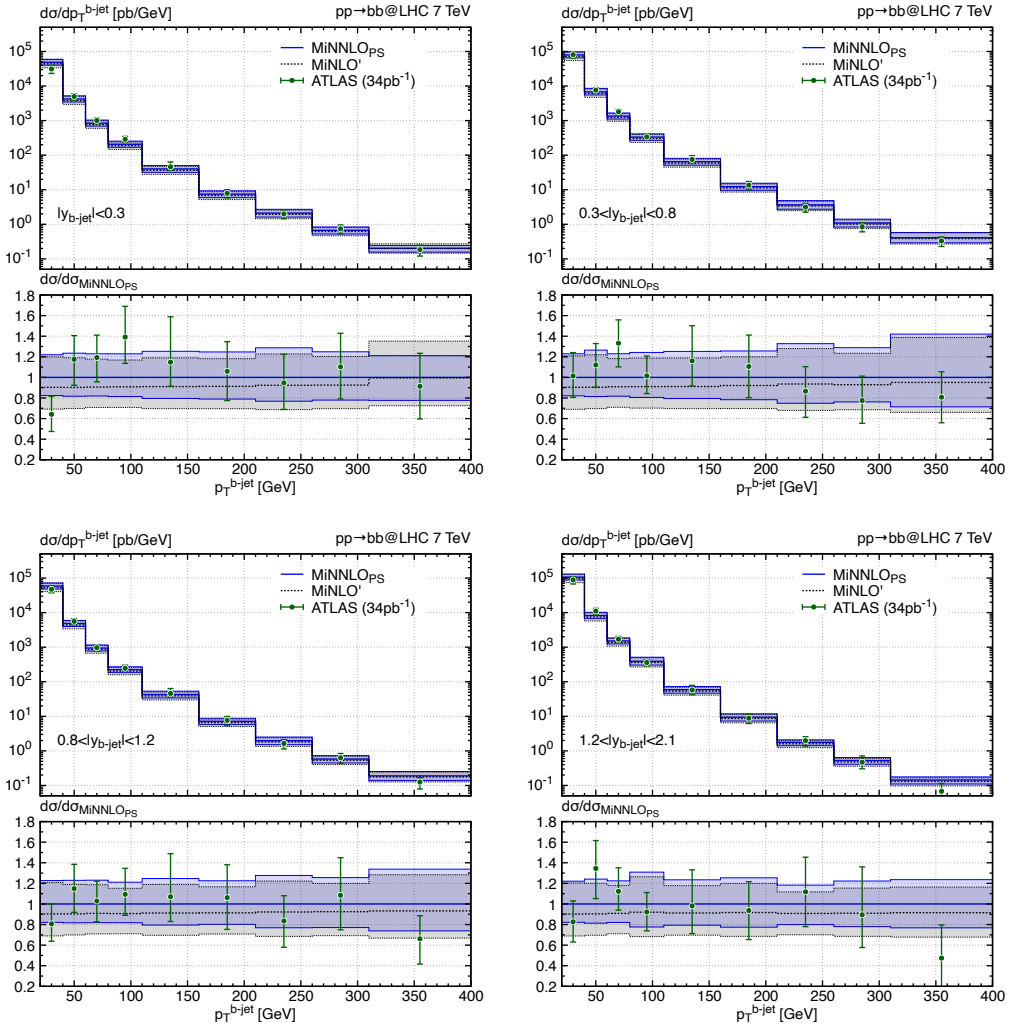

Figure 7.9: Comparison with ATLAS: Transverse momentum of inclusive b-jet, integrated over different ranges of $|y_{\text{b-jet}}|$ (specified on the bottom-left corner of the upper panels).

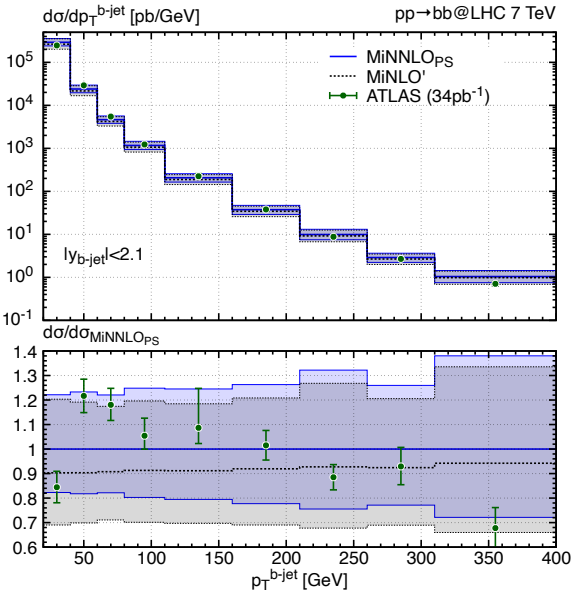

Figure 7.10: Comparison with ATLAS: Inclusive b-jet transverse momentum, integrated over the fiducial range of $|y_{\text{b-jet}}|$ (see table 7.2).

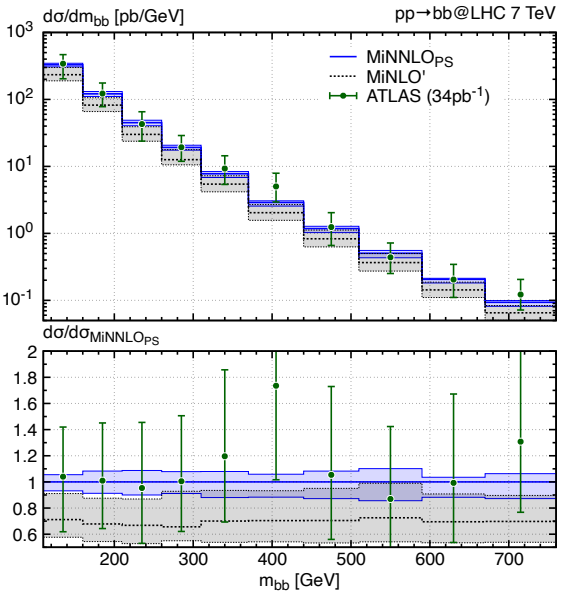

Figure 7.11: Comparison with ATLAS: Invariant mass of the di-b-jet system. The fiducial cuts are reported in table 7.2).

7.3.2 Di-b-jet Production in High-p_T Events at $\sqrt{s} = 7$TeV

We now consider the results of another interesting analysis carried out by the ATLAS collaboration [195]. In this case, the goal of the study was to measure a set of di-b-jet observables, in a quite exclusive setup. Events at a center-of-mass energy of $\sqrt{s} = 7$TeV have been considered, corresponding to an integrated luminosity of $4.2\, fb^{-1}$.
The setup used in this analysis appears quite peculiar and we are going to describe and comment on its motivations. In every event, all the identified tracks (including muons and neutrinos), as been clustered with the anti-k_T algorithm using a radius parameter of $R = 0.4$, which is standard at ATLAS. However, clustered events have been then selected by requiring their hardest jet to have a transverse momentum $p_T > 270$GeV. Notice that, at this point, no assumption is made on the flavour of the hardest jet, which might either be a b-jet or a light jet. Now a b-jet analysis is performed on the selected events. In particoular, b-jets are defined as jets containing at least one B hadron with a $p_T > 5$GeV and with a distance from the jet axis $\Delta R < 0.3$. Finally, b-jets must obey the following fiducial cuts. Each b-jet must have $p_T > 20$GeV and $|\eta| < 2.5$, and the relative distance between the hardest and second-hardest b-jets must be $\Delta R < 0.4$. Here we will not dive into the details of the B hadron experimental reconstruction procedure, for which we refer the reader to Ref. [195]. We just mention that the analysis is based on the reconstruction of the secondary vertices (SV) in B hadron decays, and employs a combination of the JetFitter and IP3D algorithms [196].
For the sake of clarity, the setup features detailed in the above are summarized in table 7.3. Given the fact that a really hard jet is required in the event selection, henceforth we will refer to this specific ATLAS analysis as the *High-p_T b-jet analysis*.

ATLAS b-jet definition and event selection in the high-p_T b-jet analysis at $\sqrt{s} = 7$TeV		
Jet clustering	anti-k_T with $R = 0.4$	
Event selection	Leading jet having $p_T > 270$GeV and $\|\eta\| < 3.2$;	
b-jet definition	B hadrons with $p_T > 5$GeV and $\Delta R < 0.3$;	
	b-jet cuts	$p_{T,b} > 20$GeV and $\|\eta_b\| < 2.5$
	di-b-jet cuts	$\Delta R_{bb} > 0.4$

Table 7.3: Setup of the ATLAS High-p_T b-jet analysis at $\sqrt{s} = 7$TeV.

If we want to understand what happens to di-b-jet observables, when we select events having a high transverse momentum leading jet, we must figure out how the configurations discussed in figs. 7.2a, 7.2b, 7.3a and 7.3b affect them. For most of the observables we will examine, the $b\bar{b}$ system will have to recoil against additional radiation, thus making the observables defined on a three-jet configuration. In these cases, there will be effectively no contribution from the FCR production channel at the leading order, and the formal ac-

curacy of MiNLO' and MiNNLO$_{\rm PS}$ will coincide, essentially reproducing the NLO QCD result. For other observables where the back-to-back production events will have an impact, the MiNNLO$_{\rm PS}$ results will provide NNLO accuracy. Moreover, the impact of the GSP configuration in the quasi-collinear $b\bar{b}$ emission will be also suppressed by the fiducial cuts required on the separation of the two hardest b-jets (see table 7.3). However, given the possible different behaviour of the di-b-jet observables, it is convenient to look at each one of them separately and see which of the considerations just discussed holds. We also mention that, in Ref. [195], data have been compared to POWHEG+PYTHIA and MC@NLO+Herwig, as well as the standalone Pythia and Herwig (after a proper normalization). Broadly speaking, the theoretical predictions faced difficulties in describing regions of phase space that are not dominated by two hard b-jets.

We present now the results of our comparison with the MiNLO' and the MiNNLO$_{\rm PS}$ results. In fig. 7.12, we show the dijet invariant mass distribution, denoted by m_{bb}. As we can see, the differential cross-section decreases of one magnitude order when going from small values of m_{bb} to $m_{bb} \sim 550$GeV. At this point, we encounter a threshold due to the fiducial cut of the leading jet transverse momentum. Indeed, this value corresponds to a local peak, located approximately at twice the value of the $p_T = 270$GeV cut. After these points, events that contribute can have two hard back-to-back b-jets originating from the FCR channel, which becomes the dominant one. To understand this point, we can write down the momenta of the two back-to-back b-quarks in the center-of-mass reference frame

$$P_b^\mu \;=\; \left(\sqrt{m_b^2 + |\vec{p}|^2}, \vec{p}\right) \;\approx\; \left(|\vec{p}|, \vec{p}\right), \tag{7.17}$$

$$P_{\bar{b}}^\mu \;=\; \left(\sqrt{m_b^2 + |\vec{p}|^2}, -\vec{p}\right) \;\approx\; \left(|\vec{p}|, -\vec{p}\right), \tag{7.18}$$

and their invariant mass will be given by the square root of $(P_b + P_{\bar{b}})^2$, namely

$$m_{b\bar{b}} \;\approx\; 2|\vec{p}|\,. \tag{7.19}$$

In this case, the lowest value of $|\vec{p}|$ admitted for FCR events passing the $p_T > 270$GeV fiducial cut is really the $|\vec{p}| = p_T = 270$GeV, corresponding to a back-to-back $b\bar{b}$ emission on a plane orthogonal to the beam axis. We can image the extra soft and collinear emissions to have a smearing effect on this picture, but still, we can explain the threshold effect at around twice the value of 270GeV.

The MiNLO' and MiNNLO$_{\rm PS}$ correctly predict the described behaviour. In fact, the two predictions essentially overlap at $m_{bb} \lesssim 400$GeV, while they consistently differ in the m_{bb} tail. In the low m_{bb} regions, they both provide the NLO accuracy guaranteed by merging with the $b\bar{b}+J$ Powheg generator, and are characterised by large scale uncertainties. In the tail of the distribution, the MiNNLO$_{\rm PS}$ uncertainties go down to $\mathcal{O}(\pm 15\%)$, and the central values of the two predictions differ by $\sim 30 - 40\%$. Data appear to be well described by MiNNLO$_{\rm PS}$ in the intermediate m_{bb} region, while some tensions are observed in the first two and in the last three bins of the distribution. However, we must observe that theoretical uncertainties are really large at low m_{bb}, while experimental uncertainties dramatically increase at high m_{bb}, making the quoted tensions not really conclusive in the present comparison.

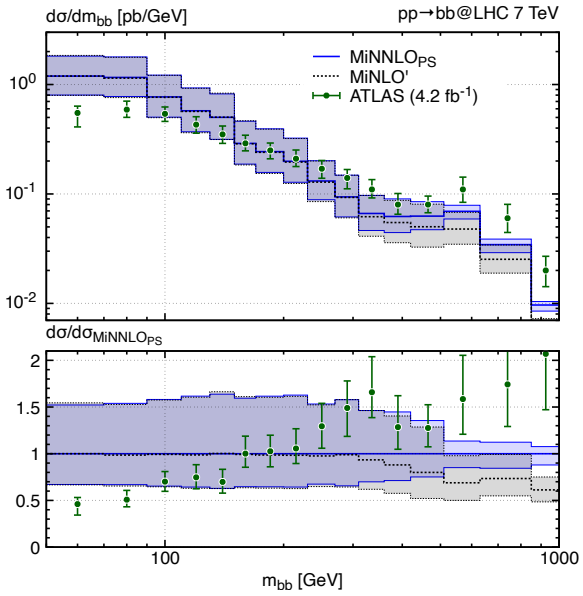

Figure 7.12: Comparison with ATLAS: invariant mass of the di-b-jet system in the high-p_T b-jet analysis.

We can now look at the differential cross-section as a function of the di-b-jet transverse momentum $p_{T,\,bb}$, reported in fig. 7.13. The distribution ranges from 0 to 400GeV and two peaks can be observed, a first one around 50GeV and a second one around 270GeV. The first peak can be interpreted as an effect of the fiducial cut on the transverse momentum of each identified b-jet, which must be harder than 20GeV. The second peak has a value corresponding to the cut on the hardest jet, and can be understood as follows. When it comes to high values of $p_{T,\,bb}$, the GSP channel is the dominant one, with a hard gluon recoiling against the $b\bar{b}$ pair. Indeed, the FCR channel can only have an impact at small values of $p_{T,\,bb}$, as the total momentum conservation imposes the system of two back-to-back bottom quark to have zero transverse momentum. In the GSP channel, for $p_{T,bb} < 270$GeV, the recoiling gluon will be forced to have a transverse momentum corresponding to $p_{T,bb}$, so that the selected events will need either b or $\bar{b}$ to be harder than 270GeV[11]. However, for $p_{T,bb} > 270$GeV, a threshold appears due to GSP events with a hard gluon that passes the fiducial cut, and can be clearly observed in the trend of data.
Regarding our predictions, we find that the two peaks are correctly predicted. Given that the GSP channel is the dominant one throughout almost the full range of the distribution, MiNLO' and MiNNLO$_{\rm PS}$ overlap almost everywhere, and are affected by quite large scale uncertainties compatible with an NLO calculation. Small differences can be observed at low $p_{T,bb}$, where the two predictions come to differ for $\sim 10\%$ and the MiNNLO$_{\rm PS}$ uncertainties shrink down to $\mathcal{O}(\pm 20\%)$. In general, data are well described by our predictions, although we observe a clear shape difference in the region 50GeV $< p_{T,bb} <$ 200GeV, where most of data are actually collected.

[11] this is valid, of course, only when neglecting higher order corrections to the GSP channel.

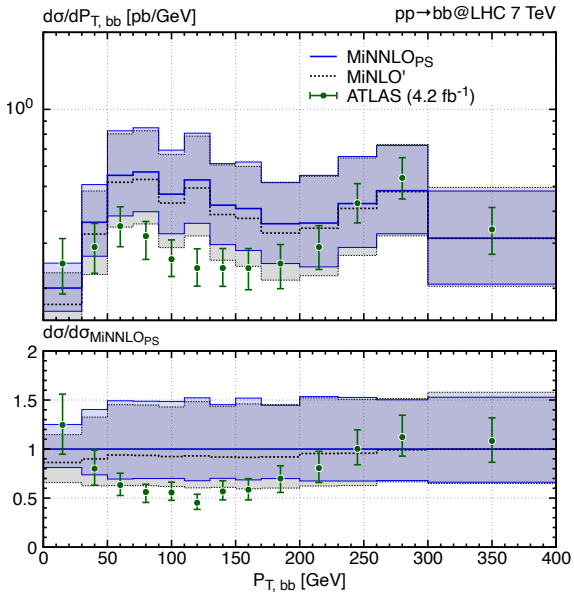

Figure 7.13: Comparison with ATLAS: tranverse momentum of the di-b-jet system in the high-p_T b-jet analysis.

We proceed by considering two observables related to the distance between the leading and the sub-leading b-jets, namely their azimuthal angle difference $\Delta\phi$ and their angular distance $\Delta R = \sqrt{(\Delta\phi)^2 + (\Delta\eta)^2}$. Also in this set of data, the double peak pattern observed above points to the transition from GSP to FCR-dominated regions. Indeed, small b-jet angular separations receive their main contributions from primary events where two close b quarks recoiled against a hard gluon, a configuration dominated by the GSP channel. Nevertheless, the more the b-jet separation increases, the more likely it is that events in the FCR channel give a contribution. This is proven by the presence of peaks at around $\Delta\phi = \pi$ and $\Delta R = 3$. Our theoretical predictions successfully reproduce the trend of data. For small b-jet separation values, MiNLO' and MiNNLO$_{\rm PS}$ showcase the same behaviour, as they retain NLO accuracy in the $b\bar{b} + J$ configurations. This is also manifest in the sizes of their scale uncertainty bands, that are here compatibles with the ones of an NLO calculation for bottom-pair hadroproduction. Towards the tails of the distributions, the perturbative accuracy of MiNNLO$_{\rm PS}$ increases and its prediction deviates from the one provided by MiNLO'. In general, we notice a good agreement between the measurements and our predictions, apart from some consistent discrepancies at low values of ΔR. Remarkably, MiNNLO$_{\rm PS}$ seems to improve the description of data for large values of $\Delta\phi$ and ΔR.

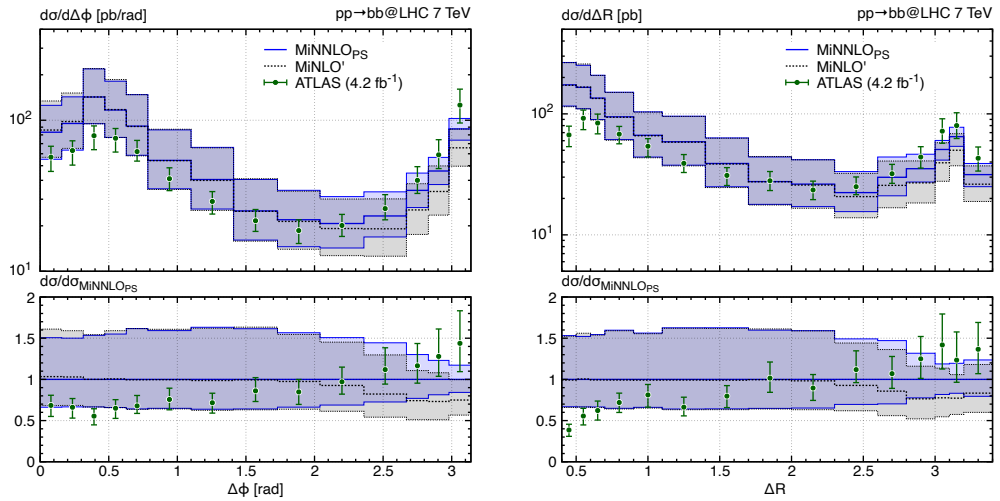

Figure 7.14: Comparison with ATLAS: differential cross-sections as a function of the azimuthal angle $\Delta\phi$ between the two hardest b-jets (left figure), and of their angular distance ΔR (right figure).

In fig. 7.15, we finally consider the differential distributions of the rapidity variables[12] $y_B = \frac{1}{2}|y_1 + y_2|$ and $y^* = \frac{1}{2}|y_1 - y_2|$. Notice that the former observable is effectively related to the boost of the di-b-jet system, and thus provides information on the kinematics of the initial-state partons. In general, both observables are dominated by the GSP channel contribution. As a consequence, no big differences can be spotted between the MiNLO' and the MiNNLO$_{\rm PS}$ predictions. For the same reasons explained above, these are affected by rather large theoretical uncertainties, making the comparison with data not really conclusive. However, we observe a good agreement between predictions and data, apart from deviations at high values of y_B.

[12]Where y_1 and y_2 are the rapidities of, respectively, the hardest and the second-hardest b-jets.

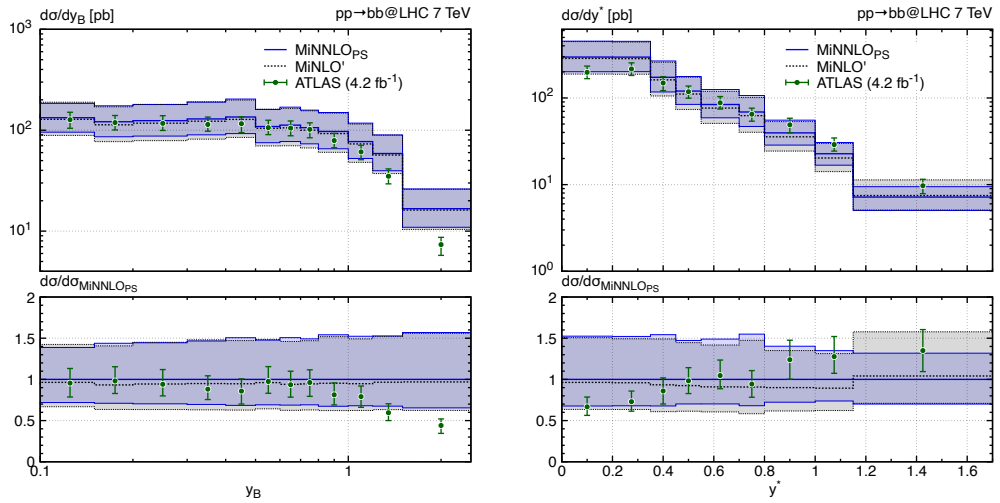

Figure 7.15: Comparison with ATLAS: differential cross-sections as a function of the rapidity variables $y_B = \frac{1}{2}|y_1 + y_2|$ (left figure) and $y^* = \frac{1}{2}|y_1 - y_2|$ (right figure).

7.4 Comparison with Data from the CMS Collaboration

Another study that we considered was a measurement of the inclusive b-jet production at $\sqrt{s} = 7$TeV, carried out by the CMS collaboration during Run-1 of the LHC [197]. The results were expressed in terms of differential cross-sections for the transverse momentum $p_T^{\text{b-jet}}$. The distributions presented are inclusive in the b-flavoured jets, meaning that every b-jet passing the fiducial cuts has been accounted for in the final result. No distinction has been made between b- and $\bar{b}$-jets.
Similarly to what wasdone by the ATLAS collaboration in [193], two independent analyses have been considered when performing the measurements:

- A *jet-analysis*, selecting events with at least one identified b-jet, on a sample at integrated luminosity of $34\,\text{pb}^{-1}$.
- A *muon-analysis*, selecting events having a b-jet in association with a muon, at an integrated luminosity of $3\,\text{pb}^{-1}$.

Although the two analyses differed both in terms of trigger selection and b-jet identification, they gave compatible results and were totally comparable in terms of the precisions of the two measurements. We only considered the results of the *jet-analysis* in comparing data with our theoretical predictions.
To reconstruct the jets in the events, a particle-flow algorithm [198] was employed, that identifies a list of tracks in each event. Tracks are then clustered with the anti-k_T algorithm, setting a radius $R = 0.5$. B-hadrons have been identified by reconstructing their secondary vertices (SV), where they decayed. Each b-jet was required to be associated with at least one SV. To compute the double differential inclusive b-jet cross-section, the following formula

was applied[13]

$$\frac{d^2\sigma}{dp_T\, dy} \sim \frac{N_{\text{tagged}}}{\Delta p_T\, \Delta y\, \mathcal{L}}\,, \tag{7.20}$$

which populates every (p_T, y) bin with the corresponding measured number of b- and $\bar{b}$-tagged jets N_{tagged}. Effectively, the cross-section is the sum of the b and $\bar{b}$ flavoured jet production. $\mathcal{L}$ is the integrated luminosity of the sample considered. Regarding the fiducial cuts, we reported the ones adopted by the *jet-analysis* in table 7.4.

CMS setup of the jet analysis at $\sqrt{s} = 7$TeV
Anti-k_T clustering with $R = 0.5$
At least one reconstructed B hadron (SV)
$18\text{GeV} \;\leq\; p_{\text{T}}^{\text{b-jet}} \;\leq\; 200\text{GeV}$
$\lvert y^{\text{b-jet}} \rvert \;\leq\; 2.2$

Table 7.4: Setup of the inclusive b-jet production measurements at $\sqrt{s} = 7$TeV at CMS, within the jet-analysis.

The double differential cross-section in rapidity and transverse momentum of the inclusive b-jet was then integrated over different rapidity ranges and compared to theoretical predictions obtained within the MC@NLO framework, and with PYTHIA. In fig. 7.16, we report the results for these distributions and compare data with predictions from MiNLO' and MiNNLO$_{\text{PS}}$. In table 7.5, we report the comparison for the fiducial cross-sections, integrated over $|y^{\text{b-jet}}| < 2.2$ and over two different ranges of $p_T^{\text{b-jet}}$.

Inclusive b-jet production cross-sections at CMS			
$p_T^{\text{b-jet}}$ range	Measured by CMS (μb)	MiNLO' (μb)	MiNNLO$_{\text{PS}}$ (μb)
$18\text{GeV} < p_T^{\text{b-jet}} < 200\text{GeV}$	$9.75.0 \pm 0.32_{(\text{stat})} \pm 1.67_{(\text{syst})} \pm 0.39_{(\text{lumi})}$	$9.3(7)^{+35.8\%}_{-24.4\%}$	$10.1(7)^{+20.4\%}_{-23.4\%}$
$32\text{GeV} < p_T^{\text{b-jet}} < 200\text{GeV}$	$1.73 \pm 0.07_{(\text{stat})} \pm 0.20_{(\text{syst})} \pm 0.07_{(\text{lumi})}$	$1.42(9)^{+31.6\%}_{-22.9\%}$	$1.55(7)^{+19.2\%}_{-23.4\%}$

Table 7.5: Comparison with CMS: Fiducial cross-sections for the inclusive b-jet production at $\sqrt{s} = 7$TeV, integrated over $|y^{\text{b-jet}}| < 2.2$ and different ranges of $p_T^{\text{b-jet}}$.

When considering the b-jet transverse momentum distributions, where we see how the cross-section decreases by more than four magnitude orders from the low $p_T^{\text{b-jet}}$ to the high $p_T^{\text{b-jet}}$ tails. This behaviour is correctly predicted by our calculations, which in general showcase a good agreement with data. At values of $p_T^{\text{b-jet}}$ lower than $\sim 100 - 120$GeV, the measurements fall within the MiNLO' and MiNNLO$_{\text{PS}}$ uncertainty bands. in the tails of

[13]For the sake of clarity, in eq. (7.20) we did not report some experimental ingredients like the b-tagging purity, the unfolding correction, and the efficiency. For a detailed explanation, we refer the reader to Ref. [197].

$p_T^{\text{b-jet}}$, it appears that the theory predicts a harder behaviour than the one experimentally observed. In these regions, while data are still covered by the MiNLO' bundles, they fall below the MiNNLO$_{\text{PS}}$ minima. However, it must be noticed that there is still an overlap between the upper experimental errors and the lower MiNNLO$_{\text{PS}}$ uncertainty bands, which are in general big. Regarding MiNLO' and the MiNNLO$_{\text{PS}}$ compare, we see they essentially differ by a flat K-factor, being the MiNLO' central values $\sim 10\%$ lower than MiNNLO$_{\text{PS}}$ throughout the whole $p_T^{\text{b-jet}}$ spectrum, in all rapidity ranges. In terms of uncertainties, MiNNLO$_{\text{PS}}$ does not bring a dramatic improvement. In fact, we pass from MiNLO' uncertainties of $\mathcal{O}(\pm 25\%)$ to MiNNLO$_{\text{PS}}$ uncertainties of $\mathcal{O}(\pm 20\%)$.

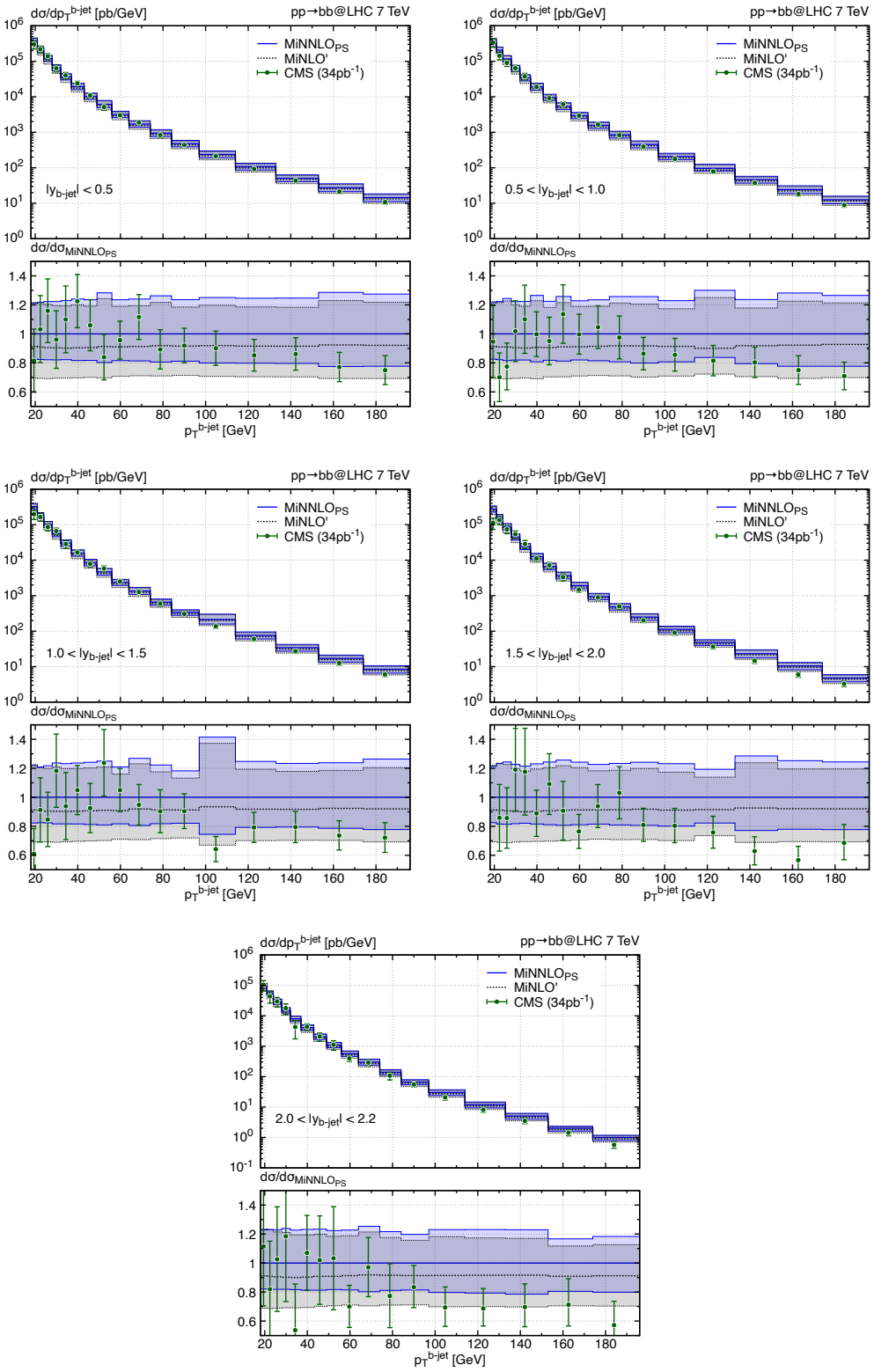

Figure 7.16: Comparison with CMS: inclusive b-jet transverse momentum distributions, integrated over different $|y^{\text{b-jet}}|$ regions.

7.5 Comparison with Data from the LHCb Collaboration

The last experimental results that we will discuss are from a study carried out by the LHCb collaboration [199], based on the analysis of events at $\sqrt{s} = 13$TeV and integrated luminosity of $1.6\, fb^{-1}$. Here, the inclusive di-b-jet and di-c-jet production in the forward region was considered, and measurements were expressed as differential distributions of the transverse momentum and of the pseudorapidity of the leading jet, of the rapidity difference between the jets, and of the dijet invariant mass. As the focus of this thesis is on the bottom-pair production phenomenology, we will show theoretical predictions for the di-b-jet observables, and leave the understanding of di-c-jet observables to future studies.
In this experimental analysis, jets have been identified by clustering particle flow objects with the anti-k_T algorithm, setting a jet radius parameter of $R = 0.5$. After requiring the jet components to obey some kinematical criteria[14], conceived to optimize the rejection of *fake jets*, a heavy-flavour jet-tagging algorithm (referred to as "SV-tagging"[201]) has been employed to assign flavour to jets. To select events, a set of fiducial cuts of the single b-jet transverse momentum and rapidity, and on the azimuthal opening of the dijet system have been applied and are reported in table 7.6.

Setup of the LHCb b-jet analysis at $\sqrt{s} = 13$TeV	
Jet clustering	anti-k_T with $R = 0.5$
b-jet cuts	$p_T(j_0), p_T(j_1) > 20$GeV
	$2.2 < \eta(j_0), \eta(j_1) < 4.2$
di-b-jet cuts	$\lvert\Delta\phi_{j_0 j_1}\rvert > 1.5$

Table 7.6: Setup of the LHCb b-jet analysis at $\sqrt{s} = 13$TeV. j_0 labels the leading b-jet and j_1 the sub-leading one.

In Ref. [199], measurements have been compared to theoretical predictions obtained within two different frameworks. In one case, NLO+PS calculations have been obtained by using MC@NLO interfaced with PYTHIA, and in the other PYTHIA was run to get LO results. It was observed that measurements were generally below the predictions, although the large theoretical uncertainties prevented from driving to conclusions.
We now present the results of our comparison with MiNLO' and MiNNLO$_{\rm PS}$. In fig. 7.17 we report two differential distributions for the hardest b-jet, namely its transverse momentum and pseudorapidity. In fig. 7.18, we report the invariant mass m_{ij} of the di-b-jet system and the differential distribution for the observable $\Delta y^*_{ij} = \frac{1}{2}|y_i - y_j|$[15].
When looking at these distributions, what appears evident is the large discrepancy in the normalization of the MiNLO' and MiNNLO$_{\rm PS}$ central curves, compared to the data normalization. While the MiNLO' result is still compatible at its lower uncertainty band with the data, the quite significant NNLO QCD corrections of +20–30% induced by MiNNLO$_{\rm PS}$

[14] See [200].
[15] y_i and y_j denote the rapidities of the leading and of the sub-leading b-jets.

lead to a facor ~ 2 difference between data and MiNNLO$_{\rm PS}$ prediction. We remark that the MiNLO' calculation is fully comparable with the behaviour observed in the NLO+PS prediction from MC@NLO reported in fig. 7.17, and that the MiNNLO$_{\rm PS}$ result represents the first NNLO+PS prediction ever compared to this set of data. For the time being, we did not achieve a clear explanation for these discrepancies, which might lie in the experimental analysis or in a statistical fluctuation downwards of the data. Otherwise, new-physics effects might be responsible for it.

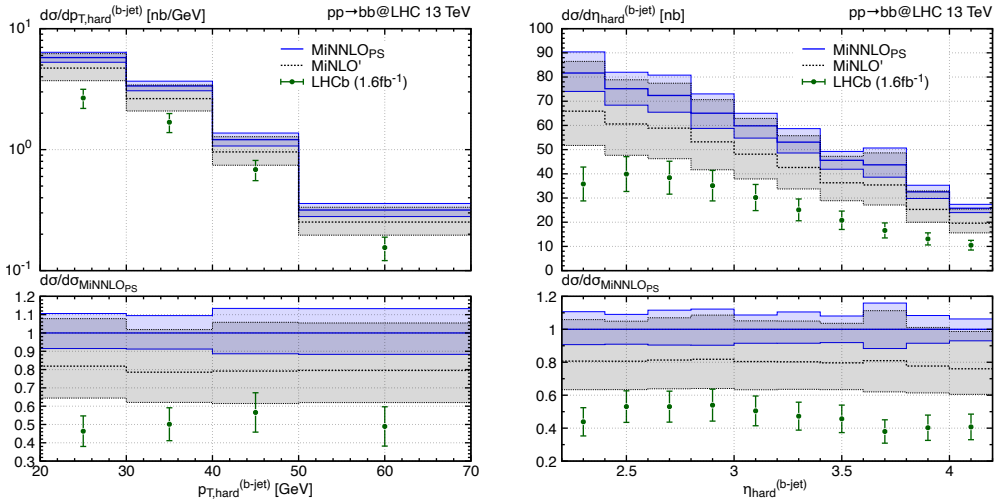

Figure 7.17: Comparison with LHCb: Differential cross-sections as function of the hardest b-jet transverse momentum (left figure), and of its pseudorapidity (right figure).

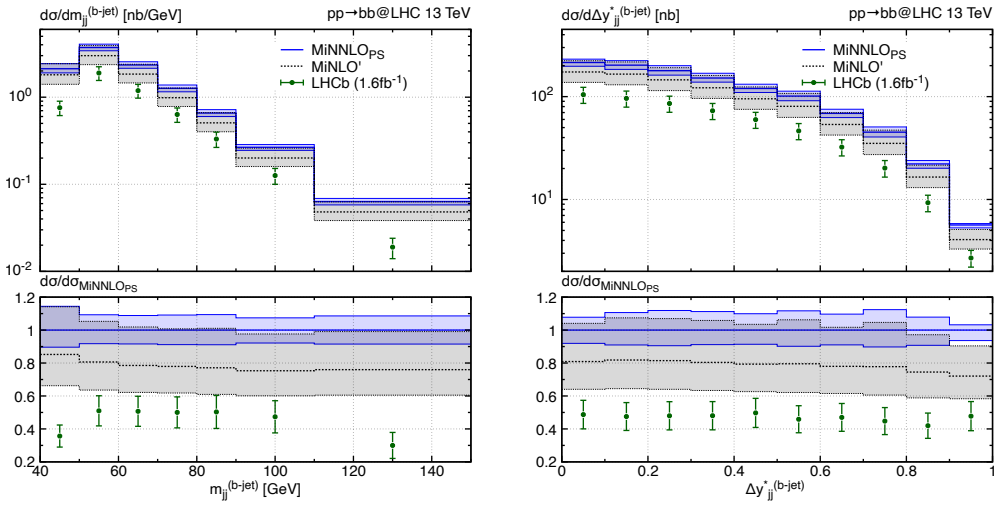

Figure 7.18: Comparison with LHCb: Differential cross-sections as function of the di-b-jet invariant mass (left figure), and of $\Delta y^*_{ij} = \frac{1}{2}|y_i - y_j|$ (right figure).

Chapter 8

Conclusions

In this thesis, we presented the results of our phenomenological studies on the bottom-pair production process at the LHC. Our predictions have been obtained within the POWHEG framework, after implementing the MiNNLO$_{\rm PS}$ prescriptions. This allowed us to consistently match the generated events with the *Pythia* GPMC program, achieving for the first time in literature NNLO+PS accuracy on the observables inclusive over extra QCD emissions in the $b\bar{b}$ phase-space.

To introduce the tools that we employed, we devoted the first part of the thesis to reviewing their underlying theory. In chapter 2, we summarized the main features of the fixed order computations in QCD, with particular emphasis on the next-to-leading order predictions. In chapter 3, we presented the basics of parton showers, and the POWHEG matching between NLO QCD and parton showers was broadly reviewed. Finally, we discussed the derivation of the MiNLO' and MiNNLO$_{\rm PS}$ method, as in their first application to the color-singlet production in hadronic collisions. In chapter 4, we introduced the concept of hadronic jets and summarized some of the most widespread clustering algorithms used to study jet phenomenology in modern colliders.

Our novel implementation of the bottom-pair production in MiNNLO$_{\rm PS}$ was detailed in chapter 5, after recalling the recent extension of the MiNNLO$_{\rm PS}$ method to the heavy quark pair production at the LHC. Our starting point was the implementation of the $pp \to b\bar{b}+$jet process in POWHEG-BOX-RES. To validate our program, we performed a comparison at fixed order against results obtained within the MATRIX framework, considering exclusive observables over the leading light-jet emission. We then followed the MiNNLO$_{\rm PS}$ implementation of the top-pair production process originally realized in POWHEG-BOX-V2, to design our MiNNLO$_{\rm PS}$ $b\bar{b}$ code in POWHEG-BOX-RES. The calculations were carried out in the four-flavour scheme, setting the bottom quark mass to its pole value $m_b = 4.92$GeV. Also in this case, we compared our results to the NNLO predictions from MATRIX, considering inclusive observables over the $b\bar{b}$ phase space. We witnessed a perfect agreement between MiNNLO$_{\rm PS}$ and the NNLO distributions, both in terms of central values and theoretical scale uncertainties. Moreover, we observed a remarkable improvement from MiNLO' to MiNNLO$_{\rm PS}$, with a reduction of the scale uncertainties from about $\pm 25\%$ in the former case to about $\pm 10 - 15\%$ in the latter.

In chapter 6, we exploited the bottom-pair production events generated at the center-of-mass energies of $\sqrt{s} = 7$TeV and $\sqrt{s} = 13$TeV to obtain predictions for several B-hadron production observables. We carried out an extensive comparison of our results with measurements published by the ATLAS, CMS, and LHCb collaborations during RUN-1 and RUN-2 of the LHC. The POWHEG interface with PYTHIA8 was used to simulate both the parton shower and hadronization effects, within the Lund string Model in the MONASH2013

tune. In this way, we obtained the first NNLO+PS calculations available in literature for these kinds of observables. In general, we observed a remarkable agreement between the MiNNLO$_{\rm PS}$ results and the experimental data, apart from some tensions that we observed in the inclusive $pp \to b\bar{b} + X$ measurements at LHCb.

In chapter 7, we focused on the phenomenology of b-jets originating from the $pp \to b\bar{b} + X$ hard events. To this extent, we reviewed two of the most recent infrared-safe clustering algorithms designed to deal with heavy flavoured jets, namely the *Flavour dressing* and the *Interleaved flavour neutralisation* (*IFN*). We then analyzed the impact of four different b-jet definitions on a set of hardest b-jet and di-b-jet observables. Specifically, the predictions that we compared were obtained by adopting the anti-k_T jet clustering and defining the b flavour according to: the *any-flavour* recombination scheme (for the predictions labeled **EXP**); the *flavour modulo-2* scheme (**Naive**); the flavour dressing equipped with the flavour modulo-2 prescriptions (**FD**); the IFN method in the flavour modulo-2 recombination scheme (**IFN**). Also in this case, we interfaced Powheg with Pythia8 to obtain hadron-level events, and we used the FastJet package routines to perform the anti-k_T clustering on events.

In general, the hardest b-jet distributions displayed evident discrepancies between the **EXP** predictions and the other three, increasing with b-jet transverse momentum. On the other hand, small differences were observed between the **Naive**, **FD**, and **IFN** results. The reason for this behavior can be consistently explained by considering the impact of the logarithmic enhancement due to the quasi-collinear $b\bar{b}$ emissions produced in the *gluon-splitting* and *flavour-excitation* channels of the $b\bar{b}g$ production, and by the parton shower $g \to b\bar{b}$ splittings. While these configurations contribute to the b-jet production in the **EXP** scheme, they do not enter calculations involving the flavour modulo-2 recombination scheme. All four schemes produced compatible results for the di-b-jet observables, requiring two well-separated b-tagged jets.

Finally, we compared our MiNNLO$_{\rm PS}$ b-jet predictions against experimental data from the ATLAS, CMS, and LHCb collaborations. We observed very good agreement between our calculations and the experimental results in the inclusive b-jet observables, as measured by ATLAS and CMS. In the comparison with the ATLAS analysis with a large fiducial cut on the transverse momentum of the leading-jet, we observed some tensions in specific ranges of the phase-space. In this particular setup, however, we could not claim exact NNLO accuracy, as we essentially achieved NLO accuracy for most observables. A large offset was instead observed in the comparison with the LHCb differential cross-sections at $\sqrt{s} = 13$TeV, whose origins will be the subject of future investigations.

Finally, we would like to discuss some recent developments and possible outlooks of our work. The natural next step of our research is undoubtedly represented by the implementation of the charm-pair production process in MiNNLO$_{\rm PS}$. While this task might not be conceptually more involved than the bottom-pair production case, The relatively low value of the charm-quark pole mass ($m_c = 1.67$GeV) implies low values of the scales entering calculations, often giving rise to numerical instabilities. With a NNLO+PS event generator for this process, it will be possible to carry out new interesting phenomenological analyses, ultimately deepening our understanding of heavy quark production in high energy collisions. For example, it will be possible to compare with new interesting inclusive D-meson production measurements at the LHC[1]. Moreover, as pointed out in Ref. [165], ratio distributions at

[1] See, e.g., Ref. [202].

different center-of-mass energies for the charm-pair production can be employed to constrain the gluon PDF uncertainties at small x. Many relevant predictions can also be obtained for the inclusive c-jet hadroproduction, and ratios of b-jet and c-jet observables also find applications in BSM studies.

Finally, we would like to mention an important application of the $b\bar{b}$ and $c\bar{c}$ event generators beyond collider physics [203, 204]. When cosmic rays from deep space hit the earth's atmosphere, a vast number of collisions between the protons they carry and the atmospheric nuclei occur. These events, which can be effectively modeled as proton-proton collisions at high center-of-mass energies, are suitable to be simulated through the tools we explored in our thesis. Eventually, the collisions will produce high energetic B and D mesons, then decaying leptonically and giving rise to neutrino fluxes. In fact, this phenomenon represents a large background in cosmic neutrino searches carried out, e.g., by the IceCube experiment in Antarctica. Together with our NNLO+PS $b\bar{b}$ event generator, a MiNNLO$_{\text{PS}}$ implementation of the $c\bar{c}$ production process will allow us to predict this *prompt atmospheric neutrino flux* at an unprecedented perturbative accuracy, possibly increasing the precision of cosmic neutrino measurements.

Bibliography

[1] F. Englert and R. Brout. Broken Symmetry and the Mass of Gauge Vector Mesons. *Phys. Rev. Lett.*, 13:321–323, 1964. doi: 10.1103/PhysRevLett.13.321.

[2] Peter W. Higgs. Broken Symmetries and the Masses of Gauge Bosons. *Phys. Rev. Lett.*, 13:508–509, 1964. doi: 10.1103/PhysRevLett.13.508.

[3] G. S. Guralnik, C. R. Hagen, and T. W. B. Kibble. Global Conservation Laws and Massless Particles. *Phys. Rev. Lett.*, 13:585–587, 1964. doi: 10.1103/PhysRevLett.13.585.

[4] John C. Collins, Davison E. Soper, and George F. Sterman. Factorization for Short Distance Hadron - Hadron Scattering. *Nucl. Phys. B*, 261:104–142, 1985. doi: 10.1016/0550-3213(85)90565-6.

[5] Javier Mazzitelli, Alessandro Ratti, Marius Wiesemann, and Giulia Zanderighi. B-hadron production at the LHC from bottom-quark pair production at NNLO+PS. *Phys. Lett. B*, 843:137991, 2023. doi: 10.1016/j.physletb.2023.137991.

[6] Michael E. Peskin and Daniel V. Schroeder. *An Introduction to quantum field theory*. Addison-Wesley, Reading, USA, 1995. ISBN 978-0-201-50397-5, 978-0-429-50355-9, 978-0-429-49417-8. doi: 10.1201/9780429503559.

[7] Gionata Luisoni and Simone Marzani. QCD resummation for hadronic final states. *J. Phys. G*, 42(10):103101, 2015. doi: 10.1088/0954-3899/42/10/103101.

[8] T. Kinoshita. Mass singularities of Feynman amplitudes. *J. Math. Phys.*, 3:650–677, 1962. doi: 10.1063/1.1724268.

[9] T. D. Lee and M. Nauenberg. Degenerate Systems and Mass Singularities. *Phys. Rev.*, 133:B1549–B1562, 1964. doi: 10.1103/PhysRev.133.B1549.

[10] Stefano Catani and Massimiliano Grazzini. Collinear factorization and splitting functions for next-to-next-to-leading order QCD calculations. *Phys. Lett. B*, 446:143–152, 1999. doi: 10.1016/S0370-2693(98)01513-5.

[11] Stefano Catani and Massimiliano Grazzini. Infrared factorization of tree level QCD amplitudes at the next-to-next-to-leading order and beyond. *Nucl. Phys. B*, 570:287–325, 2000. doi: 10.1016/S0550-3213(99)00778-6.

[12] Stefano Catani, Daniel de Florian, and German Rodrigo. Space-like (versus time-like) collinear limits in QCD: Is factorization violated? *JHEP*, 07:026, 2012. doi: 10.1007/JHEP07(2012)026.

[13] Guido Altarelli and G. Parisi. Asymptotic Freedom in Parton Language. *Nucl. Phys.*, B126:298–318, 1977. doi: 10.1016/0550-3213(77)90384-4.

[14] Yuri L. Dokshitzer. Calculation of the Structure Functions for Deep Inelastic Scattering and e+ e- Annihilation by Perturbation Theory in Quantum Chromodynamics. *Sov. Phys. JETP*, 46:641–653, 1977. [Zh. Eksp. Teor. Fiz.73,1216(1977)].

[15] V. N. Gribov and L. N. Lipatov. Deep inelastic e p scattering in perturbation theory. *Sov. J. Nucl. Phys.*, 15:438–450, 1972. [Yad. Fiz.15,781(1972)].

[16] Paolo Nason. A New method for combining NLO QCD with shower Monte Carlo algorithms. *JHEP*, 11:040, 2004. doi: 10.1088/1126-6708/2004/11/040.

[17] Stefano Frixione, Paolo Nason, and Carlo Oleari. Matching NLO QCD computations with Parton Shower simulations: the POWHEG method. *JHEP*, 11:070, 2007. doi: 10.1088/1126-6708/2007/11/070.

[18] Simone Alioli, Paolo Nason, Carlo Oleari, and Emanuele Re. A general framework for implementing NLO calculations in shower Monte Carlo programs: the POWHEG BOX. *JHEP*, 06:043, 2010. doi: 10.1007/JHEP06(2010)043.

[19] W. T. Giele, E. W. Nigel Glover, and David A. Kosower. Higher order corrections to jet cross-sections in hadron colliders. *Nucl. Phys. B*, 403:633–670, 1993. doi: 10.1016/0550-3213(93)90365-V.

[20] W. T. Giele, E. W. Nigel Glover, and David A. Kosower. The inclusive two jet triply differential cross-section. *Phys. Rev. D*, 52:1486–1499, 1995. doi: 10.1103/PhysRevD.52.1486.

[21] S. Frixione, Z. Kunszt, and A. Signer. Three jet cross-sections to next-to-leading order. *Nucl. Phys.*, B467:399–442, 1996. doi: 10.1016/0550-3213(96)00110-1.

[22] S. Catani and M.H. Seymour. A General algorithm for calculating jet cross-sections in NLO QCD. *Nucl. Phys.*, B485:291–419, 1997. doi: 10.1016/S0550-3213(96)00589-5.

[23] Zoltan Nagy and Davison E. Soper. General subtraction method for numerical calculation of one loop QCD matrix elements. *JHEP*, 09:055, 2003. doi: 10.1088/1126-6708/2003/09/055.

[24] G. Bevilacqua, M. Czakon, M. Kubocz, and M. Worek. Complete Nagy-Soper subtraction for next-to-leading order calculations in QCD. *JHEP*, 10:204, 2013. doi: 10.1007/JHEP10(2013)204.

[25] Renato Maria Prisco and Francesco Tramontano. Dual subtractions. *JHEP*, 06:089, 2021. doi: 10.1007/JHEP06(2021)089.

[26] Massimiliano Grazzini, Stefan Kallweit, and Marius Wiesemann. Fully differential NNLO computations with MATRIX. *Eur. Phys. J.*, C78(7):537, 2018. doi: 10.1140/epjc/s10052-018-5771-7.

[27] Stefano Frixione and Massimiliano Grazzini. Subtraction at NNLO. *JHEP*, 06:010, 2005. doi: 10.1088/1126-6708/2005/06/010.

[28] A. Gehrmann-De Ridder, T. Gehrmann, and E. W. Nigel Glover. Antenna subtraction at NNLO. *JHEP*, 09:056, 2005. doi: 10.1088/1126-6708/2005/09/056.

[29] James Currie, E. W. N. Glover, and Steven Wells. Infrared Structure at NNLO Using Antenna Subtraction. *JHEP*, 04:066, 2013. doi: 10.1007/JHEP04(2013)066.

[30] Gabor Somogyi, Zoltan Trocsanyi, and Vittorio Del Duca. Matching of singly- and doubly-unresolved limits of tree-level QCD squared matrix elements. *JHEP*, 06:024, 2005. doi: 10.1088/1126-6708/2005/06/024.

[31] Gabor Somogyi, Zoltan Trocsanyi, and Vittorio Del Duca. A Subtraction scheme for computing QCD jet cross sections at NNLO: Regularization of doubly-real emissions. *JHEP*, 01:070, 2007. doi: 10.1088/1126-6708/2007/01/070.

[32] Gabor Somogyi and Zoltan Trocsanyi. A Subtraction scheme for computing QCD jet cross sections at NNLO: Regularization of real-virtual emission. *JHEP*, 01:052, 2007. doi: 10.1088/1126-6708/2007/01/052.

[33] M. Czakon. A novel subtraction scheme for double-real radiation at NNLO. *Phys. Lett.*, B693:259–268, 2010. doi: 10.1016/j.physletb.2010.08.036.

[34] M. Czakon. Double-real radiation in hadronic top quark pair production as a proof of a certain concept. *Nucl. Phys.*, B849:250–295, 2011. doi: 10.1016/j.nuclphysb.2011.03.020.

[35] Charalampos Anastasiou, Kirill Melnikov, and Frank Petriello. A new method for real radiation at NNLO. *Phys. Rev.*, D69:076010, 2004. doi: 10.1103/PhysRevD.69.076010.

[36] Fabrizio Caola, Kirill Melnikov, and Raoul Röntsch. Nested soft-collinear subtractions in NNLO QCD computations. *Eur. Phys. J. C*, 77(4):248, 2017. doi: 10.1140/epjc/s10052-017-4774-0.

[37] Stefano Catani and Massimiliano Grazzini. An NNLO subtraction formalism in hadron collisions and its application to Higgs boson production at the LHC. *Phys. Rev. Lett.*, 98:222002, 2007. doi: 10.1103/PhysRevLett.98.222002.

[38] Radja Boughezal, Kirill Melnikov, and Frank Petriello. A subtraction scheme for NNLO computations. *Phys. Rev. D*, 85:034025, 2012. doi: 10.1103/PhysRevD.85.034025.

[39] Radja Boughezal, Christfried Focke, Xiaohui Liu, and Frank Petriello. W-boson production in association with a jet at next-to-next-to-leading order in perturbative QCD. *Phys. Rev. Lett.*, 115(6):062002, 2015. doi: 10.1103/PhysRevLett.115.062002.

[40] Radja Boughezal, Christfried Focke, Walter Giele, Xiaohui Liu, and Frank Petriello. Higgs boson production in association with a jet at NNLO using jettiness subtraction. *Phys. Lett.*, B748:5–8, 2015. doi: 10.1016/j.physletb.2015.06.055.

[41] Jonathan Gaunt, Maximilian Stahlhofen, Frank J. Tackmann, and Jonathan R. Walsh. N-jettiness Subtractions for NNLO QCD Calculations. *JHEP*, 09:058, 2015. doi: 10.1007/JHEP09(2015)058.

[42] Matteo Cacciari, FrÃ©dÃ©ric A. Dreyer, Alexander Karlberg, Gavin P. Salam, and Giulia Zanderighi. Fully Differential Vector-Boson-Fusion Higgs Production at Next-to-Next-to-Leading Order. *Phys. Rev. Lett.*, 115(8):082002, 2015. doi: 10.1103/PhysRevLett.115.082002.

[43] German F. R. Sborlini, Felix Driencourt-Mangin, and German Rodrigo. Four-dimensional unsubtraction with massive particles. *JHEP*, 10:162, 2016. doi: 10.1007/JHEP10(2016)162.

[44] Franz Herzog. Geometric IR subtraction for final state real radiation. *JHEP*, 08:006, 2018. doi: 10.1007/JHEP08(2018)006.

[45] L. Magnea, E. Maina, G. Pelliccioli, C. Signorile-Signorile, P. Torrielli, and S. Uccirati. Local analytic sector subtraction at NNLO. *JHEP*, 12:107, 2018. doi: 10.1007/JHEP12(2018)107. [Erratum: JHEP 06, 013 (2019)].

[46] Lorenzo Magnea, Ezio Maina, Giovanni Pelliccioli, Chiara Signorile-Signorile, Paolo Torrielli, and Sandro Uccirati. Factorisation and Subtraction beyond NLO. *JHEP*, 12:062, 2018. doi: 10.1007/JHEP12(2018)062.

[47] Zeno Capatti, Valentin Hirschi, Dario Kermanschah, and Ben Ruijl. Loop-Tree Duality for Multiloop Numerical Integration. *Phys. Rev. Lett.*, 123(15):151602, 2019. doi: 10.1103/PhysRevLett.123.151602.

[48] Lorenzo Magnea, Giovanni Pelliccioli, Chiara Signorile-Signorile, Paolo Torrielli, and Sandro Uccirati. Analytic integration of soft and collinear radiation in factorised QCD cross sections at NNLO. *JHEP*, 02:037, 2021. doi: 10.1007/JHEP02(2021)037.

[49] Gloria Bertolotti, Lorenzo Magnea, Giovanni Pelliccioli, Alessandro Ratti, Chiara Signorile-Signorile, Paolo Torrielli, and Sandro Uccirati. NNLO subtraction for any massless final state: a complete analytic expression. *JHEP*, 07:140, 2023. doi: 10.1007/JHEP07(2023)140. [Erratum: JHEP 05, 019 (2024)].

[50] Gloria Bertolotti, Paolo Torrielli, Sandro Uccirati, and Marco Zaro. Local analytic sector subtraction for initial- and final-state radiation at NLO in massless QCD. *JHEP*, 12:042, 2022. doi: 10.1007/JHEP12(2022)042.

[51] Torbjorn Sjostrand, Patrik Eden, Christer Friberg, Leif Lonnblad, Gabriela Miu, Stephen Mrenna, and Emanuel Norrbin. High-energy physics event generation with PYTHIA 6.1. *Comput. Phys. Commun.*, 135:238–259, 2001. doi: 10.1016/S0010-4655(00)00236-8.

[52] G. Corcella, I. G. Knowles, G. Marchesini, S. Moretti, K. Odagiri, P. Richardson, M. H. Seymour, and B. R. Webber. HERWIG 6: An Event generator for hadron emission reactions with interfering gluons (including supersymmetric processes). *JHEP*, 01:010, 2001. doi: 10.1088/1126-6708/2001/01/010.

[53] T. Gleisberg, Stefan. Hoeche, F. Krauss, M. Schonherr, S. Schumann, F. Siegert, and J. Winter. Event generation with SHERPA 1.1. *JHEP*, 02:007, 2009. doi: 10.1088/1126-6708/2009/02/007.

[54] Stefano Frixione and Bryan R. Webber. Matching NLO QCD computations and parton shower simulations. *JHEP*, 06:029, 2002. doi: 10.1088/1126-6708/2002/06/029.

[55] John C. Collins, Davison E. Soper, and George F. Sterman. Transverse Momentum Distribution in Drell-Yan Pair and W and Z Boson Production. *Nucl. Phys.*, B250: 199–224, 1985. doi: 10.1016/0550-3213(85)90479-1.

[56] S. Catani, L. Trentadue, G. Turnock, and B. R. Webber. Resummation of large logarithms in e+ e- event shape distributions. *Nucl. Phys.*, B407:3–42, 1993. doi: 10.1016/0550-3213(93)90271-P.

[57] Roberto Bonciani, Stefano Catani, Michelangelo L. Mangano, and Paolo Nason. Sudakov resummation of multiparton QCD cross-sections. *Phys. Lett. B*, 575:268–278, 2003. doi: 10.1016/j.physletb.2003.09.068.

[58] Melissa van Beekveld, Silvia Ferrario Ravasio, Gavin P. Salam, Alba Soto-Ontoso, Gregory Soyez, and Rob Verheyen. PanScales parton showers for hadron collisions: formulation and fixed-order studies. *JHEP*, 11:019, 2022. doi: 10.1007/JHEP11(2022)019.

[59] Melissa van Beekveld, Silvia Ferrario Ravasio, Keith Hamilton, Gavin P. Salam, Alba Soto-Ontoso, Gregory Soyez, and Rob Verheyen. PanScales showers for hadron collisions: all-order validation. *JHEP*, 11:020, 2022. doi: 10.1007/JHEP11(2022)020.

[60] Melissa van Beekveld et al. Introduction to the PanScales framework, version 0.1. 12 2023. doi: 10.21468/SciPostPhysCodeb.31.

[61] Melissa van Beekveld et al. A new standard for the logarithmic accuracy of parton showers. 6 2024.

[62] Bo Andersson, G. Gustafson, and B. Soderberg. A General Model for Jet Fragmentation. *Z. Phys. C*, 20:317, 1983. doi: 10.1007/BF01407824.

[63] Torbjorn Sjostrand. Jet Fragmentation of Nearby Partons. *Nucl. Phys. B*, 248:469–502, 1984. doi: 10.1016/0550-3213(84)90607-2.

[64] Peter Skands, Stefano Carrazza, and Juan Rojo. Tuning PYTHIA 8.1: the Monash 2013 Tune. *Eur. Phys. J. C*, 74(8):3024, 2014. doi: 10.1140/epjc/s10052-014-3024-y.

[65] Simone Alioli, Keith Hamilton, Paolo Nason, Carlo Oleari, and Emanuele Re. Jet pair production in POWHEG. *JHEP*, 04:081, 2011. doi: 10.1007/JHEP04(2011)081.

[66] Adam Kardos, Paolo Nason, and Carlo Oleari. Three-jet production in POWHEG. *JHEP*, 04:043, 2014. doi: 10.1007/JHEP04(2014)043.

[67] Tom Melia, Paolo Nason, Raoul Röntsch, and Giulia Zanderighi. W+W-, WZ and ZZ production in the POWHEG BOX. *JHEP*, 11:078, 2011. doi: 10.1007/JHEP11(2011)078.

[68] Paolo Nason and Giulia Zanderighi. W^+W^- , WZ and ZZ production in the POWHEG-BOX-V2. *Eur. Phys. J.*, C74(1):2702, 2014. doi: 10.1140/epjc/s10052-013-2702-5.

[69] Jonas M. Lindert, Daniele Lombardi, Marius Wiesemann, Giulia Zanderighi, and Silvia Zanoli. W$^{\pm}$Z production at NNLO QCD and NLO EW matched to parton showers with MiNNLO$_{PS}$. *JHEP*, 11:036, 2022. doi: 10.1007/JHEP11(2022)036.

[70] John M. Campbell, R. Keith Ellis, Rikkert Frederix, Paolo Nason, Carlo Oleari, and Ciaran Williams. NLO Higgs Boson Production Plus One and Two Jets Using the POWHEG BOX, MadGraph4 and MCFM. *JHEP*, 07:092, 2012. doi: 10.1007/JHEP07(2012)092.

[71] Barbara Jäger, F. Schissler, and D. Zeppenfeld. Parton-shower effects on Higgs boson production via vector-boson fusion in association with three jets. *JHEP*, 07:125, 2014. doi: 10.1007/JHEP07(2014)125.

[72] S. Catani, F. Krauss, R. Kuhn, and B. R. Webber. QCD matrix elements + parton showers. *JHEP*, 11:063, 2001. doi: 10.1088/1126-6708/2001/11/063.

[73] Keith Hamilton, Paolo Nason, Carlo Oleari, and Giulia Zanderighi. Merging H/W/Z + 0 and 1 jet at NLO with no merging scale: a path to parton shower + NNLO matching. *JHEP*, 05:082, 2013. doi: 10.1007/JHEP05(2013)082.

[74] Keith Hamilton, Paolo Nason, and Giulia Zanderighi. MINLO: Multi-Scale Improved NLO. *JHEP*, 10:155, 2012. doi: 10.1007/JHEP10(2012)155.

[75] Pier Francesco Monni, Paolo Nason, Emanuele Re, Marius Wiesemann, and Giulia Zanderighi. MiNNLO$_{\rm PS}$: A new method to match NNLO QCD to parton showers. *JHEP*, 05:143, 2020. doi: 10.1007/JHEP05(2020)143.

[76] Keith Hamilton, Tom Melia, Pier Francesco Monni, Emanuele Re, and Giulia Zanderighi. Merging WW and WW+jet with MINLO. *JHEP*, 09:057, 2016. doi: 10.1007/JHEP09(2016)057.

[77] Daniele Lombardi, Marius Wiesemann, and Giulia Zanderighi. Advancing MiNNLO$_{PS}$ to diboson processes: Zγ production at NNLO+PS. *JHEP*, 06:095, 2021. doi: 10.1007/JHEP06(2021)095.

[78] Daniele Lombardi, Marius Wiesemann, and Giulia Zanderighi. W$^+$W$^-$ production at NNLO+PS with MiNNLO$_{PS}$. *JHEP*, 11:230, 2021. doi: 10.1007/JHEP11(2021)230.

[79] Luca Buonocore, Gabriël Koole, Daniele Lombardi, Luca Rottoli, Marius Wiesemann, and Giulia Zanderighi. ZZ production at nNNLO+PS with MiNNLO$_{PS}$. *JHEP*, 01:072, 2022. doi: 10.1007/JHEP01(2022)072.

[80] Silvia Zanoli, Mauro Chiesa, Emanuele Re, Marius Wiesemann, and Giulia Zanderighi. Next-to-next-to-leading order event generation for VH production with $H \to b\bar{b}$ decay. *JHEP*, 07:008, 2022. doi: 10.1007/JHEP07(2022)008.

[81] Pier Francesco Monni, Emanuele Re, and Paolo Torrielli. Higgs Transverse-Momentum Resummation in Direct Space. *Phys. Rev. Lett.*, 116(24):242001, 2016. doi: 10.1103/PhysRevLett.116.242001.

[82] Wojciech Bizon, Pier Francesco Monni, Emanuele Re, Luca Rottoli, and Paolo Torrielli. Momentum-space resummation for transverse observables and the Higgs $p_\perp$ at N^{3}LL+NNLO. 2017.

[83] Pier Francesco Monni, Emanuele Re, and Marius Wiesemann. MiNNLO$_{\rm PS}$: optimizing $2 \to 1$ hadronic processes. *Eur. Phys. J. C*, 80(11):1075, 2020. doi: 10.1140/epjc/s10052-020-08658-5.

[84] Gavin P. Salam and Juan Rojo. A Higher Order Perturbative Parton Evolution Toolkit (HOPPET). *Comput. Phys. Commun.*, 180:120–156, 2009. doi: 10.1016/j.cpc.2008.08.010.

[85] Daniele Lombardi, Marius Wiesemann, and Giulia Zanderighi. Anomalous couplings in Zγ events at NNLO+PS and improving $\nu\bar{\nu}\gamma$ backgrounds in dark-matter searches. *Phys. Lett. B*, 824:136846, 2022. doi: 10.1016/j.physletb.2021.136846.

[86] Alessandro Gavardi, Carlo Oleari, and Emanuele Re. NNLO+PS Monte Carlo simulation of photon pair production with MiNNLO$_{PS}$. *JHEP*, 09:061, 2022. doi: 10.1007/JHEP09(2022)061.

[87] Ulrich Haisch, Darren J. Scott, Marius Wiesemann, Giulia Zanderighi, and Silvia Zanoli. NNLO event generation for $pp \to Zh \to \ell^+\ell^- b\bar{b}$ production in the SM effective field theory. *JHEP*, 07:054, 2022. doi: 10.1007/JHEP07(2022)054.

[88] Javier Mazzitelli, Pier Francesco Monni, Paolo Nason, Emanuele Re, Marius Wiesemann, and Giulia Zanderighi. Next-to-Next-to-Leading Order Event Generation for Top-Quark Pair Production. *Phys. Rev. Lett.*, 127(6):062001, 2021. doi: 10.1103/PhysRevLett.127.062001.

[89] Javier Mazzitelli, Pier Francesco Monni, Paolo Nason, Emanuele Re, Marius Wiesemann, and Giulia Zanderighi. Top-pair production at the LHC with MINNLO$_{PS}$. *JHEP*, 04:079, 2022. doi: 10.1007/JHEP04(2022)079.

[90] Markus Ebert, Luca Rottoli, Marius Wiesemann, Giulia Zanderighi, and Silvia Zanoli. Jettiness formulation of the MiNNLO$_{PS}$ method. *JHEP*, 07:085, 2024. doi: 10.1007/JHEP07(2024)085.

[91] Christian Biello, Aparna Sankar, Marius Wiesemann, and Giulia Zanderighi. NNLO+PS predictions for Higgs production through bottom-quark annihilation with MiNNLO$_{PS}$. *Eur. Phys. J. C*, 84(5):479, 2024. doi: 10.1140/epjc/s10052-024-12845-z.

[92] Marco Niggetiedt and Marius Wiesemann. Higgs-boson production in the full theory at NNLO+PS. 7 2024.

[93] Javier Mazzitelli, Vasily Sotnikov, and Marius Wiesemann. Next-to-next-to-leading order event generation for Z-boson production in association with a bottom-quark pair. 4 2024.

[94] D. J. Gross and Frank Wilczek. Asymptotically Free Gauge Theories - I. *Phys. Rev. D*, 8:3633–3652, 1973. doi: 10.1103/PhysRevD.8.3633.

[95] H. David Politzer. Asymptotic Freedom: An Approach to Strong Interactions. *Phys. Rept.*, 14:129–180, 1974. doi: 10.1016/0370-1573(74)90014-3.

[96] Andrea Banfi, Gavin P. Salam, and Giulia Zanderighi. Infrared safe definition of jet flavor. *Eur. Phys. J. C*, 47:113–124, 2006. doi: 10.1140/epjc/s2006-02552-4.

[97] Gavin P. Salam. Towards Jetography. *Eur. Phys. J. C*, 67:637–686, 2010. doi: 10.1140/epjc/s10052-010-1314-6.

[98] Klaus Rabbertz. *Jet Physics at the LHC: The Strong Force beyond the TeV Scale*, volume 268 of *Springer Tracts in Modern Physics*. Springer, Berlin, 2017. ISBN 978-3-319-42113-1, 978-3-319-42115-5. doi: 10.1007/978-3-319-42115-5.

[99] John E. Huth et al. Toward a standardization of jet definitions. In *1990 DPF Summer Study on High-energy Physics: Research Directions for the Decade (Snowmass 90)*, pages 0134–136, 12 1990.

[100] S. Chekanov. A New jet algorithm based on the k-means clustering for the reconstruction of heavy states from jets. *Eur. Phys. J. C*, 47:611–616, 2006. doi: 10.1140/epjc/s2006-02618-3.

[101] L. Angelini, P. De Felice, M. Maggi, G. Nardulli, L. Nitti, M. Pellicoro, and S. Stramaglia. Jet analysis by deterministic annealing. *Phys. Lett. B*, 545:315–322, 2002. doi: 10.1016/S0370-2693(02)02475-9.

[102] L. Angelini, G. Nardulli, L. Nitti, M. Pellicoro, D. Perrino, and S. Stramaglia. Deterministic annealing as a jet clustering algorithm in hadronic collisions. *Phys. Lett. B*, 601:56–63, 2004. doi: 10.1016/j.physletb.2004.09.024.

[103] D. Yu. Grigoriev, E. Jankowski, and F. V. Tkachov. Towards a standard jet definition. *Phys. Rev. Lett.*, 91:061801, 2003. doi: 10.1103/PhysRevLett.91.061801.

[104] D. Yu. Grigoriev, E. Jankowski, and F. V. Tkachov. Optimal jet finder. *Comput. Phys. Commun.*, 155:42–64, 2003. doi: 10.1016/S0010-4655(03)00291-1.

[105] W. Bartel et al. Experimental Studies on Multi-Jet Production in e+ e- Annihilation at PETRA Energies. *Z. Phys. C*, 33:23, 1986. doi: 10.1007/BF01410449.

[106] S. Bethke et al. Experimental Investigation of the Energy Dependence of the Strong Coupling Strength. *Phys. Lett. B*, 213:235–241, 1988. doi: 10.1016/0370-2693(88)91032-5.

[107] S. Catani, Yuri L. Dokshitzer, M. Olsson, G. Turnock, and B. R. Webber. New clustering algorithm for multi - jet cross-sections in e+ e- annihilation. *Phys. Lett. B*, 269:432–438, 1991. doi: 10.1016/0370-2693(91)90196-W.

[108] M. Wobisch and T. Wengler. Hadronization corrections to jet cross-sections in deep inelastic scattering. In *Monte Carlo generators for HERA physics. Proceedings, Workshop, Hamburg, Germany, 1998-1999*, pages 270–279, 1998.

[109] Matteo Cacciari, Gavin P. Salam, and Gregory Soyez. The anti-k_t jet clustering algorithm. *JHEP*, 04:063, 2008. doi: 10.1088/1126-6708/2008/04/063.

[110] George F. Sterman and Steven Weinberg. Jets from Quantum Chromodynamics. *Phys. Rev. Lett.*, 39:1436, 1977. doi: 10.1103/PhysRevLett.39.1436.

[111] G. Arnison et al. Hadronic Jet Production at the CERN Proton - anti-Proton Collider. *Phys. Lett. B*, 132:214, 1983. doi: 10.1016/0370-2693(83)90254-X.

[112] F. Abe et al. The Topology of three jet events in $\bar{p}p$ collisions at $\sqrt{s} = 1.8$ TeV. *Phys. Rev. D*, 45:1448–1458, 1992. doi: 10.1103/PhysRevD.45.1448.

[113] N. Brown and W. James Stirling. Jet cross-sections at leading double logarithm in e+ e- annihilation. *Phys. Lett. B*, 252:657–662, 1990. doi: 10.1016/0370-2693(90)90502-W.

[114] Stefano Catani. Jet topology and new jet counting algorithms. *Ettore Majorana Int. Sci. Ser. Phys. Sci.*, 60:21–41, 1992. doi: 10.1007/978-1-4615-3440-2_2.

[115] Garth Leder. Jet fractions in e+ e- annihilation. *Nucl. Phys. B*, 497:334–344, 1997. doi: 10.1016/S0550-3213(97)00240-X.

[116] Andrea Banfi, Gavin P. Salam, and Giulia Zanderighi. Principles of general final-state resummation and automated implementation. *JHEP*, 03:073, 2005. doi: 10.1088/1126-6708/2005/03/073.

[117] S. Catani, Yuri L. Dokshitzer, and B. R. Webber. The K^- perpendicular clustering algorithm for jets in deep inelastic scattering and hadron collisions. *Phys. Lett. B*, 285: 291–299, 1992. doi: 10.1016/0370-2693(92)91467-N.

[118] S. Catani, Yuri L. Dokshitzer, M. H. Seymour, and B. R. Webber. Longitudinally invariant K_t clustering algorithms for hadron hadron collisions. *Nucl. Phys.*, B406: 187–224, 1993. doi: 10.1016/0550-3213(93)90166-M.

[119] Stephen D. Ellis and Davison E. Soper. Successive combination jet algorithm for hadron collisions. *Phys. Rev.*, D48:3160–3166, 1993. doi: 10.1103/PhysRevD.48.3160.

[120] J. M. Butterworth, J. P. Couchman, B. E. Cox, and B. M. Waugh. KtJet: A C++ implementation of the K-perpendicular clustering algorithm. *Comput. Phys. Commun.*, 153:85–96, 2003. doi: 10.1016/S0010-4655(03)00156-5.

[121] Yuri L. Dokshitzer, G. D. Leder, S. Moretti, and B. R. Webber. Better jet clustering algorithms. *JHEP*, 08:001, 1997. doi: 10.1088/1126-6708/1997/08/001.

[122] Gerald C. Blazey et al. Run II jet physics. In *Physics at Run II: QCD and Weak Boson Physics Workshop: Final General Meeting*, pages 47–77, 5 2000.

[123] P. Nason, S. Dawson, and R. Keith Ellis. The Total Cross-Section for the Production of Heavy Quarks in Hadronic Collisions. *Nucl. Phys. B*, 303:607–633, 1988. doi: 10.1016/0550-3213(88)90422-1.

[124] P. Nason, S. Dawson, and R. Keith Ellis. The One Particle Inclusive Differential Cross-Section for Heavy Quark Production in Hadronic Collisions. *Nucl. Phys. B*, 327: 49–92, 1989. doi: 10.1016/0550-3213(89)90286-1. [Erratum: Nucl.Phys.B 335, 260–260 (1990)].

[125] W. Beenakker, H. Kuijf, W. L. van Neerven, and J. Smith. QCD Corrections to Heavy Quark Production in p anti-p Collisions. *Phys. Rev. D*, 40:54–82, 1989. doi: 10.1103/PhysRevD.40.54.

[126] Michelangelo L. Mangano, Paolo Nason, and Giovanni Ridolfi. Heavy quark correlations in hadron collisions at next-to-leading order. *Nucl. Phys. B*, 373:295–345, 1992. doi: 10.1016/0550-3213(92)90435-E.

[127] M. V. Garzelli, L. Kemmler, S. Moch, and O. Zenaiev. Heavy-flavor hadro-production with heavy-quark masses renormalized in the $\overline{\mathrm{MS}}$, MSR and on-shell schemes. *JHEP*, 04:043, 2021. doi: 10.1007/JHEP04(2021)043.

[128] Matteo Cacciari and Mario Greco. Large p_T hadroproduction of heavy quarks. *Nucl. Phys. B*, 421:530–544, 1994. doi: 10.1016/0550-3213(94)90515-0.

[129] B. Mele and P. Nason. The Fragmentation function for heavy quarks in QCD. *Nucl. Phys. B*, 361:626–644, 1991. doi: 10.1016/0550-3213(91)90597-Q. [Erratum: Nucl.Phys.B 921, 841–842 (2017)].

[130] Matteo Cacciari and Stefano Catani. Soft gluon resummation for the fragmentation of light and heavy quarks at large x. *Nucl. Phys. B*, 617:253–290, 2001. doi: 10.1016/S0550-3213(01)00469-2.

[131] B. A. Kniehl, G. Kramer, I. Schienbein, and H. Spiesberger. Inclusive D*+- production in p anti-p collisions with massive charm quarks. *Phys. Rev. D*, 71:014018, 2005. doi: 10.1103/PhysRevD.71.014018.

[132] B. A. Kniehl, G. Kramer, I. Schienbein, and H. Spiesberger. Collinear subtractions in hadroproduction of heavy quarks. *Eur. Phys. J. C*, 41:199–212, 2005. doi: 10.1140/epjc/s2005-02200-7.

[133] G. Kramer and H. Spiesberger. b-hadron production in the general-mass variable-flavour-number scheme and LHC data. *Phys. Rev. D*, 98(11):114010, 2018. doi: 10.1103/PhysRevD.98.114010.

[134] M. Benzke, B. A. Kniehl, G. Kramer, I. Schienbein, and H. Spiesberger. B-meson production in the general-mass variable-flavour-number scheme and LHC data. *Eur. Phys. J. C*, 79(10):814, 2019. doi: 10.1140/epjc/s10052-019-7326-y.

[135] Matteo Cacciari, Mario Greco, and Paolo Nason. The P(T) spectrum in heavy flavor hadroproduction. *JHEP*, 05:007, 1998. doi: 10.1088/1126-6708/1998/05/007.

[136] Matteo Cacciari, Stefano Frixione, and Paolo Nason. The p(T) spectrum in heavy flavor photoproduction. *JHEP*, 03:006, 2001. doi: 10.1088/1126-6708/2001/03/006.

[137] Matteo Cacciari and Paolo Nason. Is there a significant excess in bottom hadroproduction at the Tevatron? *Phys. Rev. Lett.*, 89:122003, 2002. doi: 10.1103/PhysRevLett.89.122003.

[138] Matteo Cacciari, Stefano Frixione, Nicolas Houdeau, Michelangelo L. Mangano, Paolo Nason, and Giovanni Ridolfi. Theoretical predictions for charm and bottom production at the LHC. *JHEP*, 10:137, 2012. doi: 10.1007/JHEP10(2012)137.

[139] V. G. Kartvelishvili, A. K. Likhoded, and V. A. Petrov. On the Fragmentation Functions of Heavy Quarks Into Hadrons. *Phys. Lett. B*, 78:615–617, 1978. doi: 10.1016/0370-2693(78)90653-6.

[140] C. Peterson, D. Schlatter, I. Schmitt, and Peter M. Zerwas. Scaling Violations in Inclusive e+ e- Annihilation Spectra. *Phys. Rev. D*, 27:105, 1983. doi: 10.1103/PhysRevD.27.105.

[141] Stefano Frixione, Paolo Nason, and Giovanni Ridolfi. A Positive-weight next-to-leading-order Monte Carlo for heavy flavour hadroproduction. *JHEP*, 09:126, 2007. doi: 10.1088/1126-6708/2007/09/126.

[142] L. Buonocore, P. Nason, and F. Tramontano. Heavy quark radiation in NLO+PS POWHEG generators. *Eur. Phys. J. C*, 78(2):151, 2018. doi: 10.1140/epjc/s10052-018-5638-y.

[143] J. Alwall, R. Frederix, S. Frixione, V. Hirschi, F. Maltoni, O. Mattelaer, H. S. Shao, T. Stelzer, P. Torrielli, and M. Zaro. The automated computation of tree-level and next-to-leading order differential cross sections, and their matching to parton shower simulations. *JHEP*, 07:079, 2014. doi: 10.1007/JHEP07(2014)079.

[144] M. L. Mangano et al. Physics at a 100 TeV pp Collider: Standard Model Processes. 7 2016. doi: 10.23731/CYRM-2017-003.1.

[145] David d'Enterria and Alexander M. Snigirev. Triple parton scatterings in high-energy proton-proton collisions. *Phys. Rev. Lett.*, 118(12):122001, 2017. doi: 10.1103/PhysRevLett.118.122001.

[146] U. Langenfeld, S. Moch, and P. Uwer. Measuring the running top-quark mass. *Phys. Rev. D*, 80:054009, 2009. doi: 10.1103/PhysRevD.80.054009.

[147] M. Aliev, H. Lacker, U. Langenfeld, S. Moch, P. Uwer, and M. Wiedermann. HATHOR: HAdronic Top and Heavy quarks crOss section calculatoR. *Comput. Phys. Commun.*, 182:1034–1046, 2011. doi: 10.1016/j.cpc.2010.12.040.

[148] Stefano Catani, Simone Devoto, Massimiliano Grazzini, Stefan Kallweit, and Javier Mazzitelli. Bottom-quark production at hadron colliders: fully differential predictions in NNLO QCD. *JHEP*, 03:029, 2021. doi: 10.1007/JHEP03(2021)029.

[149] Hua Xing Zhu, Chong Sheng Li, Hai Tao Li, Ding Yu Shao, and Li Lin Yang. Transverse-momentum resummation for top-quark pairs at hadron colliders. *Phys. Rev. Lett.*, 110(8):082001, 2013. doi: 10.1103/PhysRevLett.110.082001.

[150] Hai Tao Li, Chong Sheng Li, Ding Yu Shao, Li Lin Yang, and Hua Xing Zhu. Top quark pair production at small transverse momentum in hadronic collisions. *Phys. Rev. D*, 88:074004, 2013. doi: 10.1103/PhysRevD.88.074004.

[151] Stefano Catani, Massimiliano Grazzini, and Hayk Sargsyan. Transverse-momentum resummation for top-quark pair production at the LHC. *JHEP*, 11:061, 2018. doi: 10.1007/JHEP11(2018)061.

[152] Stefano Catani, Massimiliano Grazzini, and A. Torre. Transverse-momentum resummation for heavy-quark hadroproduction. *Nucl. Phys.*, B890:518–538, 2014. doi: 10.1016/j.nuclphysb.2014.11.019.

[153] Fabio Cascioli, Philipp Maierhöfer, and Stefano Pozzorini. Scattering Amplitudes with Open Loops. *Phys. Rev. Lett.*, 108:111601, 2012. doi: 10.1103/PhysRevLett.108.111601.

[154] Federico Buccioni, Stefano Pozzorini, and Max Zoller. On-the-fly reduction of open loops. *Eur. Phys. J.*, C78(1):70, 2018. doi: 10.1140/epjc/s10052-018-5562-1.

[155] Federico Buccioni, Jean-Nicolas Lang, Jonas M. Lindert, Philipp Maierhöfer, Stefano Pozzorini, Hantian Zhang, and Max F. Zoller. OpenLoops 2. *Eur. Phys. J. C*, 79(10):866, 2019. doi: 10.1140/epjc/s10052-019-7306-2.

[156] Tomáš Ježo, Jonas M. Lindert, Paolo Nason, Carlo Oleari, and Stefano Pozzorini. An NLO+PS generator for $t\bar{t}$ and Wt production and decay including non-resonant and interference effects. *Eur. Phys. J. C*, 76(12):691, 2016. doi: 10.1140/epjc/s10052-016-4538-2.

[157] Andy Buckley, James Ferrando, Stephen Lloyd, Karl Nordström, Ben Page, Martin Rüfenacht, Marek Schönherr, and Graeme Watt. LHAPDF6: parton density access in the LHC precision era. *Eur. Phys. J.*, C75:132, 2015. doi: 10.1140/epjc/s10052-015-3318-8.

[158] Richard D. Ball et al. Parton distributions from high-precision collider data. *Eur. Phys. J.*, C77(10):663, 2017. doi: 10.1140/epjc/s10052-017-5199-5.

[159] P. Bärnreuther, M. Czakon, and P. Fiedler. Virtual amplitudes and threshold behaviour of hadronic top-quark pair-production cross sections. *JHEP*, 02:078, 2014. doi: 10.1007/JHEP02(2014)078.

[160] Georges Aad et al. Measurement of the b-hadron production cross section using decays to $D^*\mu^- X$ final states in pp collisions at sqrt(s) = 7 TeV with the ATLAS detector. *Nucl. Phys. B*, 864:341–381, 2012. doi: 10.1016/j.nuclphysb.2012.07.009.

[161] Vardan Khachatryan et al. Measurement of the total and differential inclusive B^+ hadron cross sections in pp collisions at $\sqrt{s} = 13$ TeV. *Phys. Lett. B*, 771:435–456, 2017. doi: 10.1016/j.physletb.2017.05.074.

[162] R Aaij et al. Measurement of B meson production cross-sections in proton-proton collisions at $\sqrt{s} = 7$ TeV. *JHEP*, 08:117, 2013. doi: 10.1007/JHEP08(2013)117.

[163] Roel Aaij et al. Measurement of the $B^\pm$ production cross-section in pp collisions at $\sqrt{s} = 7$ and 13 TeV. *JHEP*, 12:026, 2017. doi: 10.1007/JHEP12(2017)026.

[164] Roel Aaij et al. Measurement of the b-quark production cross-section in 7 and 13 TeV pp collisions. *Phys. Rev. Lett.*, 118(5):052002, 2017. doi: 10.1103/PhysRevLett.118.052002. [Erratum: Phys.Rev.Lett. 119, 169901 (2017)].

[165] Matteo Cacciari, Michelangelo L. Mangano, and Paolo Nason. Gluon PDF constraints from the ratio of forward heavy-quark production at the LHC at $\sqrt{S} = 7$ and 13 TeV. *Eur. Phys. J. C*, 75(12):610, 2015. doi: 10.1140/epjc/s10052-015-3814-x.

[166] Georges Aad et al. Measurement of the differential cross-section of B^+ meson production in pp collisions at $\sqrt{s} = 7$ TeV at ATLAS. *JHEP*, 10:042, 2013. doi: 10.1007/JHEP10(2013)042.

[167] J. Beringer et al. Review of Particle Physics (RPP). *Phys. Rev. D*, 86:010001, 2012. doi: 10.1103/PhysRevD.86.010001.

[168] Stefano Frixione, Paolo Nason, and Giovanni Ridolfi. The POWHEG-hvq manual version 1.0. 7 2007.

[169] K. A. Olive et al. Review of Particle Physics. *Chin. Phys. C*, 38:090001, 2014. doi: 10.1088/1674-1137/38/9/090001.

[170] Kazuo Abe et al. Measurements of branching fractions and decay amplitudes in $B \to J/\psi K^*$ decays. *Phys. Lett. B*, 538:11–20, 2002. doi: 10.1016/S0370-2693(02)01969-X.

[171] R Aaij et al. Amplitude analysis and the branching fraction measurement of $\bar{B}^0_s \to J/\psi K^+ K^-$. *Phys. Rev. D*, 87(7):072004, 2013. doi: 10.1103/PhysRevD.87.072004.

[172] M. B. Voloshin. Remarks on measurement of the decay $\Xi_b^- \to \Lambda_b \pi^-$. 10 2015.

[173] Roel Aaij et al. Precision measurement of CP violation in $B^0_s \to J/\psi K^+ K^-$ decays. *Phys. Rev. Lett.*, 114(4):041801, 2015. doi: 10.1103/PhysRevLett.114.041801.

[174] Rhorry Gauld. Understanding forward B hadron production. *JHEP*, 05:084, 2017. doi: 10.1007/JHEP05(2017)084.

[175] Georges Aad et al. Measurement of the $t\bar{t}$ production cross-section in the lepton+jets channel at $\sqrt{s} = 13$ TeV with the ATLAS experiment. *Phys. Lett. B*, 810:135797, 2020. doi: 10.1016/j.physletb.2020.135797.

[176] Albert M Sirunyan et al. Measurement of the $\mathrm{t\bar{t}}$ production cross section, the top quark mass, and the strong coupling constant using dilepton events in pp collisions at $\sqrt{s} =$ 13 TeV. *Eur. Phys. J. C*, 79(5):368, 2019. doi: 10.1140/epjc/s10052-019-6863-8.

[177] Roel Aaij et al. Test of lepton universality in beauty-quark decays. *Nature Phys.*, 18 (3):277–282, 2022. doi: 10.1038/s41567-023-02095-3. [Addendum: Nature Phys. 19, (2023)].

[178] Georges Aad et al. Search for new phenomena with top quark pairs in final states with one lepton, jets, and missing transverse momentum in pp collisions at $\sqrt{s} = 13$ TeV with the ATLAS detector. *JHEP*, 04:174, 2021. doi: 10.1007/JHEP04(2021)174.

[179] Albert M Sirunyan et al. Search for top squark pair production using dilepton final states in pp collision data collected at $\sqrt{s} = 13\,\mathrm{TeV}$. *Eur. Phys. J. C*, 81(1):3, 2021. doi: 10.1140/epjc/s10052-020-08701-5.

[180] Georges Aad et al. Measurements of WH and ZH production in the $H \to b\bar{b}$ decay channel in pp collisions at 13 TeV with the ATLAS detector. *Eur. Phys. J. C*, 81(2): 178, 2021. doi: 10.1140/epjc/s10052-020-08677-2.

[181] A. M. Sirunyan et al. Observation of Higgs boson decay to bottom quarks. *Phys. Rev. Lett.*, 121(12):121801, 2018. doi: 10.1103/PhysRevLett.121.121801.

[182] Rhorry Gauld, Alexander Huss, and Giovanni Stagnitto. Flavor Identification of Reconstructed Hadronic Jets. *Phys. Rev. Lett.*, 130(16):161901, 2023. doi: 10.1103/PhysRevLett.130.161901. [Erratum: Phys.Rev.Lett. 132, 159901 (2024)].

[183] Michal Czakon, Alexander Mitov, and Rene Poncelet. Infrared-safe flavoured anti-k_T jets. 5 2022.

[184] Fabrizio Caola, Radoslaw Grabarczyk, Maxwell L. Hutt, Gavin P. Salam, Ludovic Scyboz, and Jesse Thaler. Flavored jets with exact anti-kt kinematics and tests of infrared and collinear safety. *Phys. Rev. D*, 108(9):094010, 2023. doi: 10.1103/PhysRevD.108.094010.

[185] Georges Aad et al. ATLAS flavour-tagging algorithms for the LHC Run 2 pp collision dataset. *Eur. Phys. J. C*, 83(7):681, 2023. doi: 10.1140/epjc/s10052-023-11699-1.

[186] Andrea Banfi, Gavin P. Salam, and Giulia Zanderighi. Accurate QCD predictions for heavy-quark jets at the Tevatron and LHC. *JHEP*, 07:026, 2007. doi: 10.1088/1126-6708/2007/07/026.

[187] R. Gauld, A. Gehrmann-De Ridder, E. W. N. Glover, A. Huss, A. Rodriguez Garcia, and G. Stagnitto. NNLO QCD predictions for Z-boson production in association with a charm jet within the LHCb fiducial region. *Eur. Phys. J. C*, 83(4):336, 2023. doi: 10.1140/epjc/s10052-023-11530-x.

[188] Nick Ellis and Anne Kernan. Heavy Quark Production at the CERN p$\bar{p}$ Collider. *Phys. Rept.*, 195:23–125, 1990. doi: 10.1016/0370-1573(90)90079-H.

[189] R. Akers et al. Measurement of the multiplicity of charm quark pairs from gluons in hadronic Z0 decays. *Phys. Lett. B*, 353:595–605, 1995. doi: 10.1016/0370-2693(95)00633-V.

[190] M. H. Seymour. Heavy quark pair multiplicity in e+ e- events. *Nucl. Phys. B*, 436: 163–183, 1995. doi: 10.1016/0550-3213(94)00565-V.

[191] G. Marchesini and A. H. Mueller. BFKL dynamics in jet evolution. *Phys. Lett. B*, 575: 37–44, 2003. doi: 10.1016/j.physletb.2003.09.041.

[192] G. Marchesini and E. Onofri. Exact solution of BFKL equation in jet-physics. *JHEP*, 07:031, 2004. doi: 10.1088/1126-6708/2004/07/031.

[193] Georges Aad et al. Measurement of the inclusive and dijet cross-sections of b^- jets in pp collisions at $\sqrt{s} = 7$ TeV with the ATLAS detector. *Eur. Phys. J. C*, 71:1846, 2011. doi: 10.1140/epjc/s10052-011-1846-4.

[194] Performance of the ATLAS Secondary Vertex b-tagging Algorithm in 900 GeV Collision Data. 6 2010.

[195] Morad Aaboud et al. Measurement of the $b\bar{b}$ dijet cross section in pp collisions at $\sqrt{s} = 7$ TeV with the ATLAS detector. *Eur. Phys. J. C*, 76(12):670, 2016. doi: 10.1140/epjc/s10052-016-4521-y.

[196] Commissioning of the ATLAS high-performance b-tagging algorithms in the 7 TeV collision data. 7 2011.

[197] Serguei Chatrchyan et al. Inclusive b-Jet Production in pp Collisions at $\sqrt{s} = 7$ TeV. *JHEP*, 04:084, 2012. doi: 10.1007/JHEP04(2012)084.

[198] Serguei Chatrchyan et al. Measurement of the Inclusive Jet Cross Section in pp Collisions at $\sqrt{s} = 7$ TeV. *Phys. Rev. Lett.*, 107:132001, 2011. doi: 10.1103/PhysRevLett.107.132001.

[199] Roel Aaij et al. Measurement of differential $b\bar{b}$- and $c\bar{c}$-dijet cross-sections in the forward region of pp collisions at $\sqrt{s} = 13$ TeV. *JHEP*, 02:023, 2021. doi: 10.1007/JHEP02(2021)023.

[200] Roel Aaij et al. Study of forward Z + jet production in pp collisions at $\sqrt{s} = 7$ TeV. *JHEP*, 01:033, 2014. doi: 10.1007/JHEP01(2014)033.

[201] Roel Aaij et al. Identification of beauty and charm quark jets at LHCb. *JINST*, 10 (06):P06013, 2015. doi: 10.1088/1748-0221/10/06/P06013.

[202] Georges Aad et al. Measurement of $D^{*\pm}$, $D^{\pm}$ and $D_s^{\pm}$ meson production cross sections in pp collisions at $\sqrt{s} = 7$ TeV with the ATLAS detector. *Nucl. Phys. B*, 907:717–763, 2016. doi: 10.1016/j.nuclphysb.2016.04.032.

[203] Rhorry Gauld, Juan Rojo, Luca Rottoli, and Jim Talbert. Charm production in the forward region: constraints on the small-x gluon and backgrounds for neutrino astronomy. *JHEP*, 11:009, 2015. doi: 10.1007/JHEP11(2015)009.

[204] Rhorry Gauld, Juan Rojo, Luca Rottoli, Subir Sarkar, and Jim Talbert. The prompt atmospheric neutrino flux in the light of LHCb. *JHEP*, 02:130, 2016. doi: 10.1007/JHEP02(2016)130.

List of Figures

List of Tables

Acknowledgements

First and foremost, I would like to thank Prof. Dr. Giulia Zanderighi. I am grateful to Giulia for welcoming me into her group, for her supervision, and for the numerous opportunities she provided during my studies. I would also like to thank to Dr. Rhorry Gauld, Dr. Javier Mazzitelli, and Dr. Marius Wiesemann for their essential collaboration in my research activities. In particular, I am deeply thankful to Rhorry for his wise and patient guidance, which was crucial during the most challenging moments of this journey.

Being a PhD student at the Max-Planck-Institute for Physics has been a great honor and an extraordinary experience for both my personal and professional development. In my research group, I had the opportunity to meet incredible people, and I would like to express my deepest gratitude to all of them. Special thanks to Dr. Daniele Lombardi, especially for his support during my first year of doctoral studies. My most sincere thanks to Christian Biello[2] and Dr. Silvia Zanoli, for all the fun moments, deep conversations, and amazing experiences we shared together. A huge thanks to Dr. Marco Niggetiedt, for all the laughs we had and for his unwavering support. Thanks to Dr. Chiara Signorile-Signorile and Dr. Giovanni Pelliccioli, for their senior advice throughout my PhD. Thanks to Ann-Sophie Mahr, Joachim Weiss, Jakob Linder, Florian König, and Luc Schnell for making our workplace enjoyable every day. A huge thanks to all the other friends I met during my time at the Institute, particularly to Giacomo Contri, Giordano Cintia, and Francesco Calisto.

I thank my parents, Roberta and Luciano, for making everything possible with their love and support, and Marcella, Giovanni, Davide, and Matteo for always keeping me close to their hearts despite the distance.

To my old friends Barbara, Carlotta, Francesco, and Vesna, all my gratitude for the adventures we shared and for their constant presence whenever I returned to my homeland. A sincere thank you to my friends Giuliana, Silvio, and Adrien.

[2]Whom I should also thank for being my loyal and stable partner in our workout sessions and during our many trips.